October 2023
Report No. 23-048



# Ultra-High Performance Concrete Reinforced with Multi-Scale Hybrid Fibers and Its Durability-Related Properties

Principal Investigator (s)
Dr. Jianqiang Wei
Dr. Sergio Breña

University of Massachusetts Lowell
University of Massachusetts Amherst

Research and Technology Transfer Section
MassDOT Office of Transportation Planning

U.S. Department of Transportation
Federal Highway Administration

# Technical Report Document Page

| | | |
|---|---|---|
| 1. Report No.<br>23-048 | 2. Government Accession No. | 3. Recipient's Catalog No. |
| 4. Title and Subtitle<br>Ultra-High Performance Concrete Reinforced with Multi-Scale Hybrid Fibers and Its Durability-Related Properties: Final Report | | 5. Report Date<br>October 2023<br>6. Performing Organization Code |
| 7. Author(s)<br>Jianqiang Wei, Sergio Breña, Cameron Ritchie, Hitesh Bhaskar More | | 8. Performing Organization Report No.<br>23-048 |
| 9. Performing Organization Name and Address<br>University of Massachusetts Lowell, 1 University Ave., Shah 200, Lowell, MA 01854 and University of Massachusetts Amherst 130 Natural Resources Way, Amherst, MA 01003 | | 10. Work Unit No. (TRAIS)<br>11. Contract or Grant No. |
| 12. Sponsoring Agency Name and Address<br>Massachusetts Department of Transportation<br>Office of Transportation Planning<br>Ten Park Plaza, Suite 4150, Boston, MA 02116 | | 13. Type of Report and Period Covered<br>Final Report - October 2023 [September 2021 – October 2023]<br>14. Sponsoring Agency Code<br>n/a |
| 15. Supplementary Notes<br>Richard Mulcahy - Project Champion, MassDOT | | |


16. Abstract

Due to its excellent mechanical properties, dense microstructure, low permeability, ease of placement and volume stability, ultra-high performance concrete (UHPC) is considered the next-generation structural concrete and is increasingly used in transportation infrastructure. While previous research efforts generated valuable results, to achieve the desired performance, UHPC needs to be well formulated with precise and optimized quantities of cementitious materials, fillers, fine aggregate, water, chemical admixtures, and fibers. In addition, the mixture design of UHPC and its correlation with the performance evolution under different curing conditions remain unclear, and there exist critical significant gaps in understanding the efficiency of fibers and mixture design on the properties of UHPC, especially the mechanical and durability-related performance. Massachusetts Department of Transportation (MassDOT) is exploring multiple infrastructure applications that can incorporate UHPC, including joints, overlays, repairs, rehabilitation, and bridge beam fabrication. This project aims to develop UHPC mix design formulations that can be implemented at ready-mix batching plants or precast/prestressed concrete fabrication facilities by identifying and maximizing the roles of fibers and additives in enhancing mechanical and durability-related properties. Four fiber-reinforced mixes and seven UHPC mixes with different fibers were investigated and a UHPC mix for large-scale batching and field applications was recommended.


| | | | |
|---|---|---|---|
| 17. Key Word<br>Ultra-High Performance Concrete (UHPC), Fiber-reinforced concrete, mixture design, fibers, strength development, permeability, durability, closure gap test | 18. Distribution Statement | | |
| 19. Security Classif. (of this report)<br>unclassified | 20. Security Classif. (of this page)<br>unclassified | 21. No. of Pages<br>211 | 22. Price<br>n/a |

**Form DOT F 1700.7** (8-72) Reproduction of completed page authorized

This page left blank intentionally.

# Ultra-High Performance Concrete Reinforced with Multi-Scale Hybrid Fibers and Its Durability-Related Properties

Final Report

Prepared By:

**Jianqiang Wei**
Principal Investigator
University of Massachusetts Lowell

**Sergio Breña**
Co-Principal Investigator
University of Massachusetts Amherst

**Cameron Ritchie**
Graduate Researcher
University of Massachusetts Amherst

**Hitesh Bhaskar More**
Graduate Researcher
University of Massachusetts Lowell

Prepared For:
Massachusetts Department of Transportation Office of Transportation Planning
Ten Park Plaza,
Boston, MA 02116

October 2023

This page left blank intentionally.

# Acknowledgements

This study was prepared in cooperation with the Massachusetts Department of Transportation, Office of Transportation Planning, and the United States Department of Transportation, Federal Highway Administration.

The Project Team would like to acknowledge the efforts of Cameron Ritchie (graduate student), Hitesh Bhaskar More (graduate student), Dr. Sergio Breña (Co-PI), and Dr. Jianqiang Wei (PI). We would like to acknowledge the help from Mark Gauthier at UMass Amherst and Gary Howe at UMass Lowell for their help with laboratory tests.

# Disclaimer

This page left blank intentionally.

# Executive Summary

This study of Ultra-High Performance Concrete Reinforced with Multi-Scale Hybrid Fibers and Its Durability-Related Properties was undertaken as part of the Massachusetts Department of Transportation (MassDOT) Research Program. This program is funded with Federal Highway Administration (FHWA) State Planning and Research (SPR) funds. Through this program, applied research is conducted on topics of importance to the Commonwealth of Massachusetts transportation agencies.

Ultra-high performance concrete (UHPC), a cementitious composite composed of optimized gradation of granular constituents, high volume of supplementary cementitious materials (SCMs), low water-to-cementitious materials ratios, and reinforcement with discontinuous fibers, is considered the next-generation structural concrete developed based on advances in the science of materials and cement chemistry. Due to its excellent mechanical properties, dense microstructure, low permeability, ease of placement and volume stability, UHPC is increasingly used in transportation infrastructure including underground structures, bridges, and structural repair. While research efforts have been invested and generated valuable results regarding concrete mixture design, utilization of chemical admixtures, incorporation of reactive additives (e.g. fly ash, slag, silica fume, etc.) and fillers (e.g. nano-silica, limestone powders), to achieve the desired performance, UHPC needs to be well formulated with precise and optimized quantities of cementitious materials, fillers, fine aggregate, water, chemical admixtures, and fibers. In addition, the mixture design of UHPC and its correlation with the performance evolution under different curing conditions remain unclear, which impedes large-scale batching and wide applications of UHPC in transportation infrastructure. In particular, there exist critical significant gaps in understanding the efficiency of fibers and mixture design on the properties of UHPC, especially the mechanical and durability-related performance.

The Massachusetts Department of Transportation (MassDOT) is exploring multiple infrastructure applications that can incorporate UHPC, including joints, overlays, repairs, rehabilitation, and bridge beam fabrication. This project aims to develop UHPC mix design formulations with locally sourced and attainable materials that can be implemented at ready-mix batching plants or precast/prestressed concrete fabrication facilities. The innovations in standard specification and practice recommendations for the mixture design will further strengthen the merits of UHPC to achieve unprecedented longevity and constructability of new structures and repair of existing structural elements such as columns, bent caps, closure caps, girders, decks, and overlays. The outcomes of this project are instrumental in taking this superior concrete material out of laboratories into real transportation infrastructures, especially in critical load-bearing structural elements, where constructability, reliability, and longevity are critically needed. The proposed database, engineering procedure, and property assessment directly benefit the MassDOT Standard Specification Development for materials for transportation structures.

The overall research objective of this project is to develop FRC and UHPC mixtures to identify and maximize the roles of fibers and additives in enhancing mechanical and

durability-related properties. In this project, a state-of-the-art methodology coordinating with MassDOT's effort on the deployment and development of high-quality fiber-reinforced concrete (FRC) and UHPC was investigated. The key outcomes of this project include:

- A solid literature review and fundamental understanding of the current state of knowledge in materials, testing standards, and applications of FRC and UHPC.
- Comprehensive characterizations of macro-fibers for FRC and micro-fibers for UHPC, including physical properties, strength, elongation rate, and microstructure analysis. An experimentation-based database for qualified fibers selection and screening for FRC and UHPC was developed.
- Development of mixture designs of both FRC and UHPC based on selections of Portland cement type, aggregate size distribution, fibers, supplementary cementitious materials (SCMs), and chemical admixtures. This effort includes the investigations of four FRC mixes and seven UHPC mixtures with a variety of cement, SCMs, and fibers.
- Laboratory investigations for a comprehensive understanding of FRC and UHPC properties including physical, mechanical, and durability performance. The autogenous shrinkage, compressive strength, flexural strength, direct tensile strength, permeability, and resistance against sulfate attack were investigated.
- Based on the property evaluations, a mixture of UHPC for large-scale batching and field applications was recommended.
- Laboratory mock-up tests on concrete closure gap connections cast between two panels were conducted to simulate the connection between two bridge deck panels and to confirm the viable applications of the developed UHPC mixture in this type of transportation infrastructure in narrow closure pours and straight rebars.

This project report consists of 10 sections. Section 1 is a brief introduction to the problem and a description of the scope of the research. Section 2 describes the effects of the literature review on RFC and UHPC. Section 3 presents the characterizations of macro-fibers and micro-fibers used for RFC and UHPC, respectively. Section 4 reports the efforts on mixture design of FRC and UHPC, as well as the hydration behavior of the cementitious binders in the developed UHPC mixes. Section 5 details the results of testing of physical, mechanical, and durability of FRC and UHPC with different fibers under different curing conditions. Section 6 overviews the UHPC mixture for large-scale batching and field applications. Section 7 details the testing and results of the closure gap test. Section 8 summarizes the key conclusions drawn from this project. Section 9 present the cited references.

# Table of Contents

This page left blank intentionally.

# List of Tables

# List of Figures

This page left blank intentionally.

# List of Acronyms

| Acronym | Expansion |
|---|---|
| MassDOT | Massachusetts Department of Transportation |
| FHWA | Federal Highway Administration |
| SPR | State Planning and Research |
| UHPC | Ultra-high performance concrete |
| FRC | Fiber-reinforced concrete |
| SCMs | Supplementary cementitious materials |
| w/c | Water to cement ratio |
| PVA | Poly vinyl alcohol |
| AR | Alkali-resistant |
| ACI | American Concrete Institute |
| FDOT | Florida Department of Transportation |
| TxDOT | Texas Department of Transportation |
| GGBS | Ground granulated blast furnace slag |
| OPC | Ordinary Portland cement |
| PCA | Portland Cement Association |
| ASTM | American Society for Testing and Materials |
| CPM | Compressible packing model |
| A&A model | Andersen-Andreassen model |
| TFHRC | Turner-Fairbank Highway Research Center |
| NYSDOT | New York State Department of Transportation |
| SFRC | Steel fiber reinforced concrete |
| MK | Metakaolin |
| PSDs | Particle size distributions |
| d50 | Median particle size |
| HRWR | High-range water-reducing |
| RSS | Summation of squares of the residuals |
| FTIR | Fourier Transform Infrared |
| TGA | Thermogravimetric analysis |
| XRD | X-ray diffraction analysis |
| CH | Calcium hydroxide |
| CC | Calcium carbonate |
| C-S-H | Calcium silicate hydrate |
| UFFA | Ultra-fine micro-fly ash |
| $C_3S$ | Tricalcium silicate (alite) |
| $C_2S$ | Dicalcium silicate (belite) |
| PCI | Precast/Prestressed Concrete Institute |
| NEDBT | Northeast Deck Bulb Tee Guidelines |
| AASHTO | American Association of State Highway and Transportation Officials |

This page left blank intentionally.

# 1.0 Introduction

This study of Ultra-High Performance Concrete Reinforced with Multi-Scale Hybrid Fibers and Its Durability-Related Properties was undertaken as part of the Massachusetts Department of Transportation (MassDOT) Research Program. This program is funded with Federal Highway Administration (FHWA) State Planning and Research (SPR) funds. Through this program, applied research is conducted on topics of importance to the Commonwealth of Massachusetts transportation agencies.

Ultra-high performance concrete (UHPC) is a cementitious composite consisting of cement, supplementary cementitious materials (SCMs), fine aggregates, chemical admixtures, a low water-to-cement ratio (w/c), and fibers. It is considered the next generation of structural concrete developed based on advances in cement chemistry, materials science and optimized packing of granular constituents, and fiber reinforcement. Due to the excellent mechanical properties, low permeability, ease of placement, and volume stability, in recent decades, the use of UHPC has been widely accepted by the construction industry for a variety of civil infrastructure, including buildings and bridges. The exceptional properties of UHPC on strength and durability (freezing-thawing resistance, abrasion resistance, chloride ion penetration resistance) make it a promising construction material for durable and sustainable civil infrastructure systems. While research efforts have been invested and generated valuable results, there still exist critical significant gaps in understanding the efficiency of fibers and mixture design on UHPC performance, especially the mechanical and durability-related properties. The overall research objective of this project is to develop novel UHPC mix design formulations with locally sourced and attainable materials that can be implemented at ready-mix batching plants or precast/prestressed concrete fabrication facilities. Mechanical and durability-related properties of UHPC and fiber-reinforced concrete (FRC) with different fibers and mixture designs were investigated via laboratory and mock-up tests. To accomplish the objectives of the project, the following six tasks were conducted in this project:

## 1.1 Task 1: Literature Review on Materials, Testing Standards and Applications of FRC and UHPC

This project starts with a comprehensive literature review on the current state of UHPC mixture design, fiber reinforcement, and applications of UHPC in transportation infrastructure projects by collecting and synthesizing available research papers and reports, committee documents, testing standards and testing protocols. The typical properties of UHPC, type and volume fractions of fibers, and the role of UHPC in new and existing structures were discussed. We also reviewed publications in the field of UHPC to include the latest material innovations and testing methods.

### 1.2 Task 2: Quantified Fiber Selection and Characterization

In Task 2, four types of micro-fibers, including steel fiber, poly vinyl alcohol (PVA) fiber, basalt fiber, and alkali-resistant (AR) glass fiber, have been collected and characterized. Microstructure analysis and tensile strength tests on single fibers have been conducted. The fibers were compared in terms of dimension, surface features, strength, and modulus. These fiber properties were correlated to the ease of dispersion, interfacial bonding with the concrete matrix, and efficiency in improving the strength of concrete in the following tasks.

### 1.3 Task 3: Mixture Design of FRC and UHPC

In Task 3, seven mix design formulations of UHPC based on different materials were developed. Two types of Portland cement (Type I/II and type III), three types of fly ash (Class F, Class C, and Micro-fly ash), silica fume, metakaolin, and the four types of fibers studied in Task 2 were investigated as the raw materials for UHPC. Upon the availability or selection of raw materials, it is also important to determine their amounts and proportions to ensure adequate packing of fine and coarse particles in the concrete system to achieve a dense microstructure, which plays a critical role in determining the mechanical and durability properties of concrete. It should be noted that, if only relying on the Modified Andersen-Andersen model and the least square method, the proportions of UHPC will not be reasonable and practical. In this study, a novel two-step particle-packing density optimization method was developed by covering the optimum binder content and the optimum contents of each SCM in the binder, as well as the optimized particle packing density. The hydration of cementitious binders of the seven UHPC groups was investigated by monitoring the release of hydration heat and the evolution of reaction products.

### 1.4 Task 4: Laboratory tests of Physical, Mechanical and Durability Properties of FRC and UHPC

In this task, the permeability, autogenous shrinkage, compressive strength, flexural strength, and tensile strength of UHPC were investigated. The influences of two curing conditions (regular lime water curing and steam curing) and four types of fibers (steel, PVA, basalt, and AR glass fibers) on the properties of UHPC were uncovered. The fracture surface and crack propagation in UHPC after the flexural and direct tensile tests were analyzed. The resistance of UHPC against sulfate attack was also investigated.

### 1.5 Task 5: Mixtures for Large-Scale Batching and Field Applications

Based on the mixture design work in Task 3 and the concrete property evaluation in Task 4, the UHPC mixture for large-scale batching and commercial field applications was recommended. The application of UHPC in a sidewalk project on the PI's campus was conducted.

### 1.6 Task 6: Mockup and Field Tests

In this task, large-scale laboratory tests on concrete closure gap connections were conducted to determine if the UHPC mixture developed was viable to be used in this type of transportation infrastructure. The UHPC mixture was used to fabricate the longitudinal closure pour cast between two panels to simulate the connection between two bridge deck panels. The objectives were to evaluate whether the connection develops the required strength, whether narrow closure pours could be used in combination with the developed mixture without negative effects on transverse strength between the panels, and whether straight bars, rather than the typical hooped bars, were able to develop the required strength within the UHPC for closure gaps.

This page left blank intentionally.

# 2.0 Literature Review

## 2.1 Fiber Reinforced Concrete

### 2.1.1 About fiber-reinforced concrete

The concept of using fiber in construction dates back centuries, when straw and horsehair were used in mud bricks and mortar, the application of which was known to increase the toughness and reduce the cracks in structures. In modern concrete, more research efforts have been conducted on a variety of fiber types to improve tension resistance and ductility. American Concrete Institute (ACI) Committee 544 prescribes the standards practices and manual for FRC, which is defined as concrete containing dispersed randomly oriented fibers [1]. These fibers can be made up of steel, carbon, synthetic materials, or naturally occurring asbestos or cellulose fiber. It has been found that the addition of fibers can significantly improve tensile strength, toughness, and post-cracking strength, and decrease plastic and drying shrinkages with increased long-term performance and extended service life. In summary, compared with plain concrete, the advantages of FRC include:

- FRC is used in structures where high tensile and reduced cracking is desirable and where conventional reinforcement cannot be provided because of size restrictions.
- It minimizes the requirement of steel reinforcement.
- The toughness of FRC is 10-40 times higher than that of normal concrete.
- Improved impact and abrasion resistance.
- Improved freeze-thaw resistance and hence is durable and requires less maintenance.
- Improved resistance to plastic shrinkage and drying shrinkage over time by arresting the initial propagation of cracks and controlling the width of cracks over time.
- In the case of fire accidents, it improves the resistance to spalling.
- Lower life-cycle cost than plain concrete and steel-reinforced concrete.

The properties of FRC can be affected by the following factors:

- *Type of fibers.*

ASTM C1116 [2] classifies FRC by the material type of the fiber incorporated into 4 types:

  - Type I Steel Fiber-Reinforced concrete,
  - Type II Glass Fiber-Reinforced concrete,
  - Type III Synthetic Fiber-Reinforced concrete,
  - Type IV Natural Fiber-Reinforced concrete.

- *Aspect ratio of fibers.*

Aspect ratio (l/d) is defined as the ratio of length (l) to diameter (d) of the fibers. The aspect ratio varies from 10 to 300 depending on the fibers used.

- *Quantity of fibers.*

Typically, the fiber quantity is expressed in percentage (%) by the volume of concrete, which varies from 0.5% to 3%. There are a few studies incorporating 4% to 5% of fibers, which did not yield the desirable quality of FRC.

- *Tensile strength and modulus of elasticity.*

To achieve an effective stress transfer between the fibers and the concrete, the modulus of elasticity of fibers should be greater than that of concrete. Steel, carbon, and glass are high-modulus fibers. These fibers impart strength and stiffness to the concrete. Within an appropriate range, positive correlations between fiber fraction and tensile, compressive and flexural strength, and toughness were observed. The use of these fibers can delay the appearance of the first crack and increase the post-crack loading capacity of the concrete.

Low-modulus fibers like synthetic fibers (polypropylene, polyester) play an effective role in bridging micro-cracks due to drying and plastic shrinkage, which are formed even before the application of load to the concrete. Overall microstructure of the concrete can be improved with the addition of these fibers thereby reducing water bleeding and permeability.

- *Single or hybrid fibers.*

- *Size of fibers.*

Based on the diameter less or more than 0.3 mm, fibers can be derived into micro-fiber and macro-fibers.

- *Fiber orientation and distribution of fibers.*

- *Fiber shape.*

### 2.1.2 Mixture design of fiber-reinforced concrete

Like plain concrete, FRC employs a variety of mixture proportions depending on the applications in different structures like hydraulic structures, airport, and highway paving and overlays, industrial floors, bridge decks, and shotcrete. The type and properties of fiber play important roles in the mix design of FRC as the inclusion of different fibers affects the fresh and hardened state of FRC. Steel fiber is one of the most commonly used fibers for concrete. While the addition of steel fibers seems to reduce the workability of the concrete, the workability is noticed to be improved with vibration. The use of polymeric fibers inherently reduces the workability of the concrete. American concrete institute (ACI 544.4R [1]) specifies the guidelines for proportioning, mixing, placing, and finishing steel fiber reinforced concrete. It suggests that, when a higher dosage of steel fibers is used in concrete, adjustments in mix design to provide better workability should be done by increasing the fine aggregate over coarse aggregate using a maximum coarse aggregate factor of 0.55. Many state DOTs, like the Florida DOT (FDOT) and the Texas DOT (TxDOT) suggest a similar design.

A literature review based on [3-17] indicates that the mix design of FRC is typically developed with a certain percentage of fiber between 0.5%-3% by the total volume of concrete. Due to the fact that a variety of fibers can be used for concrete and each fiber has its unique influence on workability physical and mechanical properties of concrete, practical methods for optimum mixture design are needed. Natraja et.al [10] proposed the reproportioning steel fiber mix design method, where a trial-and-error procedure was used by adjusting the workability of the concrete using superplasticizers. A nomogram-based mix design method for steel FRC was developed by Ulas et. al [18], in which both fresh and hardened properties of concrete, such as workability, flexural strength, and modulus of toughness, are considered. Typical proportions of normal-weight steel FRC as mentioned by ACI 544 are given in Table 2.1.

**Table 2.1: Range of proportions for normal weight steel FRC [1]**

| Mateial contents according to aggregate size | Aggregate sieze of 3/8-in | Aggregate sieze of ¾-in | Aggregate sieze of 1 1/2-in |
|---|---|---|---|
| Cement ($kg/m^3$) | 350-600 | 300-550 | 270-420 |
| Water to cement ratio | 0.35-0.45 | 0.35-0.50 | 0.35-0.55 |
| Percent of fine to coarse aggregate | 45-60 | 45-55 | 40-55 |
| Entrained air content, percent | 4-8 | 4-6 | 4-5 |
| Deformed fiber content (volume percent) | 0.4-1.0 | 0.3-0.8 | 0.2-0.7 |
| Smooth fiber content (volume percent) | 0.8-2.0 | 0.6-1.6 | 0.4-1.4 |

As the most important ingredient of concrete, cement involves hydration reaction, setting and hardening, and binding all the other ingredients together responsible for the strength development of concrete. ASTM C150 [19] classifies Portland cement into five types, including Type I ordinary Portland cement, Type II sulfate-resistant cement, Type III high early strength cement, Type IV low heat cement, and Type V high sulfate-resistant cement. Among these types of cement, Type I or I/II cement is the most commonly used cement for FRC, the amount of which is correlated to the size of aggregates.

Aggregates are inert components of concrete, which do not involve in the hydration process. These constitutes take up to 60-75% volume of concrete and are divided into two distinct categories, i.e., fine and coarse aggregates. River sand and crushed/powdered gravel are used as fine aggregates. These are well graded with particle size less than 4.75 mm and pass through the No.4 sieve. Coarse aggregates are usually gravels retained on the No.4 sieve with a size range from 4.75 mm to 20 mm.

As the name suggests, supplementary cementitious materials (SCMs) or mineral admixtures are the materials used as a supplement or addition to modifying cement. These materials are available as industry by-products, such as fly ash, silica fume, metakaolin, and ground

granulated blast furnace slag (GGBS). The incorporation of SCMs into cement has two major advantages in FRC:

(i) It reduces the amount of cement used in concrete thereby reducing the amount of carbon dioxide ($CO_2$) emission making concrete more sustainable.
(ii) These materials have similar or smaller particle sizes than cement with high pozzolanic reactivity, which can improve particle packing density and enhance the hydration of the cement paste, thereby resulting in the formation of additional C-S-H gel and providing higher strength and durability to concrete.

It is worth noting that SCMs are not the major ingredient but an alternative, the addition of which is dependent on the needs of the project, while there are studies indicating the use of SCMs, like silica fume, and fly ash, has additional advantages in FRC. In the presence of silica fume, increased effectiveness of steel fiber on the properties improvement of concrete, such as long-term compressive strength, bulk resistivity, and water absorptivity, was obtained [7-9]. It is reported that the use of fly ash can benefit the dispersion of polymeric fibers in the matrix of concrete, ultimately increasing the strength of FRC [17].

Admixtures are chemicals added to concrete during mixing to modify the fresh or hardened properties of concrete. Depending on the necessity, the admixtures can be a single chemical or a combination of multiple agents. Based on the function, chemical admixtures can be classified into the following types:

- Accelerators and retarders, which chemically interact with cement to either speed up or retard the hydration, setting, and hardening rates.
- Plasticizers/superplasticizers, which are surfactants interplay with cement particles to decrease agglomeration of the cement particles, improve dispersion, and improve the workability of concrete thereby improving the flowability consistency of concrete with lower water-to-cement ratios.
- Air entraining agents, which can introduce small air voids into concrete to improve resistance to freezing and thawing cycles and surface scaling.
- Viscosity modifier, which modifies rheological properties of concrete.
- Corrosion inhibitors that inhibit corrosion of steel rebar in reinforced concrete.

In FRC, it is observed that the concrete workability decreases with the volume of fibers, which in most cases is compensated by increasing the water-to-cement ratio. Due to the fact that an increase in water-to-cement ratio can result in compromising the physical, mechanical, and durability properties of concrete, the use of admixtures at a high fiber fraction level is suggested to prevent the fiber balling and improve the workability of FRC without compromising structural performance [3-5]. The use of superplasticizers, including polycarboxylic-ether-based, naphthalene sulphonate [20], and melamine [30] based superplasticizers [6, 7, 9, 11, 17], with a low dosage of less than 2% by volume is commonly observed in FRC.

### 2.1.3 Fibers

Fiber is one of the most important ingredients in the manufacturing of FRC and is the key ingredient distinguishing FRC from regular concrete. Physically, fibers are longer and

slenderer than other granular/spherical ingredients of concrete such as cement, aggregates, and supplementary cementitious particles. Chemically, inert components that are not involved in reaction with concrete are used. Functionally, fibers are used to provide the tensile strength to concrete to compensate for its inherent brittle nature. It helps in delaying the appearance of cracking in concrete and plays an effective role in bridging cracks. The materials, aspect ratios, quantity, and key functions of fibers in FRC are summarized in Table 2.2 and Table 2.3. It can be seen that the material (e.g., steel, carbon, polymer, natural fiber), geometry (i.e., its length (l), diameter (d), aspect ratio (l/d)), and the content of fibers all affect the fresh and hardened properties of concrete. Moreover, steel fibers can be manufactured in different shapes and sizes like straight, hooked end, corrugated, etc., which also impact the role of fibers in the concrete mixture.

**Table 2.2: Review of single fibers used in FRC**

| Fiber (Type) | Aspect ratio (l/d) | Quantity | Combination | Key findings | Reference |
|---|---|---|---|---|---|
| Glass | 12/0.015 | 0.5 3.5% | Single | • Strength is increased at 1.5% volume of fibers;<br>• Workability decreases with the volume of fibers. | [3] |
| Glass | 12/0.014 | 0.03% | Single | • Increases in compressive, split tensile, and flexural strength;<br>• Decrease in bleeding due to the addition of fibers. | [4] |
| Steel *Hooked*<br>*Wavy*<br>*Wavy*<br>*Flattened ends*<br>Polyolefin | 60/0.9<br>60/1.0<br>50/1.0<br>50/1.0<br>40/(0.2x3) | 30 kg/m$^3$<br>50 kg/m$^3$<br><br><br>4.5-5.3 kg/m$^3$ | Single | • The volume fraction of synthetic fibers is less than steel fiber;<br>• Steel fibers increased the compressive strength more effectively than synthetic fibers;<br>• A slight increase in flexural strength was observed. | [5] |
| Basalt<br><br>Steel<br>*Hooked ends* | 36/(0.6*)<br>50/(0.6*)<br><br>38/0.9 | 0%, 0.15%, 0.31%, 0.46%<br><br><br>0.51% | Single | • Higher dosage of fibers leads to fiber balling;<br>• The addition of fibers increases the first crack load in the flexural test but no significant increase in impact is found. | [6] |
| Steel<br>Polypropylene<br>glass | 13/0.02<br>12/0.040<br>112/0.014 | 0%, 0.5%,<br>1%,<br>1.5%, 2% | Single | • Compressive strength increases;<br>• The mixture containing polypropylene and glass hybrid fibers shows lower porosity. | [8] |
| Steel<br>*Hooked end* | | 0%, 0.5%,<br>1% | Single | • Increase in strength is obtained with the addition of the fibers | [9] |
| Polyolefin | 48/0.903<br>60/0.903 | 0.66% | Single | • The minimum post-cracking load and the maximum post-cracking remaining load are proportional to the content of fibers located in the lower third of the fracture surface. | [11] |
| Polypropylene | 58/(64mm$^2$) | 0.44%<br>0.88% | Single | • A significant loss in capacity soon after cracking is observed | [13] |
| Steel<br>*Hooked ends*<br>*waved* | 31/0.75<br>25/0.75 | 0%, 0.5%,<br>1%, 1.5%, | Single | • Specimens with hooked ends performed better than wavy fibers;<br>• Post-cracking strength is improved by both hooked and wavy fibers. | [14] |
| Hemp fiber | Width<br>23.15mm | - | Single | • Decreased strength in hemp fiber-reinforced concrete | [15] |
| Steel<br>*Hooked ends* | 35/0.53 | 0.5 | single | • Orientation and distribution are dependent on yield stress;<br>• Reduced compressive strength;<br>• Fiber orientation plays a major role in affecting concrete strength | [16] |

**Table 2.3: Review of hybrid fibers used in FRC**

| Fiber (Type) | Aspect ratio (l/d) | Quantity | Combination | Key findings | Reference |
|---|---|---|---|---|---|
| Steel<br>*Hooked ends*<br>Polypropylene<br>Glass<br>Polyester | 30/0.5<br>20/0.10<br>6/0.01<br>12/0.05 | 0.5%<br>(0.38+0.12)%<br>(0.25+0.25)%<br>(0.12+0.38)% | Single<br>+<br>hybrid | • Hybrid fibers are more efficient in crack reduction than single fibers;<br>• Steel-polyester hybrid fibers caused the best crack reduction (99%);<br>• Combinations of high and low-modulus fibers, such as steel-polyester or steel-polypropylene, perform better than steel-glass hybrid fibers. | [7] |
| Steel<br>*Hooked end*<br>polyolefin | 35/0.55<br>60/0.903 | 0.33%<br>0.49%<br>0.82% | single<br>+<br>Hybrid | • No change in compressive strength;<br>• Self-compacting concrete can be developed by adding steel and polyolefin hybrid fibers. | [12] |
| Steel<br>Hooked ends<br>Hooked ends<br>Straight<br>Polypropylene | 40/0.3<br>30/0.3<br>6/0.1<br>12/0.018 | 0.9%, 0.75% | Hybrid | • Fly ash helped in the dispersion of polypropylene fibers<br>• Straight steel fibers increase the compressive strength of concrete | [17] |

### 2.1.4 Testing standards of fiber-reinforced concrete

The commonly used testing standards for evaluations of the physical, mechanical, and durability of FRC are summarized in Table 2.4 to Table 2.6.

**Table 2.4: Testing standards for physical properties of FRC**

| Testing method | Specimen | Equipment | Standard |
|---|---|---|---|
| Flowability -Inverted slump cone test | Fresh concrete | Inverted slump cone and vibrator | ASTM C995 |
| Flowability -Slump flow test | Fresh concrete | Slump cone | ASTM C143 |
| Flowability-J-ring method | Fresh concrete | J ring | ASTM C1621 |
| Flowability -V-funnel method | Fresh concrete | V-funnel | EN 12350 |
| Flowability-L-box method | Fresh concrete | L-box | EN 12350 |
| Porosity-Apparent porosity test | Cylinder or beam with a volume not less than 350 $cm^3$ | Balance, container to weigh concrete in water | ASTM C948 |
| Porosity-Percent void method | Cylinder or beam with a volume not less than 350 $cm^3$ | Balance, container to weigh concrete in water | ASTM C642 |
| Water Permeability Test | 2” thick specimen, cracked using the splitting tension test | Compressive testing machine | ACI 544.9R-17 [20] ASTM 1202 |
| Gas permeability Test | 8 x 4 in. diameter specimens subjected to axial compressive loading; disc extracted from the middle of the cylinder for gas permeability test | Constant head permeameter | ACI 544.9R-17 |
| Plastic shrinkage test | At least two control specimens and at least two FRC specimens with the same mixture proportions. Cast test panels in accordance with ASTM C192/C192M. | Stress riser, vibrating platform | ASTM C1579 |
| Restrained shrinkage test | 16” diameter tube, 3” thick, 6” tall | Instrumented steel ring with at least 2 strain gauges | ASTM C1581 |

**Table 2.5: Testing standards for mechanical properties of FRC**

| Testing method | Specimen | Equipment | Standard |
|---|---|---|---|
| Compressive strength- Cylinder compression testing per ASTM C 39 | 4 x 8 in. cylinders or 6 x 12 in. cylinders | Compression testing machine | ACI 544.9R-17 |
| Flexural strength- Third point or center point bending test | Beams per ASTM C 78 or C 293 | Third-point or center-point bending machine | ACI 544.9R-17 |
| Flexural strength- Toughness after matrix failure | 4 x 4 x 14 in. or 6 x 6 x 20 in. prisms | Third point testing machine | ASTM C1609 |
| Flexural strength- Third point or center point bending test(post-cracking strength) | 4 x 4 x 14 in. or 6 x 6 x 20 in. prisms | Third point testing machine- displacement rate control | ASTM C1399 |
| Tensile strength- Direct tension | Thin prisms or dogbones of various shapes | Universal testing machine | ACI 544.9R-17 |
| Tensile strength- Indirect tension; similar to splitting test(direct tension preferred) | 4 x 8 in. cylinders or 6 x 12 in. cylinders | Compression testing machine, cylinder loaded along the diameter | Similar to ASTM C496 |
| Shear test- Push off test | No standard size. Cubes or cylinders with 2 notches (e.g. 5 x 12 x 23 in. notched specimen, see Swamy et al. 1987) | Universal testing machine | ACI 544.9R-17 |

**Table 2.6: Testing standards for durability of FRC**

| Testing method | Specimen | Equipment | Standard |
|---|---|---|---|
| Corrosion-<br>Half-cell potential method | Reinforced concrete regardless of size or depth of concrete cover | Reference electrode, electrical junction device, voltmeter, electrical lead wire | ASTM C876 |
| Corrosion-<br>Ponding method | 11 in. by 6 in. 4.5 in. concrete beams with two embedded bars | Vomiter, a reference electrode | ASTM G109 |
| ASR-<br>Mortar bar test | 1 by 1 by 10 in. mortar bar | Comparator | ASTM C1260 |
| ASR-<br>Concrete prism test | 3 by 3 by 10 in. concrete prism | Comparator | ASTM C1293 |
| Sulfate attack-<br>Mortar bar test | 1 by 1 by 10 in. mortar bar | Comparator | ASTM C1012 |
| Sulfate attack-<br>Concrete prism test | 3 by 3 by 10 in. concrete prism | Comparator | ASTM C1293 |
| Sulfate attack-<br>Cylinder method | 3 by 6 in. cylinders | Environmental chamber | PCA R&D No. 2486 |
| Surface scaling-<br>Deicing chemical method | Slab with an area of 72 inch$^2$ and 3 in. depth. | Freezing chamber | ASTM C672 |
| Freeze-thaw cycles<br>Rapid freezing and thawing method 1 | 3 by 3 by 10 in. concrete prism | Freezing-thawing chamber | ASTM C666 |
| Freeze-thaw cycles<br>Rapid freezing and thawing method 2 | Full-sized units, or cut units with a surface area of at least 29.5 inch$^2$ | Freezing-thawing chamber | ASTM C1645 |

## 2.2 Ultra-High Performance Concrete

### 2.2.1 Mixture design of UHPC

While there is no guideline or a specific code for the design of UHPC, extensive research efforts have been carried out in the development of UHPC. As per ACI Committee 363, UHPC is characterized by compressive strength greater than 150 MPa and is also characterized by higher ductility and durability. With the invention of water-reducing agents, water to binder ratio of less than 0.2 is achievable, which helps in reducing the porosity and hence increases the density of concrete. The densely packed constituent particles of concrete are the primary reason for the high strength. To achieve the maximum particle packing density, small particles must fill up the voids between the large ones. Over the years, many analytical models have been developed aimed at reducing the pores and thereby increasing the particle packing density. More practically, the compressible packing model (CPM) and the modified Andersen-Andreassen (modified A&A) model [21] have been widely used in the mixture design of UHPC. The compressible packing model uses the particle size distribution of both reactive and nonreactive phases alongside their virtual packing densities to calculate a compaction index, K. The original Andersen and Andreasen model was first published in 1930 [21], and Funk and Dinger [22] modified the model to include a minimum particle diameter. The modified equation is shown in Equation (2.1)

$$P(D) = \frac{D^q - D_{min}^q}{D_{max}^q - D_{min}^q} \tag{2.1}$$

where P(D) is the fraction of total solids smaller than diameter D [22, 23]. q is the distribution modulus, which varies between 0.22 and 0.25 [24, 25]. $D_{max}$ and $D_{min}$ are the maximum and minimum sizes of solid particles, respectively.

According to [26-47], Type I/II cement and Type IV cement with low tricalcium aluminate (C3A) are commonly used in UHPC. An important factor for the high strength of UHPC is the high quantity of cement (more than 700 kg/m$^3$), which is 2-3 times more than OPC. Different from regular concrete, coarse aggregates are normally omitted in the mix design of UHPC. Only sand with particle size between 150 mm and 4.75 mm, without defects, abnormalities or anomalies are used to maximize particle packing of UHPC. In a unique study by Arora et.al. [43], coarse aggregates with sizes of 6.25 mm, 4.75 mm, and 2.36 mm were used in the design of UHPC based on the compression packing models.

To achieve ultra-high strength in UHPC, SCMs become inevitable ingredients as the particle sizes of SCMs are smaller cement grains, which is favorable to reducing voids in concrete. Also, by adding SCMs, the pozzolanic reactions can be triggered, which can significantly enhance the hydration of cement and densify the microstructure of the hydrated cement paste, thereby obtaining increased strength, low permeability, and improved deterioration resistance. The use of silica fume is seen in most of the pieces of literature [26-47], the dosage of which is found to be 20% to 30% by weight of cement. Arel [32] investigated the effect of silica fume fineness on the impact resistance of UHPC, where three different silica

fume with surface areas of 17,200, 20,000 27,600 $m^2$/kg were used. The results indicated that the silica fume with the largest surface area 27,600 $m^2$/kg increased the impact and compressive strength of the UHPC most effectively. Another commonly used SCM in UHPC is fly ash [43], which is usually used tother with silica fume and limestone powder for synergistic effects.

In addition to the reactive SCMs, inert nano-particles, such as nano quartz and limestone powders at around 3.2% by weight of cementitious materials, which can further improve the particle packing density, are also commonly used in UHPC [39, 40, 43]. The ITZ around the steel fiber is improved with the usage of nano limestone powders, and hence the bond properties between the fibers and the concrete matrix, and eventually, the strength of concrete can be increased.

Besides the difference in aggregates and mixture proportions, a water-to-cement ratio lower than 0.2 is typically used in UHPC, which is much lower than that of FRC. This reduction in water to cement ratio decreases the number of capillary pores and voids thus the principle of compact particle packing is achieved in UHPC. Due to the low amount of mixing water, superplasticizers or high-range water reducers are a must component of UHPC. Typical mixture proportions of UHPC are summarized in Table 2.7.

**Table 2.7: Typical proportions of UHPC**

| Materials | Ductal | Teichmann and Schmidt | Teichmann and Schmidt | Yu et.al. |
|---|---|---|---|---|
| Portland Cement | 712 | 733 | 580 | 700 |
| Fine sand | 1020 | 1008 | 354 | 1055 |
| Micro sand | - | - | - | 219 |
| Silica Fume | 231 | 230 | 177 | 44 |
| Ground Quartz 1 | 211 | 183 | 131 | 175 |
| Ground Quartz 2 | 0 | 848 | 324 | 0 |
| HRWR | 30.7 | 32.9 | 33.4 | 46 |
| Accelerators | 30.0 | - | - | - |
| Steel fibers | 156 | 194 | 192 | - |
| Water | 184 | 161 | 141 | - |

### 2.2.2 Fibers

Among a variety of fibers, steel fiber is the most widely used one in UHPC, while the aspect ratio, quantity, and quality of fibers remain the critical criteria in determining the properties of the fresh and hardened state of UHPC. Different from regular steel fibers used in FRC, the steel fibers for UHPC have a smaller size, e.g., with a length of 0.31 to 0.63 in. and a

diameter of 0.008 in., which are called micro-steel fibers. These micro-sized fibers are a key ingredient of UHPC to provide ductility, strength, and durability to concrete. Table 2.8 to Table 2.10 summarize the types of fibers based on a comprehensive lecture review. The fibers that have been investigated in UHPC include steel fibers, basalt fibers, polymeric fibers, and glass fiber, as well as the combinations of multiple fibers, which can bridge the cracks more effectively than single fibers.

**Table 2.8: Fibers used in UHPC**

| Fiber (type) | Aspect ratio (*l*/*d*) | Volume fraction | Single/ hybrid | Key findings | Reference |
|---|---|---|---|---|---|
| Steel (Straight) | 13/0.2 | 2% | Single | • Parallel fibers result in 61% higher flexural strength. | [26] |
| Steel (Straight) (Hooked end) (Twisted) | 13/0.2<br>30/0.3<br>30/0.375<br>62/0.375<br>30/0.3 | 1%<br>1.5%<br>2%<br>2.5% | Single + Hybrid | • Four types of macro-fibers combined with micro-fibers to form a hybrid fiber-reinforced UHPC;<br>• The UHPC with hybrid fibers (1.5% of hooked fiber + 1% of short steel fibers) show better overall properties | [27] |
| Steel (Straight) | 13/0.2 | 0%<br>2% | Single | • UHPC with fibers shows double tensile strength than that without fibers. | [28] |
| Steel (straight) | 8/0.2<br>12/0.2<br>16/0.2 | 0%<br>1%<br>3%<br>6% | Single | • While fiber length, dosage, and shape have no significant effect on compressive strength, the split tensile strength, flexural strength, and peak crack load show a significant increase. | [29] |
| Steel (Straight) | 13/0.2 | 1%<br>2%<br>3%<br>4% | Single | • Compressive strength is high at 3% fiber volume and low at 4%;<br>• Fiber pull-out strength reaches the highest value at a fiber fraction of 2%. | [30] |
| Steel (Straight) (Hooked) | 13/0.2<br>6/0.16<br>35/0.55 | 2% | Single + Hybrid | • The UHPC with hybrid fibers shows better workability and higher compressive strength when compared to that containing single fibers. | [31] |
| Steel (Hooked end) | 8/0.2<br>13/0.2<br>16/0.2 | 1.9% | Single | • Compressive strength increases by 1.5–2.1% with increasing fiber content;<br>• Under steam curing, a 90-day compressive strength of 177 MPa is obtained;<br>• Impact resistance is directly proportional to the compressive strength value;<br>• The best compressive strength and impact resistance results are obtained from the silica fume with a specific surface area of 27,600 $m^2$/kg. | [32] |
| Steel (Straight) (Hooked end) | 6/0.16<br>30/0.55 | 0%<br>0.25%<br>0.5%<br>0.75%<br>1%<br>1.5%<br>2% | Single | • The UHPC with 2% micro-steel fiber exhibits the best compressive strength of 180 MPa and the highest split tension strength and modulus of elasticity;<br>• The UHPC with 2% of hooked steel fiber displays a strain-hardening load-displacement behavior with substantially enhanced ductility;<br>• The beneficial effect of micro-glass fiber decrease after 1.5% fiber volume. | [33] |

**Table 2.9: Fibers used in UHPC (continued)**

| Fiber (type) | Aspect ratio (*l*/*d*) | Volume fraction | Single/ hybrid | • Key findings | Reference |
|---|---|---|---|---|---|
| Steel<br>(smooth)<br>(spiral)<br>(hooked A)<br>(hooked B) | 13/0.2<br>13/0.2<br>13/0.2<br>30/0.6 | 1%<br>1.75%<br>2.5% | Single | • The UHPC with deformed fibers shows better tensile properties than that with smooth fibers;<br>• Fiber type shows no effect on strain-hardening behavior. | [34] |
| Steel<br>Basalt<br>PVA<br>PE | 16.3/0.2<br>19.5/0.2<br>12/0.012<br>12/0.040<br>18/0.012 | 1.5% | Single + Hybrid | • Single steel fibers result in a marginal improvement in compressive strength, while the hybrid fiber system results in decreased compressive strength, increased tensile strength, and higher first crack strength. | [35] |
| Steel<br>(Straight)<br>(Hooked end)<br>(Corrugated) | 13/0.2<br>13/0.2<br>13/0.2 | 0%<br>1%<br>2%<br>3% | Single | • Significant increases in compressive (over 150 MPa) and flexural strength (35 MPa) are obtained from the UHPC;<br>• The reinforcing efficiency in an order of corrugated fibers (59%) > hooked fibers (48%) > straight fibers is observed;<br>• Fiber content has the least effect on the first cracking behavior of UHPC but shows a considerable effect on peak load. | [36] |
| Steel<br>(straight) | 12.7/0.2 | 0%<br>3% | Single | • The use of 3% steel fibers by volume increases the compressive strength by 4% on cylindrical specimens and by 8% on square specimens. | [37] |
| Steel<br>(Straight) | 13/0.2<br>19.5/0.2<br>30/0.3 | 0.5%<br>1%<br>1.5%<br>2% | Single | • Long fibers show better performance in improving flexural performance;<br>• When the fibers' volume fraction is higher than 2%, the flexural performance of UHPC is diminished.<br>• By replacing short fibers with medium and long fibers, the volume fraction of steel fibers can be reduced by 0.5% without effect on physical properties.<br>• The toughness of UHPC increases with fiber length and volume fraction. | [38] |
| Steel | 15/0.12 | 2.5% | Single | • An embedding length of 60 mm of the steel fiber yields a peak pull-out load of 54 N, which is 80% higher than that of fibers with a 30 mm embedding length. | [39] |
| Steel<br>(Straight) | 13/0.2 | 0%<br>2% | Single | • With 2% of steel fibers, the compressive strength and flexural strength of UHPC are increased when a nano-limestone content of 3.2% is used, while decreased strength is obtained with the addition of more nano-limestone powders. | [40] |

**Table 2.10: Fibers used in UHPC (continued)**

| Fiber (type) | Aspect ratio (*l/d*) | Volume fraction | Single/ hybrid | • Key findings | Reference |
|---|---|---|---|---|---|
| Steel (Straight)<br><br>(Hooked end)<br>(Twisted) | 13/0.2<br>30/0.3<br>30/0.375<br>30/0.3 | 2% | Single + hybrid | • The bond strength and normalized pullout energy of the macro straight fibers in UHPC were improved after their replacement with microfibers;<br>• The post cracking tensile strength and energy absorption capacity of UHPC reinforced with hooked and twisted fibers increased when they were replaced by the microfibers; | [41] |
| Steel (Straight)<br>(Hooked)<br>(Corrugated) | 13/0.2<br>13/0.2<br>13/0.2 | 0%<br>2% | Single+ Hybrid | • The corrugated fibers enhance interfacial bond properties between fibers and the UHPC matrix;<br>• The deformed fibers significantly increased the ultimate flexural strength of UHPC. | [42] |
| Steel (Straight) | 13/0.2 | 0%<br>1%<br>3% | Single | • The UHPC mixture with 3% fiber volume showed higher flexural strength than the unreinforced and 1% fiber volume mixtures;<br>• Micro-crack bridging was observed in the post-peak stage. | [43] |
| Steel (Hooked end) | 30/0.5 | 0%<br>0.5%<br>1.5%<br>2%<br>2.5% | Single | • The curing of 2 days at 60°C plus 3 days at 80°C, gives the maximum strength;<br>• A more considerable increase in the tensile strength than compression strength;<br>• A steel fiber volume fraction of 2% results in a 150 MPa compressive strength;<br>• The fine sand performs better than the regular sand in increasing strength;<br>• A silica fume content of 25% is considered the optimal dosage. | [44] |
| Basalt<br>Polypropylene<br>Glass | 18/**<br>10/**<br>12/** | 0.5%<br>1.0%<br>1.5%<br>2.0%<br>2.5% | Single | • Workability decreases with the addition of fibers;<br>• At a fiber volume fraction of 2.5%, compressive strength decreases, while the flexural strength increases for all the fiber types;<br>• The reinforcing efficiency of the fibers is in an order of glass fibers > polypropylene fibers > basalt fibers;<br>• Post-peak and ductility are enhanced due to the addition of fibers. | [47] |
| Steel (Straight) | 13/0.2 | 0.65%<br>1.4%<br>2% | Single | • Higher compressive strength is achieved with higher curing temperature;<br>• The inclusion of up to 2% steel fibers improves the compressive and ultimate flexural strength, toughness, and fracture parameters of UHPC. | [48] |

From the literature review, it is found that the micro-steel fiber with a length of 13 mm, a diameter of 0.2mm, and an aspect ratio of 65 is the most commonly used fiber that, at a volume fraction of 2%, results in significant improvement of mechanical performance of UHPC. A few studies reported the volume of fibers at 3%, beyond which the agglomeration of the fibers might result in an adverse effect on the strength development. Steel fibers with a length of 30 mm and a diameter of 0.3 mm are the next most important type of fibers used in the manufacturing of UHPC. The literature reported that the workability of UHPC decreases with the addition of fibers. The shape of fibers also affects the workability of UHPC, where the UHPC with hooked-end steel fibers shows lower workability than that with straight or corrugated fibers. Compressive strength, tensile strength, and flexural strength are the most frequently measured parameters of UHPC.

### 2.2.3 Applications

Owing to its superior mechanical and durable properties, UHPC has been applied in many civil structures, especially in transportation infrastructure projects. UHPC became commercially available in the United States around 2000. The Federal Highway Administration (FHWA) began studying the use of UHPC for highway infrastructure in 2001 and has been working with various state transportation departments since 2002 in order to successfully implement UHPC for use in highway bridges. This research has led to several different applications of UHPC in bridges. The following is a review of some of those applications that have been completed which includes precast and prestressed girders, precast waffle panels for bridge decks, and as a jointing material between precast concrete deck panels and girders and between the flanges of adjacent girders. Additionally, there are summaries of several research projects conducted by the FHWA and other institutions highlighting several different applications of UHPC in transportation infrastructure both in the laboratory and in the field.

2.2.3 A Deployments in bridges

Since its first development in 2006, extensive investigations and applications of UHPC in brides have been performed in the United States. To date, there are more than 250 bridges using UHPC for construction or repair maintenance. Fig. 2.1 shows a map of the bridges in the United States that used UHPC in their construction. A full list of the bridges can be found on the FHWA website.

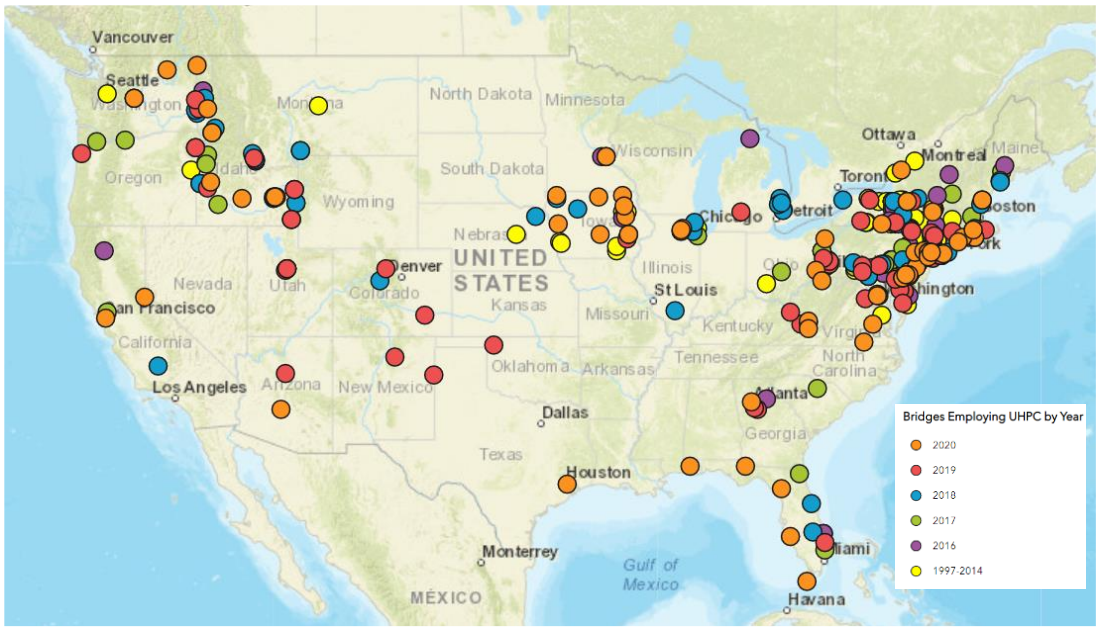


**Figure 2.1: A map of the bridges in the United States that used UHPC in their construction.**

Below is a summary of a few bridges that demonstrate the different applications of UHPC that have been implemented in transportation infrastructure. There are also summaries of two bridges that the Massachusetts Department of Transportation (MassDOT) has completed that utilize UHPC.

### 2.2.3 B Mars Hill Bridge

The first bridge in the U.S. to use UHPC members was the Mars Hill Bridge in Wapello County, Iowa. Constructed in 2006 the bridge spans 110’ and includes three 45” deep UHPC prestressed I-girders. The girders were also modified from the standard Iowa Bulb Tee design using shallower top and bottom flanges and a narrower web. The web thickness was reduced from 6 1⁄2 in. to 4 1⁄2 in., the bottom flange from 7 1⁄2 in. to 5 1⁄2 in., and the top flange dimension from 3 3⁄4 in. to 2 3⁄4 in. Additionally, the normal mild steel shear reinforcement was eliminated from the girder webs as testing demonstrated that the UHPC with its steel fiber reinforcement (approximately 2% by volume) was sufficient to carry the design loads. A cross-section of the I-girder can be found in Figure 2.2. The UHPC used in this project was supplied by Lafarge North America and achieves up to 30,000 psi compressive strengths, with ductility. The bridge resulted from a collaborative effort between FHWA, Iowa DOT, Iowa State University, and Lafarge [49].

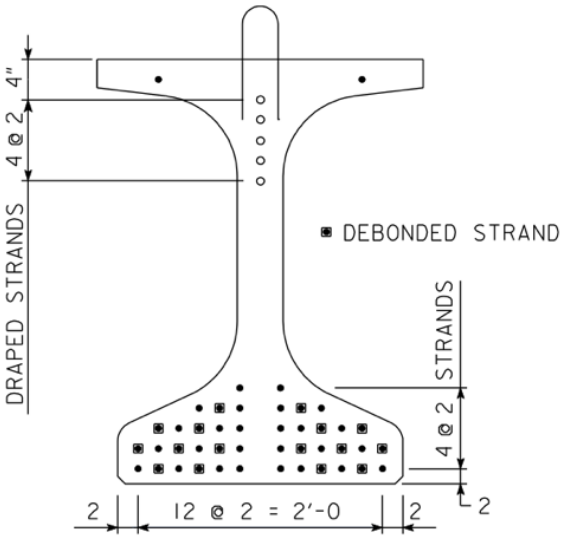


**Figure 2.2: Mars Hill Bridge I-girder cross section [49].**

**Figure 2.3: Mars Hill Bridge completed.**

### 2.2.3 C Jakway Park Bridge

Jakway Park Bridge was constructed in Buchanan County, Iowa, in 2008 and opened to traffic in 2009. This bridge utilized an optimized UHPC pi-girder and was the first application of a pi-girder for a highway bridge in the U.S. A total of three pi-girders were used in the central 51' 4" long center span of the three-span bridge. The design was based on conventional and finite element analysis, which was validated by laboratory testing of the first- and second-generation pi-girder at the FHWA's Turner-Fairbank Highway Research Center (TFHRC) in McLean, Virginia near Washington, DC. The first-generation pi shape,

which was developed by the TFHRC and the Massachusetts Institute of Technology was used to optimize the UHPC mix by minimizing the cross-section and taking advantage of the material properties of the bridge deck. Testing of this section revealed overstresses in the transverse capacity of the deck and a low transverse live load distribution between adjacent pi sections. Several design options were considered for strengthening the deck and after making changes the second-generation beams were cast [50].

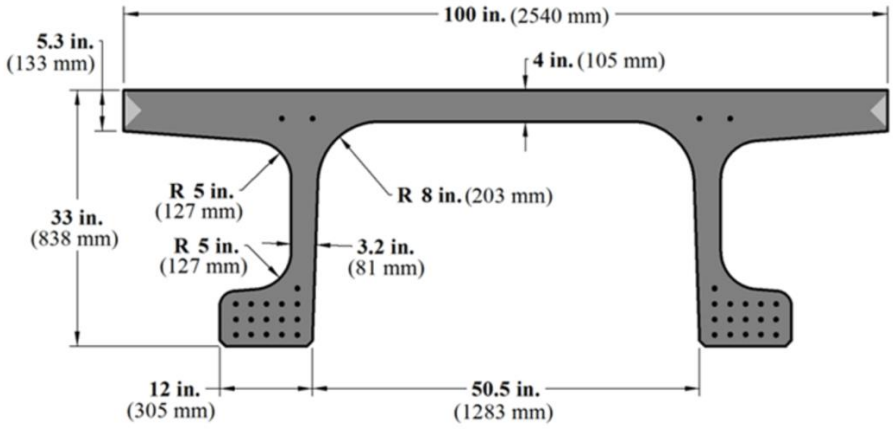


**Figure 2.4: Jakway Bridge pi-girder cross section.**

2.2.3 D State Route 31, Lyons, NY

The Route 31 Bridge located in Lyons, New York features the first application of UHPC as a closure pour material in the deck of the bridge in the U.S. To replace the bridge in the available time window of 3 months, the New York State Department of Transportation (NYSDOT) decided to use precast concrete girders. Previously, these types of deck bulb tee girders were not used due to durability concerns. So, NYSDOT customized the bulb tees to create joints between the girders that would be filled with UHPC. UHPC allows for the joint to be narrow which speeds up the curing process and allows the joint to withstand a long period of heavy traffic. The bridge is a single span that is 87 ft. 5 in. long and 42 ft. 9 in. wide, comprising eight girders that are 41 in. deep.

Since this was the first field application of UHPC as a joint material, a couple of important details were learned and should be noted about this project. One is the importance of leak-proof forms before placing UHPC to reduce corrosion of the UHPC. UHPC joints were also overfilled to make sure that the entire joint was filled with high-quality material since the top quarter inch or so of the UHPC joint fill had a low-quality flaky characteristic. The success of this experience led to the design and construction of several bridge superstructures with prefabricated deck beam elements with UHPC joints [51].

2.2.3 E Dahlonega Road, Ottumwa, IA

The single-span, two-lane Dahlonega Road Bridge crosses the Little Cedar Creek in Wapello County, Iowa, and features UHPC waffle panels. The design and initial testing of the bridge

were done by Iowa DOT. It is 63 ft, long and 32 ft. 2 in. wide and consists of fourteen precast concrete panels installed on five standard I-beams. The UHPC two-way-ribbed, modular deck panels, also known as waffle panels, are 15 ft. long, 8 ft. wide and 8 in. deep with the top flange being 2.5 in. thick. The panels are connected to the beams by reinforcement extending from the beams into the space between the ribs of the panels and the tops of the beams. This project showed how UHPC can change the way bridge decks are constructed and can significantly extend the service life of highway infrastructure [52].

2.2.3 F State Route 10 (Northampton Street), Easthampton, MA

The existing 93' span of Northampton Street crossing the Manhan River in Easthampton needed to be replaced. MassDOT opted to use UHPC as a closure pour material in the deck of the bridge. This is similar to the State Route 31 Bridge seen in section 2.3.1.C. However, these closure pours were 8" wide, 2" wider than the pours in the SR 31 Bridge.

2.2.3 G State Route 85 (Washington Street), Hudson, MA

The bridge carries Washington Street (Rte. 85) over the Assabet River in Hudson, Massachusetts and is the primary north-south route through the commercial center of Hudson carrying 21,000 vehicles per day. The bridge was replaced with NEXT-40D beams supported on concrete abutment pile caps and micro-piles.

The bridge geometry necessitated the use of narrow cast-in-place concrete closure pours between the adjacent beam flanges. Due to the reduced closure pour widths and to achieve high strength rapidly, Jacobs Engineering Group and MassDOT decided to use UHPC for the closure pours. The Hudson bridge project is one of two projects that used UHPC in Massachusetts as part of the FHWA Every Day Counts program. During design, extensive coordination was required with MassDOT and LaFarge North America, the supplier of the Ductal JS1000 Joint Fill, to develop the UHPC specifications. A mock-up of the joint was required to evaluate the bond between the UHPC and the beam flanges and to closely mimic production placement conditions.

After field-casting the closure pours, the UHPC attained minimum compressive strengths of 11,070 psi within 3 days, and the design compressive strength of 14,000 psi within 7 days. The 28-day compressive strength was 21,580 psi.

### 2.2.4 FHWA Research Projects

The FHWA Turner-Fairbank Highway Research Center has conducted various research projects looking into the potential applications of UHPC. The following list summaries projects that have been identified as relevant to the applications of UHPC in transportation infrastructure.

- Modification of existing prestressed girder cross sections for the optimal structural use of UHPC
  This research project (FHWA-PROJ-06-0039) investigated the application of UHPC in prestressed I-girders and was led by Benjamin Graybeal. The project identified I-

girders as the most likely first stage of implementing UHPC into bridge design for many states, which did occur in 2006 with the Mars Hill Bridge in Iowa. The purpose of the program was to investigate existing bridge girder cross sections to determine which are best suited to modification for use with UHPC.

- Development of a UHPC bridge superstructure system
  The research program, with a project ID FHWA-PROJ-08-0008, took place between 2008 and 2009 and was led by Benjamin Graybeal. The research program has demonstrated the viability of the decked UHPC modular girders concept for use in conventional and accelerated bridge construction. Girders of this type can be fabricated in existing prestressed girder production facilities. The initial deployment of the UHPC pi-girder was completed in the Jakway Park Bridge.
- Development of a family of UHPC pi-girders
  A family of UHPC pi-girders was developed for spans ranging up to 135 ft (41.1 m) and loaded under simply supported boundary conditions. The proposed sections were designed to resist loads more than those required by the AASHTO LRFD Bridge Design Specifications while meeting the live load deflection recommendations.
- Structural testing of field-cast UHPC connections between precast bridge elements
  In the research project FHWA-PROJ-09-0132, six slab specimens that were designed to model two different situations where UHPC might be used as a joint fill or closure pour material were investigated. The slabs were designed to either copy the types of connections that might occur between precast bridge deck elements or to mimic the type of connection that might occur between the flanges of a pair of deck-bulb-tee prestressed girders. Each of these slabs will be tested for two different behaviors, cyclic service level loads and performance under monotonic ultimate loads.

### 2.2.5 Other Research on Applications of UHPC

In addition to the FHWA, other groups and organizations have also done various types of research on the use of UHPC in transportation infrastructure. Several different uses for UHPC are summarized in the following section. A large focus of research on UHPC is centered on the use of the material to repair different aspects of damaged infrastructure. A research team [53] developed a novel repair procedure for corroded steel beam ends using UHPC. It was implemented on two bridges in Connecticut. The two repairs used different designs, UHPC mixes, and casting procedures showcasing the flexibility of the repair. Another issue that could potentially be solved by UHPC is corrosion damage of steel girder ends caused by leaking expansion joints. Section loss at these critical locations can be detrimental to the bearing capacity of the girder. Current repair methods are costly, time-consuming, and disruptive to traffic. A new repair method has been proposed by McMullen and Zaghi [54] at the University of Connecticut and the Connecticut Department of Transportation that uses UHPC to repair the corroded steel girder ends. The repair consists of welding headed shear studs to the undamaged portions of the web and encasing the girder in UHPC, which provides an alternate load path from the girder to the UHPC panels to bypass the corroded region. Farzard et al. [55] at the Florida International University, investigated the performance of UHPC as a retrofit material for damaged bridge columns. A repair method was developed that uses UHPC which could provide an efficient solution to solve the issues with bridge rehabilitation.

A report by Sritharan et al. [56]. explains that deterioration of existing bridge decks, which usually originates with the deck cracking on the top surface, is a common problem in North America. Cracking of the deck results in the need for frequent repair of the decks to further prevent damage resulting from water and chloride. A thixotropic mix design for UHPC allows for a UHPC overlay to be used in certain decks. The feasibility of applying this technology in the field was then investigated on Mud Creek Bridge in Iowa for the first time in North America in May 2016. A project was conducted for the Montana Department of Transportation by Berry et al. [57], with the purpose of developing and characterizing an economical non-proprietary UHPC made with materials readily available in Montana. This research focused on investigating the potential variability in performance related to differences in constituent materials, investigating issues related to the field batching/mixing of these UHPC mixes, testing rebar bond strength, and studying how this will affect requisite development lengths.

### 2.2.6 Testing standards of UHPC

The commonly used testing standards for evaluations of the physical, mechanical, and durability of UHPC are summarized in Table 2.11 to Table 2.13.

**Table 2.11: Testing standards for physical properties of UHPC**

| Test | Testing method | Specimen | Equipment | Reference |
|---|---|---|---|---|
| Flowability | Flow test | Fresh concrete | Flow table with conical mold | [58-60] |
| Flowability | V- funnel test | V-shape | V- Funnel | [61, 62] |
| Porosity | Porosity | 10 mm by 10 mm by 10mm cube | Mercury Intrusion porosimeter | [63, 64] |
| Porosity | Vacuum-saturation technique | 100 mm by 20 mm cylinder | Vacuum Saturation Apparatus | [65, 66] |
| Porosity | Porosity | The individual portions may be pieces of cylinders, cores, or beams | Balance and container | [67, 68] |
| Permeability | Gas permeability test | 37 mm by 70 mm cylinder | Permeability device | [69, 70] |
| Permeability | Liquid permeability test (water & ethanol) | 37 mm by 70 mm cylinder | Permeability device | [70] |
| Permeability | Chloride permeability – AASHTO test | 100 mm (4 in.) diameter core or cylinder sample | Chloride permeability machine | [71, 72] |
| Shrinkage | Autogenous shrinkage test | 75 mm by 75 mm by 285 mm prism | Prism | [73-75] |
| Shrinkage | Shrinkage test | 60 by 100 by 1000-mm prism | Double-walled steel rig | [76] |
| Shrinkage | Early age laser shrinkage test | 25 mm by 25 mm by 290 mm specimen | Steel mold with a moveable stop-end with steel pin and laser sensor | [77] |
| Shrinkage | Drying shrinkage | 25 by 25 by 285-mm prismatic samples | Length compactor | [78] |
| Creep | Creep test | 3 by 6 in. cylinder | Sustained loading machine | [79] |
| Creep | Creep test | 100 by 100 by 300-mm prism | Creep testing machines | [80] |
| Creep | Tensile creep Test | 3 by 3 by 19 in. prism | Tensile creep test setup | [81] |
| Creep | Compressive creep test | 4 by 15 in. cylinder (modified) | Compressive creep test setup | [81, 82] |

**Table 2.12: Testing standards for mechanical properties of UHPC**

| Testing method | Specimen | Equipment | Reference |
|---|---|---|---|
| Compressive strength test | 3in X 6 in (Cylinder) | Universal testing machine | [79] |
| Compressive strength test | 100 mm and a height of 200 mm Cylinder | Universal testing machine | [83] |
| Uniaxial compressive strength test | 100 mm x 100 mm x 100 mm Cube | Universal testing machine | [83-87] |
| Compressive strength test | 50-mm cube | Universal testing machine | [88-90] |
| K-fold validation of 1-day compressive strength | 50-mm cube | - | [91] |
| Flexural test | 6 by 6 by 20 in. prism | MTS testing machine | [90] |
| 3-Point bending test | 40 by 40 by 160-mm beam with a span of 100 mm | MTS testing machine and LVDT | [42] |
| Drop weight impact flexural test | 40 by 40 by 160-mm with a span of 100 mm | Drop-weight impact testing machine | [92] |
| Split tensile test | 75 mm diameter X 37 mm height cylinder | Compressive loading machine | [85] |
| Direct tensile test (Briquette tension test) | Dog-bone shaped briquette with a 3-in. (75 mm) length, 1-in. (25 mm) thickness, and a 1-in.$^2$ (625 mm$^2$) cross-section at mid-length | MTS testing machine | [86] |
| Bending tension method | 40 by 40 by 160-mm beam | Tension testing machine | [83] |
| Direct shear test | 250 by 200-mm with a UHPC layer of 50mm double-sided shear specimen | Shear testing machine | [93] |
| Transverse Shear Test | 25 by 160-mm cylinder | Steel double shear Test device | [94, 95] |
| Push-off Test | 150 by 300 by 640 mm L-shaped joint specimen | Actuator and LVDT | [96] |

**Table 2.13: Testing standards for durability of UHPC**

| Testing method | Specimen | Equipment | Reference |
|---|---|---|---|
| Corrosion Potential Method With Electrochemical Method | 100 by 100 by 100-mm cube<br>40 by 40 by 160-mm beam | Electrochemical workstation | [97] |
| Accelerated Corrosion Test | 4 by 8 in. cylinder with embedded rebar | Accelerated corrosion testing setup | [98] |
| Dynamic polarization tests | 4 by 8 in. cylinder with embedded rebar | Three-electrode system in the same set-up of accelerated corrosion test | [98] |
| Tafel analysis | 4 by 8 in. cylinder with embedded rebar | - | [98] |
| Linear polarization resistance technique | 4 by 8 in. cylinder with embedded rebar | - | [99] |
| Mortar bar test | 1 by 1 by 10 in. mortar bar | Comparator | [100] |
| Oberholster test | 2 by 4 in.cylinder | Water tank | [101, 102] |
| ASR testing Method | 1 by 1 by 10 in. mortar bar | Comparator | [103, 104] |
| CUR Recommendation | 40 by 40 by 160-mm prism | - | [101] |
| ASTM standard Method | 1 by 1 by 10 in. mortar bar | Comparator | [105] |
| Sulphate attack test | 100 by 100 by 100 mm cube | Tank | [106] |
| Sulphate attack test | 75 by 75 by 75-mm cube | Tank | [107] |
| Salt-scaling of concrete | 70 by 70 by 210-mm prism | - | [101] |
| Surfaces scaling resistance test | 150 by 200-mm planar with 50 mm depth | Freezing and thawing chamber | [108] |
| ASTM scaling resistance test | Surface area of at least 72 square in. with a depth of at least 3.0 ines | Freezing chamber | [109] |
| Freezing and Thawing test | 3 to 5 in. in Width, depth, or diameter not than 11 in. and maximum length of 16 in. | Freezing and thawing chamber | [110] |
| Slab Test | Full sized units, or cut units with a surface area of at least 29.5 $inch^2$ | Freezing and thawing chamber | [101] |

# 3.0 Fiber Characterization

## 3.1 Macro-Fibers for Fiber Reinforced Concrete

### 3.1.1 Application of macro-fibers in fiber-reinforced concrete

Fiber-reinforced concrete (FRC) is concrete with the addition of discrete reinforcing fibers made of steel, glass, synthetic (nylon, polyester, and polypropylene), or natural fiber materials. At appropriate dosages, the addition of fibers may provide various benefits to concrete including increased resistance to plastic and drying shrinkage cracking, reduced crack widths, and enhanced energy absorption and impact resistance. The major benefit derived from the use of FRC is improved concrete durability. The primary durability-enhancing feature of FRC is crack control which limits the rate at which corrosive substances such as water, chlorides, and carbon dioxide ingress into structural elements, thereby prolonging the service life of the structure [111]. To choose the appropriate fiber, it is important to understand what types of fibers are currently available and to understand what type of fiber is best suited for different applications. The properties of concrete are durability, flexural strength, toughness, impact resistance, and compressive strength. The physical improvement depends on the fiber type, size, configuration, and fiber amount.

ASTM C116, Standard Specification for Fiber Reinforced Concrete, outlines four classifications for FRC:

- Type I - Steel fiber-reinforced concrete or shotcrete
  This is the classification of concrete made with carbon steel, alloy steel, or stainless-steel fibers, detailed in ASTM A820.
- Type II - Glass fiber-reinforced concrete or shotcrete
  This is the classification of concrete made with alkali-resistant glass fibers, detailed in ASTM C1666
- Type III - Synthetic fiber-reinforced concrete or shotcrete
  This is the classification of concrete made with synthetic fibers. Currently, only polyolefin fibers have a standard specification for use in concrete which is found in ASTM D7508.
- Type IV - Natural fiber-reinforced concrete or shotcrete
  This classification is for concrete made with natural fibers. Only cellulose fibers have a standard specification for use in concrete, which can be found in ASTM D7357.

For this research project, it was decided that both steel and polypropylene (the most used synthetic fiber) fibers would be investigated due to their widespread use and ease of availability. According to Guerini et al. [112], steel fibers are the most commonly used fiber type and synthetic fibers have significantly improved over the last several years and are now also used in many different applications.

Steel fibers have several advantages including improving the ductility of the concrete, improving durability by controlling crack widths, and overall improving flexural strength,

toughness, and ductility. Steel fiber reinforced concrete (SFRC) can be used in tunnel lining, rock stabilization, thin shell dome construction, repairing surfaces, and providing protective coatings [113]. Different dosages of steel fibers can, depending on the type and length of fibers used, increase flexural strength, fatigue strength, toughness, shear strength, impact resistance, and ductility over that of unreinforced concrete [114]. Steel fibers should be added to the concrete batch mixer at a uniform rate to prevent segregation or balling during mixing. Results from various research projects on the effect of steel fibers on various properties can be found in Table 3.1.

Polypropylene fibers can improve impact resistance, reduce the requirement for steel reinforcement, improve ductility, and improve the freezing point where exposed concrete contains cracks [113]. The standard dosage range for polypropylene fibers varies widely from 0.1% to 2.0% by volume. According to the synthetic fiber section of the ACI Educational Bulletin E2-00 (2006), at lower dosages, synthetic fibers are used to modify plastic shrinkage and plastic settlement properties of concrete. Less bled water is the visually observable result of reduced plastic settlement. Uses include slabs-on-grade, precast concrete, and wet-method shotcrete. Cast-in-place concrete can accommodate up to 0.5% by volume with mixture proportion modifications required when the fiber volume is above 0.3%. Wet shotcrete mixtures with up to 0.75% by volume can be used to enhance toughness/residual strength. The use of 0.2% synthetic fiber in ultra-thin white-topping (a concrete replacement for hot-mixed asphalt as the wearing surface) has become a standard based on proven performance. Results from various research projects on the effect of polypropylene fibers on various properties can also be found in Table 3.1 and Table 3.2.

In this project, a fiber dosage of 1% by volume was used for both steel and polypropylene fibers. Table 3.3. is a summary of various applications of FRC, and which fibers are best to use for each application.

**Table 3.1: Best performing geometry and content of steel fiber for different properties**

| Property | Diameter | Length | Shape | Fiber content | Notes | Reference |
|---|---|---|---|---|---|---|
| Permeability | Aspect ratio: 65 | Aspect ratio: 65 | Crimped | 4% | The permeability decreased significantly with increasing fiber content. Also was observed to increase with an increasing aspect ratio of fibers but the decrease was not very significant. | [115] |
| Plastic shrinkage cracking | Aspect ratio: 80 | Aspect ratio: 80 | Hooked | 1.50% | - | [116] |
| Ductility | 0.2 mm | 13 mm | Straight | 1.50% | - | [8] |
| Compressive Strength | 0.2 mm | 13 mm | Straight | 1.50% | - | [8] |
| Compressive Strength | 1.2 mm | 32 mm | Corrugated | 2.00% | When the steel fiber content increases from 0.5% to 2.0%: compressive strengths increase by about 4–24% | [117] |
| Tensile Strength | 1.2 mm | 32 mm | Corrugated | 2.00% | splitting tensile strengths increase about 33–122% | [117] |
| Shear Strength | 1.0 mm | 32 mm | Hooked | 1.50% | shear strengths increase by about 31–79% | [117] |
| Shear Strength | 1.0 mm | 32 mm | Straight | 2.00% | shear strengths increase by about 31–79% | [117] |
| Flexural Strength | 1.2 mm | 32 mm | Corrugated | 2.00% | flexural strengths increase by about 25–111% | [117] |
| Interface Bonding/ Pullout | - | 15 mm (embedment length) | - | - | The slippage dropped rapidly after reaching the peak pull-out load. Therefore, a shorter embedment length indicates expected slip-hardening effects for ductile behavior. | [118] |

**Table 3.2: Best performing geometry and content of Polypropylene fiber for different properties**

| Property | Diameter | Length | Shape | Fiber content | Notes | Reference |
|---|---|---|---|---|---|---|
| Permeability | 20 μm | 6 mm | Mono-filament | Lower for lower permeability coefficient | Permeability coefficients increase for increased fiber content | [119] |
| Plastic shrinkage cracking | 20 μm | 6 mm | Mono-filament | 0.30% | 0.1–0.3% fiber indicated that plastic shrinkage cracks were reduced by 50–99%. The inclusion of 0.1% fiber reduced the crack width down to 1 mm (less than 3 mm specified by ACI 224) and the trend continued with the addition of more fibers. | [119] |
| Plastic Shrinkage/ settlement | - | - | Mono-filament | ~0.10% | Less bleed water is the visually observable result of a reduced plastic settlement. | [120] |
| Ductility | 34-45 μm | 12 mm | Multi-filament | 2.00% (High for this study to allow for direct comparisons with steel fibers) | Cracks have more fibers linking their boundaries, this way showing more energy absorption capacity and, thus, the toughness indexes grow. In the polypropylene-reinforced mixtures, this behavior occurs for all the reinforcement percentages, which suggests that in the studied reinforcement range, increasing the fiber's percentage improves the ductility. | [8] |
| Compressive Strength | 34-45 μm | 12 mm | Multi-filament | 2.00% (High for this study to allow for direct comparisons with steel fibers) | The compressive strength of the polypropylene FRCM increases with the reinforcement ratio. However, the strength found with the 0.5% fiber content is 10% lower than the reference, whilst all other reinforcement ratios show higher strengths. | [8] |
| Tensile Strength | 20 μm | 6 mm | Mono-filament | 0.10% | The inclusion of 0.1% fiber gave a minor reduction in compressive strength while the tensile strength increased by 39% | [119] |
| Pull out | - | - | - | - | A sufficient embedment length leads to mechanical bond strength and fiber plastic deformation. With a decrease in the embedment length, the maximum pull-out force is reduced. | [118] |

**Table 3.3: Applications of FRC with recommended fibers**

| Applications | Recommended Fiber | Aspect ratio | Shape | Fiber Content | Notes | Reference |
|---|---|---|---|---|---|---|
| Pedestrian bridge decks | Steel | Aspect ratio ~ 65 | 5DH | 1.0% is needed to replace the minimum longitudinal steel rebars and guarantee a ductile flexural behavior with multiple cracks for concrete pedestrian decks. | 5DH greatest flexural strengths compared with 3DH and 4DH | [121] |
| Slabs-on-grade | Polypropylene | - | - | 0.1% | - | [120] |
| Precast concrete | Polypropylene | - | - | Up to 0.5% | - | [120] |
| Ultra-thin white-topping (a concrete replacement for hot-mixed asphalt as the wearing surface) | Polypropylene | - | - | 0.2% | - | [120] |
| Thin overlays subject to heavy/high traffic volume | 94% of projects used synthetic (polypropylene)<br><br>6% used steel | Varying | Varying (see below) | 6.5 $lb/yd^3$ for polypropylene fibers | Structural fibers were found to improve the post-crack performance of concrete by keeping cracks tight, which helps reduce the severity of panel fatigue cracking. Overall, these fibers increase the long-term performance of overlays. | [122, 123] |

While both steel and synthetic fibers have successfully been implemented in FRC overlays, synthetic macro-fibers have become the most prevalent because they are easier to handle and less prone to balling. Regardless of the fiber type, the fiber content can be adjusted to achieve the specified residual strength performance. For example, in one study the desired residual strengths were achieved using fiber volumes of 0.26% synthetic (straight fiber), 0.40% synthetic (crimped fiber), 0.5% synthetic (twisted fiber), 0.19% steel (hooked-end fiber), or 0.50% steel (crimped fiber). Therefore, the concrete residual strength (ASTM C1609) should be specified and then verified through laboratory testing to determine the fiber content for a particular fiber type.

In addition to what material the fibers are made from and the dosage, another important aspect is the geometry of the fiber. An important aspect ratio of the fiber is the ratio of its length to its diameter. The typical aspect ratio ranges from 30 to 150. An increase in the aspect ratio of the fiber usually increases the flexural strength and toughness of the matrix. However, fibers that are too long tend to ball in the mix and create workability problems, as they cannot disperse evenly throughout the mixture. Another part of the geometry that is important is the shape. Fibers for FRC come in many different types of shapes including straight, hooked, corrugated, monofilament, and multifilament.

The known benefits of FRC for pavements are providing additional structural capacity, reducing crack widths, maintaining joint or crack load transfer efficiency, and extending the pavement's serviceability through reduced crack deterioration. For highway bridge overlays, eleven different types of fibers were included in a study, with varying fiber types, geometry, length, aspect ratio, and manufacturer. Ten of these fibers were synthetic polypropylene, while only one fiber was steel. Of the eleven fibers in this study, four fibers were flat, three were embossed, two were twisted, one fiber was continuously crimped, and one was end-crimped (steel). Testing of mixes with synthetic structural fibers demonstrated the fact that their inclusion has little effect on compressive strength and modulus of rupture. Steel structural fibers, however, offer increases in both properties. For structural synthetic fibers, the fiber volume fraction, as well as the stiffness and geometry of the fibers, significantly influence the residual strength. Embossed, twisted, and crimped fibers performed better on average than straight, flat synthetic fibers.

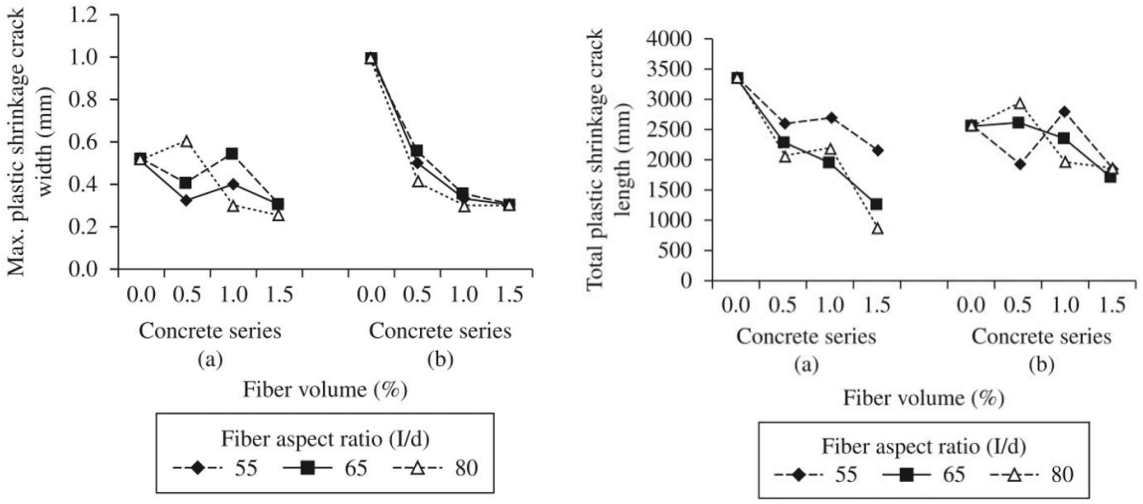


**Figure 3.1: Plastic shrinkage crack width and length vs fiber content and aspect ratios [116].**

a

| Mixture | I5 | I10 | I20 |
|---|---|---|---|
| Reference | 1.00 | 1.00 | 1.00 |
| St 0.5 | 4.06 | 8.41 | 18.20 |
| St 1.0 | 6.23 | 14.61 | 32.57 |
| St 1.5 | 6.80 | 15.85 | 35.08 |
| St 2.0 | 6.19 | 13.45 | 25.35 |
| Po 0.5 | 2.02 | 3.32 | 6.52 |
| Po 1.0 | 2.90 | 5.61 | 10.92 |
| Po 1.5 | 3.61 | 7.47 | 15.75 |
| Po 2.0 | 4.30 | 9.38 | 20.57 |
| Gl 0.5 | 1.00 | 1.00 | 1.00 |
| Gl 1.0 | 1.00 | 1.00 | 1.00 |
| Gl 1.5 | 1.00 | 1.00 | 1.00 |
| Gl 2.0 | 1.00 | 1.00 | 1.00 |

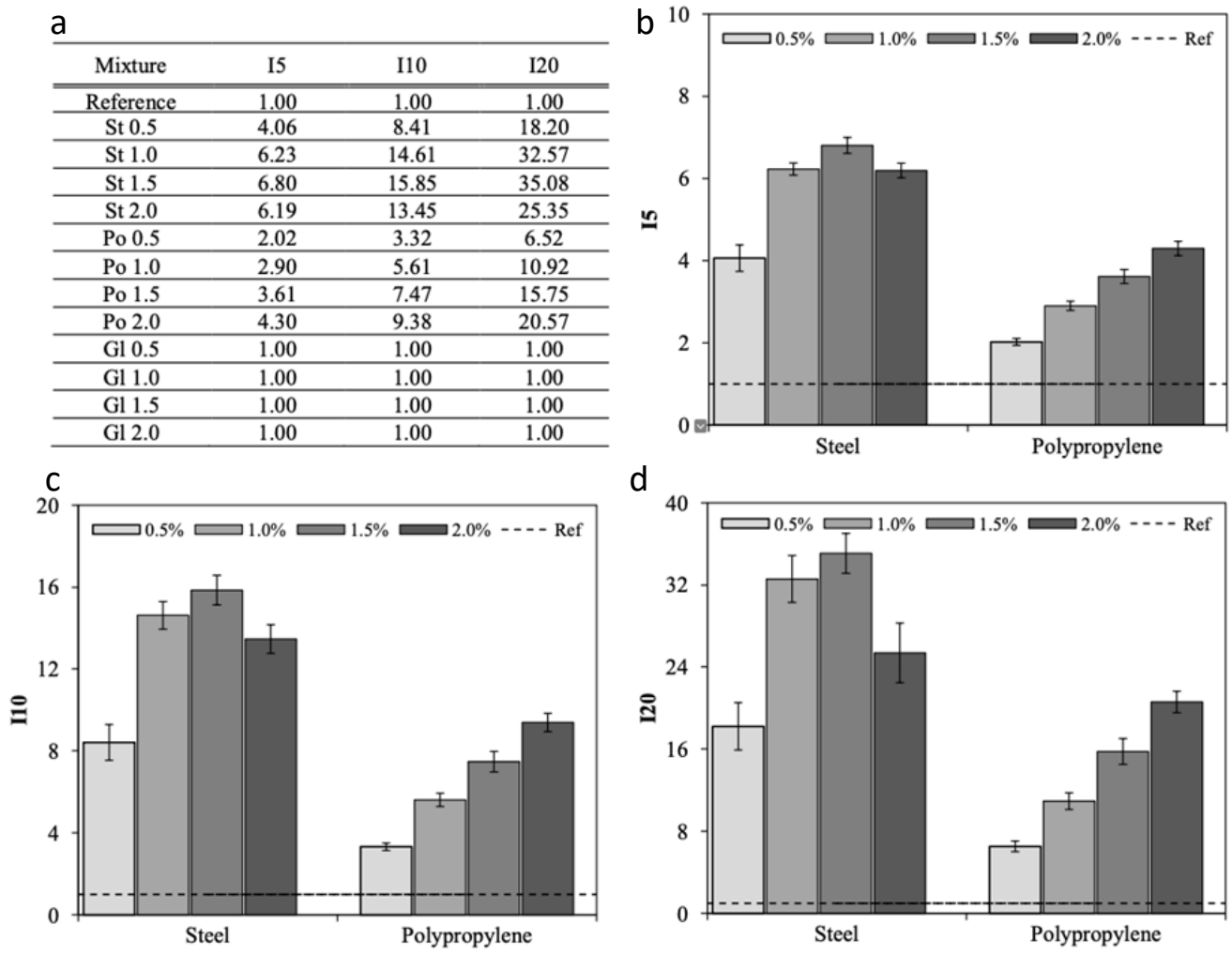


**Figure 3.2: Table with average toughness indexes for a series of mixtures and charts [8].**

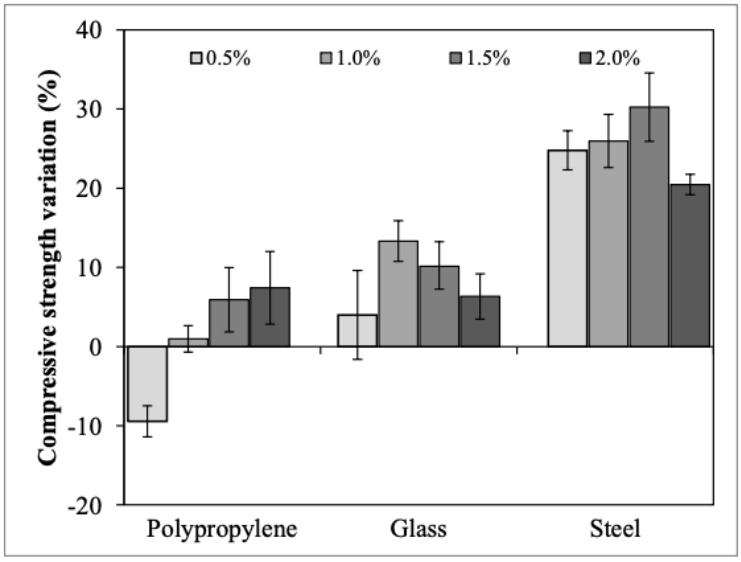


**Figure 3.3: Compressive strength variation in relation to the reference mixture [8].**

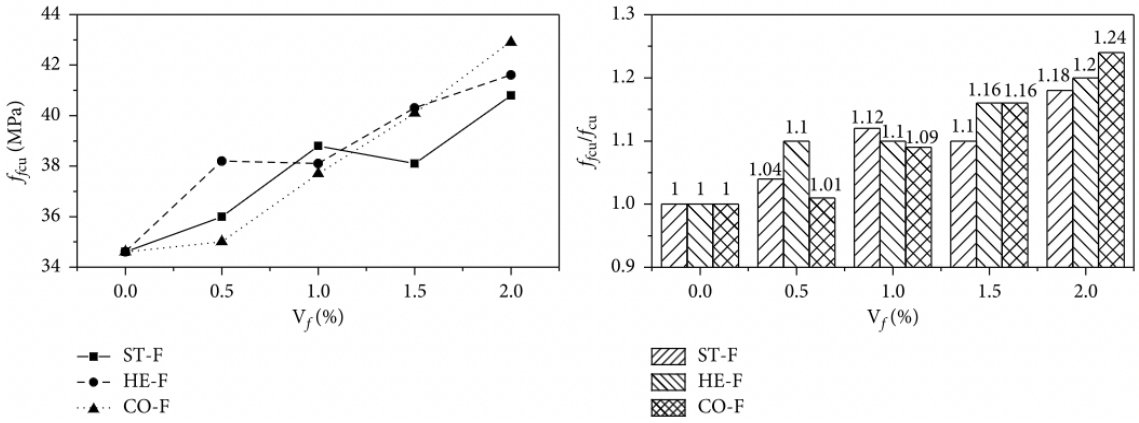


**Figure 3.4: Compressive strength of FRC [117].**

### 3.1.2. Types of macro-fibers

Four types of macro-fibers, including two synthetic fibers and two steel fibers, have been collected in this project. As shown in Table 3.4, the fibers' length is in a range from 1.5-inch to 2.4-inch, which has been proven an effective length to reinforce concrete. The four types of fibers were all provided by Fibermesh (a Sika brand). Enduro® Prime is a 100% virgin copolymer fiber with a crimped shape, an average diameter of 0.02-inch (0.56 mm), and a length of 2.4-inch (60.96 mm). Sika® Fibermesh®-650 is a macro synthetic reinforcing fiber, with an average diameter of 0.0177-inch (0.45 mm) and a length of 1.75-inch (44 mm), complying with ASTM C 1116 that can be used to reduce plastic shrinkage/settlement cracking and drying shrinkage cracking in concrete. SikaFiber® Novocon® HE-4550 steel fibers with a diameter of 0.041-inch (1.03 mm) and length of 2-inch (50 mm) are designed specifically for the reinforcement of concrete with a cold-drawn hooked end. SikaFiber® Novocon® XR steel fiber with a diameter of 0.045-inch (1.14 mm) and length of 1.5-inch (38 mm) is designed as a low carbon, cold-drawn continuously deformed steel wire fiber

with a crimped shape to provide optimum anchorage within the concrete specifically for the reinforcement of concrete. The aspect ratios of the two synthetic fibers are 1.7 and 105, respectively, while the aspect ratios of the two steel fibers are 50 (hooked) and 30 (crimped). The specific gravity of the synthetic fibers is about 0.91, while the specific gravity of the two steel fibers is 7.85. The tensile strength of the hooked and crimped steel fibers is 159.5 ksi (1,100 MPa) and 140 ksi (965 MPa), respectively, while no strength data for the two synthetic fibers is provided by the manufacturer. The physical and mechanical properties of the four macro-fibers are summarized in Table 3.4. Figure 3.5 shows the collected four macro-fibers.

**Table 3.4: Physical properties of micro-fibers**

| Fiber | Enduro® Prime-balling | Fibermesh®-650 | Novocon® HE-4550 | Novocon® XR |
|---|---|---|---|---|
| Manufacturer | Sika | Sika | Sika | Sika |
| Material | Virgin copolymer | Virgin copolymer | Steel | Steel |
| Diameter | 0.02” (0.56 mm) | 0.0177” (0.45 mm) | 0.041” (1.03 mm) | 0.045” (1.14 mm) |
| Length | 2.4” (60.96 mm) | 1.75” (44 mm) | 2” (50 mm) | 1.5” (38 mm) |
| Aspect ratio | 107 | 105 | 50 | 30 |
| Shape | Crimped | Straight | Hooked | Crimped |
| Specific gravity | 0.91 | 0.91 | 7.85 | 7.85 |
| Tensile strength | - | - | 159.5 ksi (1,100 MPa) | >140 ksi (965 Mpa) |
| Melting point | 324 °F (162 °C) | 324 °F (162 °C) | - | - |
| Color | Grey | White | Jasper | Brass |

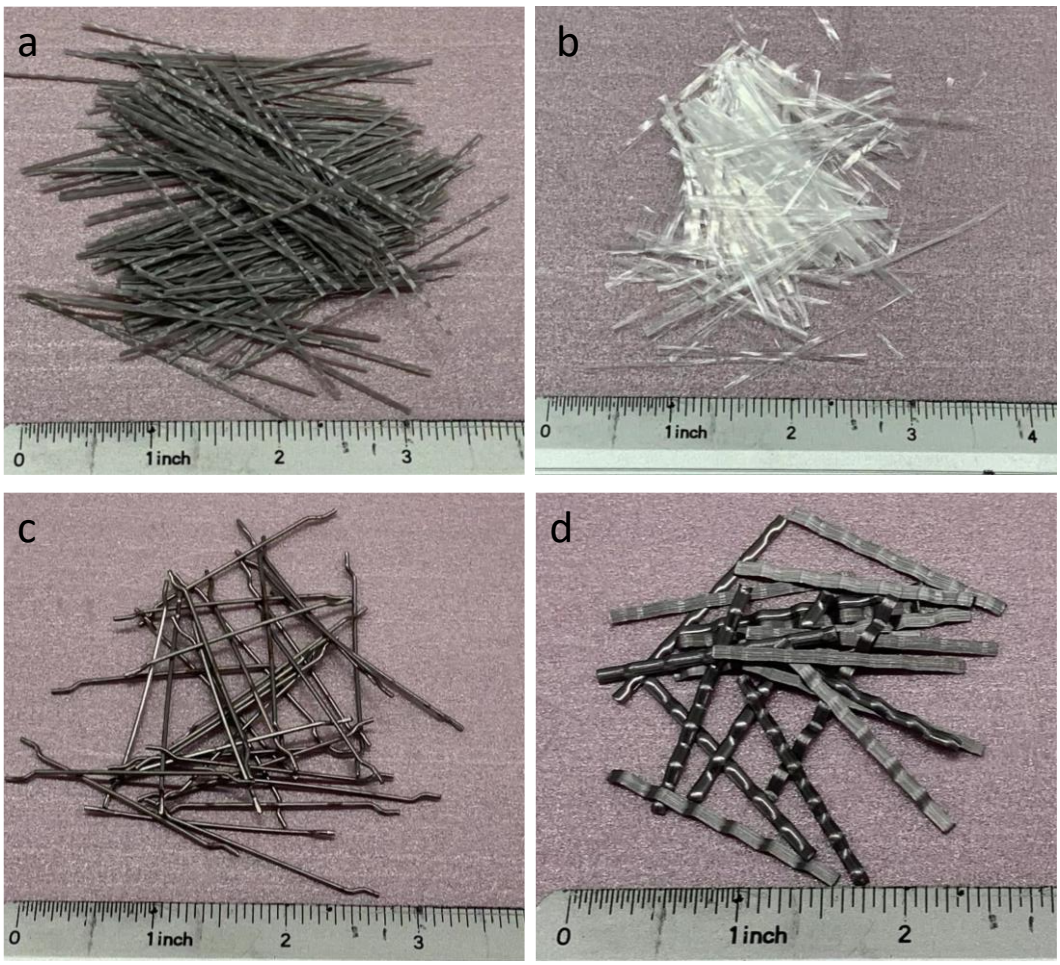


(a) crimped synthetic fiber (Enduro® Prime), (b) straight synthetic fiber (Fibermesh®-650), (c) hooked steel fiber (Novocon® HE-4550), (d) crimped steel fiber (Novocon® XR).

**Figure 3.5: The investigated macro-fibers.**

### 3.1.3. Microstructure analysis of the macro-fibers

Since the mechanical properties of the synthetic fibers, elongation capacity, and modulus of elasticity of the steel fibers are not provided by the manufacturer, tension tests of the selected four macro-fibers were performed in this project to determine the tensile strength, strain capacity, and modulus of elasticity. To determine these mechanical properties accurately, the cross-section geometry and dimensions of the fibers were first determined through microstructure analysis performed on a scanning electrical microscope (SEM). The microstructure analysis was also leveraged to analyze the micro-morphology of the rupture ends of the fibers after they failed in the tension tests.

Figure 3.6 shows the microstructure of the hooked steel fiber (Novocon® HE-4550). The cross section of the hooked steel fiber is a circle, so only the diameter was measured. From Figure 3.6a it can be seen that the fiber has a smooth surface without hump or pit. The measurements indicate that the hooked steel fibers have an average diameter of 731.8 μm. Figure 3.7 shows the ruptured end of the hooked steel fibers after failures in the tension test. From both the load-displacement curves and the microstructure, the yielding and necking

behavior of the steel fibers under tension can be observed. From Figure 3.7b, it can be seen that the fiber experience significant necking with decreasing diameters of 706.3 μm, 581.3 μm, and 446.9 μm. A classic shear failure surface with an angle of about 45° was yielded.

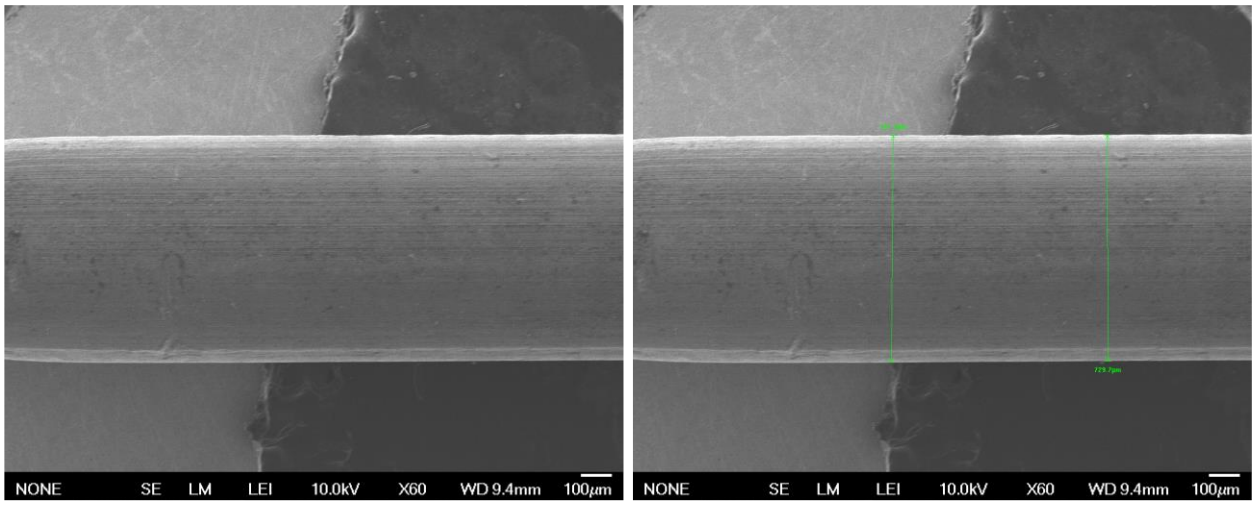


**Figure 3.6: SEM image of hooked steel fiber (Novocon® HE-4550).**

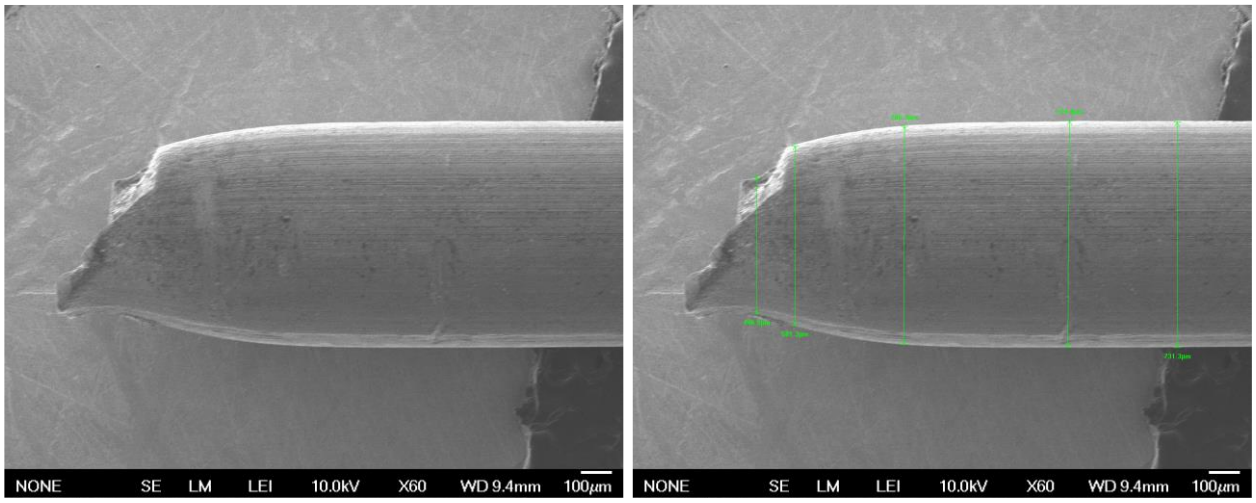


**Figure 3.7: SEM image of the ruptured end of hooked steel fiber (Novocon® HE-4550).**

Figure 3.8 shows the microstructure of the crimped steel fiber (Novocon® XR). Different from the hooked fibers, the crimped steel fibers have a nearly rectangular cross section, so both the thickness and width of the crimped steel fibers were measured. From Figure 3.8a it can be seen that the crimped steel fiber has a slightly rougher surface than the hooked steel fiber with some humps and pits. The measurements in Figure 3.8b indicate that the crimped steel fibers have an average thickness of 603.73 μm. The width of the fiber was measured using a high precision vernier caliper, and an average width of 2,361.67 μm was obtained. Figure 3.9 shows the ruptured end of the crimped steel fibers after failures in the tension test. Similar to the hooked steel fiber, the yielding and necking behavior with decreasing dimensions under tension was observed from the crimped steel fibers. A shear failure surface with an angle of about 45° was also yielded.

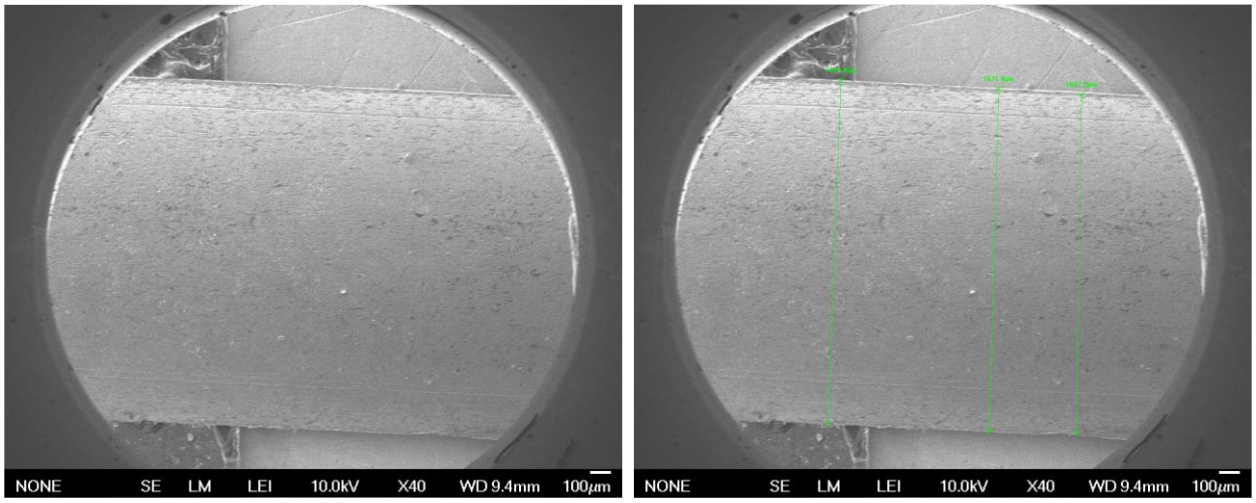


**Figure 3.8: SEM image of crimped steel fiber (Novocon® XR) with dimension measurements**

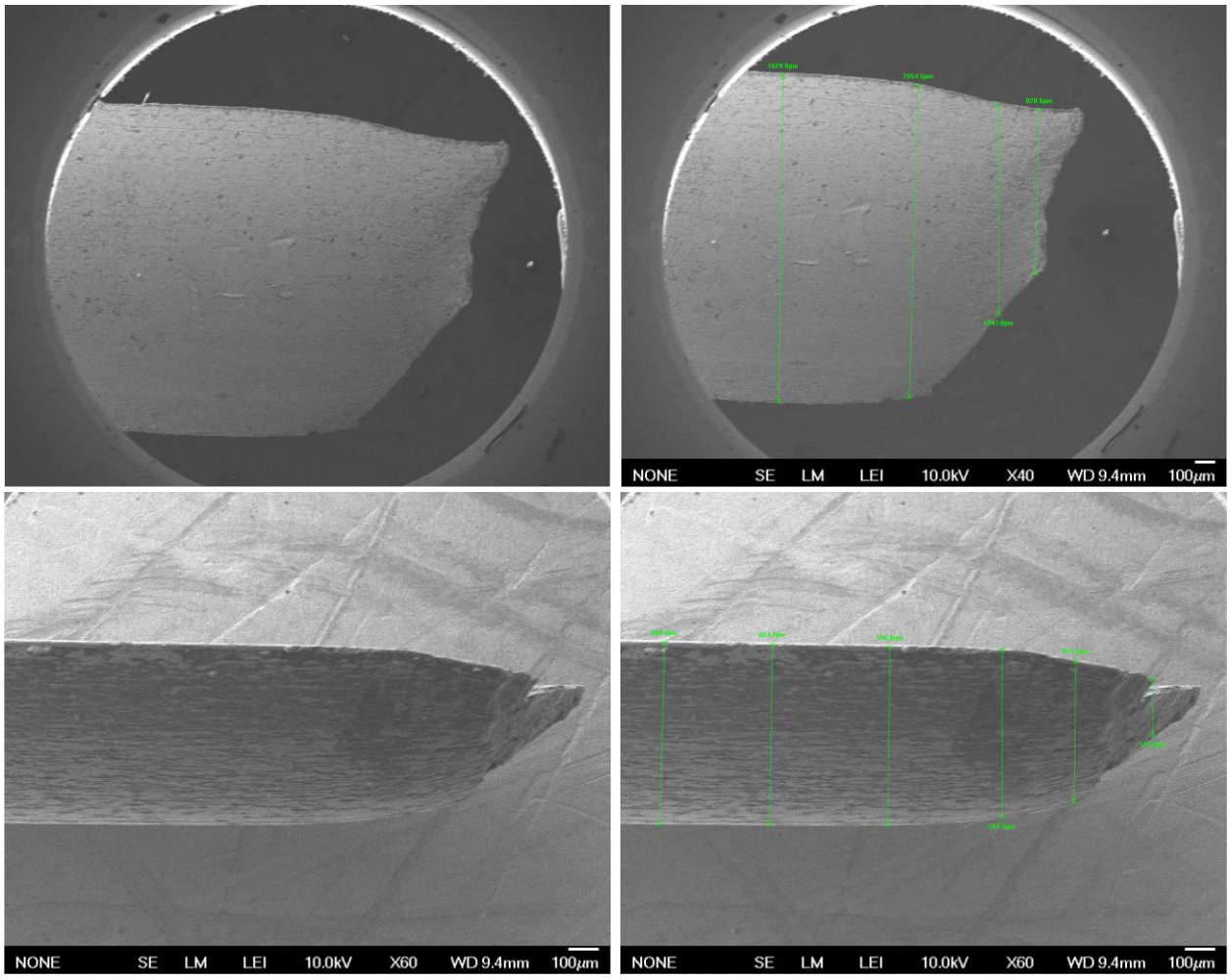


**Figure 3.9: SEM image of the ruptured end of crimped steel fiber (Novocon® XR)**

Figure 3.10 shows the microstructure of the straight synthetic fiber (Fibermesh®-650). Similar to the crimped steel fibers, the straight synthetic fibers have a nearly rectangular cross section, so both the thickness and width were measured under SEM. From Figure 3.10a it can be seen that the straight synthetic fibers have a smooth surface with a strip-shaped texture along the length formed during manufacturing. The measurements in Figure 3.10b indicate that the straight synthetic fibers have an average thickness of 114.54 μm. The width of the fiber was also measured using SEM. As shown in Figure 3.10d, the fibers have an average width of 1,206.7 μm.

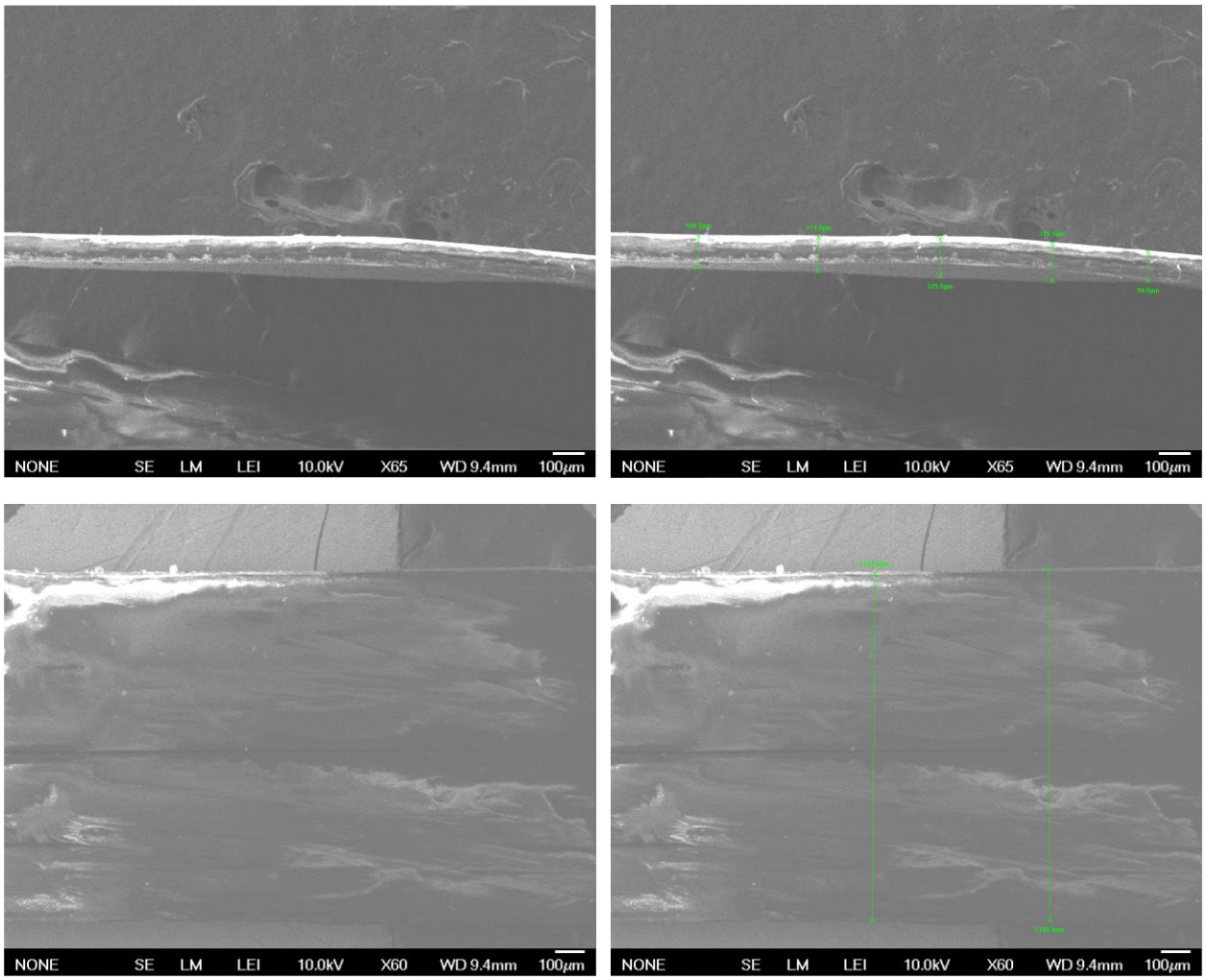


**Figure 3.10: SEM image of straight synthetic fiber (Fibermesh®-650)**

Figure 3.11 shows the microstructure of the crimped synthetic fiber (Enduro® Prime). Similar to the crimped steel fibers and the straight synthetic fibers, the crimped synthetic fibers have a nearly rectangular cross section, so both the thickness and width were measured under SEM. From Figure 3.11a it can be seen that this synthetic fiber has a deformed surface with a crimped texture, which is helpful to improve the bonding between the fiber and the cement matrix in concrete. The measurements in Figure 3.11b indicate that the crimped synthetic fibers have an average thickness of 118.5 μm, which is slightly thicker than the

straight synthetic fibers. The width of the fiber was also measured using SEM. As shown in Figure 3.11d, the fibers have an average width of 1,248.63 μm, which is slightly wider than the straight synthetic fibers.

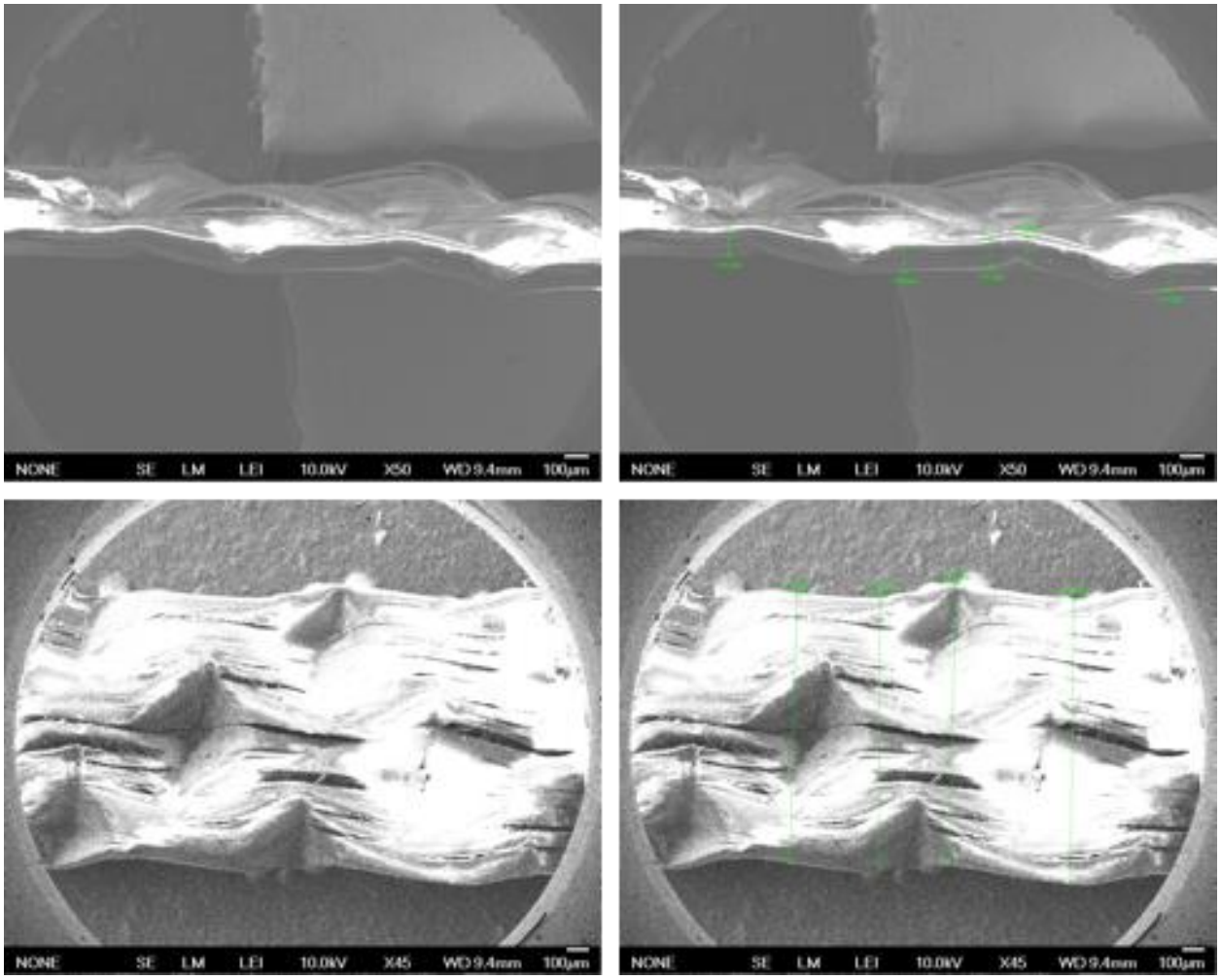


**Figure 3.11: SEM image of crimped synthetic fiber (Enduro® Prime)**

### 3.1.4. Tension test of the macro-fibers

The tension tests of the macro-fibers were performed on an Instron 8511 servo-hydraulic testing machine according to ASTM D3822 with a fixed gage length of 20 mm, where the average elongation of the fibers was first determined. The small thickness of Fibermesh®-650 synthetic fiber makes it unfeasible to be gripped by the machine. Therefore, three types of fibers, i.e., the hooked steel fiber, the crimped steel fiber, and the crimped synthetic fiber, were tested. The PIs decided to use casting resin to increase the contact area at the end of fibers. This test will be provided in the Task 3 Deliverable Report. Table 3.5 summarizes the total elongation, percentage of elongation, and the average elongation rate.

**Table 3.5: Elongation rate (%) of the fibers**

| Sample | Steel Fiber (Hooked) | Steel Fiber (Crimped) | Synthetic Fiber (Crimped) |
|---|---|---|---|
| Sample 1 | 7.4295 | 12.7 | 12.7 |
| Sample 2 | 8.039 | 13.335 | 13.97 |
| Sample 3 | 8.763 | 13.97 | 21.59 |
| Average elongation rate | 8.077 | 13.335 | 16.087 |

From Table 3.5, it can be seen that the hooked steel fiber, crimped steel fiber, and crimped synthetic fiber yield average elongation rates of 8.077, 13.335, and 16.087, respectively, which are all in the range of 8% to 100% defined in ASTM D3822. Table 3.6 summarizes the suggested testing speed of the single fiber tension test per ASTM D3822. Therefore, a displacement control of 12 mm/min (0.472 inch/min, which is 60% of the initial gauge length) was employed for the tension test. Figure 3.12 shows the tension test for the fibers.

**Table 3.6: Testing speed of the single fiber tension test**

| Average elongation rate | Testing speed, mm/min (inch/min)<br><br>Steel Fiber (Hooked) | Testing speed, mm/min (inch/min)<br><br>Steel Fiber (Crimped) | Testing speed, mm/min (inch/min)<br><br>Polymer Fiber (Crimped) |
|---|---|---|---|
| Under 8% | 2 (0.0787) | 2 (0.0787) | 2 (0.0787) |
| 8 to 100% | 12 (0.4724) | 12 (0.4724) | 12 (0.4724) |
| Over 100% | 48 (1.8898) | 48 (1.8898) | 48 (1.8898) |

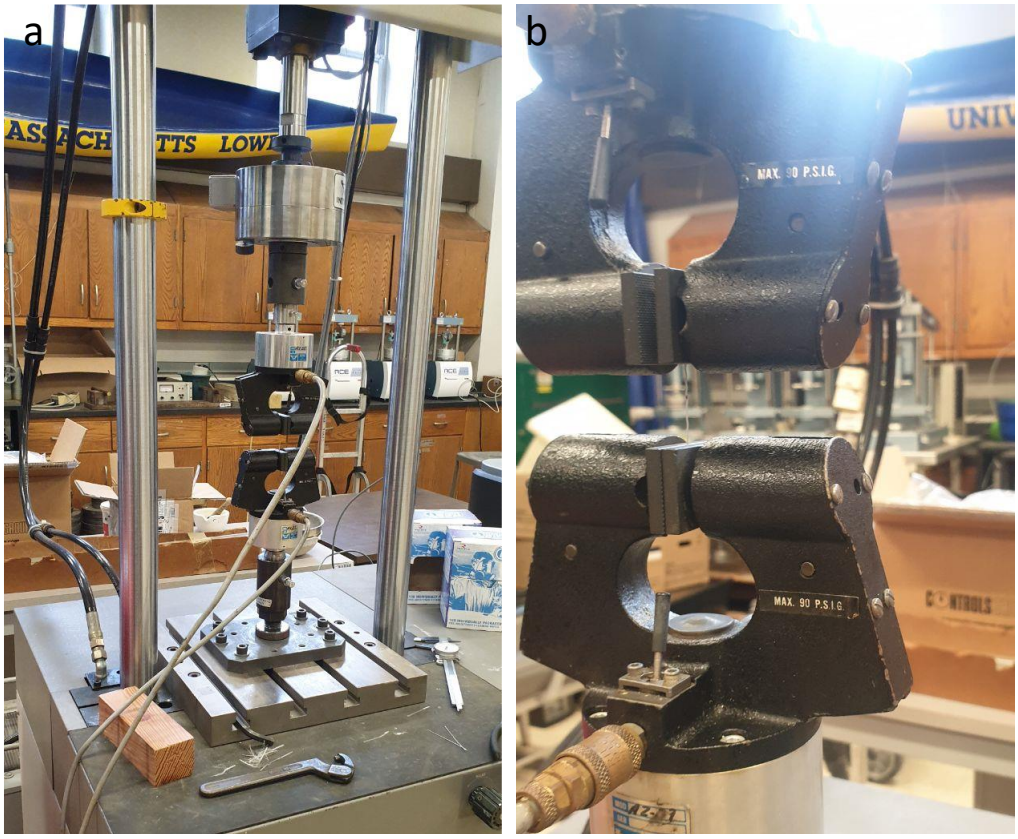


**Figure 3.12: Tension test of the macro-fibers.**

Figures 3.13a to 3.13c show the load-displacement curves of the hooked steel fiber (Novocon® HE-4550), crimped steel fiber (Novocon® XR), and crimped synthetic fiber (Enduro® Prime), respectively. Table 3.7 to Table 3.9 summarize the testing results of peak load, the load at failure, displacement at peak load, and displacement at failure. It can be seen that the two steel fibers are stronger than the synthetic fibers. The hooked steel fiber yielded an average peak load of 797.8 N, while the crimped steel fibers showed an average peak load of 896.4 N. In addition to the higher loading capacity, the crimped steel fibers also exhibited higher elongation behavior. It was found that the crimped steel fiber yielded average displacements at peak and failure loads of 2.5018 mm and 2.8493 mm, while the hooked steel fibers yielded average displacements at peak and failure loads of 1.2968 mm and 1.8448 mm, respectively. The crimped synthetic fibers yielded average peak and failure loads of 102.2 N and 87.2 N, respectively, which are 1/10 to 1/8 of the steel fiber. However, due to the low modulus of elasticity, the synthetic fibers exhibited a high elongation of 2.2490 mm at the peak load, which is comparable to the crimped steel fibers.

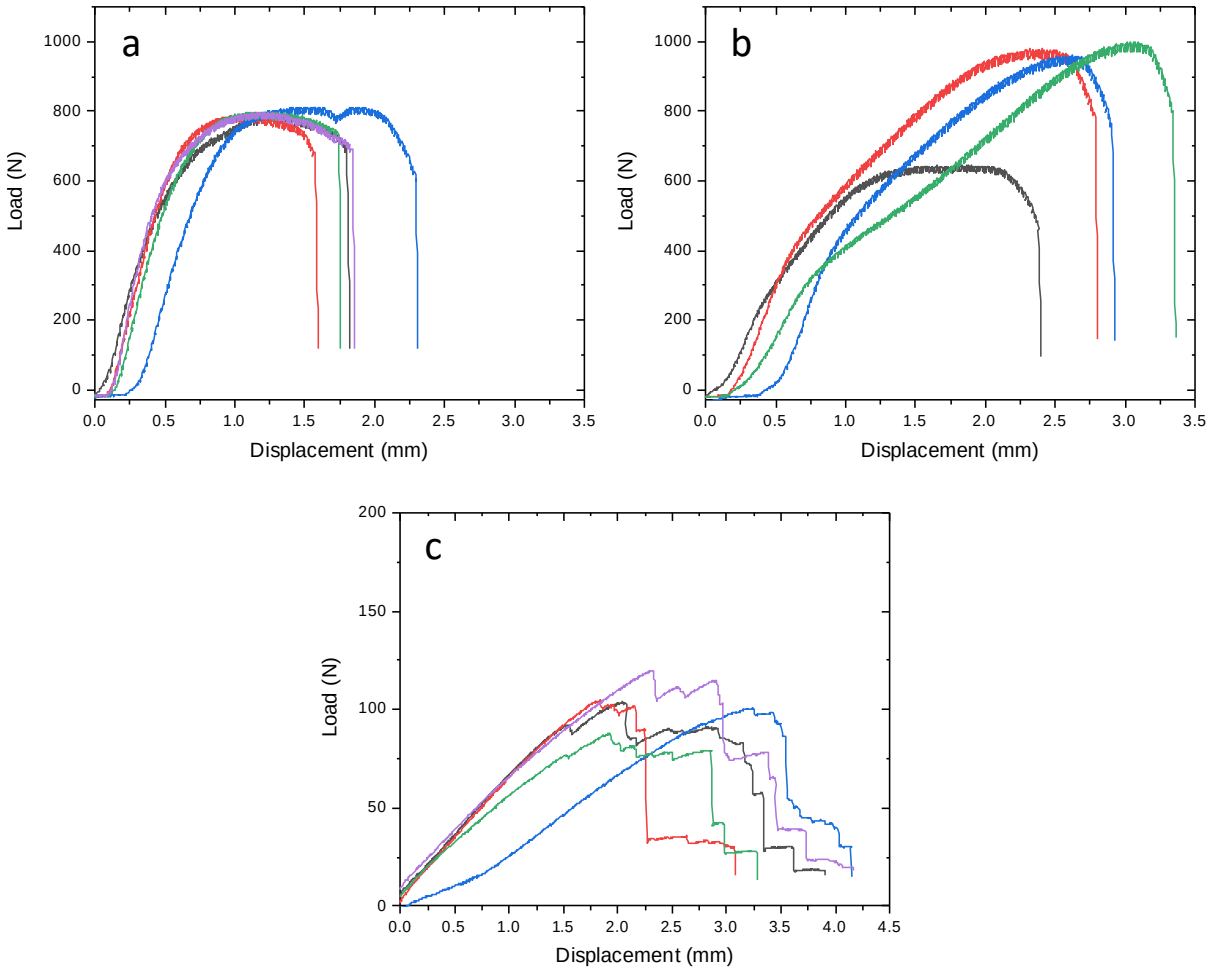


(a) hooked steel fiber (Novocon® HE-4550), (b) crimped steel fiber (Novocon® XR), and (c) crimped synthetic fiber (Enduro® Prime)

**Figure 3.13: Load-displacement curves of single-fiber tension tests.**

**Table 3.7: Testing results obtained from the load-displacement curves of the hooked steel fibers.**

| Sample | Displacement at Peak Load (mm) | Peak Load (N) | Displacement at Failure load (mm) | Failure Load (N) |
|---|---|---|---|---|
| 1 | 1.2612 | 790.2 | 1.8039 | 618.5 |
| 2 | 1.0686 | 789.8 | 1.5785 | 595.6 |
| 3 | 1.8927 | 812.3 | 2.2898 | 606.2 |
| 4 | 1.1064 | 798.8 | 1.74 | 729.6 |
| 5 | 1.155 | 798.0 | 1.8118 | 711.9 |
| Ave. | 1.2968 | 797.8 | 1.8448 | 652.4 |

**Table 3.8: Testing results obtained from the load-displacement curves of the crimped steel fibers.**

| Sample | Displacement at Peak Load (mm) | Peak Load (N) | Displacement at Failure load (mm) | Failure Load (N) |
|---|---|---|---|---|
| 1 | 1.899 | 645.9 | 2.3618 | 500.4 |
| 2 | 2.4051 | 979.3 | 2.7851 | 755.2 |
| 3 | 2.6264 | 960.9 | 2.9056 | 734.4 |
| 4 | 3.0766 | 999.5 | 3.3448 | 760.0 |
| Ave. | 2.5018 | 896.4 | 2.8493 | 687.4 |

**Table 3.9: Testing results obtained from the load-displacement curves of the crimped synthetic fibers.**

| Sample | Displacement at Peak Load (mm) | Peak Load (N) | Displacement at Failure load (mm) | Failure Load (N) |
|---|---|---|---|---|
| 1 | 2.0425 | 103.9 | 2.0751 | 100.1 |
| 2 | 1.8419 | 104.7 | 2.1696 | 92.1 |
| 3 | 3.2366 | 100.7 | 3.5397 | 86.5 |
| 4 | 1.9289 | 87.8 | 2.8589 | 70.2 |
| 5 | 2.3203 | 120.1 | 2.9589 | 103.1 |
| 6 | 2.1237 | 95.9 | 2.2894 | 71.0 |
| Ave. | 2.2490 | 102.2 | 2.6486 | 87.2 |

By considering the cross sections of the fibers, Figures 3.14a to 3.14c show the stress and strain curves of the hooked steel fiber, crimped steel fiber, and crimped synthetic fiber, respectively. From the figures, it can be found that different from the capable load capacity, the hooked steel fiber yielded higher strength than the crimped steel fiber, while the crimped fiber showed a higher elongation rate. Table 3.10 to Table 3.12 summarize the key stress and strain information for the fibers. The hooked steel fiber showed an average tensile strength of 1,896.8 MPa, which is 72.4% higher than the provided strength (1,100 MPa). However, the crimped steel fiber yielded an average tensile strength of 628.7 MPa, which is 34.9% lower than the manufacturer's reported strength (965 MPa). Compared with steel fibers, the crimped synthetic fiber showed a lower average tensile strength of 69.06 MPa. The hooked steel fiber yielded average elongation rates (strain) at the peak stress and failure of 0.0648 and 0.0922, while the crimped steel fiber exhibited higher elongation rates of 0.1251 and 0.1425 at the peak stress and failure, respectively. Similar to the observations from the load-displacement curves, the crimped synthetic fiber yielded average elongation rates (strain) at the peak stress and failure of 0.1124 and 0.1324, which are comparable with the values obtained from the crimped steel fiber.

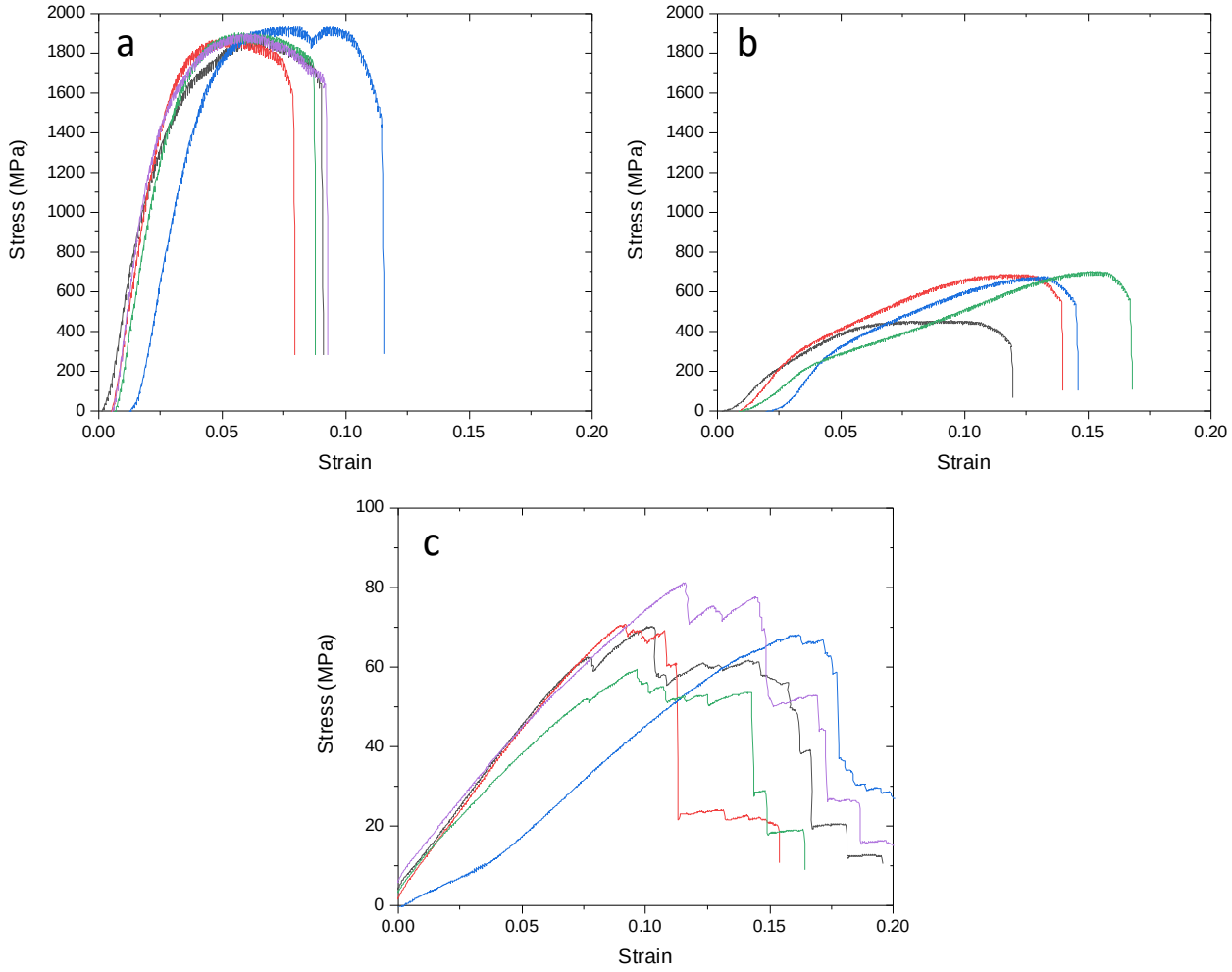


(a) hooked steel fiber (Novocon® HE-4550), (b) crimped steel fiber (Novocon® XR), and (c) crimped synthetic fiber (Enduro® Prime).

**Figure 3.14: Stress-strain curves of single-fiber tension tests**

**Table 3.10: Key stress and strain obtained from the tension test of hooked steel fibers**

| Sample | Tensile strength (MPa) | Stress at failure (MPa) | Strain at peak stress | Strain at failure |
|---|---|---|---|---|
| 1 | 1878.7 | 1470.6 | 0.0631 | 0.0902 |
| 2 | 1877.7 | 1416 | 0.0534 | 0.0789 |
| 3 | 1931.2 | 1441.2 | 0.0946 | 0.1145 |
| 4 | 1899.2 | 1734.6 | 0.0553 | 0.087 |
| 5 | 1897.4 | 1692.4 | 0.0578 | 0.0906 |
| Ave. | 1896.8 | 1551.0 | 0.0648 | 0.0922 |

**Table 3.11: Key stress and strain obtained from the tension test of the crimped steel fibers**

| Sample | Tensile strength (MPa) | Stress at failure (MPa) | Strain at peak stress | Strain at failure |
|---|---|---|---|---|
| 1 | 453.03 | 350.94 | 0.095 | 0.1181 |
| 2 | 686.83 | 529.69 | 0.1203 | 0.1393 |
| 3 | 673.93 | 515.04 | 0.1313 | 0.1453 |
| 4 | 701.02 | 533.04 | 0.1538 | 0.1672 |
| Ave. | 628.70 | 482.18 | 0.1251 | 0.1425 |

**Table 3.12: Key stress and strain obtained from the tension test of the crimped synthetic fibers**

| Sample | Tensile strength (MPa) | Stress at failure (MPa) | Strain at peak stress | Strain at failure |
|---|---|---|---|---|
| 1 | 70.217 | 67.677 | 0.1021 | 0.1038 |
| 2 | 70.787 | 62.229 | 0.0921 | 0.1085 |
| 3 | 68.055 | 58.469 | 0.1618 | 0.177 |
| 4 | 59.371 | 47.437 | 0.0964 | 0.1429 |
| 5 | 81.137 | 69.658 | 0.116 | 0.1479 |
| 6 | 64.783 | 47.99 | 0.1062 | 0.1145 |
| Ave. | 69.058 | 58.91 | 0.1124 | 0.1324 |

## 3.2 Micro-Fibers for Ultra-High Performance Concrete

### 3.2.1. Types of fibers

Based on the literature review in Task 1, four types of micro-fibers, micro-steel fiber, polyvinyl alcohol (PVA) fibers, basalt fibers, and alkali-resistant (AR) glass fibers, have been collected in this project. As shown in Figure 3.15 and Table 3.13, the four fibers share a similar length, i.e., 12 mm – 13 mm, which has been proven to be an effective length to reinforce UHPC in terms of workability and mechanical strength enhancement. The AR glass fiber with a diameter of 3.9 × 10-4-inch (10 μm), a specific gravity of 2.7, and a tensile strength of 290 ksi (2,000 MPa) is obtained from NyCon. Figure 3.15b shows the bunchy AR glass fibers. The PVA fiber with a diameter of 3.9 × 10-3-inch (100 μm), which is 10 times AR glass fibers, a specific gravity of 1.3, and tensile strength of 174 ksi (1,200 MPa) is also obtained from Nycon. The basalt fiber with a diameter of 6.3-6.7 × 10-4-inch (16 to 17 μm), length of 0.47-inch (12 mm), and specific gravity of 2.67 is obtained from BlobMarble. The tensile strength of the basalt fiber was not provided. The micro-steel fiber, which is the most commonly used fiber for UHPC, is obtained from Hiper Fiber. The diameter, length, and tensile strength of the micro-steel fiber are $7.87 \times 10^{-3}$-inch (200 μm), 0.51-inch (13 mm), and 413.36 ksi (2,850 MPa), respectively.

**Table 3.13: Physical properties of micro-fibers**

| Fiber | AR glass fiber | PVA fiber | Basalt fiber | Steel fiber |
|---|---|---|---|---|
| Manufacturer | Nycon | Nycon | - | Hiper fiber |
| Code of fiber | NYCON-AR-DM | NYCON-PVA RECS100 | BCF | SHT BP60 |
| Diameter | 0.0005” (10 μm) | 20 Denier (100 μm) | 16-17 μm | 0.2 mm (200 μm) |
| Length | 0.5” (13 mm) | 0.5” (13 mm) | 12 mm | 0.5” (13 mm) |
| Specific gravity | 2.7 | 1.3 | 2.67 | - |
| Tensile strength | 300 ksi (2,000 MPa) | 180 ksi (1,200 MPa) | - | 2,850 MPa |
| Flexural strength | 11,000 ksi (77 GPa) | 3600 ksi (25 GPa) | - | - |
| Melting point | 2075o F (1121o C) | 435o F (225o C) | - | - |
| Color | White | White | Jasper | Brass |
| Water absorption | < 1% | < 1% | - | - |

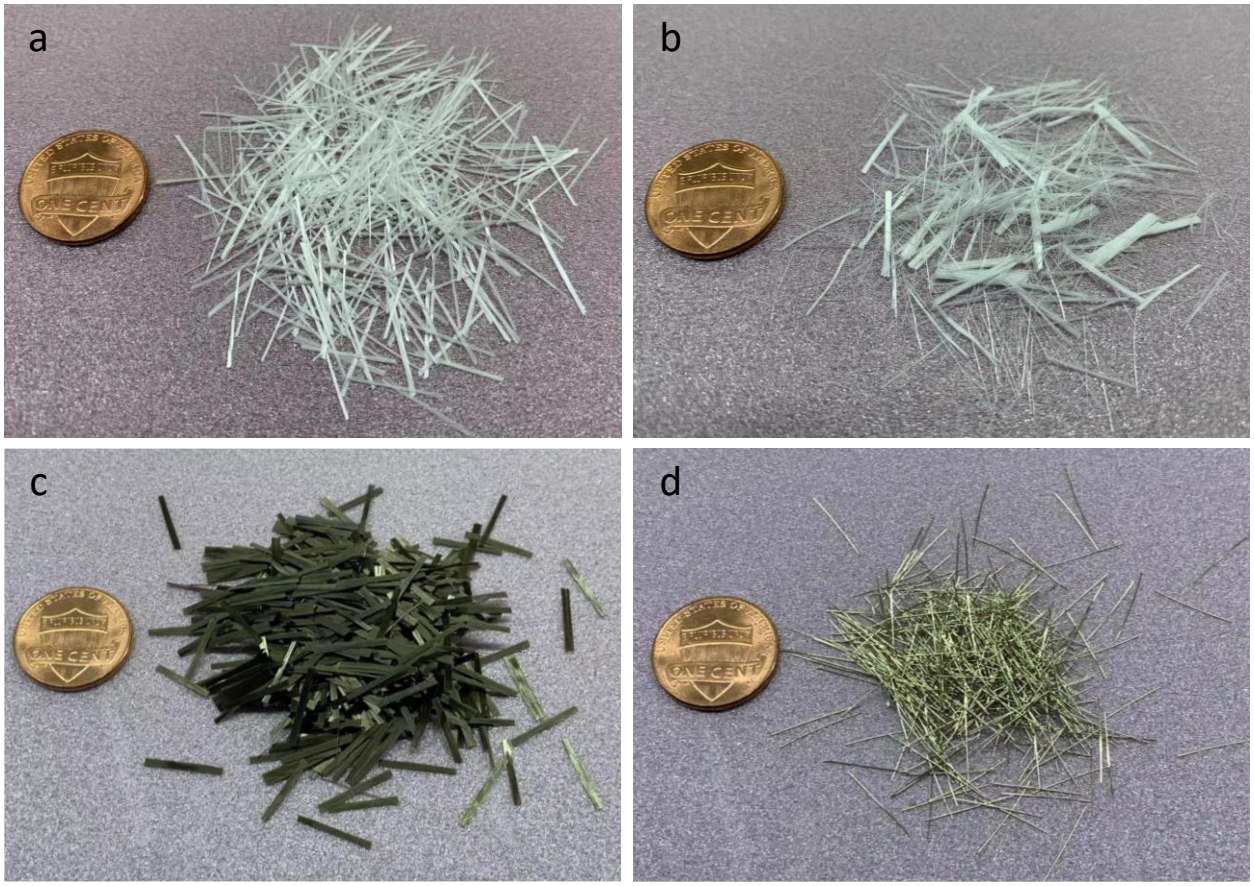


(a) PVA fiber, (b) AR glass fiber, (c) basalt fiber, and (d) steel fiber

**Figure 3.15: Micro-fibers for UHPC.**

### 3.2.2. Microstructure analysis

To characterize the micro-morphology, determine the dimensions, and accurately calculate the mechanical properties, microstructure analyses of the micro-fibers were conducted using SEM. Same with the work for the macro-fibers, the microstructure analysis was also leveraged to analyze the micro-morphology of the rupture ends of the micro-fibers after they failed in the tension tests.

Figures 3.16 to 3.19 show the microstructures of four AR glass fibers (NYCON-AR-DM). The cross section of the glass fiber is nearly a circle, so only the diameter was measured. From the figures, it can be seen that the glass fiber's surface has hump or pit. This is helpful to improve the bonding strength between the fibers and the cement matrix of UHPC. The measurements indicate that the AR glass fibers used in this project have an average diameter of 24.93 μm.

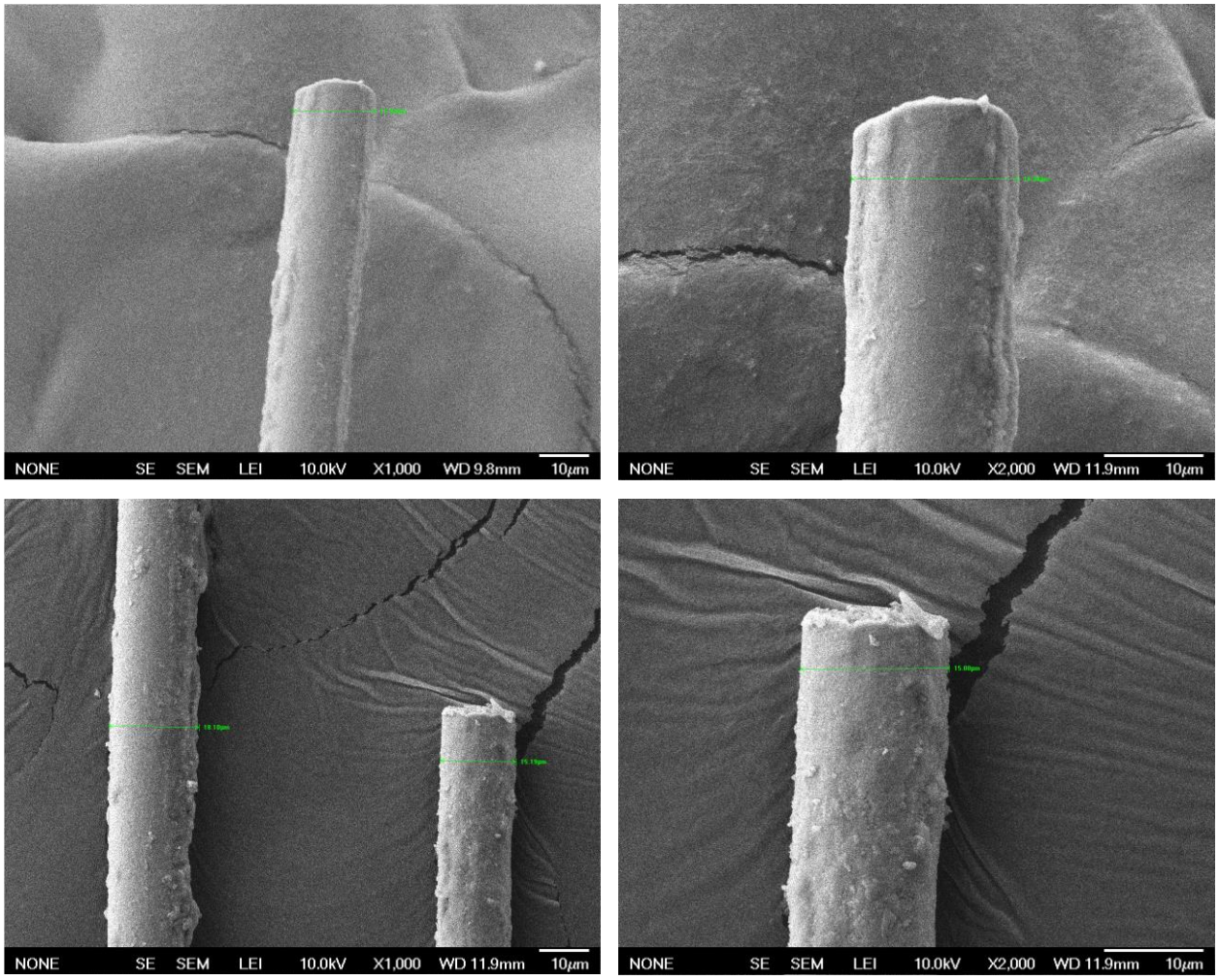


**Figure 3.16: Scanning electron microscope (SEM) image of glass fiber 1**

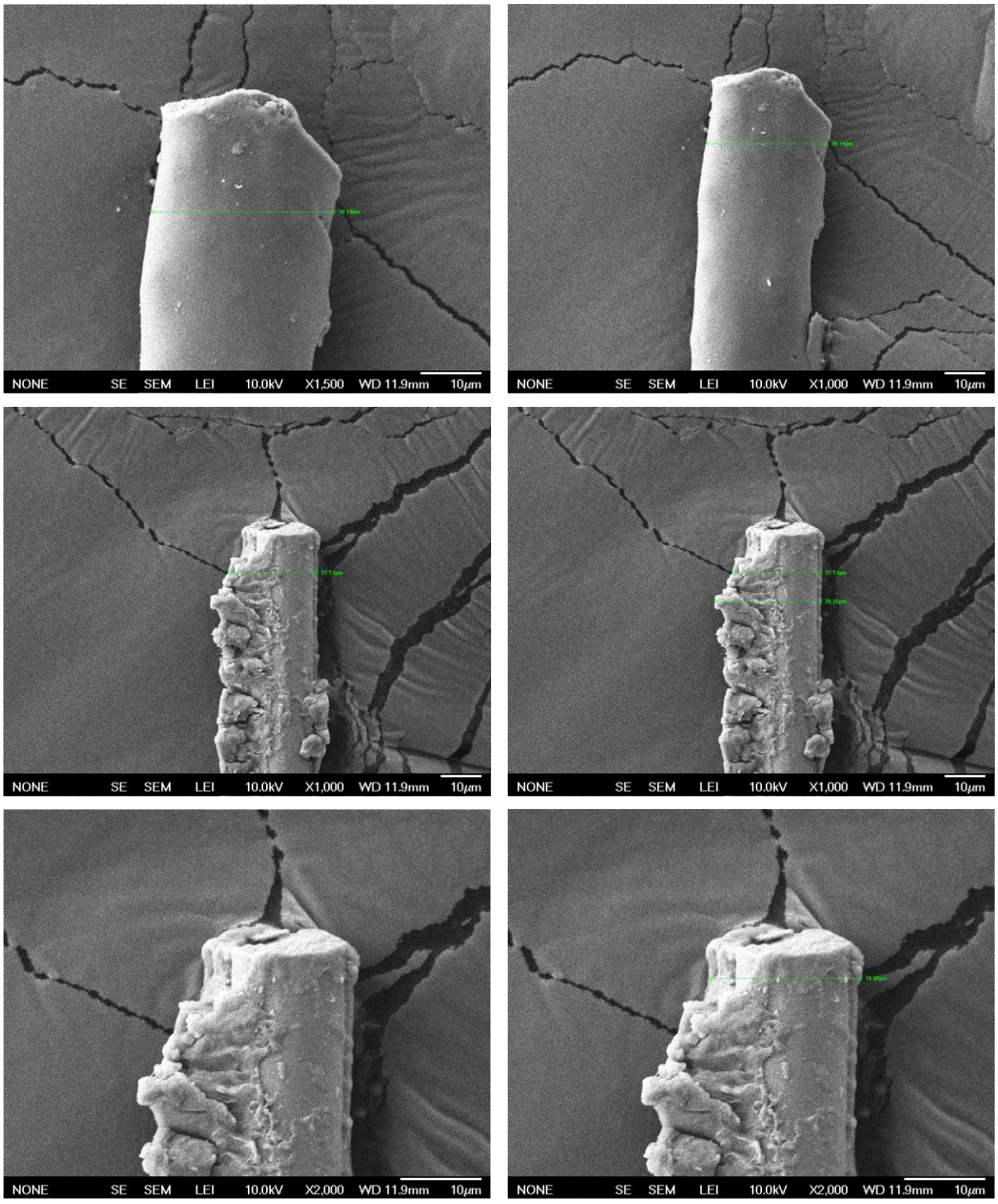


**Figure 3.17: SEM image of glass fiber 2**

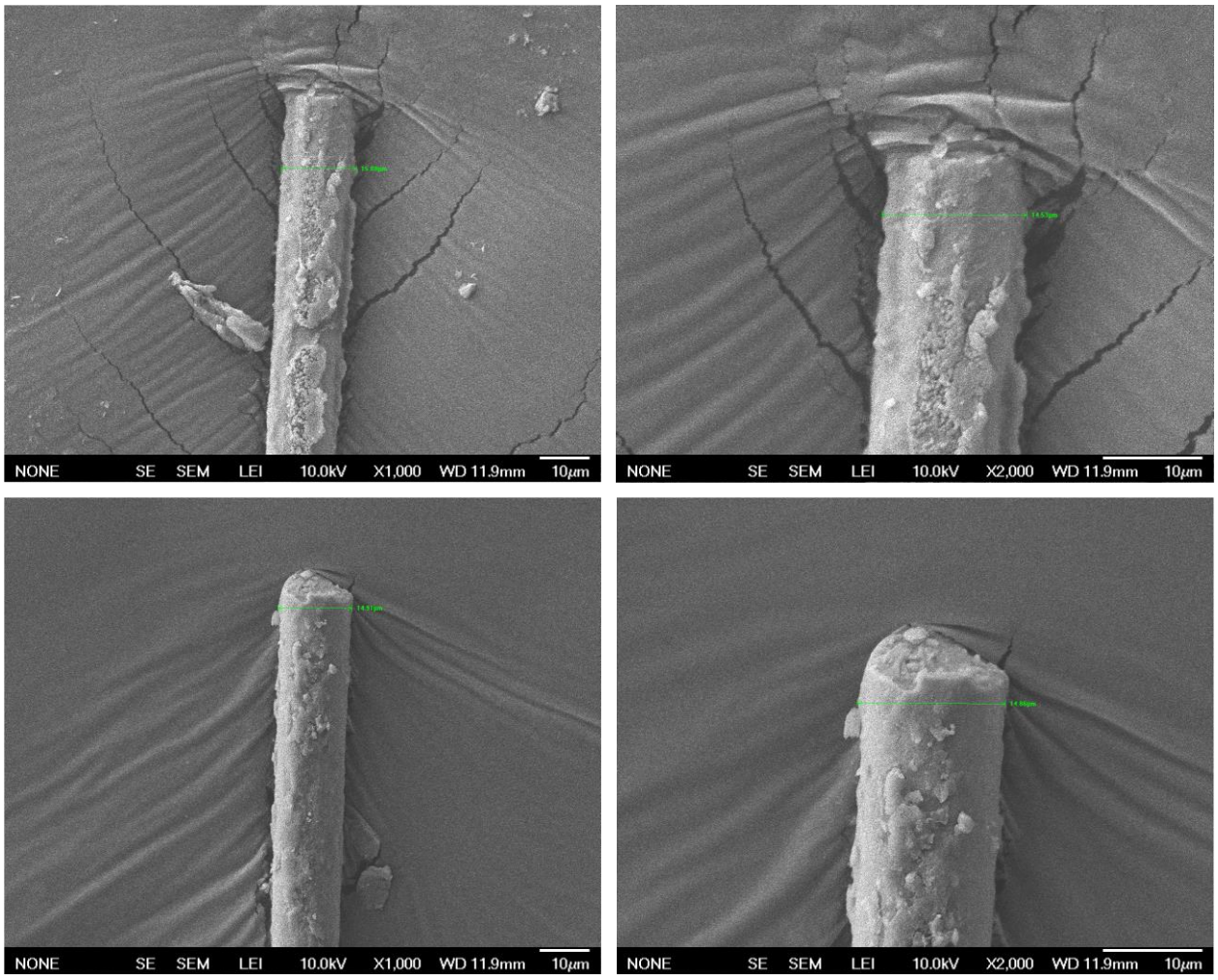


**Figure 3.18 SEM image of glass fiber 4**

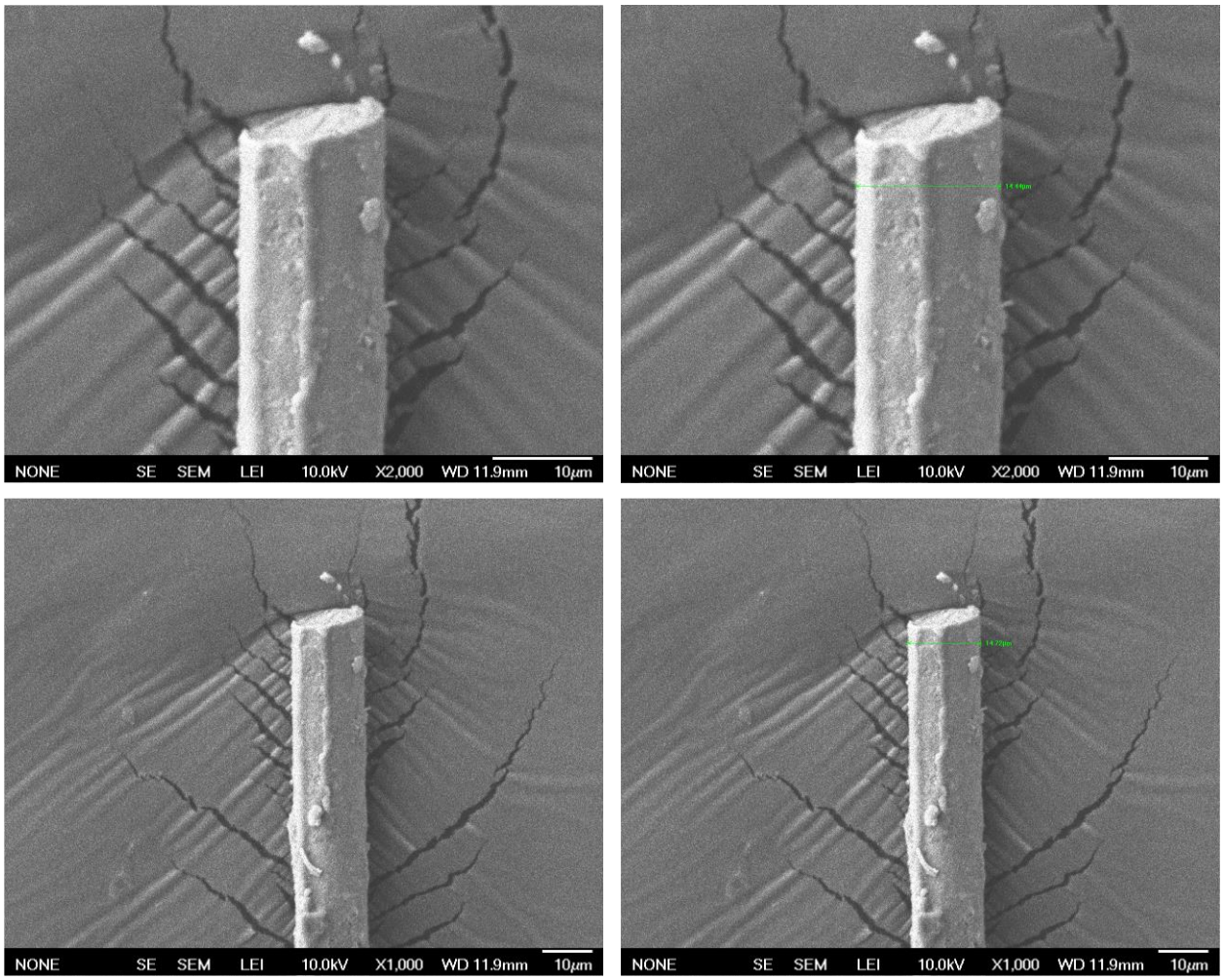


**Figure 3.19: SEM image of glass fiber 6**

Figures 3.20 to 3.21 show the microstructures of two PVA fibers (NYCON-PVA RECS100). The cross section of the PVA fiber is also nearly circular, so only the diameter was measured. The cloth-like item wrapping the end of the fiber is the carbon tape used to conduct electricity under SEM. It was found that the surface of PVA fiber is smoother than that of the glass fiber but still has hump or pit. The measurements indicate that the PVA fibers have an average diameter of 72.14 μm. Figures 3.22 to 3.24 show the rupture ends of three PVA fibers after the tension test. Similar to the macro-fibers, shear rupture surfaces with an angle of nearly 45° with stripping textures were observed.

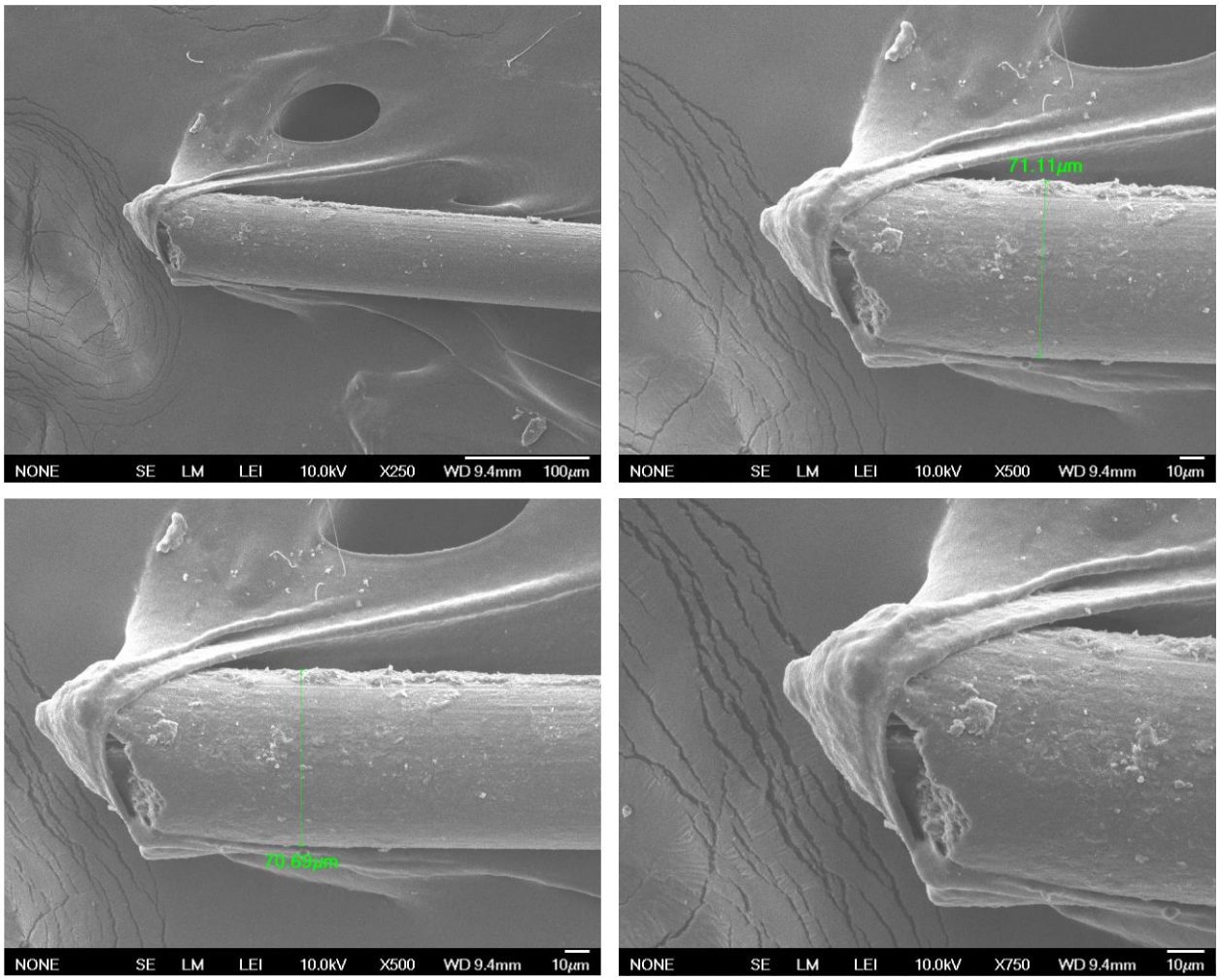


**Figure 3.20: SEM image of PVA fiber 1**

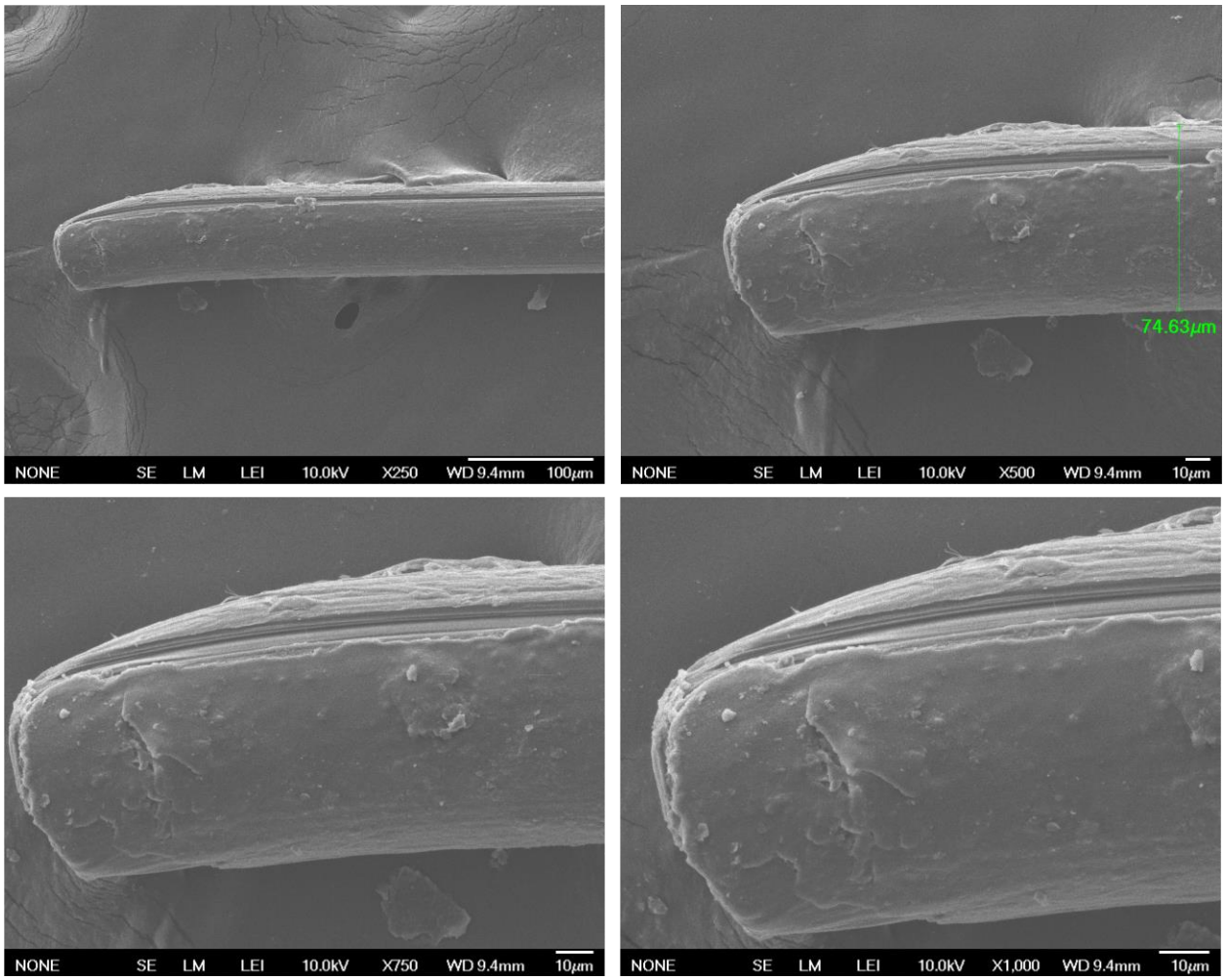


**Figure 3.21: SEM image of PVA fiber 2**

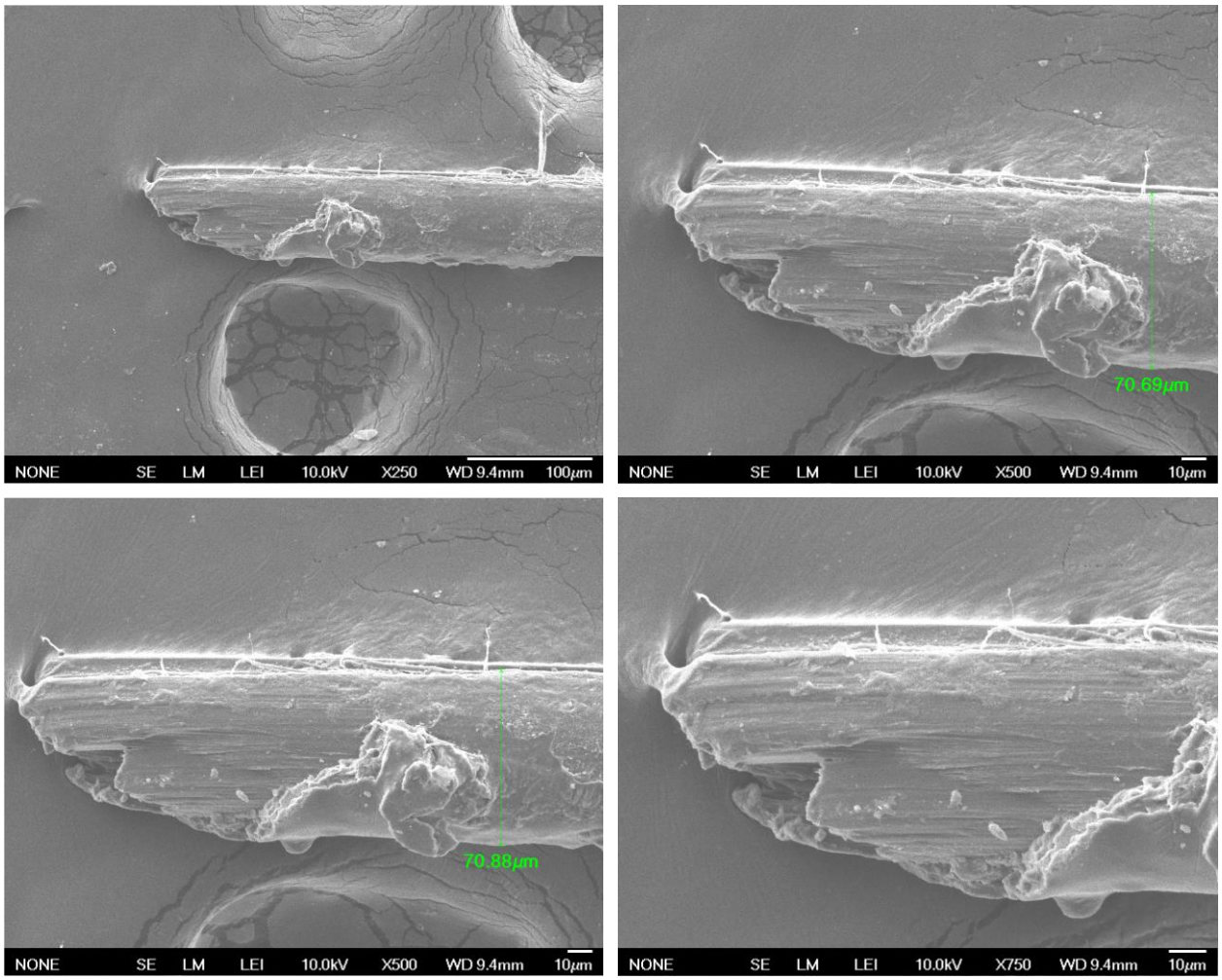


**Figure 3.22: SEM image of rupture end of PVA fiber 1**

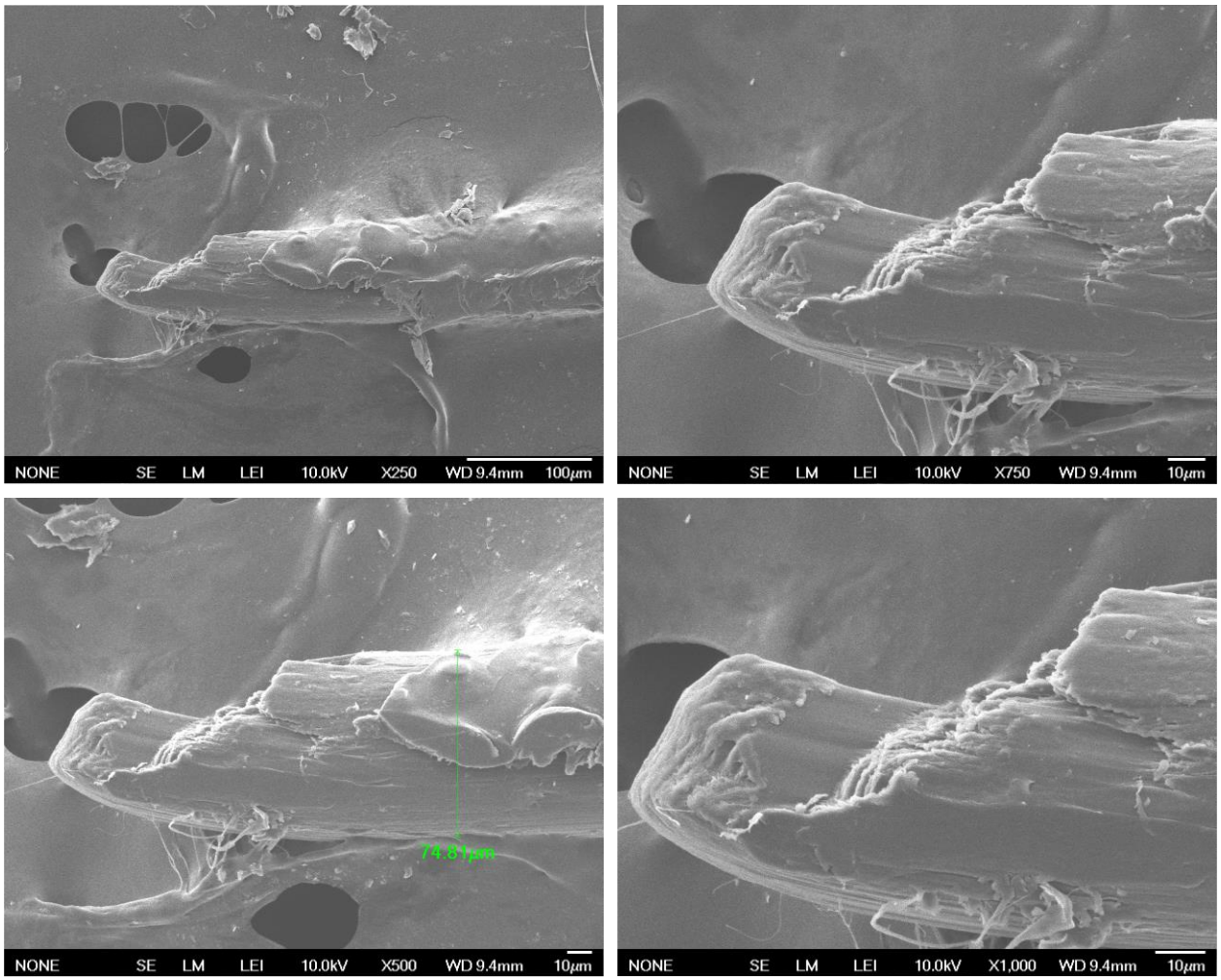


**Figure 3.23: SEM image of rupture end of PVA fiber 2**

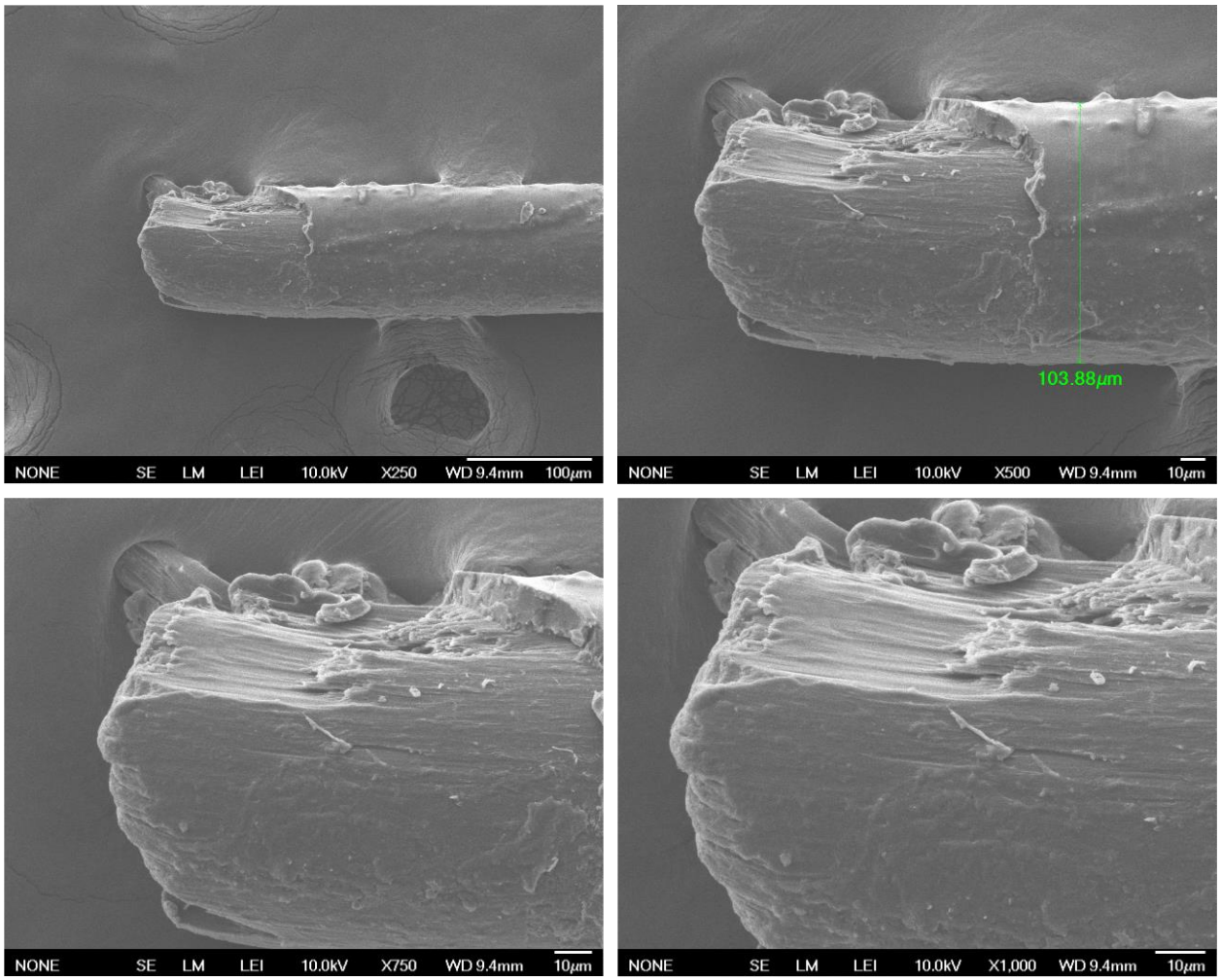


**Figure 3.24: SEM image of rupture end of PVA fiber 3**

Figure 3.25 shows the microstructure of a basalt fiber. Although still with humps and pits, this mineral fiber shows a smoother surface than both the AR glass fiber and PVA fiber. Figure 3.26 shows the fracture surface of a basalt fiber after it fails in the tension test. Although with stepped mode, it can be observed that the final rupture is still due to shear failure.

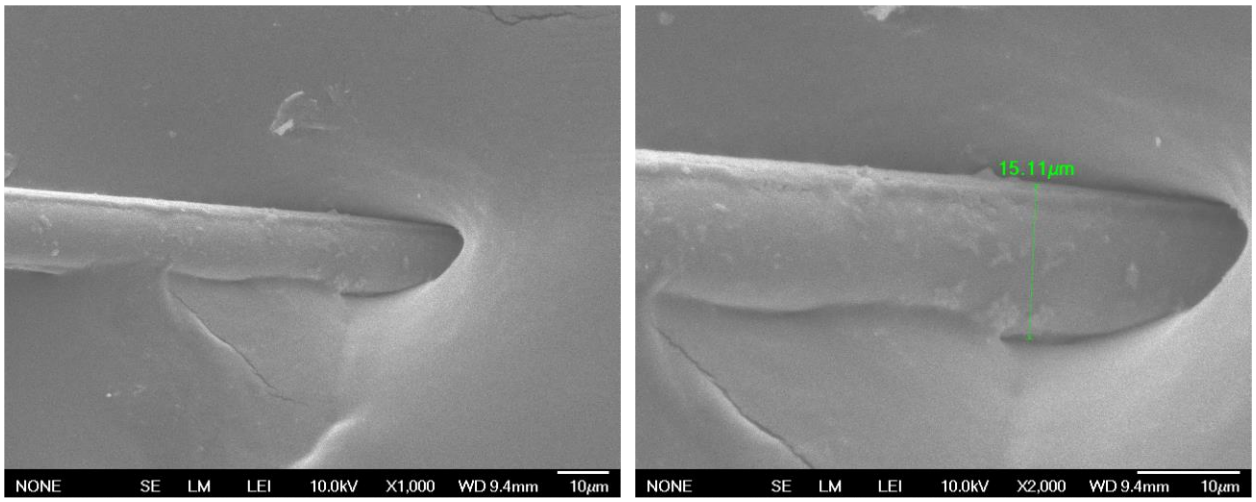


**Figure 3.25: SEM image of basalt fiber**

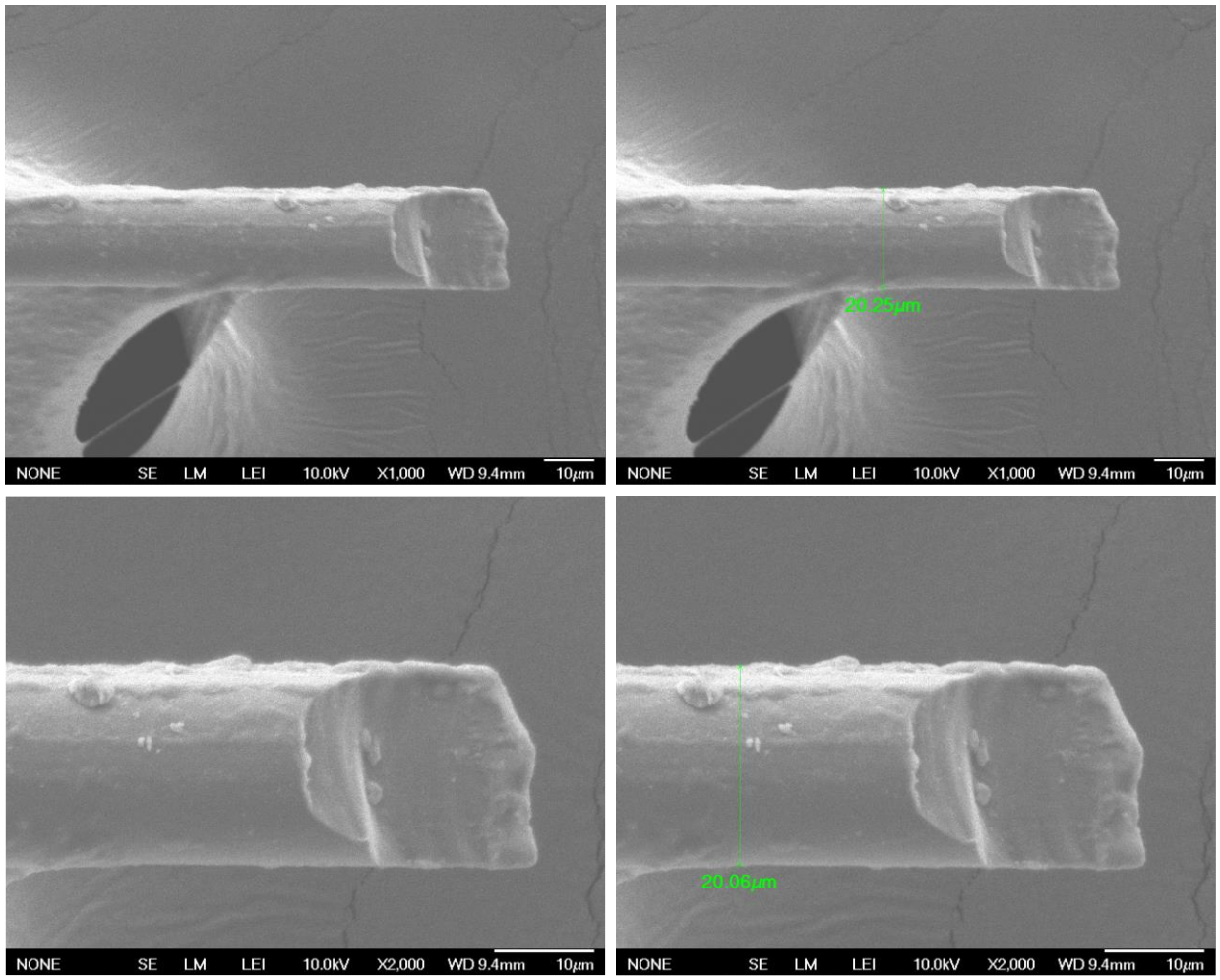


**Figure 3.26: SEM image of rupture end of basalt fiber**

### 3.2.3. Single-fiber tension test

The micro-steel fiber has been well characterized by the manufacturer will a detailed report of mechanical properties (tensile strength of 2,850 MPa and modulus of elasticity of 210 GPa). Therefore, the PVA fiber, AR glass fiber, and basalt fiber were characterized in this project. The small diameters of the fibers make it unfeasible to be gripped by the machine. To address this challenge, the single fibers were tested based on mounting tabs. As shown in Figure 3.27, mounting tabs are prepared from cardboard with a length of 14 mm and a width of 6 mm. A rectangular slot of length 6 mm and width 3 mm is cut from the tab. The center of the mounting tab is marked so that the monofilament of the fiber can be aligned exactly to the center and the monofilament of the fiber is attached to the mounting tab with the help of super glue. The glue is completely smeared on either side of the mounting tab, which allows 6 mm of the cut-out slot to be the gauge length. Care is taken under the microscope to make sure that the fiber is straight and not twisted.

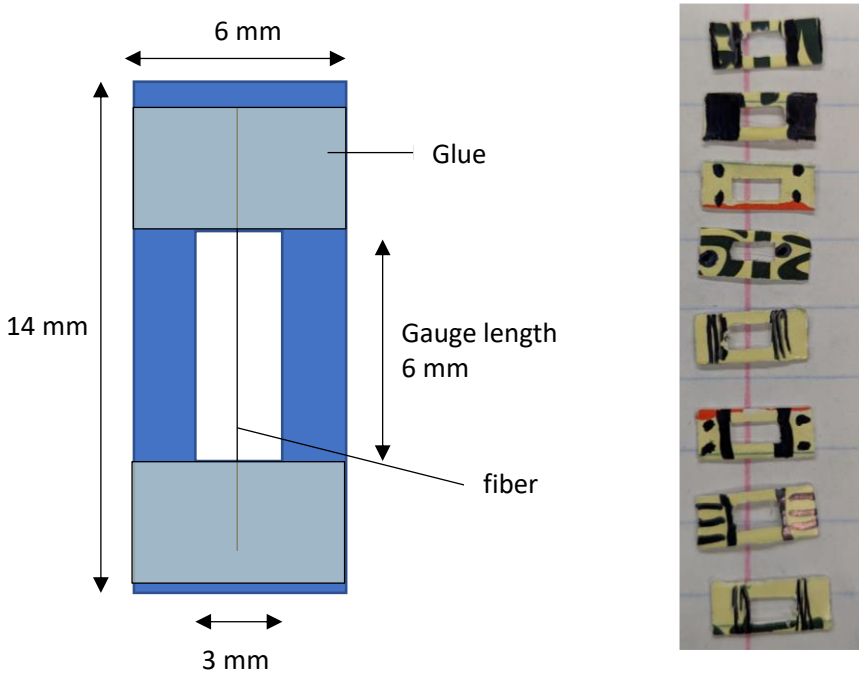


**Figure 3.27: Fiber and mounting tabs for the single-fiber tensile strength test.**

To determine the tensile strength and modulus of the tiny single fibers at a highly accurate level, the fibers were tested on a dynamic mechanical analyzer (DMA) with a loading capacity of 4 lbs. (18 N). As shown in Figure 3.28, the mounting tabs with single fibers were first gripped to DMA by adjusting the distance between the grips and ensuring a gauge length of 0.2362 inches (6 mm). Right before starting the tension test, the two sides of the mounting tab were cut so only a single fiber was subjected to tensile load. The tension tests were performed according to ASTM D3822 with testing speeds of 0.4 N/min for basalt and AR glass fibers and 4 N/min for the PVA fiber with a target to complete each of the tests within 3 minutes.

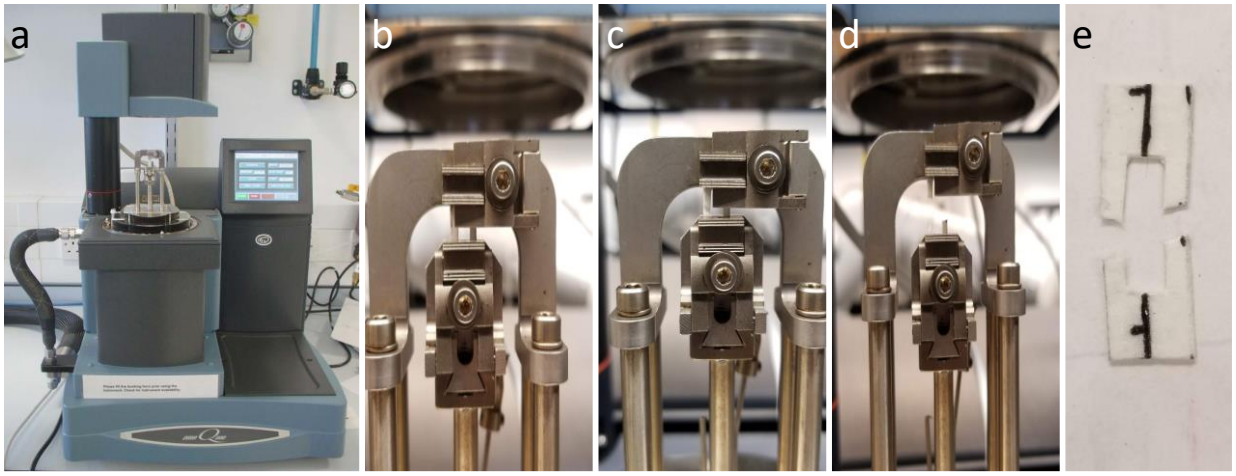


(a) dynamic mechanical analyzer (TA Instruments Q800) with a loading capacity of 18 N, (b) grip details of a mounting tab, (c) gripped mount tab after cutting, (d) after fiber's rupture and (e) fiber and mounting tab after tension test

**Figure 3.28: Apparatus for single fiber tension test.**

Figures 3.29a to 3.29c show the load-displacement curves of the AR glass fibers, PVA fibers, and basalt fibers, respectively. Different from the macro-fibers, the three micro-fibers all exhibit linear load-displacement curves and rupture at the peak load. This brittle behavior might be due to the tiny diameter of the fibers where yielding and necking cannot occur at the selected loading rates. Table 3.14 summarizes the peak load and the displacement at the failure of the fibers under tension. It can be seen that the glass fibers show a larger variation than PVA and basalt fibers in both loading and elongation capacity. Three glass fibers yielded peak loads in a range of 0.7 to 0.9 N, while the other three reached peak loads between 0.2 and 0.4 N. The PVA fiber yielded an average peak load of 9.189 N, which is the highest value among the tested three types of fibers. In addition, PVA fiber displayed an average elongation at failure of 710.92 µm, which is also the highest deformation capacity among the three fibers. The basalt fiber showed an average peak load of 0.787 N and a failure elongation of 243.83 µm, both of which are between the previous two fibers and are more comparable to the AR glass fiber.

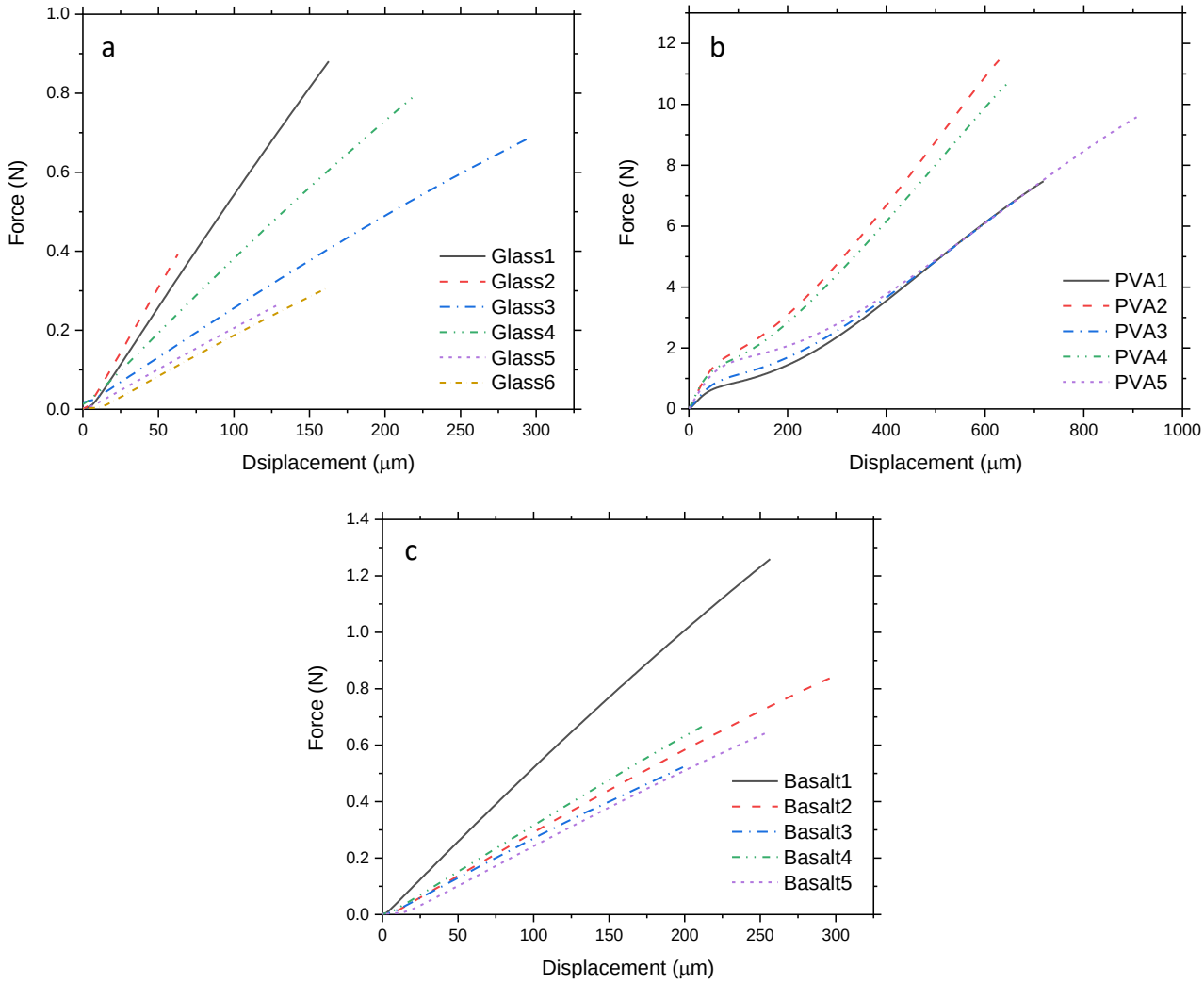


(a) AR glass fibers, (b) PVA fibers, and (c) basalt fibers

**Figure 3.29: Load-displacement curves of single-fiber tension tests.**

**Table 3.14: Peak load and displacement of the fibers under tension**

| Sample | AR glass fiber Peak load (N) | AR glass fiber Displacement at failure (μm) | PVA fiber Peak load (N) | PVA fiber Displacement at failure (μm) | Basalt fiber Peak load (N) | Basalt fiber Displacement at failure (μm) |
|---|---|---|---|---|---|---|
| 1 | 0.881 | 162.75 | 7.476 | 718.64 | 1.259 | 256.53 |
| 2 | 0.392 | 62.80 | 11.451 | 628.41 | 0.840 | 297.23 |
| 3 | 0.691 | 297.48 | 6.791 | 657.62 | 0.522 | 198.86 |
| 4 | 0.793 | 219.27 | 10.651 | 642.84 | 0.665 | 211.31 |
| 5 | 0.262 | 127.88 | 9.578 | 907.10 | 0.647 | 255.20 |
| 6 | 0.305 | 160.41 | - | - | - | - |
| Ave. | 0.554 | 171.77 | 9.189 | 710.92 | 0.787 | 243.83 |

By considering the size of the fiber cross section, Figures 3.30a to 3.30c show the stress and strain curves of the AR glass fiber, PVA fiber, and basalt fiber, respectively. From the figures, it can be observed that different from the capable load capacity, the salt fiber yielded the highest tensile strength, while the PVA fiber showed the highest elongation rate. Table

3.15 summarizes the tensile strength and the maximum elongation rate for the fibers. The AR glass fiber showed an average tensile strength of 1134.2 MPa, which is lower than the provided strength (2,000 MPa). This might be due to the large variation among the test glass fibers since three of the fibers yielded tensile strength close to 2,000 MPa. A maximum elongation rate of 28.63 was obtained from the glass fibers. The PVA fiber yielded an average tensile strength of 2,248.6 MPa, which is 87.4% higher than the manufacturer's reported strength (1,200 MPa). Compared with the glass fibers, the PVA fiber showed 3.1 times higher strain capacity at failure. The basalt fiber yielded an average tensile strength of 2,935 MPa, which is even higher than the micro-steel fiber (2,850 MPa). However, due to the high modulus of elasticity and the brittle behavior, an average elongation rate of 40.64, which is comparable to the glass fiber but lower than PVA fiber, was obtained from the basalt fiber. The different microstructure, tensile strength, elastic modulus, and elongation rate determine the roles of these micro-fibers in the matrix of UHPC, and this will be elucidated in the following tasks.

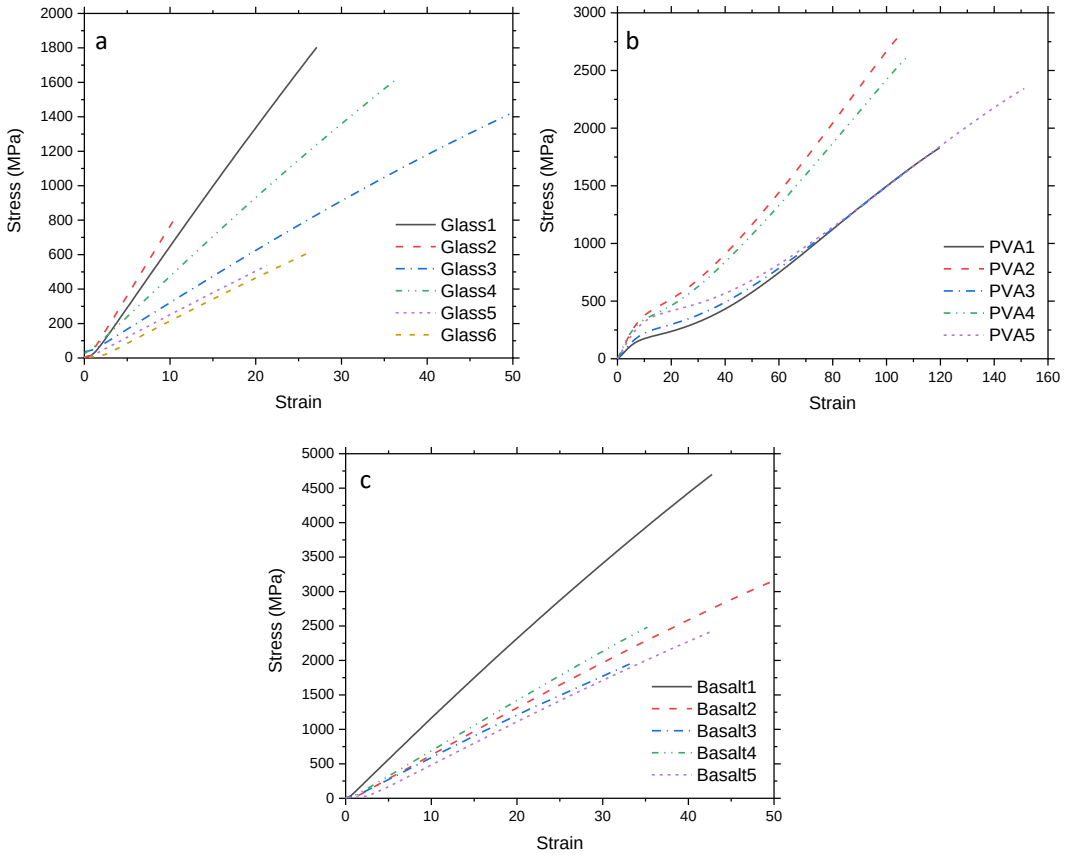


(a) AR glass fibers, (b) PVA fibers, and (c) basalt fibers

**Figure 3.30: Stress-strain curves of single-fiber tension tests.**

**Table 3.15: Tensile strength and the maximum elongation rate (strain) of the fibers under tension**

| Sample | AR glass fiber Tensile strength (MPa) | AR glass fiber Elongation rate | PVA fiber Tensile strength (MPa) | PVA fiber Elongation rate | Basalt fiber Tensile strength (MPa) | Basalt fiber Elongation rate |
|---|---|---|---|---|---|---|
| 1 | 1803.7 | 27.12 | 1829.4 | 119.77 | 4698.5 | 42.76 |
| 2 | 802.9 | 10.47 | 2802.0 | 104.73 | 3134.0 | 49.54 |
| 3 | 1414.6 | 49.58 | 1661.7 | 109.60 | 1947.6 | 33.14 |
| 4 | 1623.5 | 36.55 | 2606.2 | 107.14 | 2482.4 | 35.22 |
| 5 | 536.6 | 21.31 | 2343.6 | 151.18 | 2412.7 | 42.53 |
| 6 | 624.0 | 26.74 | - | - | - | - |
| Ave. | 1134.2 | 28.63 | 2248.6 | 118.49 | 2935.0 | 40.64 |

This page left blank intentionally.

# 4.0 Mixture Design of FRC and UHPC

## 4.1 Mixture Design of FRC

### 4.1.1. Materials

All the materials for the concrete mix were sourced from Construction Service, a ready-mix plant located in Wilbraham, MA, approved by MassDOT. It should be noted that the nominal maximum aggregate size for the coarse aggregate is 0.75 inches, type I/II cement, and Class F fly ash were used.

The fibers were sourced from Fibermesh. Two polypropylene fibers were chosen shown in Figure 4.1 below: Fibermesh-650 (1.50-inch) which is a straight fiber and Enduro Prime (2.5-inch) which is corrugated. Two steel fibers shown in Figure 4.2 below were also investigated: Novocon HE-4550 (2-inch), which is a hooked-end fiber, and Novocon XR (1.6-inch), which is a continuously deformed fiber. A 1% fiber volume ratio was used for all trial mixes which resulted in 15.3 lbs./cu.yd. of the polypropylene fibers and 132.3 lbs./cu.yd. of the steel fibers.

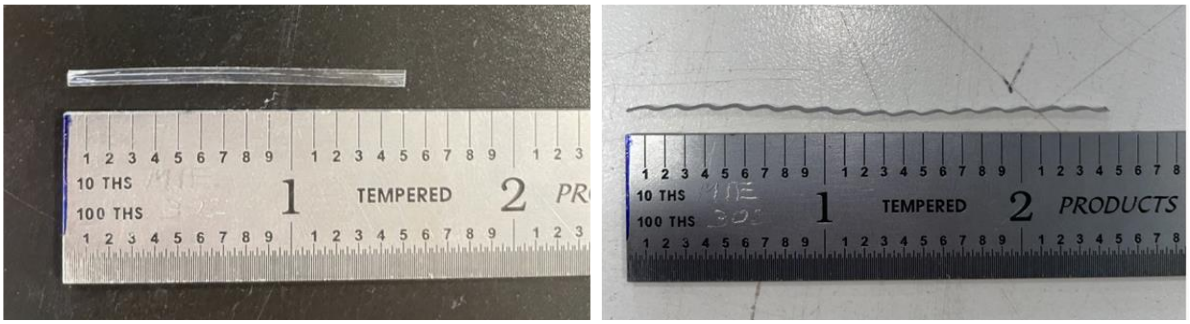


**Figure 4.1: Polypropylene fibers: Fibermesh-650 (Left), Enduro Prime (Right)**

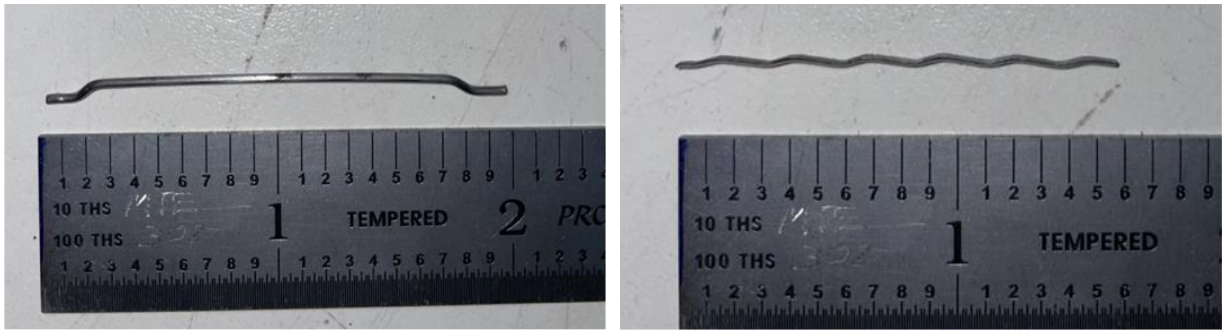


**Figure 4.2: Steel fibers: Novocon HE-4550 (Left), Novocon XR (Right)**

### 4.1.2. Mix Design

Two mix designs from MassDOT were identified to be possible candidates to use for FRC, one with fly ash and the other with slag. A mix design based on the Portland Cement Association (PCA) method for 4,000 psi concrete was also calculated to compare to the MassDOT mix. In Table 4.1 the mix designs with the amount in pounds per cubic yard are shown. The mix design that was calculated using the PCA method was close to the MassDOT mixes thus it was decided to proceed using the already approved MassDOT mix designs with both the fly ash and slag mixes being tested. Table 4.2 outlines the admixtures in ounces per cubic yard for both MassDOT mixes. The MassDOT mix identification numbers are 21-07-26-07-40-26-01 for the mix with fly ash and 21-07-26-07-40-26-02 for the mix with slag.

**Table 4.1: Mix design comparison**

| Material | MassDOT Mix-Fly ash (lbs./cu. yd.) | MassDOT Mix-Slag (lbs./cu. yd.) | PCA Method Mix (lbs./cu. yd.) |
|---|---|---|---|
| Coarse Aggregate | 1750 | 1750 | 1620 |
| Fine Aggregate | 1235 | 1250 | 1324 |
| Cement | 472 | 315 | 467.25 |
| Fly Ash | 158 | - | 155.75 |
| Slag | - | 315 | - |
| Water | 275.6 | 275.6 | 280 |

**Table 4.2: Admixtures**

| Material | MassDOT Mix-Fly ash (oz/cu. yd.) | MassDOT Mix-Slag (oz/cu. yd.) |
|---|---|---|
| Air Entraining | 2.5 | 2.0 |
| Water Reducing | 22.1 | 22.1 |
| Workability Retaining | 12.6 | 12.6 |

### 4.1.3. Trial Mixes

To determine if the MassDOT mixes would work with the introduction of the fibers, several trial mixes were performed. Four trail mixes were completed and results from slump tests and compression tests were compared which enabled the finalization of the mix design.

When completing the trial mixes, it is important to note that although there are a wide range of benefits from the use of fibers in concrete, any type of fiber added will reduce the workability of the concrete. Due to the relatively high surface area of the fibers, they will increase the water demand and can affect concrete mixing, placing, and compacting. In addition to their impact on water demand, they can also affect workability due to the challenges in the dispersion of the fibers. Consequently, an FRC that cannot be placed and compacted easily will affect constructability and will not lead to the required strength or durability characteristics of the material (Guerini et al., 2018). Therefore, the primary goal of these trial mixes is to ensure that fibers are well distributed, and the concrete is workable.

Results from the compression tests can be found in Table 4.5 following the description of each of the trial mixes.

### 4.1.3.A Trial Mix 1

The first trial mix was conducted on August 17, 2022. The MassDOT mix design with fly ash was used with 1% volume of Fibermesh-650 fibers, 15.34 lbs./cu. yd. The amount of materials used for trial mix 1 can be found in Table 4.3. The following method was followed to mix 0.5 cubic feet of concrete.

1. Weigh all materials in buckets.
2. Add the coarse aggregate and a third of the water to the mixer.
3. Start the mixer.
4. Add the fine aggregate, cement, fly ash, and remaining water while the mixer is running.
5. Add the admixtures.
6. Run the mixer for 3 minutes.
7. Stop the mixer for 2 minutes.
8. Run the mixer for 2 minutes.
9. Add the fibers while the mixer is running at a constant rate and mix for 5 minutes.

**Table 4.3: Trial mixture 1 proportion (0.5 cu. Ft.)**

| Material | Amount |
|---|---|
| Coarse Aggregate | 32.41 lbs. |
| Fine Aggregate | 22.87 lbs. |
| Cement | 8.74 lbs. |
| Fly Ash | 2.93 lbs. |
| Water | 5.10 lbs. |
| Air Entraining | 0.05 oz |
| Water Reducing | 0.41 oz |
| Workability Retaining | 0.23 oz |
| Fibermesh 650 | 0.284 lbs. |

During the mix, it was found that the resulting concrete mix was dry, segregated, and the fibers ended up clumping together (see Figure 4.3). It was likely dry due to the aggerates not being at SSD conditions as well as the timing of the addition of the fibers which did not allow them to become dispersed. A slump test was performed however there was negligible slump (see Figure 4.3). The mix was then put back in the mixer and 250 mL of water or approximately 0.5 pounds of water was added to the mix. Six 4” x 8” cylinders were cast to test compressive strengths at both 7 days and 28 days.

**Figure 4.3: Trial Mix 1 of FRC**

4.1.3.B Trial Mix 2

Following the first trial mix, several changes to the mix design were implemented. An additional amount of water, 44.8 lbs./cu. yd., was added to counteract the dry condition of the aggregates, assuming a 1.5% absorption capacity of the aggregates. The rest of the amounts of materials stayed the same. Additionally, the order in which the fibers were added was changed to try and get a better distribution of fibers. The fibers are now added directly after mixing the coarse and fine aggregates and then mixed for 5 minutes. Another change made was adding the air entrainer and workability retainer with the initial water that was added. Only the water-reducing admixture was added with the rest of the water during the second addition of the water. A new mixing procedure is detailed below.

1. Add the coarse aggregate, fine aggregate, and a third of the water which includes the air entrainer and workability retainer admixtures to the mixer.
2. Start the mixer and mix for 5 minutes, or until fibers are well dispersed.
3. Add the cement, fly ash, and remaining water which includes the water reducer while the mixer is running.
4. Run the mixer for 3 minutes.
5. Stop the mixer for 2 minutes.
6. Run the mixer for roughly 2 minutes, although it may take slightly longer to achieve a homogeneous mixture.

Another batch of 0.5 cubic feet of the MassDOT mix with fly ash with 1% volume of Fibermesh-650 fibers was mixed following the new procedure. The result of the changes resulted in a mix that was more workable and with the fibers better integrated. A slump test was also performed, and a slump of 1.5 in. was recorded (see Figure 4.4). Another six 4”x 8” cylinders for compression tests were cast.

**Figure 4.4: Trial Mix 2 of FRC**

4.1.3.C Trial mix 3

The third trial batch was used to determine if the type of fiber affected the mix at all. Thus, the MassDOT mix with fly ash was used again but with 1% volume of the steel Novocon HE-4550 fibers instead of the polypropylene Fibermesh-650 fibers. The mixing method was the same as trial mix 2. As shown in Figure 4.5, the mix was wetter and more workable, and a slump of 2.5 in. was found. Due to the longer fibers, two larger cylinders, 6” x 12”, were cast. One 4”x 8” cylinder was cast and there were no noticeable problems with the fibers in this smaller cylinder.

**Figure 4.5: Trial Mix 3 of FRC**

4.1.3.D Trial mix 4

The fourth and final 'trial mix followed the same procedure as mix 2 and mix 3, however this time the MassDOT mix with slag was tested with a 1% volume of Fibermesh-650 fibers. The aggregates at this point were like the first two trial mixes and the outcome of this mix was similar to mix 2. Additionally, three 4" x 8" cylinders were cast. After this mix was tested and deemed viable, larger-scale mixes were done to replicate these results at larger volumes.

4.1.3.E Large-scale batching

Larger scale batches of 2 cubic feet were performed to determine the compressive and tensile strengths of four different mixes developed. The four mixes are summarized in Table 4.4.

It should be noted the change in the amount of water and water-reducing admixture from the trial mixes. An initial batch of Mix 1 using the proportions from the trial batch along with the same addition of 44.8 lb./yd$^3$ of water to account for absorption by the aggregates. This mixture was segregated, and fibers were not dispersed evenly, likely due to scaling up the mix exaggerating the effects fibers have on workability. To counteract this an additional 7.9 lb./yd$^3$ of water was added, which assuming 1.5% absorption by the aggregates resulted in an increase of the water-to-cement ratio from 0.44 to 0.45. Only this additional water is included in the summary of FRC mixture proportions as the other water was added purely to counteract the dry conditions of the aggregates. Alongside the additional water, 1/3 more water-reducing (superplasticizer) admixture was used to ensure that the resulting mixes would be more homogeneous and flowable. The mixing procedure was the same as the updated procedure from trial mix 2. The batches were mixed in a larger capacity drum mixer.

**Table 4.4: FRC mixture proportions**

| Materials and contents | Mix 1 | Mix 2 | Mix 3 | Mix 4 |
|---|---|---|---|---|
| Coarse Aggregate (lb./yd$^3$) | 1750 | 1750 | 1750 | 1750 |
| Fine Aggregate (lb./yd$^3$) | 1235 | 1235 | 1235 | 1235 |
| Cement, Type I/II (lb./yd$^3$) | 472 | 472 | 472 | 472 |
| Class F Fly Ash (lb./yd$^3$) | 158 | 158 | 158 | 158 |
| Water (lb./yd$^3$) | 283.4 | 283.4 | 283.4 | 283.4 |
| Fibermesh-650 fiber (lb./yd$^3$) | 15.34 | - | - | - |
| Enduro Prime fiber (lb./yd$^3$) | - | 15.34 | - | - |
| Novocon HE-4550 fiber (lb./yd$^3$) | - | - | 132.35 | - |
| Novocon XR fiber (lb./yd$^3$) | - | - | - | 132.35 |
| Air entraining agent (oz/ yd$^3$) | 2.5 | 2.5 | 2.5 | 2.5 |
| Water reducing agent (oz/ yd$^3$) | 29.5 | 29.5 | 29.5 | 29.5 |
| Workability retaining agent (oz/ yd$^3$) | 12.6 | 12.6 | 12.6 | 12.6 |

### 4.1.4 Results and discussion

A summary of the results from the compression tests, which were run in accordance with ASTM C39, of the cylinders for each of the trial mixes at 7 days and 28 days can be found in Table 4.5. below. All mixes exceeded the design strength of 4,000 psi, except for trial mix 3. This could be because the mix was wetter than the others or due to the difference between the steel and polypropylene fibers but can explored further during the large-scale batches detailed in the next sections. It was determined that either MassDOT mix works well with the

incorporation of polypropylene or steel fibers. However, it is important to note that the fibers should be added directly after mixing the aggregates and letting it mix for 5 minutes to avoid clumping of the fibers and have a good distribution of fibers within the concrete.

**Table 4.5: Trial mix compression strength**

| Trial Mix | 7-day compressive strength (psi) | 28-day compressive strength (psi) |
|---|---|---|
| 1 | 3,636 | 4,407 |
| 2 | 2,782 | 4,220 |
| 3 | 2,975 | 3,750 |
| 4 | 2,965 | 4,263 |

## 4.2 Mixture Design of UHPC

### 4.2.1. Materials

In this project, to obtain a comprehensive understanding of UHPC design with different formulations, two types of cement and five types of supplementary cementitious materials (SCMs) were investigated. Type III Portland cement with a specific gravity of 3.15 and a Blaine fineness of 493 $m^2$/kg supplied by Lehigh Cement Company LLC was used to study the influence of high early strength cement on the properties of UHPC. Type I/II ordinary Portland cement produced by Quikrete, which is widely available on the market, was also used. The SCMs used in this project to modify the matrix of cement binder include silica fume, Class C fly ash, Class F fly ash, micro-fly ash (a finer Class F fly ash), and metakaolin (MK). Undensified silica fume with a $SiO_2$ content of 95.7% and a specific gravity of 2.24 was obtained from Norchem. Class F fly ash, Class C fly ash, and micro-fly ash (Micron ultra fine fly ash) with a median particle size of 2 to 4 microns and a specific gravity of 2.69 were supplied by Eco Material Technologies. The chemical and mineral compositions of Type I/II cement, Type III cement, silica fume, Class F fly ash, Class C fly ash, micro fly ash, and MK are summarized in Table 4.6. Compared with Type I/II cement, Type III cement contains a higher content of mineral phases that can contribute to the early-age strength gain, i.e. $C_3S$ and $C_3A$.

Masonry sand was used as aggregate for the UHPC. The particle size distributions (PSDs) of the two types of cement and the SCMs measured by laser diffraction and that of masonry sand based on sieving analysis are shown in Figure 4.6. Type I/II cement exhibits a specific surface area, Sauter mean diameter, and De Brouckere mean diameter of 1.66 m2/g, 3.61 μm, and 23.93 μm, respectively. Both Type III cement and silica fume are finer than Type I cement, but silica fume shows a higher fraction of particles with a diameter smaller than 3 μm. The median particle size (d50) of silica fume is 3.82 μm, while MK has a mean particle size of 3.79 μm and a specific surface area of 2.99 $m^2$/g, which is 1.8 times that of Type I cement. The ultra-fine fly ash exhibits a relatively narrow PSD ranging between 0.8 μm and 8 μm a median particle size (d50) of 2.81 μm, which is the finest among all the cementitious materials studied in this project. Brass-coated steel microfibers with a diameter of 0.008 in. (0.2 mm), a length of 0.51 in. (13 mm), and an average tensile strength of 421 ksi (2900 MPa) were used as fiber reinforcement in UHPC. PVA, basalt, and glass microfiber with the

same length were also used to study the influence of fiber types on the properties of UHPC. An Optimum 380 high-range water-reducing (HRWR) admixture was used to improve the workability of the concrete mix.

**Table 4.6: Chemical composition of the cementitious materials for UHPC**

| Oxides | Type I/II cement | Type III cement | Silica fume | Class F fly ash | Class C fly ash | Micro fly ash | Metakaolin |
|---|---|---|---|---|---|---|---|
| $SiO_2$ (%) | 20.1 | 19.01 | 95.67 | 48.23 | 39.00 | 50.29 | 51.8 |
| $Al_2O_3$ (%) | 4.8 | 5.46 | - | 20.37 | 20.34 | 16.27 | 42.2 |
| $Fe_2O_3$ (%) | 3.2 | 2.19 | - | 19.41 | 6.26 | 5.23 | 4.15 |
| CaO (%) | 62.7 | 61.97 | - | 4.14 | 21.83 | 11.11 | 0.071 |
| MgO (%) | 3.4 | 2.51 | - | 0.91 | 4.59 | 3.72 | - |
| $SO_3$ (%) | 3.5 | 4.63 | 0.27 | 1.43 | 1.61 | 1.66 | 0.11 |
| $C_3S$ (%) | 54 | 54.74 | - | - | - | - | - |
| $C_2S$ (%) | 17 | 13.22 | - | - | - | - | - |
| $C_3A$ (%) | 7 | 10.77 | - | - | - | - | - |
| $C_4AF$ (%) | 10 | 6.66 | - | - | - | - | - |
| $C_3S + 4.75C_3A$ (%) | 87.25 | 98 | - | - | - | - | - |
| Equivalent Alkalis (%) | 0.6 | 1 | 0.31 | 7.15 | - | - | - |

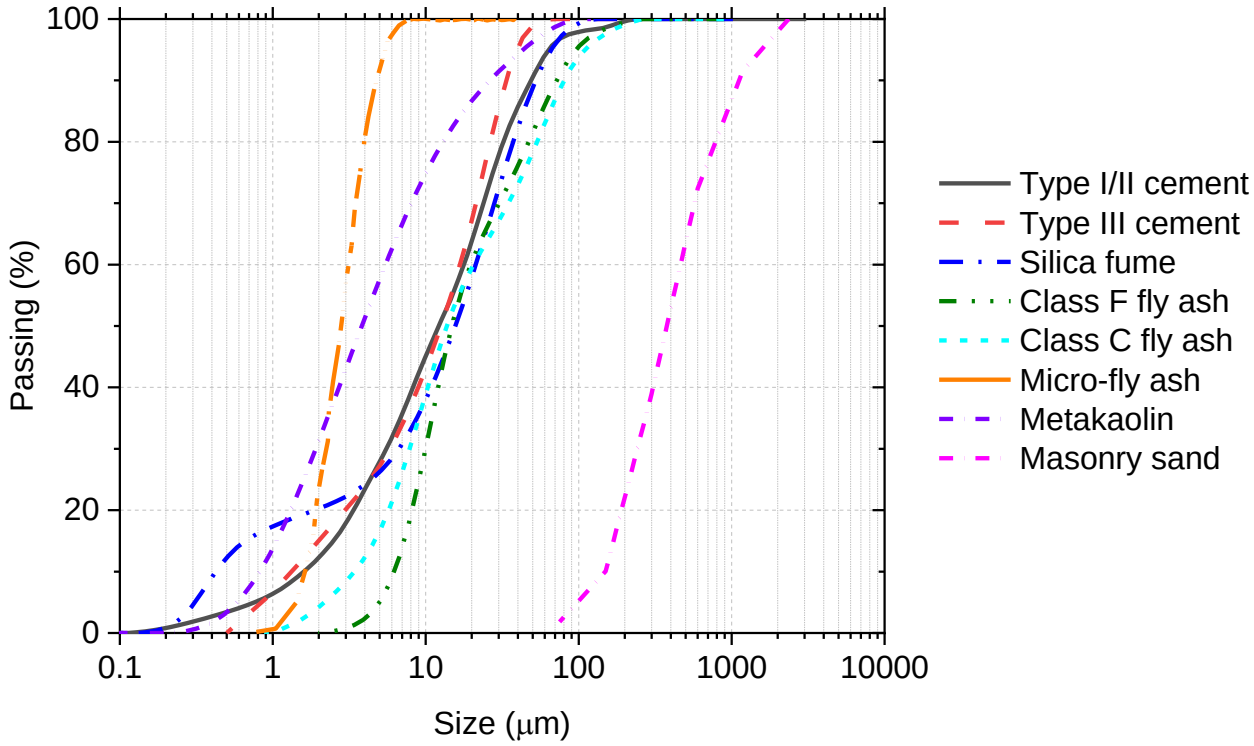


**Figure 4.6: Particle size distribution of the cementitious materials for UHPC**

### 4.2.2. Particle packing density optimization

Upon the availability or selection of raw materials, it is also important to determine their amounts and proportions to ensure adequate packing of fine and coarse particles in the concrete system to achieve a dense microstructure, which plays a critical role in determining the mechanical and durability properties of concrete. The packing density of particles can be characterized and optimized through a variety of particle packing models, which consider the size and quantity of individual particulate components within a system and indicate the distribution of their combinations for the entire mixture. In this project, the maximization of particle packing density is utilized as the primary design principle of UHPC. The Modified Andersen-Andreassen Model [21] (see Eq. (1)) was employed, via EMMA software from ELKEM Silicon Product, which uses interpolation to get unified PSDs for respective sieve sizes. This model uses a modified Andersen-Andreassen Model equation (Eq. 4.1), where P(D) is the fraction of total solids smaller than diameter D [22, 23] and q is the distribution modulus, which varies between 0.22 and 0.25 [24, 25]. $D_{max}$ and $D_{min}$ are the maximum and minimum sizes of the solid particles of the materials considered in the UHPC design, respectively. By employing a proper q value, an ideal distribution curve can be generated in EMMA (the red curve in Figure 4.7), which was treated as the target to maximize the particle packing density of the system. After importing the raw PSDs or gradations for the raw materials, such as cement, silica fume, fly ash, and masonry sand, into EMMA, adjustments of contents of the materials were made until a Composed Mix (CPFT) curve of the mix (the blue curve in Figure 2) matches the ideal packing curve. This composed mix was further refined in a toolbox developed in a spreadsheet based on the Least Square Method to minimize the deviation between the Composed Mix curve and the Model Curve, i.e., the summation of squares of the residuals (RSS) (see Eq. 4.2). To achieve this target, a generalized reduced gradient nonlinear solving method (solver) was utilized in the toolbox.

$$P(D) = \frac{D^q - D_{min}^q}{D_{max}^q - D_{min}^q} \tag{4.1}$$

$$RSS = \sum_{i=0}^{n} (P_{mix}\left(D_i^{i+1}\right) - (P_{tar}\left(D_i^{i+1}\right))^2 \tag{4.2}$$

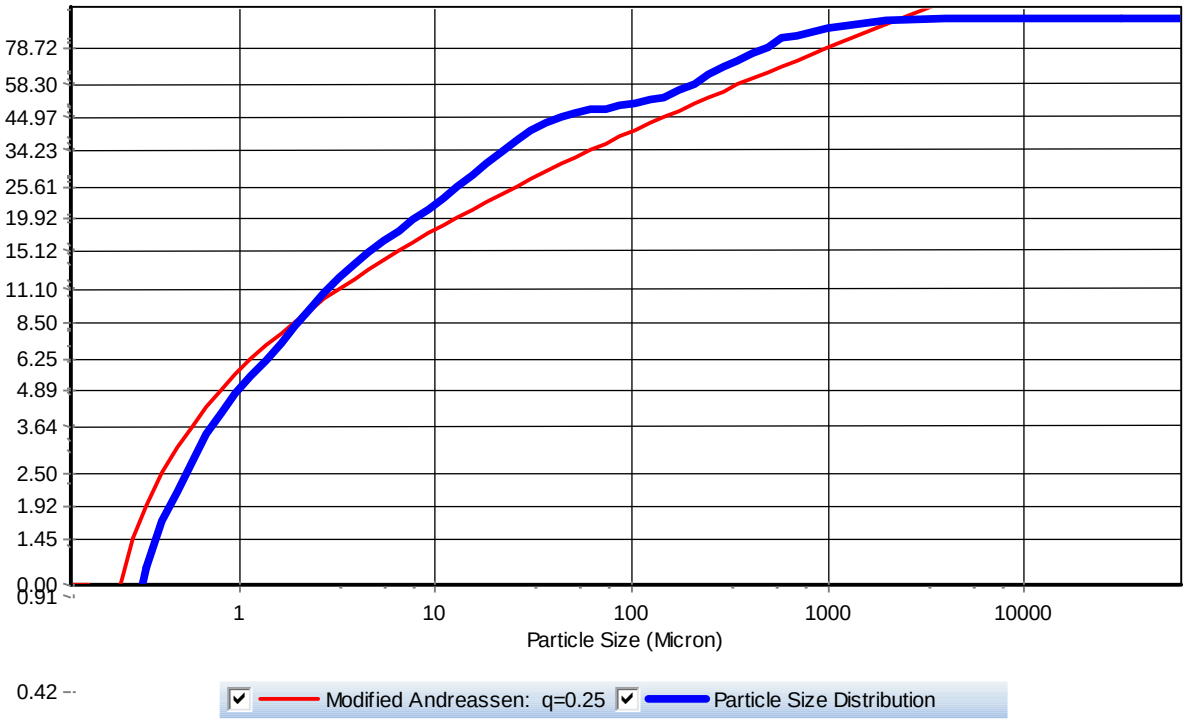


**Figure 4.7: Particle size distribution of UHPC according to EMMA**

### 4.2.3. Optimum content ranges of constituents in UHPC

It should be noted that, if only relying on the Modified Andersen-Andreassen model and the least square method, the proportions of UHPC will not be reasonable and practical. For example, when considering Type I/II cement, silica fume, micro-fly ash, Class C fly ash, and masonry sand for UHPC, the maximized particle packing density yields a cement content of 0. By taking the PSDs of the raw materials into account and guaranteeing reasonable proportions of UHPC, the content of each raw material has to be refined based on a comprehensive literature review. The target of this literature review is to identify the optimum content ranges of the entire binder and that of cement and SCMs, which can result in the highest mechanical strength of UHPC. Figure 4.8 shows the influence of the binder content (binder means cement + SCMs) on the strength of UHPC. It can be seen that a binder content between 45% and 62% is beneficial to improve the strength of UHPC. Figure 4.9 to Figure 4.12 show the correlations between UHPC strength and the contents of cement, silica fume, fly ash, and metakaolin. Based on the 28-day strength of UHPC, the optimum contents of cement, silica fume, fly ash, and metakaolin in the binder (paste) are 60% to 67%, 15% to 30%, 3.5% to 15%, and 10% to 20%, respectively, of the binder. These optimum contents will be used as constraints, along with the Modified Anderson and Anderson model and the least square method to maximize the particle packing density of the system for the studied materials within their reasonable ranges to ensure high strength.

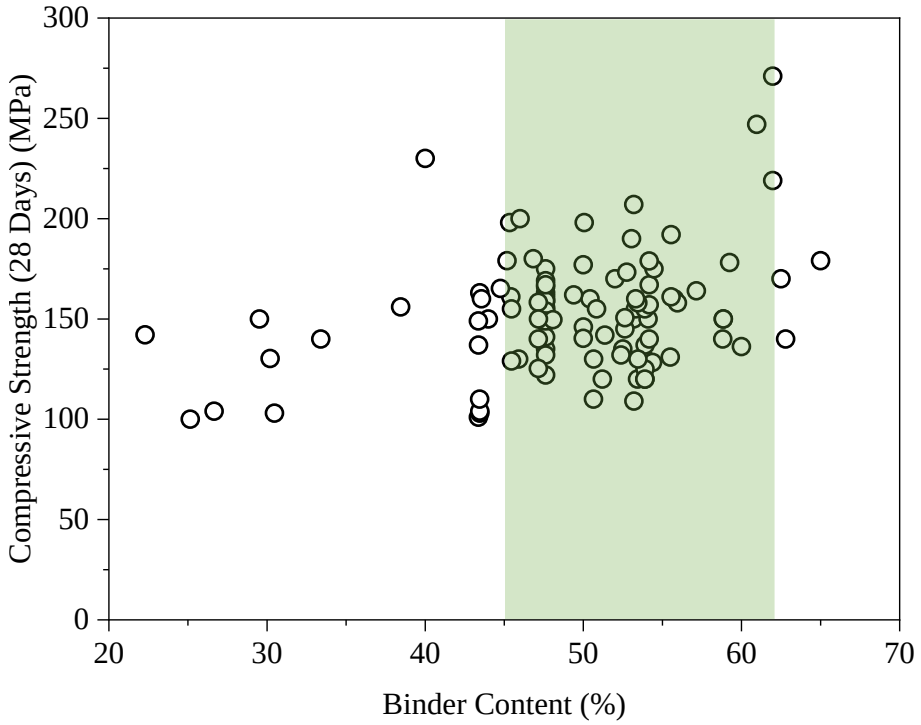


**Figure 4.8: Influence of binder content on 28-day strength of UHPC [73, 76, 92, 104, 124-183]**

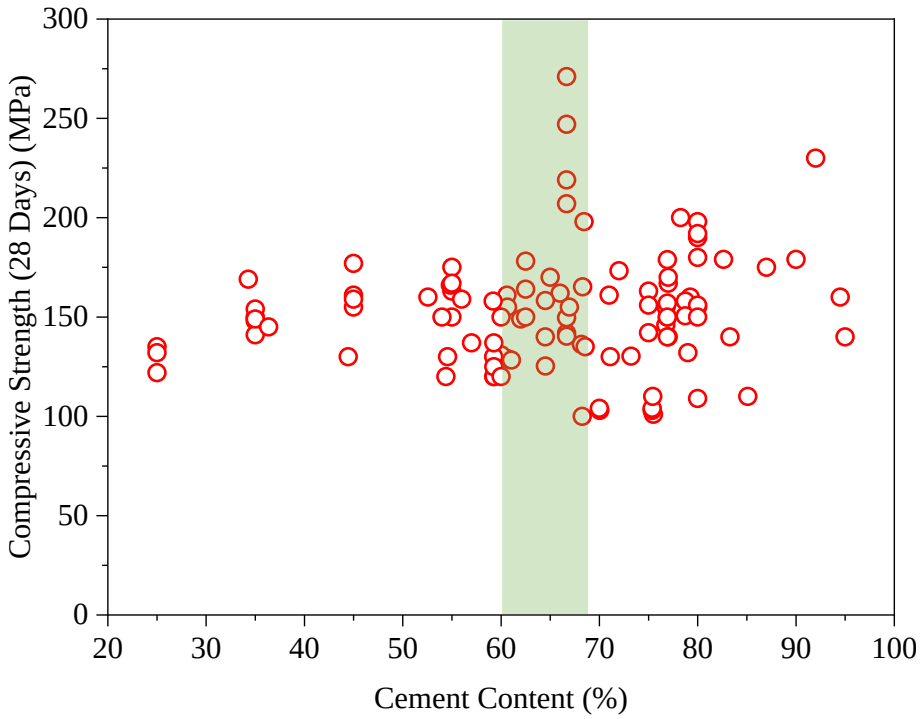


**Figure 4.9: Influence of cement content on 28-day strength of UHPC [73, 76, 92, 104, 124-183]**

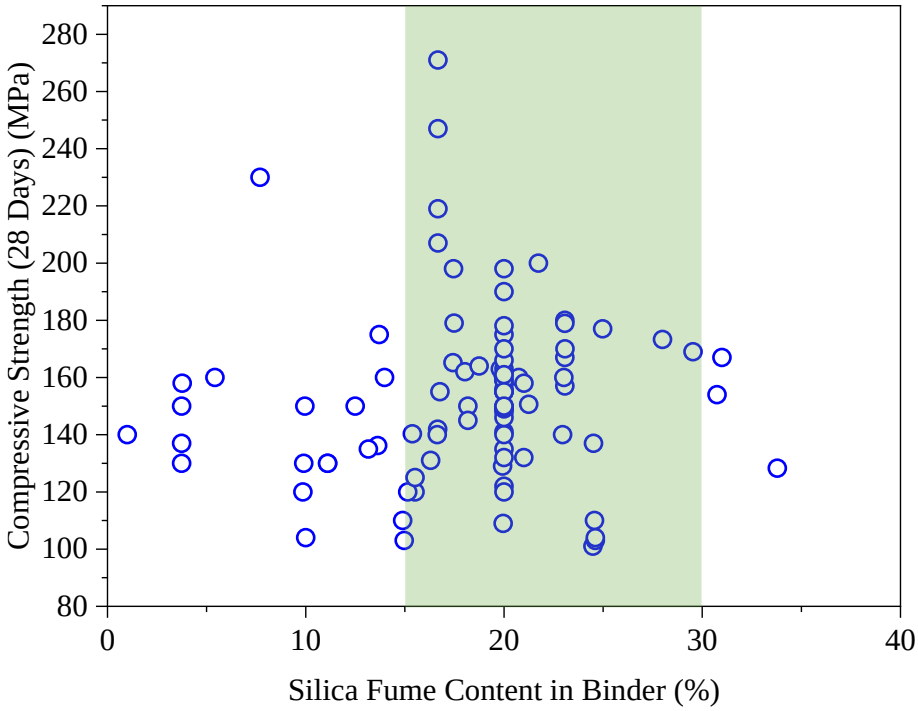


**Figure 4.10: Influence of silica fume content on 28-day strength of UHPC [73, 76, 92, 104, 124-183]**

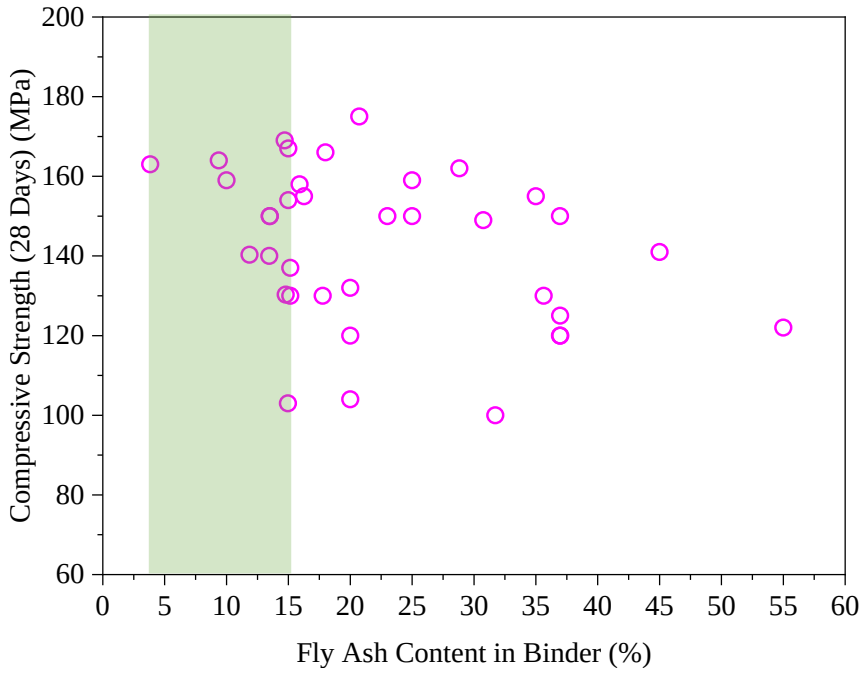


**Figure 4.11: Influence of fly ash content on 28-day strength of UHPC [73, 76, 92, 104, 124-183]**

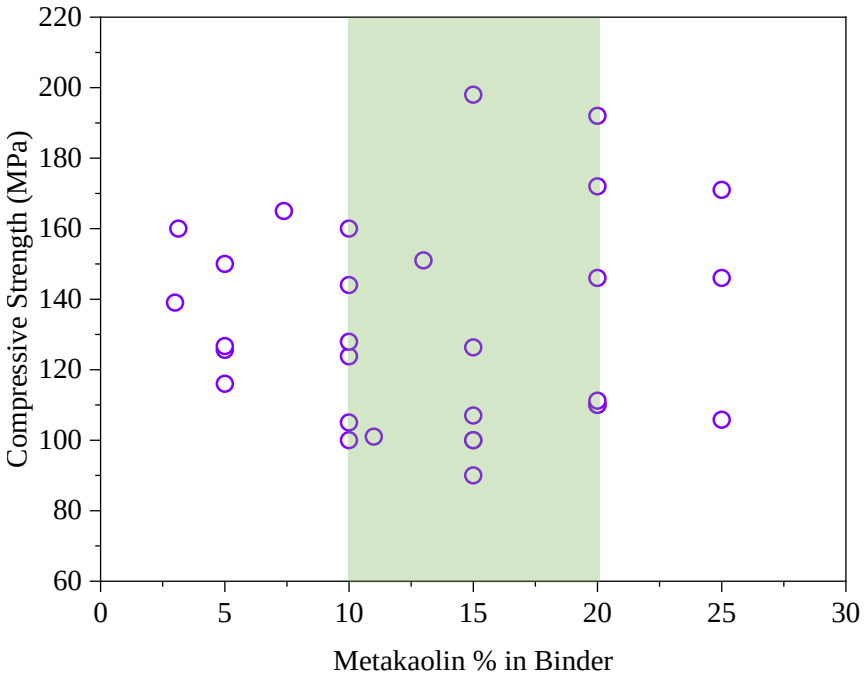


**Figure 4.12: Influence of metakaolin content on 28-day strength of UHPC [73, 76, 92, 104, 124-183].**

### 4.2.4. Two-step optimization of particle packing density

As discussed above, the optimization of particle packing density cannot only rely on the Modified Andersen-Andreassen model and the least square method. To obtain reasonable proportions of UHPC, the roles of different constituents like cement and SCMs must be taken into account. Based on the identified optimum content ranges of the materials in Section 3.1.3, a novel two-step particle-packing density optimization method was developed in this project. The procedures of this new method include:

(1) Based on the Modified Andersen-Andreassen model, PSDs of the studied materials were used to create the Composed Mix curve and the Model Curve (see Figure 4.13), which is similar to the curves obtained from EMMA as shown in Figure 4.7. By employing the optimum binder content (i.e., 45% to 62%) and the optimum contents of each SCM (e.g., 60% to 67% for cement, 15% to 30% for silica fume, and 3.5 to 15% for fly ash) in the binder, the contents of SCMs were calculated. To cover all the proportions for the maximization of particle packing density, the wider ranges of cement and SCMs were selected as constraints in the least square method through a generalized reduced gradient nonlinear solving method (solver) (Table 4.7 shows the selected SCM constraints for one of the UHPC groups: Mix 3). The outcome of this step is the optimum content of the entire binder in UHPC based on the selected materials to reach minimized RSS with the target model curve (i.e., the maximized particle packing density). In most cases, a binder content of 45% was identified as the optimum, which means the content of aggregate is 55%.

(2) Based on the identified binder content, the content ranges of cement and SCMs in the binder should be further refined, which was used as the new constraints for the least square method fitting to minimize RSS (see Table 4.8). The outputs of this step are the final proportions of the UHPC (see Table 4.9), which not only ensure the proper contents of each constituent but also ensure the optimization of particle packing density based on the selected materials.

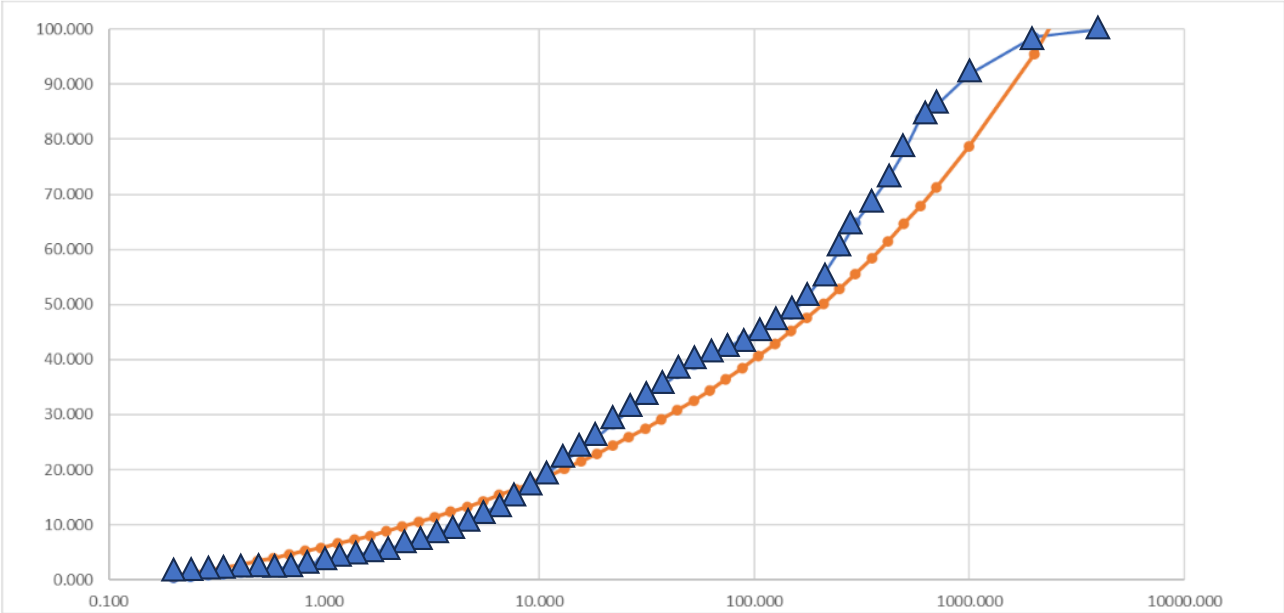


**Figure 4.13: Composed Mix curve and the Model Curve**

**Table 4.7: The content ranges of the studied cement and SCMs in UHPC based on the binder content range**

| Materials | Minimum constrains | Maximum constrains |
|---|---|---|
| Cement | 27 | 41.54 |
| Sand | 38 | 55 |
| Silica fume | 9 | 15.5 |
| Micro-fly ash | 0 | 0 |
| Metakaolin | 0 | 0 |
| Class C fly ash | 1.575 | 9.3 |

**Table 4.8: The refined content ranges of the studied cement and SCMs in UHPC based on the optimized binder content.**

| Materials | Minimum constrains | Maximum constrains |
|---|---|---|
| Cement | 27 | 41.54 |
| Sand | 38 | 55 |
| Silica fume | 9 | 15.5 |
| Micro-fly ash | 0 | 0 |
| Metakaolin | 0 | 0 |
| Class C fly ash | 1.575 | 9.3 |

**Table 4.9: Proportions of UHPC based on the two-step particle packing density optimization.**

| Materials | Density | q | New volume (%) | New mass quantity |
|---|---|---|---|---|
| Type I/II cement | 3.15 | 0.25 | 0.2621 | 30.15 |
| Sand | 2.65 | 0.25 | 0.5682 | 55.00 |
| Silica fume | 2.24 | 0.25 | 0.1122 | 9.00 |
| Micro-fly ash | 2.69 | 0.25 | 0 | 0.00 |
| Class C fly ash | 2.69 | 0.25 | 0.0596 | 5.85 |
| Metakaolin | 2.6 | 0.25 | 0 | 0.00 |
| Constrain for total volume | - | - | 1.00 | 100.0 |
| Total | - | - | 1.00 | 100.0 |

### 4.2.5. Mix Design of UHPC

The binder content and the contents of each SCM for different materials selections were determined based on the developed two-step particle packing density optimization. In this project, 7 groups of UHPC based on different combinations of cement and SCMs were studied. As shown in Table 4.10, the cementitious binder of Group 1 consists of Type III cement, silica fume, Class F fly ash, and micro fly ash. The difference between Group 2 and Group 1 is the replacement of Type III cement with Type I/II cement as well as the replacement of Class F fly ash with Class C fly ash. The difference between Group 3 and Group 2 is the absence of micro-fly ash. Group 4 and Group 3 are the same except for the type of fly ash. Class F fly ash was used in Group 4. In line with the comparison between Group 3 and Group 2, the difference between Group 5 and Group 4 is the absence of the micro-fly ash in Group 5. In Group 6 and Group 7, metakaolin is used to partially replace silica fume. The difference between the two metakaolin groups is the type of fly ash, where Group 6 used Class C fly ash and Group 7 used Class F fly ash. Based on these formulations, the influence of cement type, fly ash type, micro-fly ash, and metakaolin on the properties of UHPC at their optimization of particle packing densities will be investigated. Masonry sand

was used in all the groups as fine aggregates. The materials used in the seven groups are all commonly used cement and SCMs in regular concrete.

Table 4.11 summarizes the proportions of the seven groups of UHPC studied in this project. A water-to-binder ratio of 0.19 and a fiber volume fraction of 2% were used for the UHPC mixtures. An HRWR amount of 58-70 lbs./yd$^3$ was used to obtain a slum ranging between 8 and 10 inches. Four different fibers including micro-steel fiber, micro-PVA fiber, micro-basalt fiber, and micro-glass fiber with a length of 12 – 13 mm were used. Their influences on the mechanical strength development of UHPC will be presented in Task 4.

**Table 4.10: Materials used for the UHPC design**

| Groups | Mix 1 | Mix 2 | Mix 3 | Mix 4 | Mix 5 | Mix 6 | Mix 7 |
|---|---|---|---|---|---|---|---|
| Type I/II cement | - | X | X | X | X | X | X |
| Type III cement | X | - | - | - | - | - | - |
| Silica fume | X | X | X | X | X | X | X |
| Class F fly ash | X | - | - | X | X | - | X |
| Class C fly ash | - | X | X | - | - | X | - |
| Micro-fly ash | X | X | - | X | - | - | - |
| Metakaolin | - | - | - | - | - | X | X |
| Masonry sand | X | X | X | X | X | X | X |

**Table 4.11: Mixture proportions of UHPC**

| Groups /Materials | Mix 1 (lbs./yd$^3$) | Mix 2 (lbs./yd$^3$) | Mix 3 (lbs./yd$^3$) | Mix 4 (lbs./yd$^3$) | Mix 5 (lbs./yd$^3$) | Mix 6 (lbs./yd$^3$) | Mix 7 (lbs./yd$^3$) |
|---|---|---|---|---|---|---|---|
| Type I/II cement | - | 1391.60 | 1391.60 | 1391.60 | 1391.60 | 1378.56 | 1413.58 |
| Type III cement | 1379.54 | - | - | - | - | - | - |
| Silica fume | 607.41 | 415.40 | 415.40 | 415.40 | 415.40 | 414.61 | - |
| Class F fly ash | - | - | - | 242.98 | 270.01 | - | 316.47 |
| Class C fly ash | - | 197.32 | 270.01 | - | - | 72.56 | - |
| Micron-fly ash | 72.07 | 72.70 | - | 27.03 | - | - | - |
| Metakaolin | - | - | - | - | - | 207.30 | 379.77 |
| Water | 391.21 | 394.63 | 394.63 | 394.63 | 394.63 | 393.88 | 400.87 |
| Masonry sand | 2516.57 | 2538.57 | 2538.57 | 2538.57 | 2538.57 | 2533.70 | 2578.67 |
| Superplasticizer | 58.58 | 66.21 | 66.21 | 66.21 | 66.21 | 70 | 70 |
| Micro-steel fiber | 262.95 | 262.95 | 262.95 | 262.95 | 262.95 | 262.95 | 262.95 |
| Micro-PVA fiber | - | - | - | - | 43.82 | - | - |
| Micro-basalt fiber | - | - | - | - | 88.66 | - | - |
| Micro-glass fiber | - | - | - | - | 91.02 | - | - |

### 4.2.6. Mixing Process

Different from regular concrete, the ultra-low w/b ratio makes the initial UHPC dry until the superplasticizer is uniformly dispersed and hence the mixing was done in a shear mortar mixer. The following mixing process was conducted to obtain a homogeneous consistency of fresh UHPC:

(i) Wetting the mixing bowl and paddle of the mixer.
(ii) Dry mixing of the measured solid cementitious materials and sand for at least 2 minutes.
(iii) Adding half of the water with half of the superplasticizer and mixing for another 2 minutes.
(iv) Scraping the bowl from the bottom to ensure even distribution of superplasticizer and water.
(v) Adding the remaining was and superplasticizer and mixing until a homogenous mixture without dry lumps was obtained.
(vi) Adding half of the measured fibers and mixing for 2 minutes.
(vii) Adding the remaining fibers and mixing until a uniform dispersion of the fibers was obtained. The mixing time may vary for different groups.

### 4.3.1. Experimental Methodology

#### 4.3.1.A Isothermal Colorimetry

Figures 4.14a and 4.14b show the I-Cal 2000 HPC high precision isothermal calorimeter, which was used to get a comprehensive understanding of cement hydration kinetics in the presence of different supplementary cementitious materials, such as silica fume, ultra-fine fly ash, type C fly-ash, type F fly-ash, and metakaolin. The cementitious binders of the 7 UHPC groups (without fiber and sand) with a total mass of 50 grams with their propositions as summarized in Table 4.11 were prepared. The dry material, water, and superplasticizer were mixed by hand. Within 2 minutes after mixing, the fresh binders were immediately cast in a plastic cup, covered with the lid, and placed in the calorimetry chamber. Both the heat flow and hydration heat release during the first 50 hours of hydration of each paste were measured at 25°C.

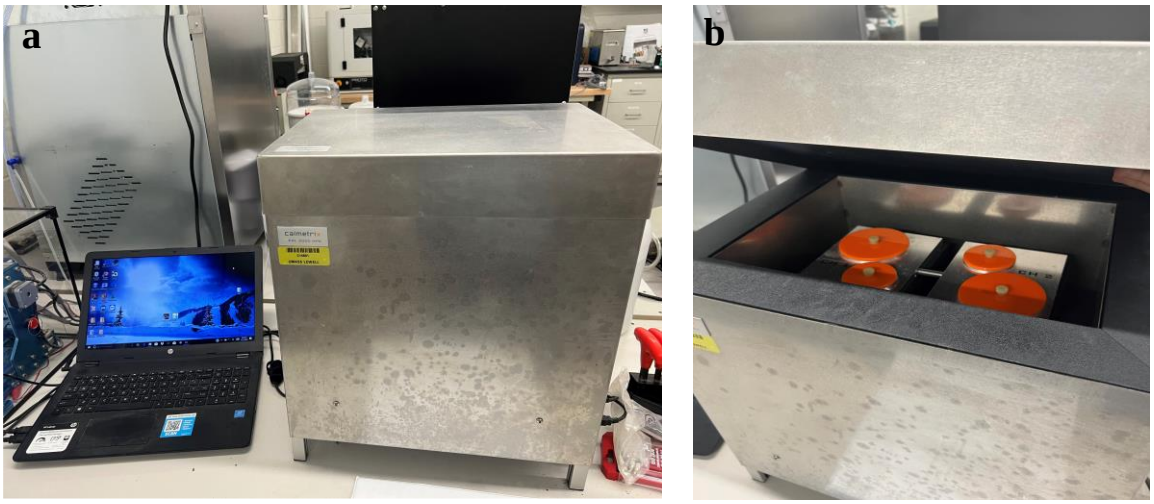


**Figure 4.14: Isothermal colorimetry testing setup.**

#### 4.3.1.B FTIR Spectroscopy

Thermo Fisher Scientific Nicolet iS10 FTIR spectrometer was used to get Fourier Transform Infrared Spectroscopy (FTIR) spectra for the hydrated cementitious binders. The spectra between 4000 and 4 cm-1 with a resolution of 4 $cm^{-1}$ were acquired on ground binder powders at the ages of 3 days, 7 days, 28 days, and 60 days. To prepare the powdered samples for FTIR, thermogravimetric analysis (TGA), and X-ray diffraction analysis (XRD), a cylindrical binder sample for each group was cast and sealed. At the desired testing ages, a disc was cut from the cylinder using a low-speed diamond saw and the core portion was ground into fine powders. To stop further hydration the fine powder is immediately immersed in alcohol for 24 hours.

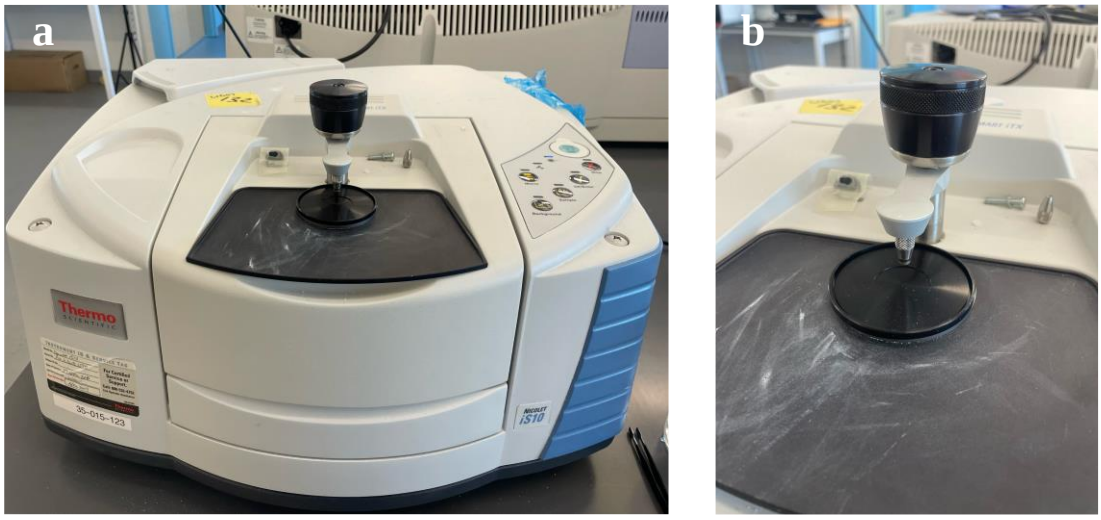


**Figure 4.15: FTIR Spectroscopy testing setup.**

4.3.1.C TGA

TGA was carried out on ground powders of the cement pastes after 3, 7, 28, and 60 days using a Perkin Elmer TGA 4000 thermogravimetric analyzer (Figure 4.16). A heating rate of 15°C/min from 30°C to 800°C under $N_2$ purge gas at a flow rate of 20 mL/min was applied. Contents of CH (portlandite) and $CaCO_3$ (CC) in the pastes, corresponding to the weight loss between 400°C to 510°C, and 590°C to 710°C based on the tangent method (the boundaries of portlandite and calcite slightly vary for each sample, i.e., the temperatures are not fixed), respectively, were determined by using:

$$CH_1 = [(W_{400} - W_{510})/W_{510}] \times M_{Ca(OH)_2}/M_{H_2O} \times 100\% \quad (4.3)$$

$$CC = [(W_{590} - W_{710})/W_{710}] \times M_{CaCO_3}/M_{CO_2} \times 100\% \quad (4.4)$$

where CH1 and CC are calcium hydroxide and calcium carbonate contents, Wn is the mass at temperature n °C, and M is the molar mass. Again, the temperatures for CH and CC thermal decomposition are determined based on a tangent method [184] rather than fixed values. CC is mainly due to the carbonation of CH during the process of sample preparation. Thus, in this study, the total CH content was calculated by summing the $CH_1$ in Eq. 4.3 and the $CH_2$ converted from CC as follows:

$$CH_2 = CC \times \frac{M_{CaCO_3}}{M_{Ca(OH)_2}} = CC \times 0.74 \quad (4.5)$$

where $CH_2$ is the portlandite converted to CC due to carbonation. Thus, the total CH content produced by the cement hydration is:

$$CH = CH_1 + CH_2 \quad (4.6)$$

The non-evaporable water content ($W_{ne}$) of the cement blends was calculated based on the

weight loss between around 115°C and around 510°C on TGA curves by using Eq. (4.7). Again, the temperature boundaries here are not fixed, which may slightly vary for each sample based on the tangent method.

$$W_{ne} = (W_{510} - W_{115})/W_{510} \times 100\% \quad (4.7)$$

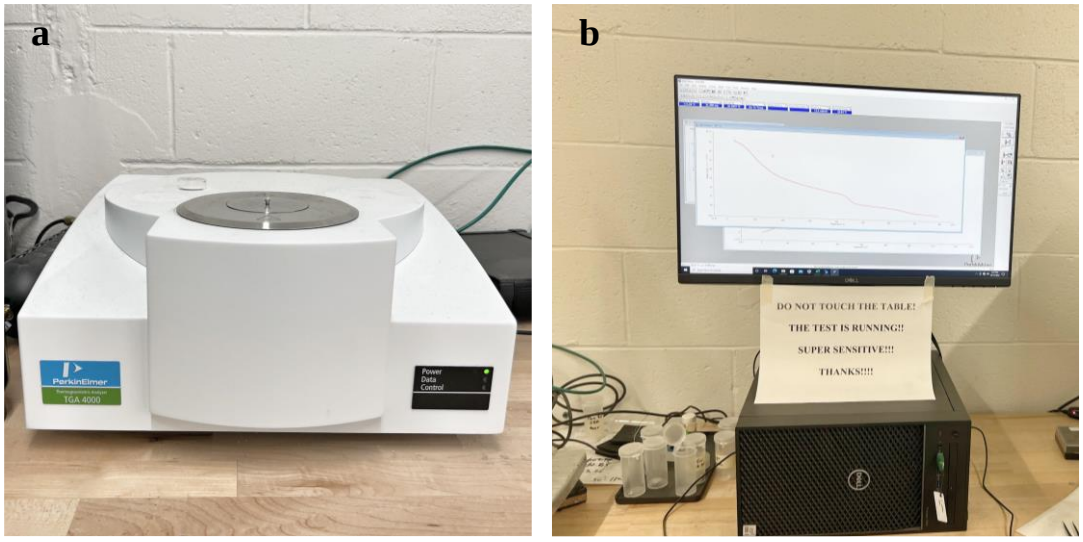


**Figure 4.16: TGA4000 testing setup.**

4.3.1.D X-Ray Diffraction

Figure 4.17 shows the X-ray diffractometer used in this study. The XRD test was conducted at 30kV and 20 mA to characterize the hydration products of the UHPC binders. Using rotary support, the samples were scanned in stepwise mode with a step size of 0.02 (2θ) with 5 s per step of scanning time in the range of 10 to 60 degrees.

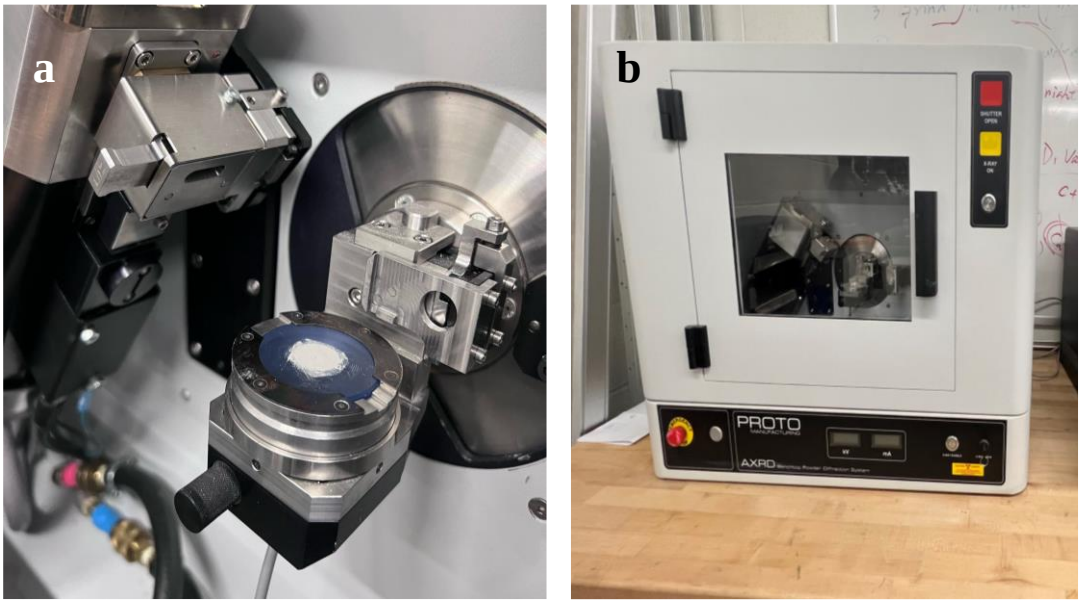


**Figure 4.17: X-ray diffractometer.**

### 4.3.2. Isothermal Calorimetry

The calorimetric measurements on neat type I/II cement normalized by the weight of cement are shown in Figures 4.18a and 4.18b. The classic five-stage heat flow curves can be identified. Due to the rapid hydration of $C_3A$ beginning immediately upon wetting [185], extreme exothermicity in the initial (pre-induction) stage was observed. Two peaks were observed from its heat flow curve at 7 and 8.5 hours during the acceleration and deceleration stages, indicating the reaction of silicate and secondary hydration of tricalcium aluminate. A subsequent broad shoulder corresponding to the conversion of ettringite to AFm was also observed between 20 and 30 hours in the stage of the slowly continued diffusion-controlled reaction. The cumulative heat released curve indicates that a total heat of 221 J can be released by each gram of cement after 50 hours (see Figure 4.18b).

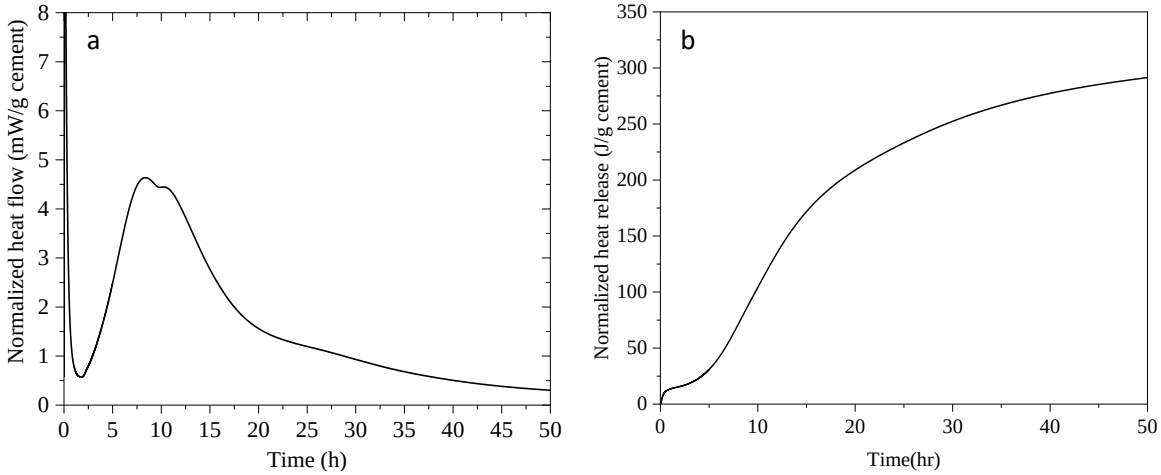


**Figure 4.18: Hydration heat of Type I/II cement.**

From Figure 4.19a, accelerated early-age cement hydration in the binder of Mix 1, i.e., Type III cement-fly ash-silica fume blend, was observed. The peaks corresponding to silicate and secondary aluminate reactions exhibited higher amplitudes. Compared with the Type I/II cement blends, not only the amplitude of the peak was further raised, but they also occurred earlier indicating the enhanced initial cement hydration from Type III cement. This might be due to its smaller particle size and higher contents of fast-reaction phases, i.e., $C_3S$ and $C_3A$, as discussed above. The same phenomenon was also observed from the cumulative heat release curves in Figure 4.19b, wherein more early-age hydration heat was released from Mix 1, which contains Type III cement. It is anticipated that Mix 1 will exhibit higher early strength than other groups. Due to the dilution effect, the total heat output of the cement blends is lower than that of pure cement. It should be noted that the hydration heat flow and heat release of Type I/II cement shown in Figure 4.18 has a water-to-cement ratio of 0.4, which was commonly used in regular concrete. However, in UHPC, a water-to-cement ratio of 0.19 was used, which is another reason for the low amplitudes of heat flow and release. With the incorporation of fly ash and silica fume, due to the high aluminate content, the pre-induction stage was shortened. Compared with Class C fly ash, although the occurrence of the exothermic peak was moved earlier, lower peaks with a larger slope of acceleration stage were observed in the presence of Class F fly ash (Mix 2 vs. Mix 4, and Mix 3 vs. Mix 5). This indicates the contribution of silicate in Class F fly ash in enhancing the hydration rate of cement, while the high content of CaO in Class C fly ash releases more heat during its

hydration. In Mix 6 and Mix 7, the secondary peak, which is related to the hydration of aluminates, was enhanced. This indicates the positive role of MK nanoparticles in the formation of calcium silicate hydrates (C-S-H) by providing additional nucleation sites [186]. More importantly, the aluminate peak corresponding to sulfate depletion was effectively enhanced and accelerated. The high aluminate content of the MK particles redefined the Al/Si ratio of the cement system and altered the reactivity of the aluminate phases.

In line with the evolutions of heat flow, the binder of Mix 1 exhibited higher accumulative heat release than other groups indicating the fast hydration of Type III cement. The difference between Mix 2 and Mix 3 lies in the use of micro-fly ash in Mix 2. Due to the absence of micro-fly ash in Mix 3, more Class C fly ash was used. It was observed that the early age hydration heat during the first 25 hours was enhanced by the Class C fly ash, which contains a high content of CaO. After 25 hours, the benefit of the micro-fly ash was observed, which resulted in a rapid increase of hydration heat in Mix 2 exceeding that of Mix 3. The same phenomenon was observed in Mix 4 and Mix 5. Compared with the groups (Mix 2 and Mix 3) with Class C fly ash, the use of Class F fly ash resulted in lower hydration heat. This might be due to the exothermic hydration of the lime (CaO) and the finer particle size of the Class C fly ash. The incorporation of MK resulted in lower hydration heat than other binders during the first 30 hours, after which high hydration heat was obtained from Mix 6 and Mix 7, which is correlated to the enhanced aluminate reaction peak shown in Figure 4.19a.

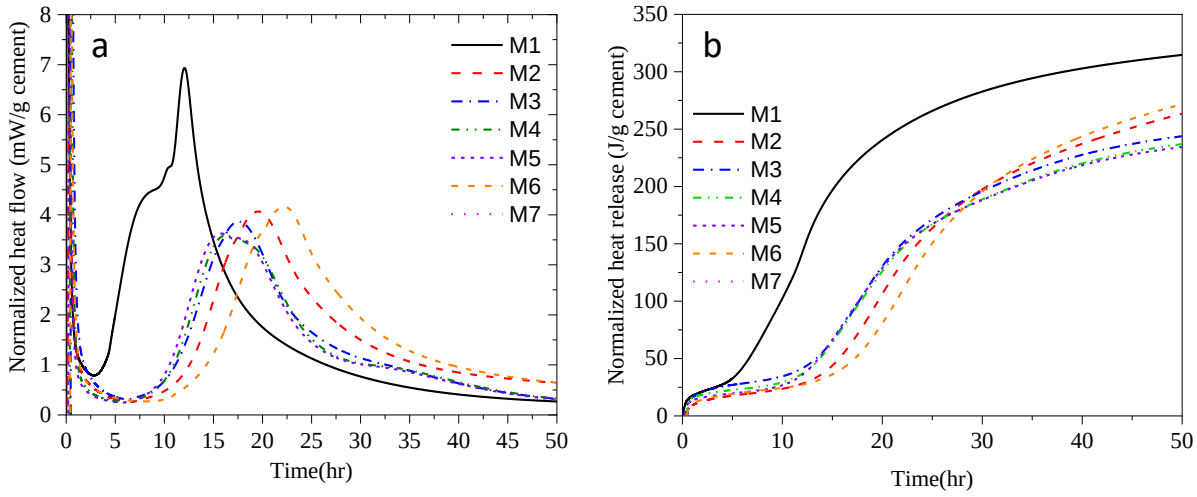


**Figure 4.19: Hydration heat of UHPC binders**

### 4.3.3. FTIR Spectroscopy

Figure 4.20a and 4.20d show the FTIR spectra of the UHPC cementitious binders after 3 days, 7 days, 28 days, and 60 days. The O-H bond of calcium hydroxide indicated by the peaks at around 3640 cm-1 was observed from neat PC suggesting the presence of portlandite. Due to the incorporation of supplementary cementitious materials, which can trigger pozzolanic reactions in the cement matrix to consume portlandite [187], the peak of the O-H bond is not that significant in the UHPC binders. The portlandite was found to disappear from the binders after 28 days and 60 days. Moreover, the peak between 1550 cm-1 and 1650 cm-1 is attributed to the H-O-H vibration of interlayer water [188]. The

absorption band of Si-O was seen at 1120 cm-1, which was related to the Si-O stretching vibration of the Si-O tetrahedron indicating the presence of calcium silicate hydrates (C-S-H). The symmetric bending of the Si-O-Si bond associated with the peak at 972 cm-1 ~ 440 cm-1 indicating the polymerization of silicate ($SiO_4^{2-}$) also suggests the presence of C-S-H. The absorption band of 551 cm-1, which indicates the formation of the Si-O-Al bond [189], was observed in Mix 6 and Mix 7. This might be due to the incorporation of metakaolin in these two groups. The absorption band at 1400 cm-1 – 1500 cm-1 associated with asymmetric stretching vibration of C-O in calcite was observed indicating the unavoidable carbonation of the binder samples during sample preparation and testing.

The key peaks for the FTIR result are Si-O and Si-O-Si bonds at 1120 cm-1 and 972 cm-1, which indicates the presence of C-S-H. It is observed that Mix 1 exhibited higher intensity than Mix 2 for both 1120 cm-1 and 972 cm-1 at 3 days (Figure 4.20a). This might be due to the use of Type III cement in Mix 1, which leads to the formation of more C-S-H in Mix 1 at an early age due to the fast hydration reactions. The comparisons between Mix 2 and Mix 3, as well as that between Mix 4 and Mix 5, indicate that the use of UFFA can enhance the formation of the Si-O bond in the presence of both Class C and Class F fly ashes. By comparing Mix 6 and Mix 7, it was observed that the complete replacement of silica fume with metakaolin decreased the intensity of the Si-O bond. The 7-day results are in line with the results obtained after 3 days except for the slightly higher intensity of the Si-O bond in Mix 3 over that of Mix 2 (Figure 4.20b). After 28 and 60 days (Figures 4.20c and 4.20d), it was observed that the intensity of the Si-O-Si bond in Mix 2 became similar to that of Mix 1. This indicates that the use of Type III cement resulted in the faster formation of C-S-H at early curing ages (3-day and 7-day), while comparable ultimate amounts of the hydration products can be formed in Type I/II at later ages. By comparing Mix 3 and Mix 6, it can be observed that the partial replacement of silica fume with metakaolin did not considerably affect the formation of C-S-H. The same phenomenon was observed from the complete replacement of silica fume with metakaolin (Mix 4 vs. Mix 7).

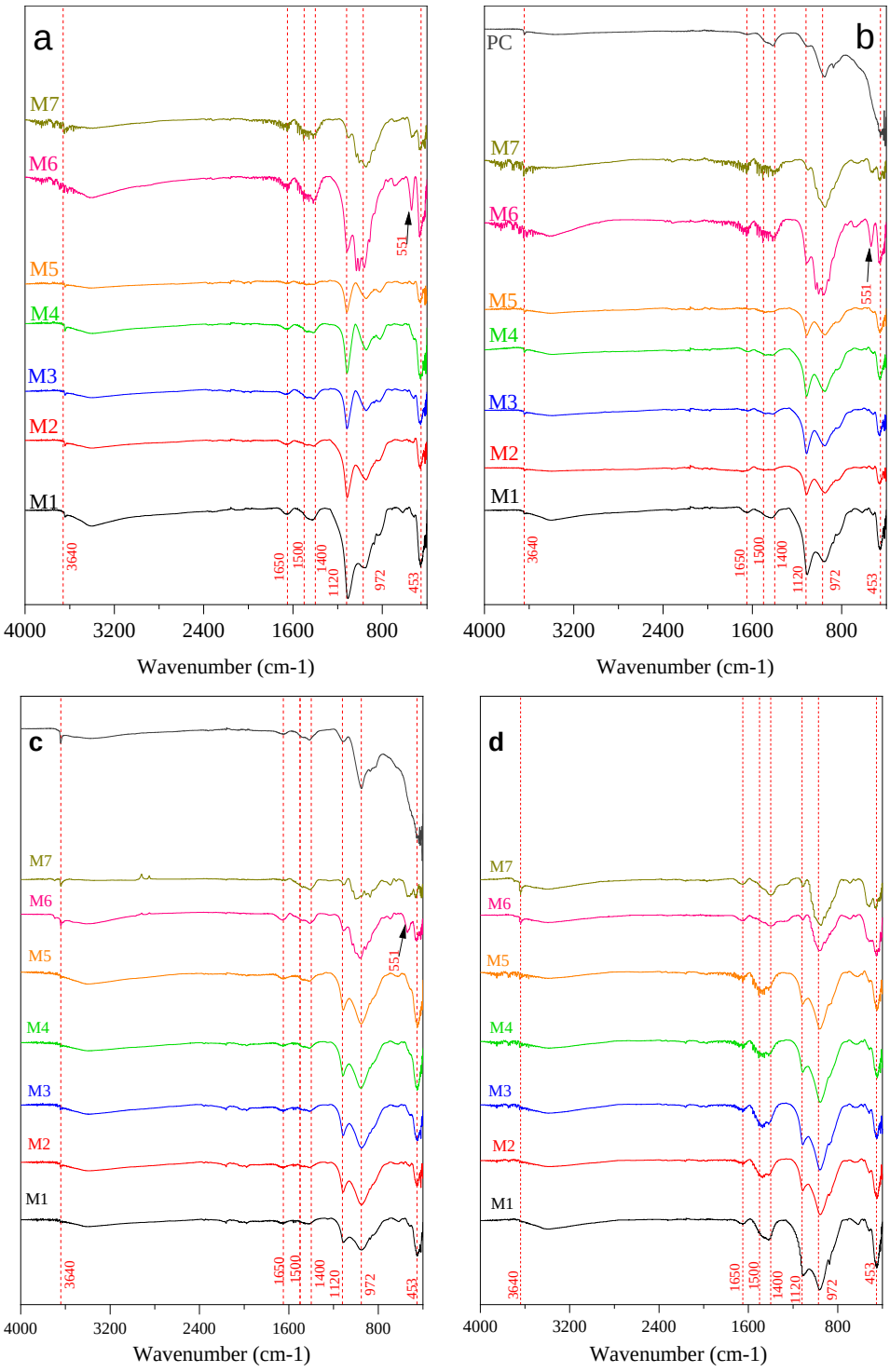


(a) 3 days, (b) 7 days, (c) 28 days, and (d) 60 days

**Figure 4.20: FTIR spectra of the UHPC binders**

### 4.3.4. TGA

Figures 4.21, 4.22, 4.23, and 4.24 show the TGA and DTG curves of the cementitious binder after 3 days, 7 days, 28 days, and 60 days, respectively. The weight losses from the TGA curves (Figures 4.21a, 4.22a, 4.23a and 4.24a) and the corresponding peaks from the DTG curves (Figures 4.21b, 4.22b, 4.23b and 4.24b) indicate the thermal decompositions of different reaction products in the binders. From 30°C to 130°C, the first mass loss is due to the loss of free and loosely bound water from the dehydration of C-S-H and ettringite. Similarly, the peaks in 400°C-510°C and 590°C-770°C are considered the dihydroxylation of calcium hydroxide (CH) and the decomposition of calcium carbonate (CC), respectively [188]. The bond water content can be determined from the weight losses from 115°C to 510°C. Considering the neat PC results, it can be seen that the degree of hydration of cement increased over the testing period as the intensity of peaks due to the decomposition of C-S-H and ettringite. The weight loss between 30°C and 105°C is considered due to the free and loosely bound water. It was observed that Mix 1 contains 8.25% and 1.56% more loosely bound water than Mix 2 after 3 and 7 days, respectively. Again, this is due to the faster hydration rate of Type III cement in Mix 1, which resulted in the formation of more C-S-H and ettringite that contain loosely bound water than Type I cement in Mix 2 at early ages. However, at 28 days, the weight loss due to the loosely bound water in Mix 1 is 4.26% less than that in Mix 2, which is in line with the evolutions of C-S-H-related chemical bonds detected from the FTIR tests (see Figure 4.20). The comparisons between Mix 2 and Mix 3, as well as that between Mix 4 and Mix 5, indicate the enhanced hydration in the presence of UFFA in the cementitious binders. Mix 6 exhibited 111.17%, 21.20%, and 23.11% higher contents of loosely bonded water than Mix 7 after 3 days, 7 days, and 28 days, respectively indicating that the coupling of metakaolin and silica fume can enhance the hydration of cement more effectively than the single use of metakaolin.

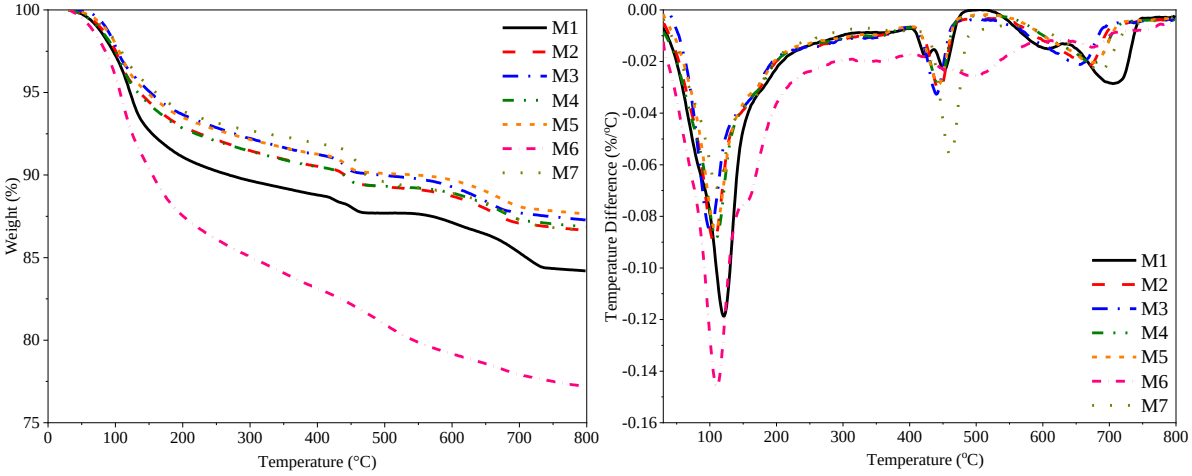


**Figure 4.21: TGA and DTG curves after 3 days**

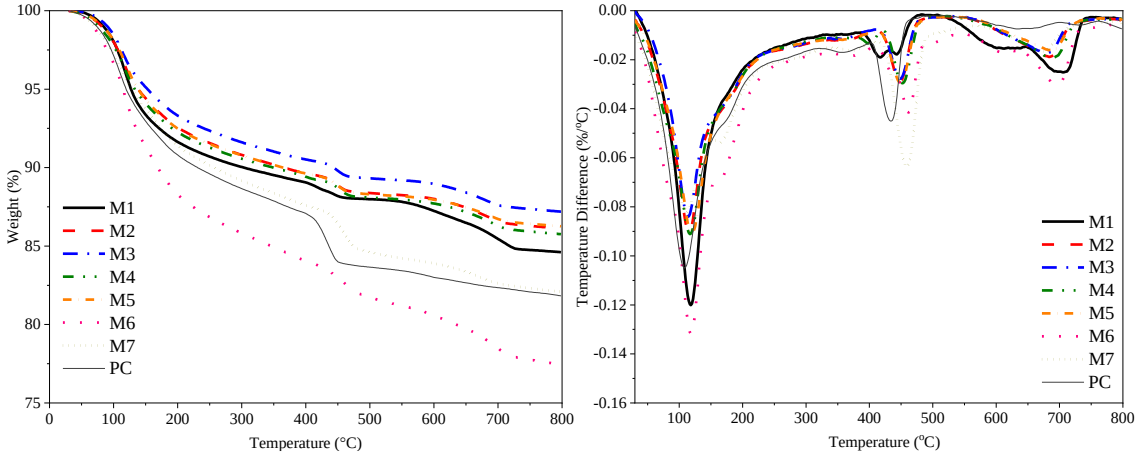


**Figure 4.22: TGA and DTG after 7 days**

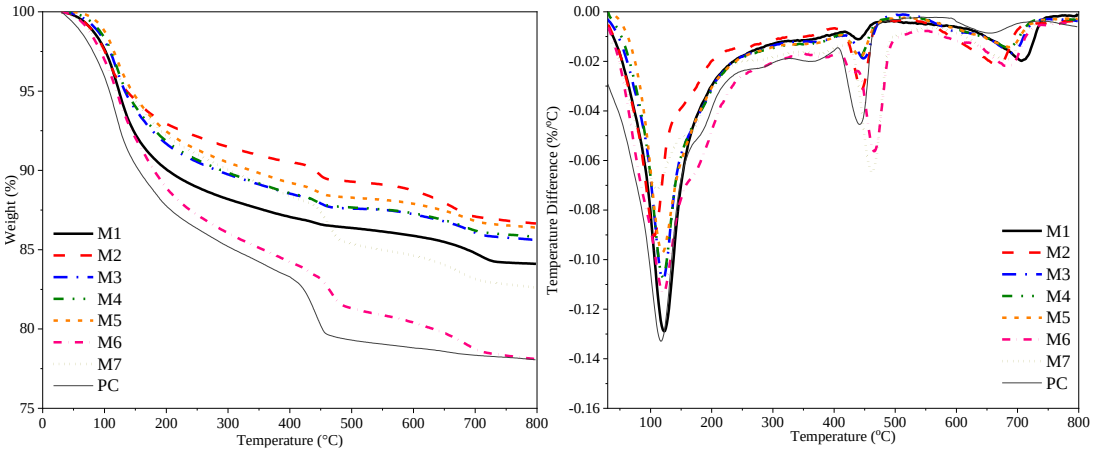


**Figure 4.23: TGA and DTG after 28 days**

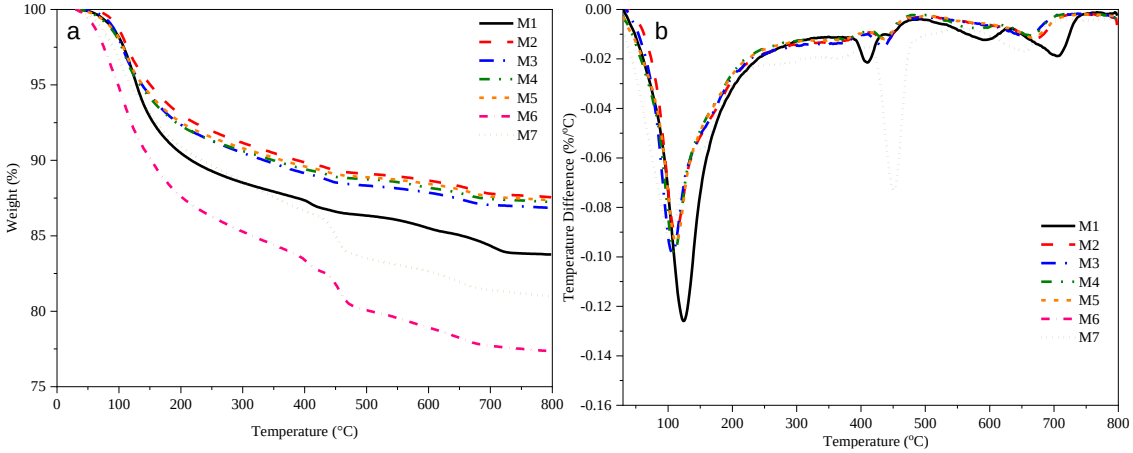


**Figure 4.24: TGA and DTG after 60 days**

Figures 4.25 and 4.26 show the development of CH and bonder water contents in the UHPC cementitious binders as a function of time, respectively. In line with the calorimetry results, Mix 1 showed a higher amount of C-S-H and ettringite than other binders. Again, this is due

to the high reaction rate of Type III cement due to its high contents of C3S and C3A, as well as its finer particle size. As the hydration and the pozzolanic reaction proceeded, the difference in C-S-H contents of the binders decreased. Another difference between Mix 1 and other groups lies in the content of calcium hydroxide. Although Type III cement exhibited a higher degree of hydration, the content of calcium hydroxide was lower than other groups. This indicates that the pozzolanic reactions between Type III cement and the SCMs, such as silica fume and micro-fly ash, have a higher reaction degree than other groups. It should be noted that the content of calcium hydroxide decreased over time in all the groups along with the increased content of C-S-H, which is believed to have a positive correlation with strength development. Mix 2 showed more C-S-H and less calcium hydroxide than Mix 3 during the first 3 and 7 days. This might be due to two reasons: (i) the hydration of CaO in Class C fly ash can form calcium hydroxide, and Mix 2 contains less Class C fly ash than Mix 3, and (ii) the micro-fly ash can play a role of nucleation for the formation of C-S-H and the pozzolanic reaction of the micro-fly ash can enhance the consumption of calcium hydroxide and the formation of C-S-H. However, after 28 days and 60 days of hydration, Mix 3 showed less calcium hydroxide than Mix 2 along with the formation of more C-S-H. This indicates the high pozzolanic reactivity of Class C fly ash for long-term reactions. A less significant role of micro-fly ash in the Class F binders (Mix 4 and Mix 5) than that in Class C fly ash binders (Mix 2 and Mix 3) was observed. This might be due to the fact that ultra-fine micro-fly ash (UFFA) is a type of Class F fly ash but with finer particles.

From Figure 4.25, the CH contents of Mix 1 are 10.44% and 9.36% after 3 days and 7 days respectively, which are 2.59% and 2.86% higher than that of Mix 2. However, after 28 days, Mix 1 showed a CH content of 6.18%, which is 34.11% lower CH content than Mix 2. This again indicates the faster hydration reactions of Type III cement than Type I/II cement forming more CH at early ages, which was then converted to C-S-H via pozzolanic reactions triggered by the incorporation of silica fume and fly ashes. The decrease in CH content with time was also observed from other UHPC binders. The 3-day CH content of Mix 3 is 10.31%, which is 1.31% higher than that of Mix 2. After 7 days and 28 days, the CH content of Mix 3 decreased to 8.52% and 7.16%, respectively, which are 6.33% and 23.68% lower than that of Mix 2. The difference between Mix 2 and Mix 3 is the use of UFFA in Mix 2 along with Class C fly ash and silica fume. The results indicate that the UFFA can enhance the cement hydration in Mix 2 at early ages, while the pozzolanic reactions that consume CH are more significant in Mix 3. The CH contents of Mix 5 after 3 days, 7 days, and 28 days are 9.36%, 9.01%, and 6.93%, respectively. The 3-day and 7-day CH contents of Mix 4 are 1.85% and 5.55% higher than that of Mix 5, while the 28-day CH content of Mix 4 is 1.93% lower than that of Mix 5. The comparison between Mix 4 and Mix 5 indicates the synergistic effect between UFFA and Class F fly ash in the phase evolution of cement hydration, in particular after 28 days, which is different from the binders containing Class C fly ash. Different from the other binders, the two groups with metakaolin (Mix 6 and Mix 7) exhibited increases in CH contents with time. The 3-day, 7-day, and 28-day CH contents of Mix 6 are 18.53%, 17.72%, and 19.37%, respectively. The 3-day CH content of Mix 6 is 79.72% higher than that of Mix 3, while Mix 7 exhibited 67.41% higher 3-day CH content than Mix 5. The comparison of 60-day CH contents between Mix 2 and Mix 3 indicates that the use of UFFA did not influence the CH content significantly. The CH content of Mix 3 is 5.69%, which is 3.45% higher than that of Mix 2. Similarly, Mix 5 showed an 8.75% higher

CH content than Mix 4. Mix 6 and Mix 7 exhibited the highest CH contents after 60 days. The CH content of Mix 6 is 20.50%, which is 260.28% higher than that of Mix 3. The CH content of Mix 7 is 18.70%, which is 289.60% higher than that of Mix 4. These two comparisons indicate that the partial and complete replacements of silica fume with metakaolin resulted in decreased CH consumption in the matrix of UHPC. Given the mixture design of these four UHPC groups, the comparisons indicate that silica fume exhibited higher pozzolanic reactivity than metakaolin in the presence of both Class C and Class F fly ashes. In the presence of sufficient water, it has been determined that metakaolin can exhibit high pozzolanic reactivity comparable with silica fume. The low reactivity of metakaolin in the UHPC mixes of this study might be due to the extremely low water-to-binder ratio (0.19) and the high water uptake capacity of metakaolin.

The chemically bound water content in the UHPC binders was calculated based on the mass change in the temperature range of 115°C to 510°C. It is the hydration process of cement, the reaction between the mineral phases and water to form hydrates. Therefore, the development of bound water content formed in the hydrates is commonly used to evaluate the degree of cement hydration. Previous studies indicated that, as the chemically bound water increases, the compressive strength of the mix increases [190]. The 3-day, 7-day, and 28-day bound water contents of Mix 1 are 9.29%, 7.16%, and 11.32%, respectively, significantly increased for 3-day, 7-day, and 28-day which are 20.04%, 9.46% and 46.34% higher than Mix 2, respectively. This is mainly due to the higher hydration rate of Type III cement in Mix 1 than that of Type I/II cement in Mix 2. The 3-day, 7-day, and 28-day bound water contents of Mix 3 are 7.44%, 6.16% and 10.64%, respectively. It was found that the 3-day and 7-day bound water contents of Mix 3 are 4% and 6.14% lower than that of Mix 2, respectively, while after 28 days, Mix 3 showed a 27.29% higher bound water content than Mix 2. The results indicate that the use of UFFA in the presence of silica fume and Class C fly ash can enhance the early-age cement hydration, while after 28 days, the mix without UFFA showed a higher hydration degree. Based on the comparison between Mix 4 and Mix 5, a less significant influence from UFFA was observed in the presence of Class F fly ash. mix does not impact significantly. The 3-day, 7-day, and 28-day bound water contents of Mix 5 are 7.30%, 6.81%, and 10.51%, respectively, and Mix 4 exhibited comparable content of bound water at the same ages. By partially replacing silica fume with metakaolin, Mix 6 yielded significantly increased bound water contents. The bound water contents of Mix 6 after 3 days, 7 days, and 28 days are 16.46%, 10.66%, and 17.61%, respectively. Compared with Mix 7, in which the silica fume was completely substituted with metakaolin, Mix 6 showed 92.41%, 38.83%, and 34.55% % higher bound water contents than Mix 7 after 3 days, 7 days, and 28 days, respectively. From the 60-day bound water contents of Mix 2 and Mix 3, it can be seen that the UFFA did not contribute significantly to the enhancement of cement hydration. The bound water of Mix 3 is 9.35%, which is 0.75% higher than that of Mix 2. A similar observation was also obtained from the comparison between Mix 4 and Mix 5. Mix 6 and Mix 7 exhibited 74.33% and 64.43% higher bound water contents than Mix 3 and Mix 4, respectively, indicating enhanced cement hydration.

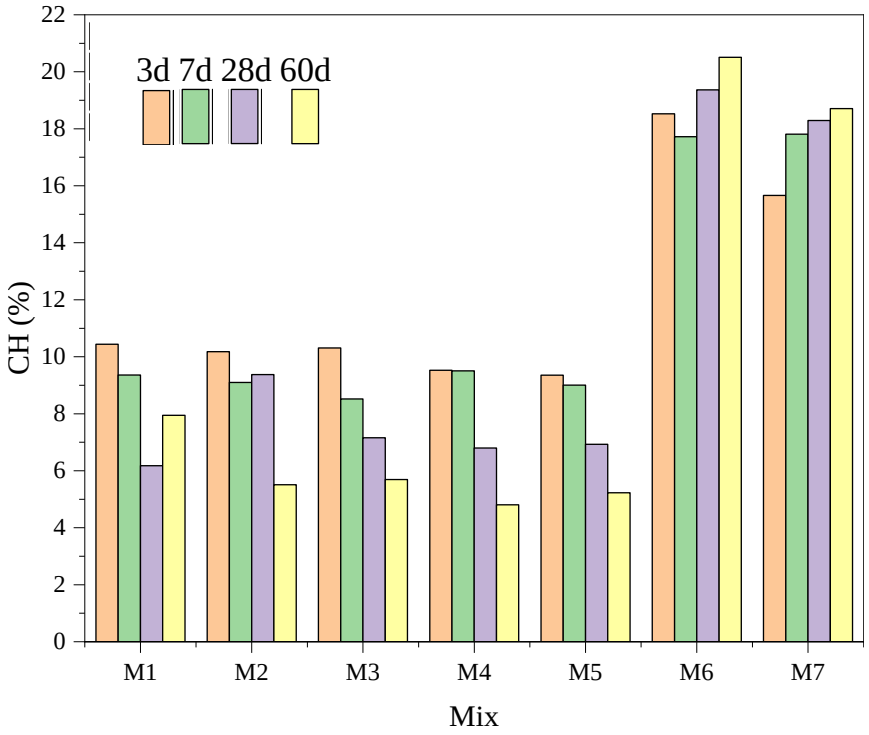


**Figure 4.25: CH contents in the UHPC binders**

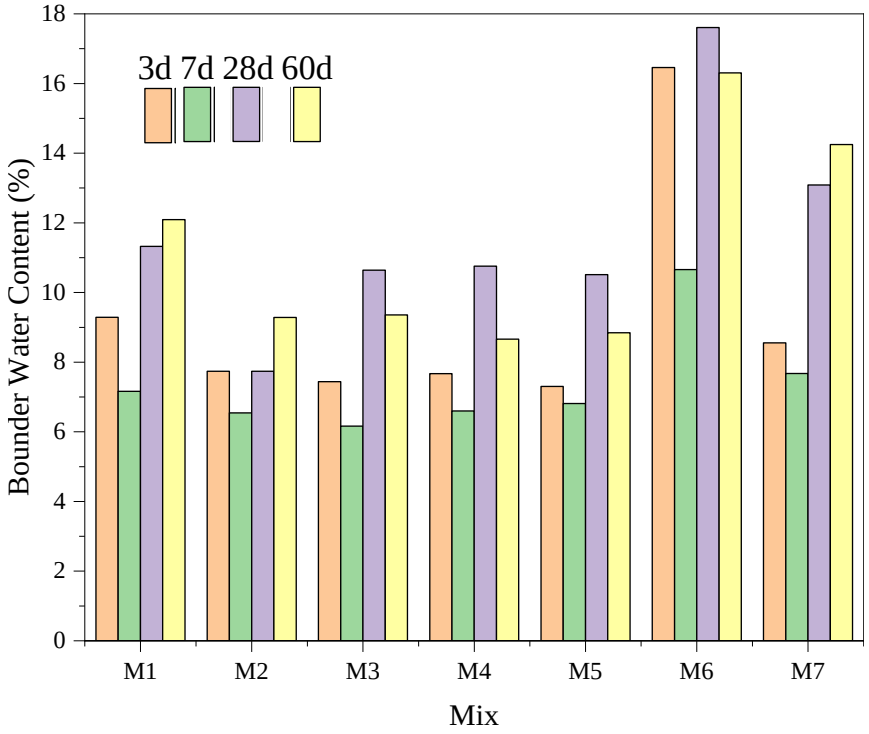


**Figure 4.26: Bound water contents in the UHPC binders**

### 4.3.5. XRD

Figures 4.27a and 4.27b present the XRD patterns of the hydrated binder after 3 days and 7 days, respectively. From these early-age XRD patterns, the main cement hydration products including ettringite, C-S-H, CH, and its carbonate (calcite), were observed. However, a large amount of unhydrated clinker phases ($C_2S$ and $C_3S$) were also detected from all the binders. This is mainly due to the low water-to-cement ratio used in the UHPC. It is well known that the strength of concrete decreases with increasing the water-to-cement ratio. To ensure high strength in UHPC, a low water-to-cement ratio is typically used. In this study, the water-to-binder ratio was kept at 0.19. However, this might induce a low degree of hydration of the cement. As shown in Figures 4.27a and 4.27b, the peaks are dominated by the unhydrated alite ($C_3S$) and belite ($C_2S$). Due to the fast hydration of the Type III cement, the binder of Mix 1 showed higher intensity of ettringite and lower anhydrated phases than other binders after 3 days of hydration. After 7 days, more significant decreases in the unhydrated phases were observed from the Type I/II cement-based binders (Mix 2 to Mix 5) along with the higher intensity of cement hydration products, such as calcium hydroxide. Due to the high CaO content in Class C fly ash and their fast hydration, the binders of Mix 2 and Mix 3 showed a higher intensity of calcium hydroxide than that of Mix 4 and Mix 5 at the early ages. Due to the incorporation of the micro-fly ash, less calcium hydroxide was formed in Mix 2 than in Mix 3. This is induced by (i) the higher content of Class C fly ash in Mix 3 and (ii) the calcium hydroxide consumption in Mix 2 due to the enhanced pozzolanic reaction triggered by the micro-fly ash. A similar benefit from the micro-fly ash was also observed from the comparison between Mix 4 and Mix 5. Mix 6 contains metakaolin along with Class C fly ash and silica fume, and Mix 7 contains metakaolin along with Class F fly ash. In line with the TGA results, it is observed that more CH was formed in the UHPC matrix with metakaolin. The difference between Mix 3 and Mix 6 lies in the partial replacement of silica fume with metakaolin in Mix 6. It can be seen that the CH peaks in Mix 3 diminished over time, while in Mix 6 the CH peaks raised as hydration proceeded. Both Mix 5 and Mix 7 contain Type I/II cement and Class F fly ash, while their difference lies in the use of silica fume in Mix 5 and the complete replacement of silica fume with metakaolin in Mix 7. It was observed that silica fume showed a more effective CH-consuming capacity than metakaolin. After 7 days of hydration, the intensity of both unhydrated phases (alite and belite) and the crystalline hydration products (calcium hydroxide and ettringite) were observed to decrease. The decreases in the unhydrated phases indicate the continuous hydration of cement with time, while the decrease in calcium hydroxide content is due to the pozzolanic reaction triggered by the SCMs. Due to the semi-crystalline and amorphous structure, the peaks of C-S-H are not identifiable from the XRD patterns. Given the increased weight loss at around 110°C from TGA, it is believed that more C-S-H was formed in these binders along with the proceeded cement hydration and consumption of calcium hydroxide.

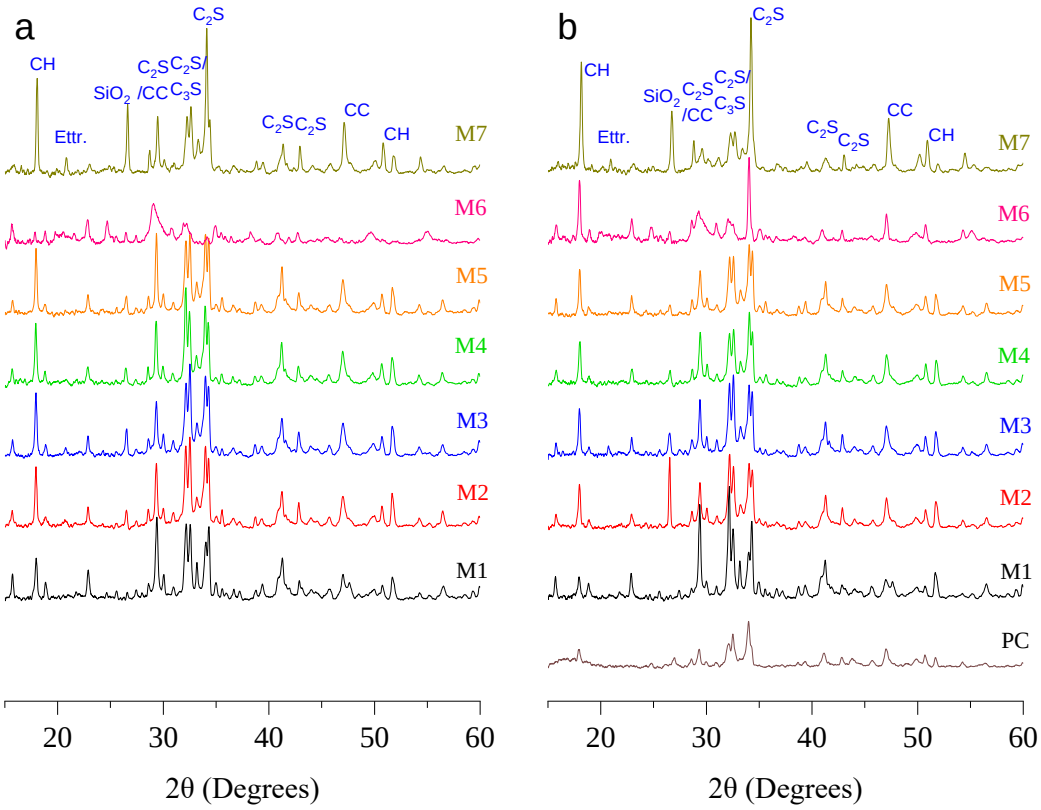


**Figure 4.27: XRD patterns of the UHPC binders**

Figures 4.28a and 4.28b present the XRD patterns of the hydrated binder after 28 days and 60 days, respectively. Compared with the early-age binder shown in Figure 4.27, the mature binders showed less unhydrated phases (alite and belite). It is interesting to see that calcium hydroxide, which was detected with high intensity after 3 and 7 days, showed a considerable decrease in intensity with time indicating the pozzolanic reaction between the SCMs and calcium hydroxide in forming additional C-S-H. This is beneficial for the strength gain of UHPC as C-S-H is considered the primary phase that endows hydrated cement with dense structure and strength. It was observed that, although Type III exhibited fast reaction rate than Type I/II cement at early ages, less unhydrated phases were detected from Type I/II cement binders after 28 days. It is anticipated that Mix 1 will yield higher early-age strength due to the rapid hydration of Type III cement, while Mix 2 to Mix 5 will gain comparable mechanical properties with Mix 1 at later ages. The influence of the micro-fly ash on the evolution of cement hydration products gradually decreases with time and no significant difference can be detected between Mix 2 and Mix 3. Compared with Mix 2 and Mix 3, which contain Class C fly ash, a slightly lower intensity of the unhydrated phases was detected from Mix 4 and Mix 5 indicating the higher reactivity of Class F fly ash due to its higher content of amorphous silicate. The comparison between Mix 3 and Mix 6 indicates that the partial replacement of silica fume with metakaolin did not improve the conversion of CH into C-S-H indicating the lower pozzolanic reactivity of metakaolin than silica fume, which was also observed from the comparison between Mix 5 and Mix 7. From Figure 4.28b, by comparing Mix 3 and Mix 6, it can be seen that the influence of metakaolin along with

silica fume significantly increased the intensity of CH peaks, indicating that the conversion of CH to C-S-H was decreased due to the replacement of silica fume with metakaolin. The higher CH peak intensity detected from Mix 7 than Mix 4 further validated this insight. It should be noted that the pozzolanic reaction discussed here is for the investigated UHPC binders only. Due to the layered clay structure, metakaolin can absorb more water than silica fume, which negatively impacts the hydration of cement and pozzolanic reactions in the UHPC binder with extremely low water-to-binder ratios. This highlights the necessity to improve the degree of reaction in the UHPC system, in particular, that with metakaolin, through physical or chemical approaches, such as steam curing.

It should be noted that the dominant peaks of the binders are still unhydrated alite and belite even after 28 days and 60 days of hydration. The main reason for this is the low water-to-binder ratio used in the UHPC groups. It has been experimentally determined that 1 g of fully hydrated cement can consume 0.25 g of water [191, 192]. In the UHPC, the hydration of cement and SCMs blends might need more than 0.25 g water/ g binder. Therefore, the cement is far from 100% degree of hydration in the UHPC groups, which have a water-to-binder ratio of 0.19. Therefore, if the degree of cement hydration at the low water-to-binder ratio can be enhanced in a proper way, the properties of UHPC will be further increased. Toward this end, steam curing was used in this study as a secondary curing condition to investigate the influence of the curing process on the strength development of UHPC.

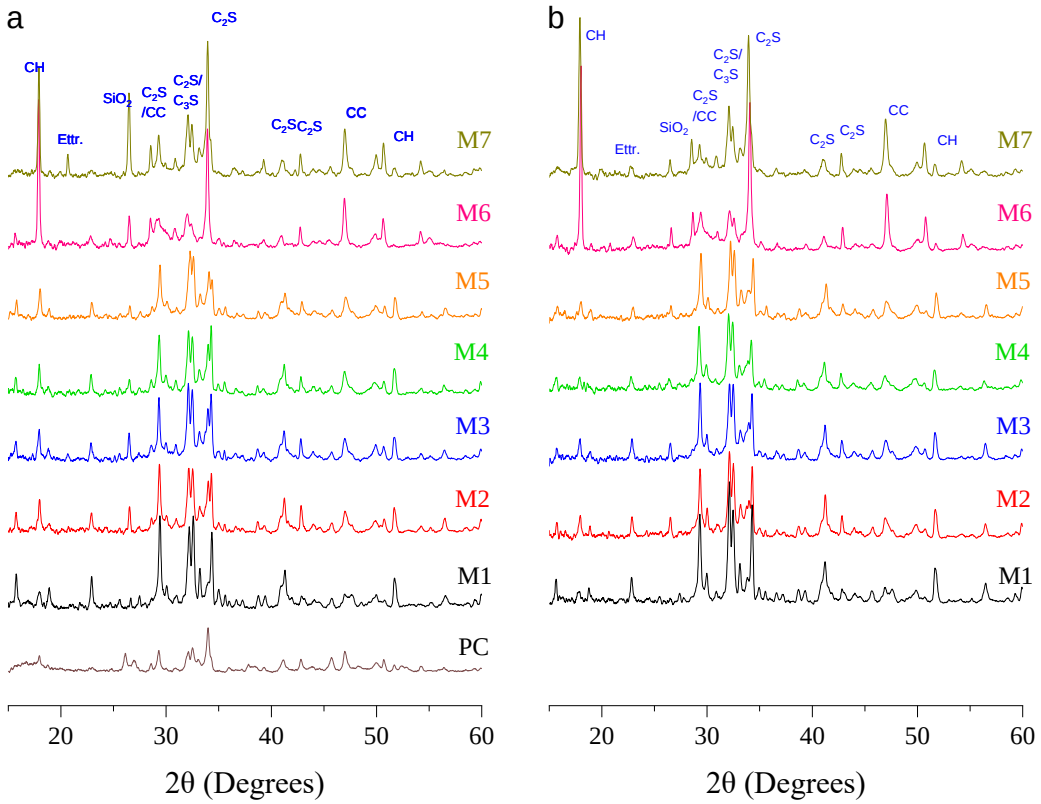


**Figure 4.28: XRD patterns of the UHPC binders**

# 5.0 Physical, Mechanical and Durability Properties

Based on the mixture design and the characterization of hydration of the cementitious binders in Task 3, this task mainly focuses on the physical and mechanical properties test of UHPC. To obtain comprehensive data for physical properties, permeability, and early-age autogenous shrinkage tests were done, and the compressive and flexural tests were performed to understand the influence of mixture design and curing conditions on the development of mechanical properties.

## 5.1 Curing Conditions

The specimens for the compressive and flexural tests were cast in their molds and covered by a plastic sheet at room temperature to eliminate the loss of moisture. After 24 hours, the specimens were demolded and then cured under two curing conditions: (i) regular lime water curing and (ii) steam curing. As shown in Figures 5.1a and 5.1b, The regular lime water curing was conducted by immersing the specimens in saturated calcium hydroxide (lime) water at 23 ± 2 ºC in accordance with ASTM-C31 [193]. As shown in Figure 5.1c, steam curing was conducted by conditioning the specimens under a temperature of 90oC and relative humidity of 100% for 48 hours. Then, the specimens were cooled down to room temperature and switched to regular lime water curing until tests. The steam curing was used to accelerate the hydration and pozzolanic reactions of the cementitious binders so that a higher strength gain rate is anticipated.

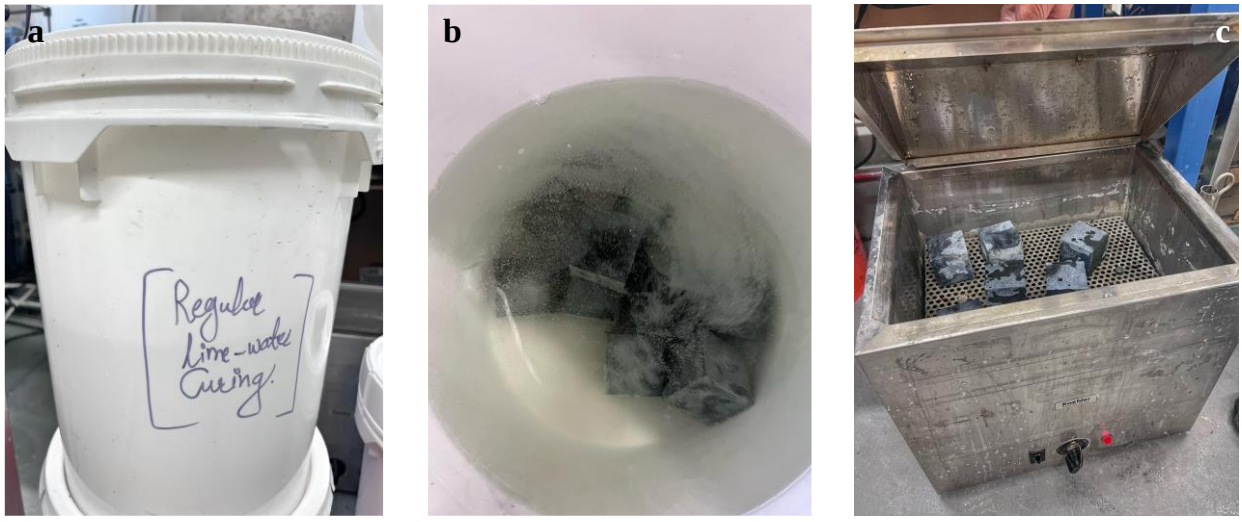


**Figure 5.1: Regular and steam curing of UHPC**

### 5.2.1. Early-Age Autogenous Shrinkage Test

To investigate the feasibility of using UHPC in practice, the early-age autogenous shrinkage test was performed for the first 100 hours after mixing. The autogenous shrinkage of concrete is commonly measured by following ASTM C1698 [194], in which a plastic corrugated tube is filled with the cement paste to measure the autogenous shrinkage. The corrugated plastic tube with a diameter of 24 mm and length of 420 mm, as well as the contact measurement make it difficult to pour the UHPC mix with micro-fibers and to obtain free volume change. To encounter this challenge, a novel shrinkage cone test was performed. Schleibinger shrinkage cone provides a touchless system to measure the height change of cone-shaped specimens using a laser sensor, enabling the measurement of initial autogenous shrinkage of the UHPC. The data was measured and recorded in the adapter shown in Figures 5.2a and 5.2b. A laser reflector is gently put in immediately after pouring the UHPC into the cone container. Paraffin oil is used to cover the UHPC to avoid a change in moisture content.

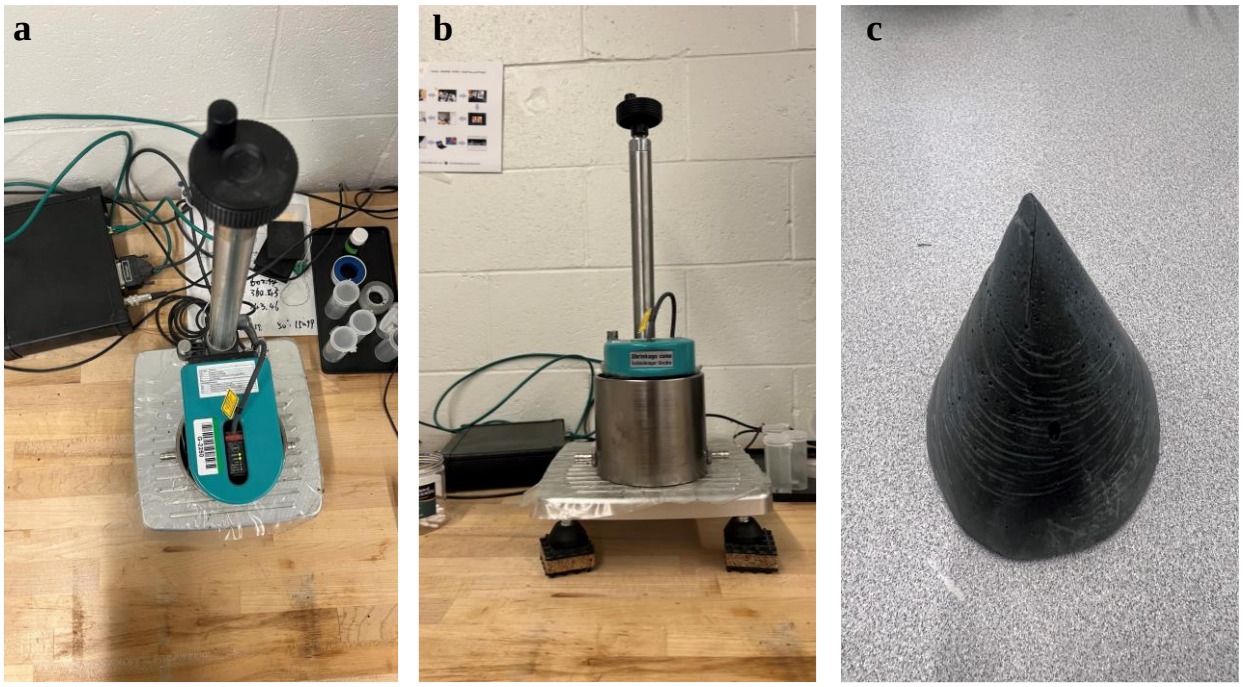


**Figure 5.2: The shrinkage cone**

### 5.2.2. Permeability Test

In addition to the higher mechanical strength, another advantage of UHPC outperforming regular concrete is its dense structure, which resulted in low permeability. Permeability is considered one of the key properties of concrete related to degradation resistance and long-term performance. In this study, the permeability of UHPC without the micro-steel fiber was measured in terms of bulk resistivity according to ASTM C1876 [195] using an RCON bulk resistivity meter from Giatec Scientific. All the seven UHPC groups designed in Chapter 3 were investigated. Two 3 by 6-inches cylinders of each UHPC group were cured for 6 days in the regular lime water curing condition. Then, the cylinders were dried in the lab for three

hours followed by a dry vacuum in a vacuum chamber at a vacuum pressure of 900-950 Pa for 2 hours and then saturated in a simulated concrete pore solution under the same vacuum condition for 1 hour. The specimens were kept immersed in the pore solution after releasing the vacuum for 24 hours. The specimens were wiped using a paper towel to remove the excess water from their surface. As shown in Figure 5.3, by placing the cylinders between two end caps lined with the conducting sponge pads the bulk resistivity was measured by recording the resistance at a frequency of 1 kHz. The permeability tests of FRC were performed by following the same testing procedure on Mix 1 and Mix 2 without steel fibers.

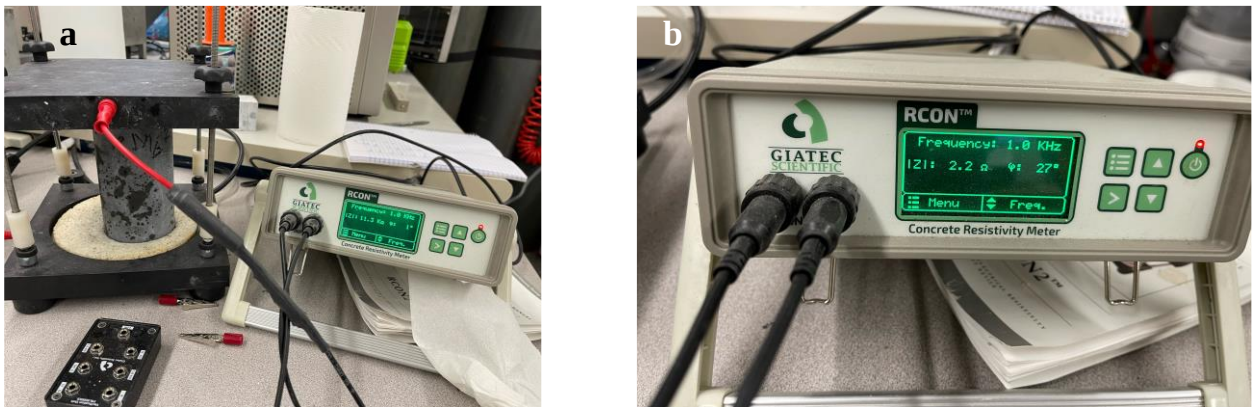


**Figure 5.3: The bulk resistivity testing setup**

### 5.2.3. Compressive Strength Test of UHPC

As shown in Figure 5.4, the compressive strength test was performed on 2-in. by 2-in. by 2-in. cubes in a Pilot compression testing machine in accordance with ASTM-109 [196]. After 3 days, 7 days, 28 days, and 60 days of curing, the specimens were taken out from the lime water and dried in the lab at room temperature for 3 hours. Then, the cubic specimens were placed in the center of the bearing blocks of the compressive testing machine. An axial compressive load with a constant loading rate of 200 lbs./second was applied until the failure of the specimens. To understand the influence of fiber reinforcement on the development of compressive strength, Polyvinyl Alcohol (PVA) fiber, basalt fiber, and glass fiber were used to replace the micro-steel fiber, and the 3-day, 7-day and 28-day strength of steam-cured specimens containing these fibers were tested. For accuracy, 3 repetitions of each group were tested to get an average value of the maximum load for each mix.

### 5.2.4. Compressive, Splitting Tensile, and Flexural Strength Test of FRC

The compression tests of FRC were performed in accordance with ASTM C39 using 4 in. by 8 in. cylinders. Splitting tensile tests of FRC were performed in accordance with ASTM C496 using 4 in. by 8 in. cylinders as well as 6 in. by 12 in. cylinders. Flexural tests of FRC were performed in accordance with ASTM C1609 using beams that were 6 in. by 6 in. by 21 in.

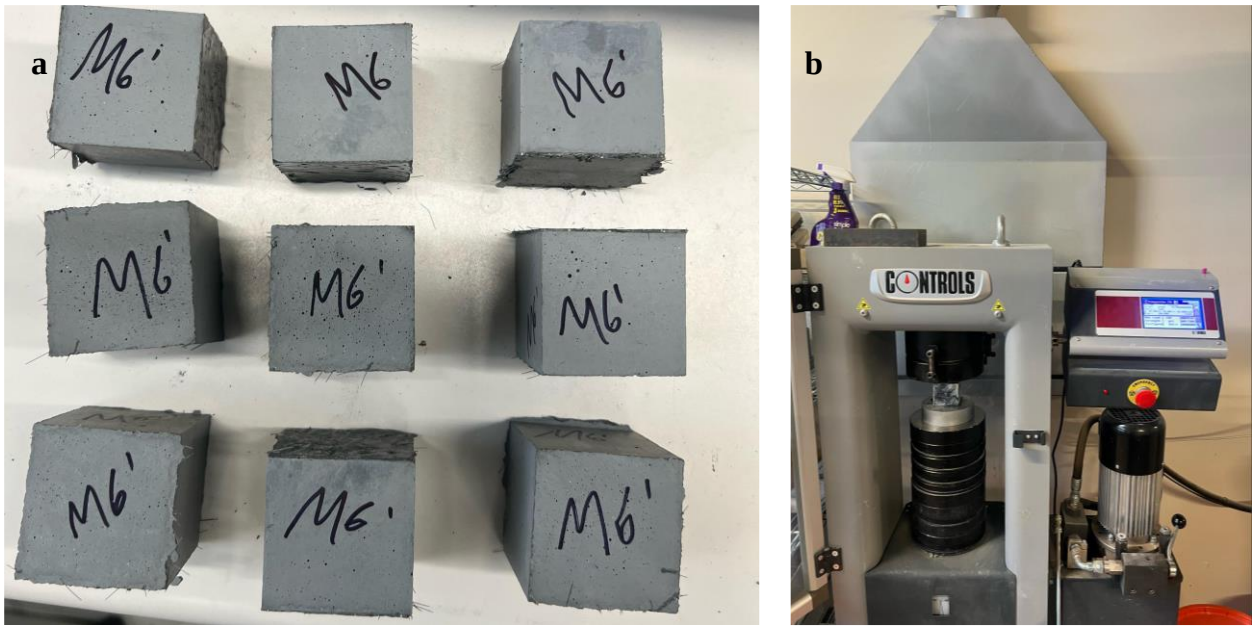


**Figure 5.4: UHPC cubes and strength test setup**

### 5.2.5. Flexural Strength Test of UHPC

As shown in Figure 5.5, the flexural test was performed in 1-in. by 2.25-in. by 12-in. beams under a 3-point bending test by following ASTM C1609 [197]. Based on the performance of the UHPC groups in compression tests, Mix 1, Mix 3, Mix 5, and Mix 6 were selected for the flexural strength test. Additionally, 2 specimens of Mix 5 for each of the different fibers, polyvinyl alcohol (PVA), basalt, and fiberglass, were tested at both 7 and 28 days under regular curing. This resulted in a total of 44 specimens being tested. After curing, the specimens were first dried in the lab for 3 hours, and two flat head screws were attached using epoxy to the top of either side of the specimens at midspan. String potentiometers were attached to these screws to measure the deflection at the midspan of the specimen. A span of 9.75 in. and a loading rate of 0.003 in./minute were employed for the flexural test until a displacement of 0.065 inches when the loading rate increased to .009 in./min. The test lasted until the load fell to approximately one-third of the peak load. The crack shape and length at different loading stages were qualitatively investigated throughout the test. Based on the experimental results, the influences of mixtures, fibers, and curing processes on the flexural strength of UHPC were analyzed.

**Figure 5.5: Flexural test setup**

### 5.2.6. Direct Tension Test of UHPC

Direct tension tests (DTT) have been typically used to determine the tensile strength as well as to capture the completed tensile responses of UHPC. However, this test also encounters some problems due to the lack of standardization. The ASTM resource from Zhou and Qiao [198] was used extensively in order to run these tests and get useful results. In total 16 dog-bone specimens were designed and tested in accordance with the method laid out in that resource.

There are several possible specimen types such as unnotched prisms or cylinders, notched prisms or cylinders, and dog-bone shaped specimens. DTT of normal concrete with dog-bone specimens has been widely used because it can provide a direct indication of tensile strength under evenly distributed tensile stress at the middle portion without the appearance of local stress concentration and relative rotation. Dog-bone specimens are also widely used for the determination of the tensile behavior of UHPC, but there is no standard test method or specimen design for the characterization of tensile behavior.

The specimen was designed by modifying the results from Zhou and Qiao [198] who developed a dog-bone shape based on using numerical finite element analysis. The specimen from this paper can be found in Figure 5.6. The specimens were tested in an Instron 3369 mechanical testing system and the design from Zhou and Qiao was modified to be able to be tested in the machine. The capacity of the machine is 11.24 kip (50 kN). The cross-section of the specimen was reduced from 2 inches by 2 inches to 1.5 inches by 1.5 inches to ensure the

specimen would break before it reached the capacity of the machine. Threaded rods like what Zhou and Qiao used, and their size depended on the grip attachments of the Instron and the capacity of the rods themselves. They were embedded 5 inches into the specimens and had a nut attached on the end to prevent pullout. In addition to pullout (ACI 318 17.4.3), concrete breakout (ACI 318 17.4.2) and side-face blowout (ACI 318 17.4.4) were all considered assuming a UHPC tensile strength of 2000 psi, and the summary of these checks can be found in Table 5.1 below.

**Figure 5.6: Dog-bone specimen from Zhou and Qiao (2020)**

**Table 5.1: Summary of anchoring to concrete failure modes**

| ACI 318 | Failure Mode | Design Strength, lbs. |
|---|---|---|
| - | UHPC capacity | 4,500 |
| 17.4.1 | Steel | 15,282 |
| 17.4.2 | Concrete breakout | 14,244 |
| 17.4.3 | Concrete pullout | 69,202 |
| 17.4.4 | Side-face blowout | 3,851 |
| 17.7.2 | Concrete splitting | Not applicable |

Even though side-face blowout controls this particular design, it was determined this design would still work as the UHPC tensile strength was unlikely to reach 2,000 psi. Additionally,

if side-face blowout was seen in the test specimens, tested before the actual specimens were tested, different grip configurations could have been used to reduce this failure mode. Ideally, the design would have been refined more and possibly used a smaller threaded rod and a larger dog-bone cross-section, which became obvious after testing was complete.

The finalized design can be seen in Figure 5.7 below. The center region's dimensions are 1.5 inches by 1.5 inches. The end region's dimensions are 1.5 inches by 2.5 inches. To join the two regions, an arc with a radius of 6 inches was used. The specimens ended up being 21.8 inches long. Two test specimens were cast and tested to determine if there were any issues with the design or fabrication. The first specimen was tested and failed in the center region as intended. However, there was an issue with the second specimen as it would not fit in the machine due to the threaded rods not being aligned. This issue was caused by the manufacturing of molds. The molds were 3D printed. However, due to the size of the specimen, the molds had to be constructed in two parts, which resulted in a seam at the hole as the threaded rod passed through. Additional molds were made by UMass Lowell, with the seam in a different location which solved this problem (see Figure 5.8).

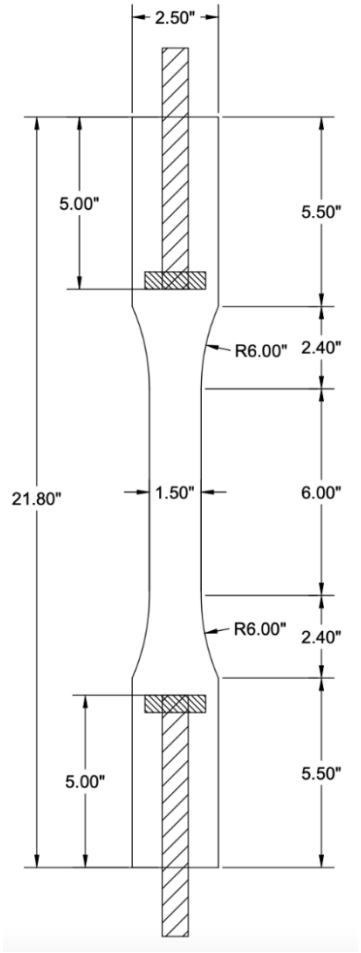


**Figure 5.7: Finalized Dog-bone specimen**


(a) the 3D printed mold for the dog-bone specimens, (b) casting of the dog-bone specimens, and (c) dog-bone specimens for tension test.

**Figure 5.8: Mold and dog-bone specimens**

There are no standardized test methods for direct tensile mechanical assessment of concrete available for UHPC, and thus researchers have experimentally not only tried different

specimen dimensions and shapes they have also tried different loading rates and procedures. For this test, it was again based on the testing by Zhou and Qiao [198]. Two specimens for Mix 1, Mix 3, Mix 5, and Mix 6 were tested at both 7 days and 28 days, meaning a total of 16 specimens were tested.

During each test, the tensile stress from load history and the average tensile strain were calculated from two string potentiometers used to generate the tensile stress–strain curves of UHPC in direct tension. The specimens were attached directly to the grips of Instron and loaded at a rate of 0.01 in./min. Two flat head screws were attached to the surface of the specimen 7 inches from the top and bottom in the center of the specimen using epoxy. These screws were used to attach the string potentiometers to measure the elongation of the center section of the specimen, which was then used to calculate the tensile strain of the UHPC. The test lasted until the load fell to 10 percent of the peak load. Two specimens for each mix were tested at both 7 days and 28 days. The test setup can be seen in Figure 5.9 below.

In addition, to investigate the tensile behavior of UHPC, the following tensile material parameters obtained from DTTs were compared: the peak tensile strength ($\sigma_c$); the tensile strain at peak strength ($\varepsilon_c$); and the tangent modulus of elasticity ($E_{cc}$), which is the ratio of the peak tensile strength ($\sigma_c$) and the corresponding tensile strain ($\varepsilon_c$), and it describes the behavior of UHPC in the whole elastic region.

**Figure 5.9: Test setup of direct tension test**

### 5.2.7. Sulfate Attack Test

To understand the durability performance of UHPC, sulfate resistance tests were conducted following the guidelines outlined in ASTM C1012-04 [199]. The procedure entailed assessing the length change of prismatic specimens immersed in a standardized sulfate solution, which had a sodium sulfate concentration of 50 grams per liter. Mix 1, Mix 2, Mix 3, and Mix 5 were investigated and compared with a control group of a regular mortar. Two prismatic bar specimens with a dimension of 1 in. by 1 in. by 10 in. (25.4 mm × 25.4 mm × 255 mm) were cast for each group. After casting, the fresh specimens were sealed in the molds to avoid loss of water. The specimens were demolded after 24 hours and cured in saturated lime water at room temperature (23±2 °C). After a 7-day curing period in lime water, two repetitions of mortar specimens from each group were subjected to length measurements and then placed in the standardized sulfate solution at a temperature of 23 ± 2 °C. Weekly measurements of length changes of the specimens were recorded, and the calculations were carried out using the following equation [199]:

$$\Delta L\ (\%)\ =\ [(L_x - L_i)/L_g] \times 100 \qquad (5.1)$$

where ΔL (%) is the change in length at the age of x; Lx is the average comparator reading of two bars at the age of x; Li is the average initial comparator reading of the same two bars, and $L_g$ is the nominal gage length.

## 5.3 Test Results and Discussion

### 5.3.1. Initial Autogenous Shrinkage

Figure 5.10 shows the development of the early-age autogenous shrinkage of the 7 UHPC groups during the first 100 hours. The shrinkage behavior of plain Type I/II cement (PC) was also measured for comparison. It can be seen that the maximum initial shrinkage was obtained from PC, which is 325.83 μm after 93 hours. Four stages were observed from the development of the early-age autogenous shrinkage patterns: i) steep sedimentation of the fresh mixtures during the first 1 hour, ii) a fallback of shrinkage (i.e., slight expansion offsetting a part of the initial shrinkage) between 1 hour and 4 hours due to the release of cement hydration heat, iii) a secondary shrinkage increase from 4 hours to 20 hours, and iv) a stable post autogenous shrinkage with negligible volume change after 20 hours as an equilibrium condition. These observations indicate that the measured early-age autogenous shrinkage of the UHPC is a result of (i) chemical shrinkage, which is caused by the volume change from reactants to products, (ii) autogenous shrinkage driven by self-desiccation or the change in capillary pressure, (iii) volume change in the presence of the varying temperature in the mixture due to reaction heat. From Figure 5.6, Mix 1 shows an ultimate autogenous of 267.77 μm, which is 17.89% lower than that of PC. Similarly, the initial autogenous shrinkage for Mix 2, Mix 3, Mix 4, Mix 5, Mix 6, and Mix 7 are 463%, 38.50%, 0.18%, 59.31%, 11.31%, and 353.63% lower than that of the initial autogenous shrinkage of neat PC. Considering Mix 2 and Mix 3, the autogenous shrinkage of Mix 2 is 75.74% less than Mix 3, which indicates the benefit of the UFFA in the shrinkage control of UHPC. The autogenous shrinkage of Mix 5 is 37.17% less than that of Mix 4. The two comparisons indicate that UFFA can help to decrease the shrinkage of UHPC in the presence of Class C fly ash, while

it can increase the initial autogenous shrinkage along with Class F fly ash. Moreover, Mix 6 exhibited an early-age shrinkage of 292.99 µm while Mix 7 displayed a volume expansion of 128.59 µm indicated by the negative shrinkage values. From the results, it can be stated that the initial autogenous shrinkage of UHPC mixes is lower than that of neat PC except Mix 4. This might be due to the optimization of the particle packing density and the dense structure formed in UHPC. In addition, the micro-streel fibers might also help reduce the volume shrinkage of UHPC.

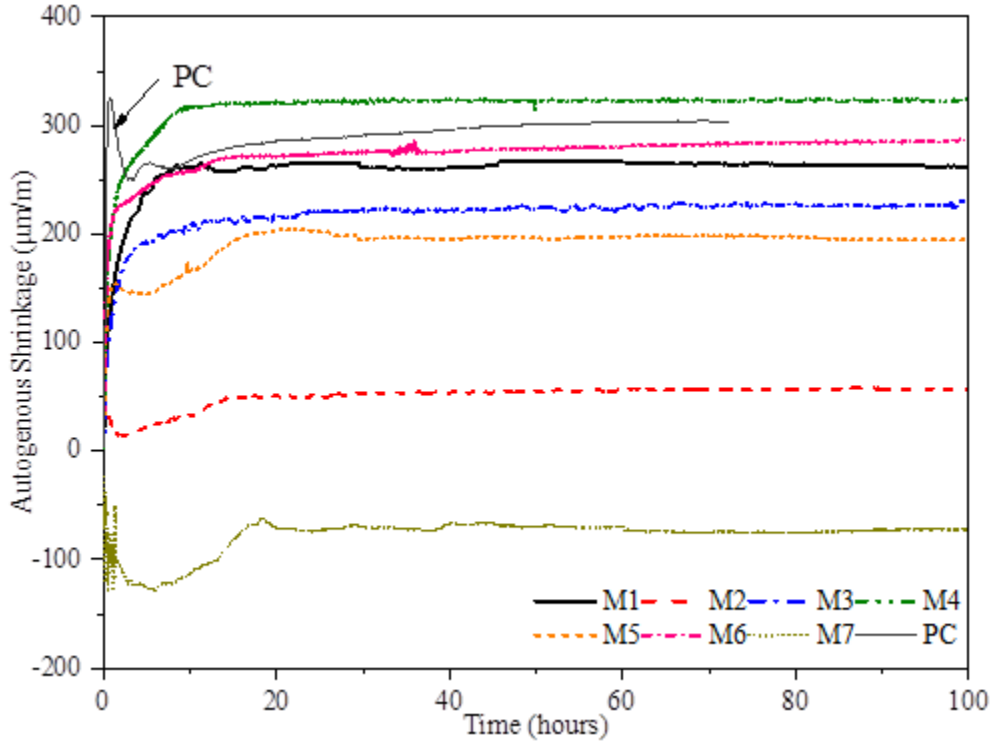


**Figure 5.10: Autogenous shrinkage of plain cement and UHPC**

### 5.3.2. Compressive Strength

5.3.2.A Development of compressive strength under regular lime water curing

The compressive strength tests were performed on the seven UHPC groups after 3 days, 7 days, 28 days, and 60 days. The mix design derived from the 2-step particle packing method is mentioned in Section 3.3. Figure 5.11 shows the development of compressive strength under regular lime water curing. Mix 1 exhibited an average 3-day compressive strength of 11,013 psi. This high early-age strength is due to the use of Type III cement, which is finer than Type I/II cement with a larger surface area. The difference between Type III (Mix 1) and Type I/II cement (Mix 2 to Mix 7) in compressive strength remained over time. After 28 days and 60 days, Mix 1 exhibited average compressive strength of 17,817 psi and 18,986 psi, respectively, which are still the highest values among the investigated UHPC groups. The difference between Mix 2 and Mix 3 lies in the use of ultra-fine fly ash (UFFA) in Mix 2. It is interesting to see that the use of UFFA did not result in a higher strength in Mix 2. The 3-day strength of Mix 3 is 10,640 psi, which is 7.92% higher than that of Mix 2. The average 28-day compressive strength of Mix 3 is 3.6% higher than that of Mix 2, while the

two groups yielded comparable strength after 60 days. The same trend is seen in the comparison of Mix 4 and Mix 5, the difference between which is the use of UFFA along with Class F fly ash. It was observed that the 3-day strength of the two groups is similar, while Mix 5 displayed higher strength than Mix 4 after 7 days. The average 28-day compressive strength of Mix 5 is 2.7% higher than that of Mix 4. Again, after 60 days, the difference in strength between Mix 4 and Mix 5 is negligible. Based on the comparison between Mix 2 and Mix 3, as well as the comparison between Mix 4 and Mix 5, the use of UFFA did not play a critical role in enhancing the compressive strength of UHPC. The difference between Mix 3 and Mix 5 lies in the type of fly ash, where Class C fly ash was used in Mix 3 and Class F fly ash was used in Mix 5. The results indicate the higher reactivity of Class F fly ash, and it resulted in an average 28-day compressive strength of 15,934 psi for Mix 5, which is 1.5% higher than that of Mix 3. Again, after 60 days, the difference in strength became small. The results indicate that the type of fly ash can trigger a slight difference in the early-age strength of UHPC, while the later-age strength is less sensitive to the fly ash type. Different from the first five groups, metakaolin was used in Mix 6 and Mix 7. It can be seen from Figure 5.7 that the use of metakaolin did not reduce the early-age strength after 3 days. However, from 7 days, the strength of Mix 6 and Mix 7 become lower than other groups. The average 28-day compressive strength of Mix 6 is 16,049 psi, which is 2.20% and 16.48% higher than that of Mix 3 and Mix 7, respectively. The difference between Mix 6 and Mix 7 is the use of silica fume in Mix 6, while Mix 7 does not contain silica fume. The results indicate that silica fume can play a critical role in enhancing the strength development of UHPC, and metakaolin cannot completely replace silica fume

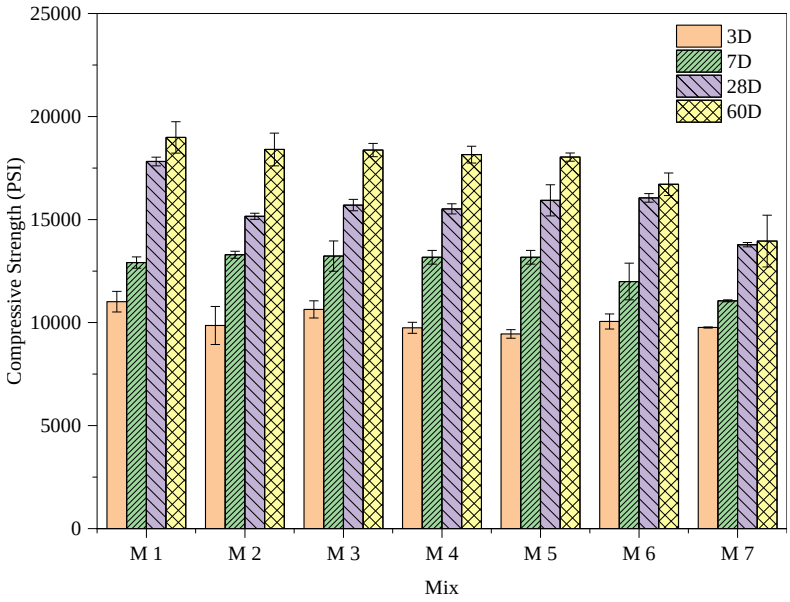


**Figure 5.11: Compressive strength of UHPC in regular lime water curing**

5.3.2.B Development of compressive strength under steam curing

From the result of the strength development of the UHPC groups under regular lime water curing, Mix 3, Mix 5, Mix 6, and Mix 7 were selected for steam curing investigations. Figure 5.12 shows the development of compressive strength of the selected groups under steam curing. From the strength gain, it was found that steam curing is an effective approach to

enhancing the compressive strength of UHPC. As discussed above, different from regular concrete, a water-to-cement binder ratio of 0.19 was used in UHPC to ensure high strength. However, this extremely low water-to-cement ratio can compromise the performance of UHPC, i.e., the reduction in workability and low degree of hydration of cement. By incorporating a high amount of superplasticizer, the workability (flowability) can be improved, while the amount of water is not enough to obtain fully hydrated cement. Therefore, an effective approach to enhance the hydration reactions of cement and the supplementary cementitious materials of UHPC in the presence of limited water becomes critically important. It was observed that the average 3-day compressive strength of Mix 3 under steam curing is 18,009 psi, which is 70% higher than its strength obtained from regular lime water curing. Likewise, the 7-day and 28-day compressive strength of the steam-cured Mix 3 is 35% and 17% higher than the regularly cured ones, respectively. Similarly, when Mix 5 is steam-cured, the average 3-day compressive strength reached 20,037 psi, which is 112% higher than that of regular lime water-cured Mix 5. The 7-day and 28-day compressive strengths of Mix 5 under steam curing were found to increase by 47% and 24.5%, respectively, when compared with the specimens from regular curing. A similar enhancement in strength was also observed from Mix 6, in which the steam curing improved the 3-day, 7-day, and 28-day compressive strength by 75%, 53.75%, and 12.33%, respectively, from the strength obtained under regular lime water curing. For Mix 7, compared with the strength from the regularly cured specimens, the steam curing resulted in 31% higher 3-day compressive strength and 23.34% higher 7-day compressive strength, but for the 28-day, regularly cured sample's results are 5.76% higher than that of the strength under steam curing. From previous studies, it was observed that steam curing can provide sufficient humidity to UHPC, which improves cement hydration [200]. This is considered the primary reason for the enhanced strength gain in steam curing, which is faster than that under regular lime water curing.

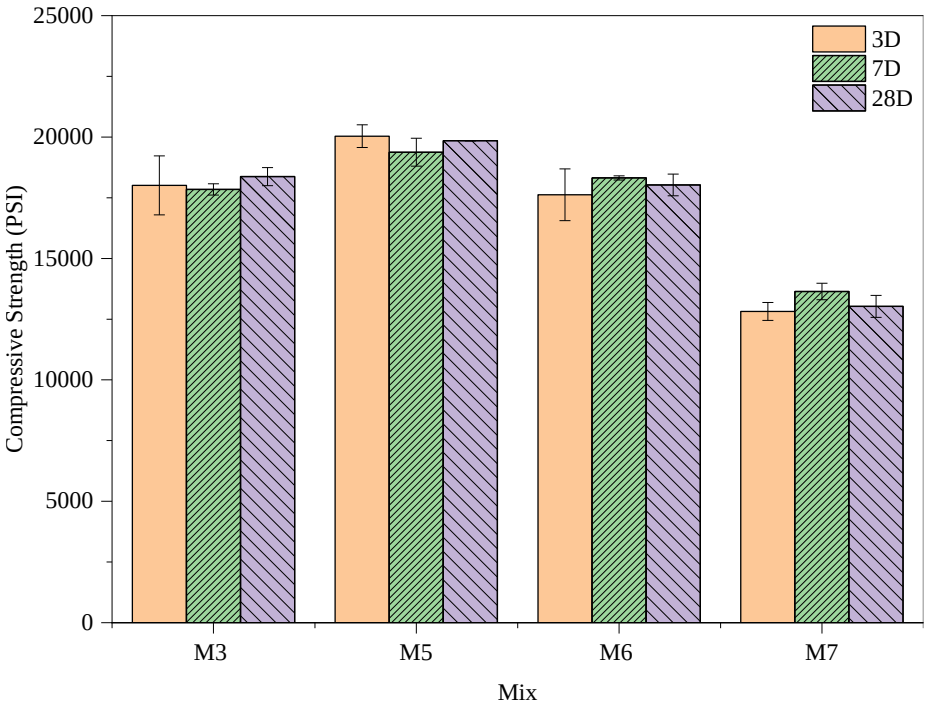


**Figure 5.12: Compressive strength of UHPC under steam curing**

5.3.2.C Development of compressive strength in the presence of different fibers

The results from steam curing indicate that Mix 5 is the best-performing UHPC mix, which was further considered for the use of different micro-fibers i.e., PVA fiber, glass fiber, and basalt fiber. The characterizations of dimension, tensile strength, and microstructure of these fibers are presented in Chapter 2. These three fibers were used to replace the micro-steel fiber and their performance was compared. Figure 5.13 shows the compressive strength of Mix 5 containing four different types of fibers. It can be seen that the use of micro-streel fiber resulted in the highest 3-day and 7-day strength of 20,037 psi and 19,375 psi, respectively, among the four groups. When replacing the micro-steel fiber with PVA fiber, the 3-day and 7-day strength decreased by 8% and 31.32%, respectively. The use of basalt fiber decreased the 3-day and 7-day compressive strength by 49.82% and 28%, respectively. When glass fiber is used the 3-day and 7-day compressive strength decreased by 54.20% and 66.11%, respectively. Compared with the 28-day strength of the UHPC with micro-steel fibers, the groups with PVA fibers, glass fibers, and basalt fibers yielded 27.40%, 44.40%, and 46.37% lower strength, respectively. In addition, the 28-day strength of these groups is lower than their 7-day strength. The decreased strength after replacing micro-steel fiber with other fibers (i.e., PVA, glass, and basalt fibers) might be due to the less effective crack bridging role as they show smaller diameters and also the poor dispersion as clusters were observed, which might increase the porosity of UHPC matrix.

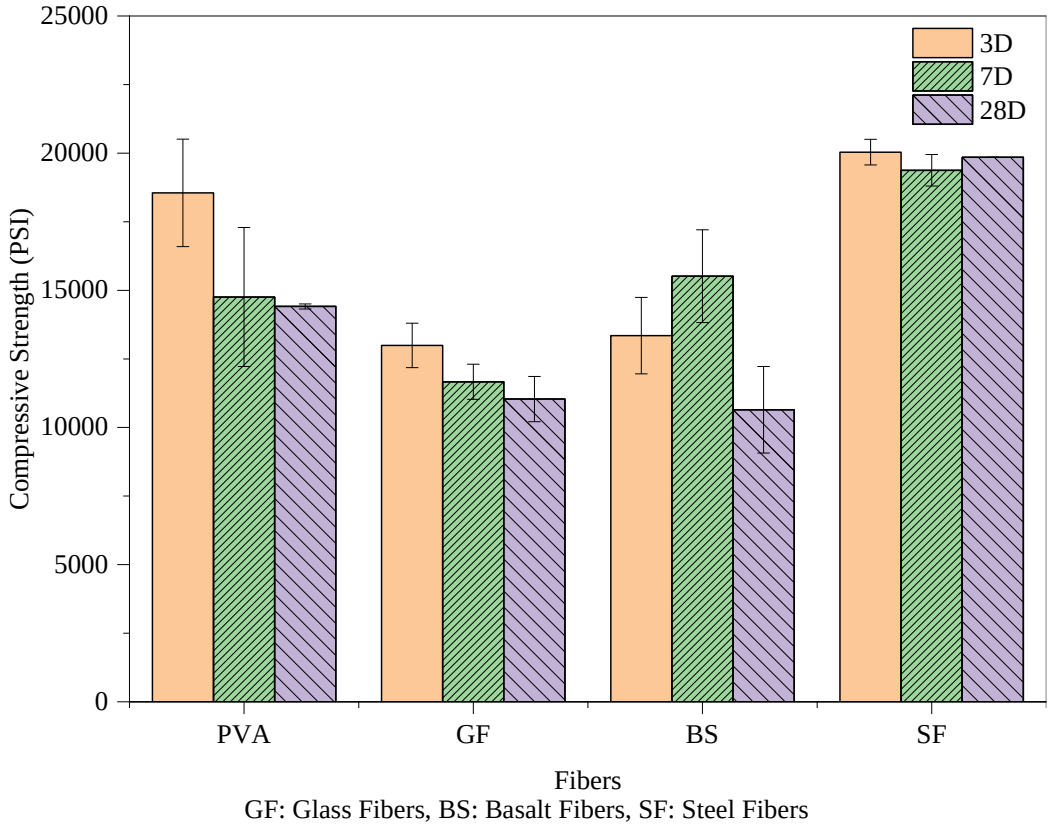


GF: Glass Fibers, BS: Basalt Fibers, SF: Steel Fibers

**Figure 5.13: Compressive strength of UHPC with different fibers under steam curing**

### 5.3.3. Flexural Strength

Based on the compressive strength development, four UHPC mixes were selected for the investigation of flexural performance, i.e., Mix 1, Mix 3, Mix 5, and Mix 6 cured in both the regular lime water curing and steam curing conditions were selected for the flexural test. It was observed that, in agreement with the development of compressive strength, the regularly cured beam samples showed lower flexural strength as compared to the steam-cured beams.

#### 5.3.3.A Load-deflection curves

The load-deflection curves are the direct data obtained from the flexural tests. It is well known that concrete is a brittle material with extremely low ductility. Without fiber reinforcement, a sudden failure would occur under flexural loading once a crack is formed. In the presence of fiber, post-cracking behavior can be triggered by the energy-consuming fiber pull-out process and the crack bridging of the fibers. Different from regular concrete, UHPC is a type of fiber-reinforced high-ductile cementitious composite. Due to the high volume fraction of fibers, dense structure, and absence of gravels, UHPC exhibits higher toughness and loading capacity under tension, thereby outperforming conventional concrete in flexural tests. In this study, the load-deflection curves obtained from the 3-point flexural test at 7 days and 28 days are analyzed. The specimens cured under two conditions, i.e., the regular lime water curing and steam curing, were tested. A linear relationship between the load and deflection followed by a non-linear ascending stage until the peak load was observed, after which a gradual saw-teeth-like descending stage [201] was exhibited. The selected UHPC groups reinforced with micro-steel fiber, PVA fiber, basalt fiber, and glass fiber were investigated.

##### 5.3.3.A.1 UHPC reinforced with micro-steel fibers

Figures 5.14a and 5.14b show the load-deflection curves of the four UHPC groups under the 3-point flexural test after 7 days under regular lime water curing. It can be seen that, due to the incorporation of micro-steel fibers, all the UHPC groups showed ductile behavior under flexural loads with post-cracking loading capacities. Compared with Mix 1, the two beams of Mix 3 exhibited lower peak loads indicating the benefit of Type III cement in strength gain of UHPC, which is in agreement with the observation from the compressive strength tests. As discussed above, the difference between Mix 3 and Mix 5 lies in the type of fly ash, where Class C fly ash was used in Mix 3 and Class F fly ash was used in Mix 5. It was observed that Mix 5 exhibited similar flexural behavior with Mix 1 with comparable peak loads. The higher loading capacity of Mix 5 over Mix 3 agrees with the results obtained from the compression test of the steam-cured cubes, in which the higher reactivity and more effective strength-enhancing role of Class F fly ash than Class C fly ash was again observed. Mix 6 exhibited lower peak loads than Mix 5, which might be due to the less effective role of metakaolin than silica fume as discussed in the compression strength section. The comparison between Mix 6 and Mix 3 indicates that the combination of metakaolin and silica fume works better than that of Class C fly ash and silica fume.

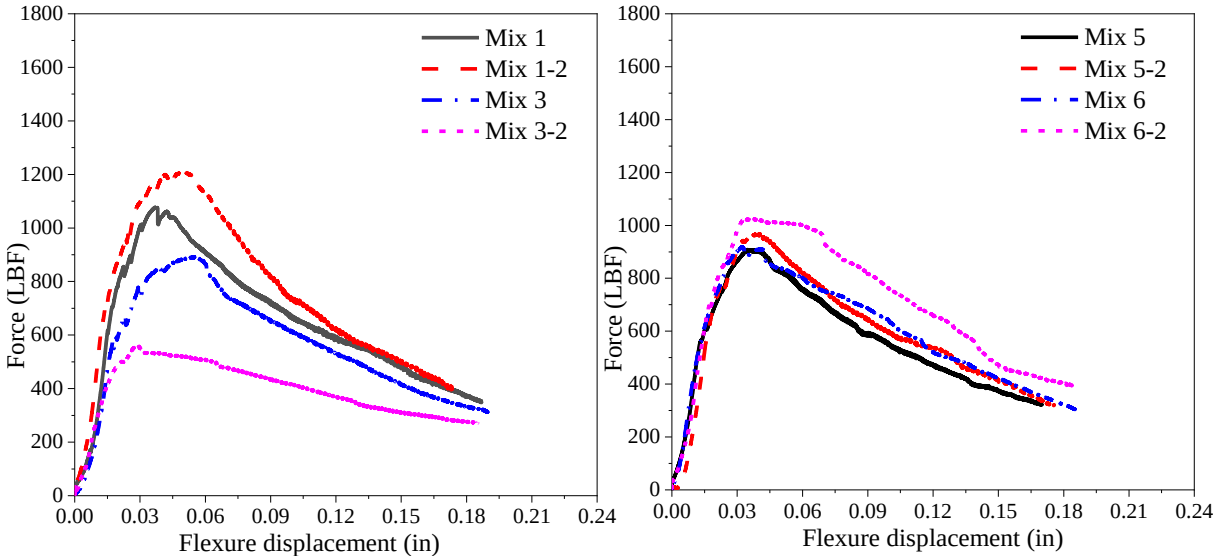


(a) Mix 1 and Mix 3, and (b) Mix 5 and Mix 6

**Figure 5.14: 7-day load-deflection curves of the regularly cured UHPC**

Figures 5.15a and 5.15b show the load-deflection curves of the four UHPC groups under the 3-point flexural test after 28 days under regular lime water curing. From the above-mentioned discussion on the use of steel fiber, it is clear that it helps to improve the flexural strength of UHPC. Compared with Mix 1, the two beams of Mix 3 exhibited slightly lower peak loads. As discussed above, the difference between Mix 3 and Mix 5 lies in the type of fly ash, where Class C fly ash was used in Mix 3 and Class F fly ash was used in Mix 5. It was observed that Mix 3 exhibited slightly higher peak loads than any other mixtures. The slightly higher loading capacity of Mix 3 over Mix 5 agrees with the results that the higher reactivity and more effective strength-enhancing role of Class C fly ash than Class F fly ash was observed. Mix 3 exhibited higher peak loads than Mix 6, which might be due to the lesser effective role of metakaolin than silica fume. The comparison between Mix 6 and Mix 3 indicates that the combination of Class C fly ash and silica fume works better than that of metakaolin and silica fume

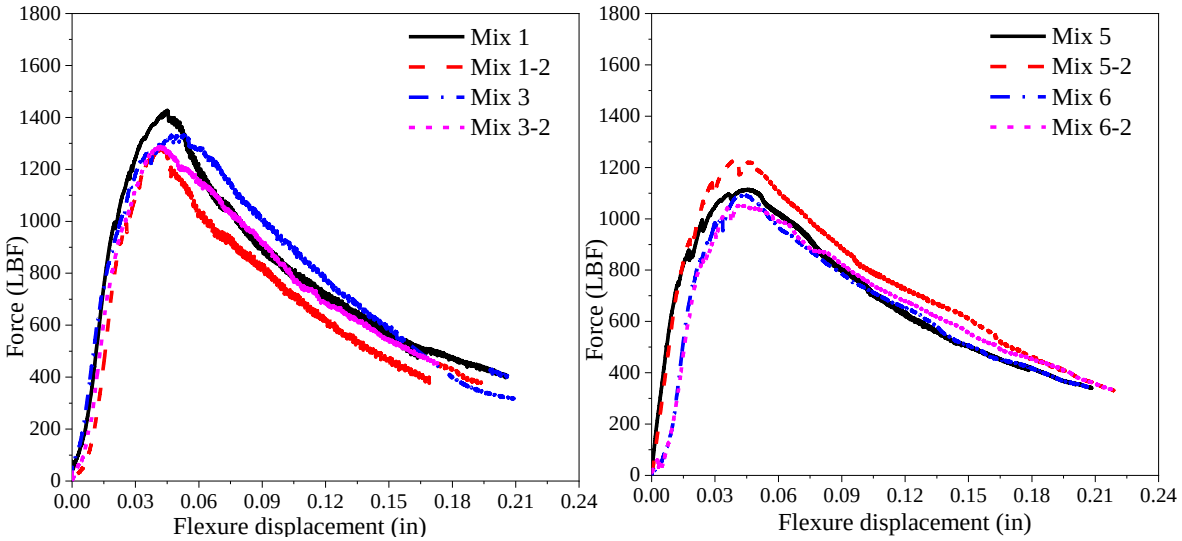


(a) Mix 1 and Mix 3, and (b) Mix 5 and Mix 6

**Figure 5.15: 28-day load-deflection curves of regularly cured UHPC**

Figures 5.16a and 5.16b show the load-deflection curves of the four UHPC groups under the 3-point flexural test after 7 days under steam curing. Compared with the curves shown in Figure 5.14, the steam-cured UHPC specimens exhibited higher overall loading capacities, which is in agreement with the development of compressive strength. The elevated temperature and relative humidity in steam curing help accelerate the hydration and strength of UHPC, in which the cement cannot fully hydrate in the presence of the extremely low water-to-cement ratio. Similar to the observations from regular cured samples, compared with Mix 1, the two beams of Mix 3 exhibited slightly lower peak loads. The comparison between Mix 3 and Mix 5 indicates the higher reactivity and more effective strength-enhancing role of Class F fly ash than Class C fly ash. Mix 3 exhibited higher peak loads than Mix 6, which might be due to the effective role of Class C fly ash than metakaolin.

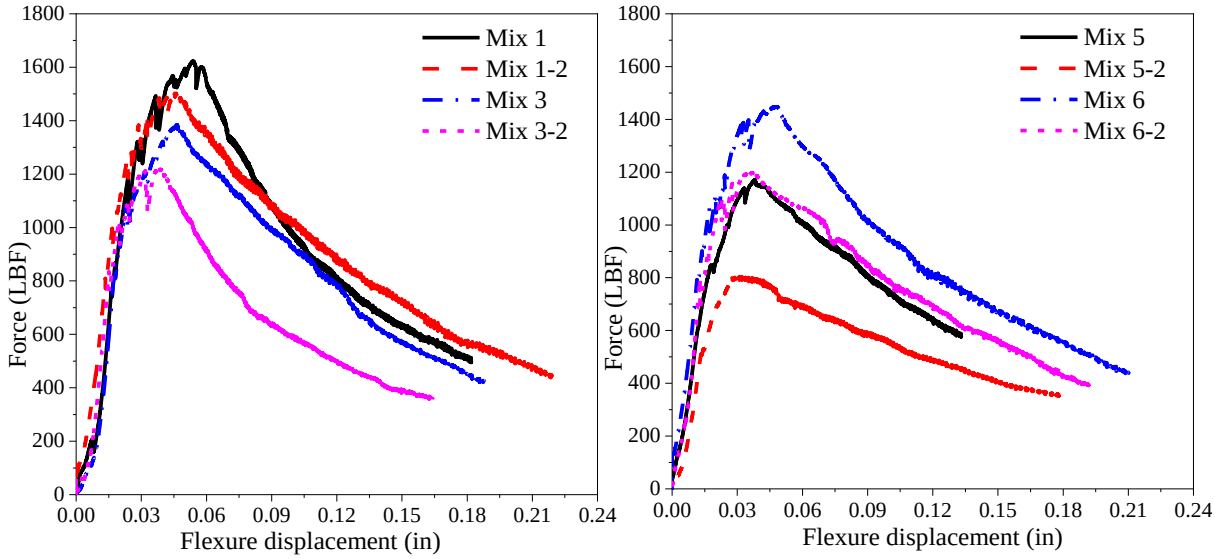


(a) Mix 1 and Mix 3, and (b) Mix 5 and Mix 6

**Figure 5.16: 7-day load-deflection curves of steam-cured UHPC**

Figures 5.17a and 5.17b show the load-deflection curves of the four UHPC groups under the 3-point flexural test after 28 days under steam curing. Again, by comparing with Mix 1, Mix 3 exhibited slightly lower peak loads. As discussed above, the difference between Mix 3 and Mix 5 lies in the type of fly ash, where Class C fly ash was used in Mix 3 and Class F fly ash was used in Mix 5. It was observed that Mix 5 exhibited slightly higher peak loads than Mix 3. Mix 6 exhibited lower peak loads than Mix 3, which might be due to the more effective role of silica fume and Class C fly ash than metakaolin under steam curing.

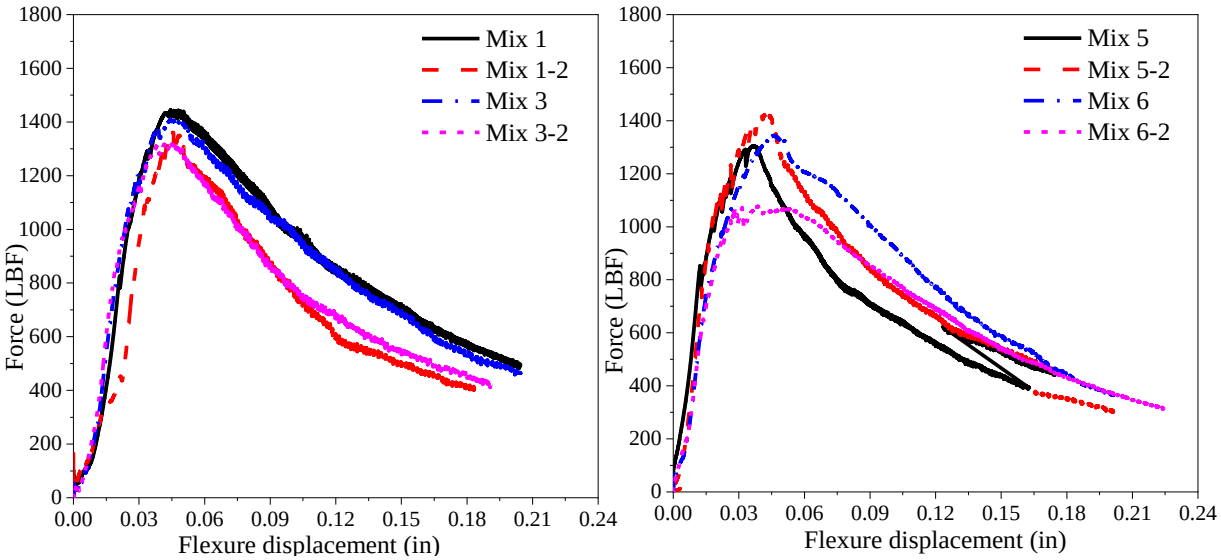


(a) Mix 1 and Mix 3, and (b) Mix 5 and Mix 6

**Figure 5.17: 28-day load-deflection curves of steam-cured UHPC**

5.3.3.A.2 UHPC reinforced with PVA fibers

Figures 5.18a and 5.18b show the load vs deflection curves of Mix 5 with PVA fibers under 3-point flexural strength after 7 days and 28 days of steam curing, respectively. Different from the UHPC specimens reinforced with the micro-streel fibers, it is seen that the load-carrying capacity of PVA fiber-reinforced UHPC drops suddenly after achieving the peak load for both curing ages. This might be due to the poor bond between the PVA fibers and the cementitious binders [202]. Although the two samples at each age exhibited slightly different flexural behavior, the samples after 28 days carried more peak loads than those after 7 days of curing.

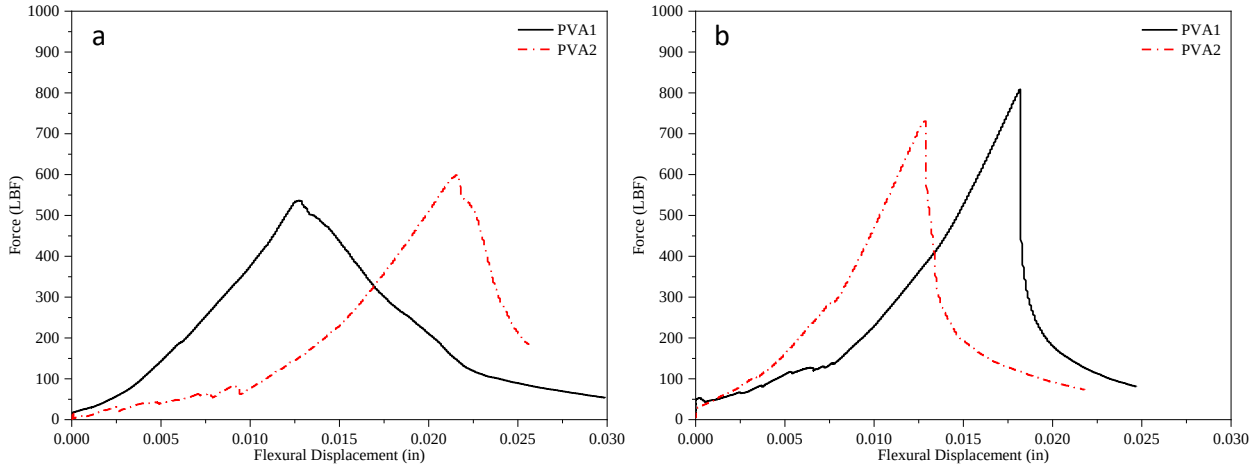


(a) 7-day and (b) 28-day flexural tests

**Figure 5.18: Load-deflection curves of steam-cured UHPC with PVA fiber**

5.3.3.A.3 UHPC reinforced with basalt fibers

Figures 5.19a and 5.19b show the load vs deflection curves for Mix 5 using basalt fibers under 3-point flexural strength after 7 days and 28 days of steam curing, respectively. Similar to the observations from PVA fiber-reinforced UHPC, the load-carrying capacity of basalt fiber-reinforced UHPC dropped suddenly after achieving the peak load for both curing ages. Compared with the steel fiber-reinforced UHPC, which yielded an average 7-day peak load of 1,225 lbf, the UHPC beams reinforced with PVA fibers showed a 656.68 lbf lower peak load. In addition, the UHPC with basalt fibers exhibited a slightly lower peak load than that with PVA fibers. Similarly, basalt fiber-reinforced UHPC yielded approximately 690 lbf and 30 lbf lower peak loading capacity than that with micro-steel fibers and PVA fibers, respectively.

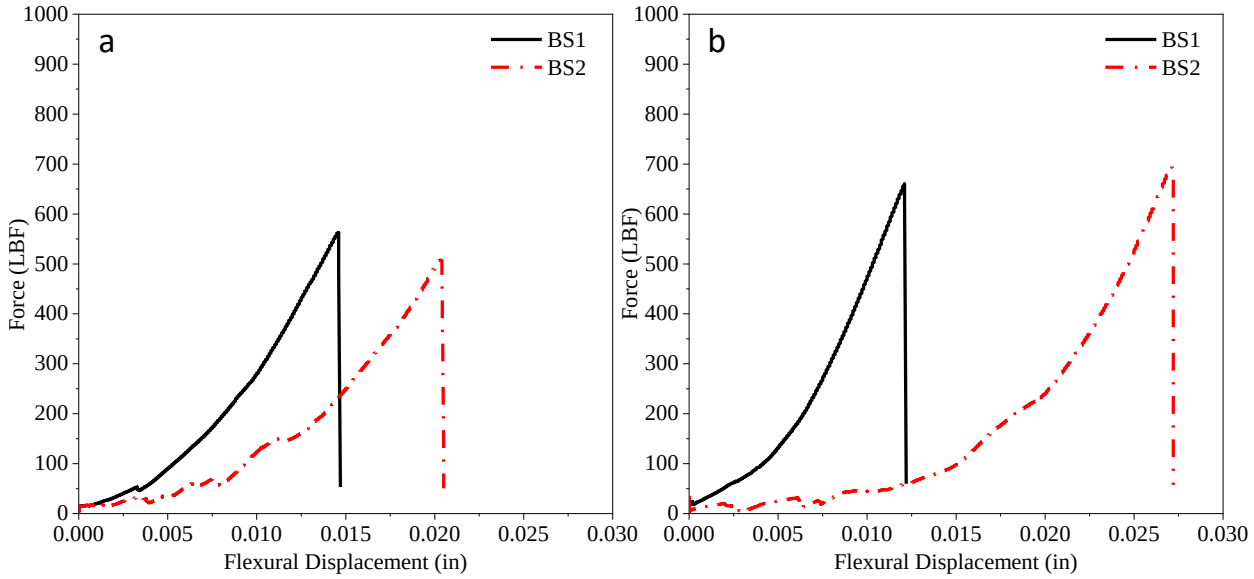


(a) 7-day and (b) 28-day flexural tests

**Figure 5.19: Load-deflection curves of UHPC with Basalt fibers**

5.3.3.A.4 UHPC reinforced with glass fibers

Figures 5.20a and 5.20b show the load vs deflection curve for Mix 5 using glass fibers under 3-point flexural strength after 7 days and 28 days of team curing, respectively. In line with the observations from the UHPC specimens reinforced with PVA fibers and basalt fibers, the load-carrying capacity of glass fiber-reinforced UHPC drops suddenly after achieving the peak load for both curing ages. After 7 days, the UHPC with glass fibers yielded an average peak load of 688 lbf, which is 43.88% lower than that with micro-steel fibers but 17.50% and 22.22% higher than that of the UHPC with PVA and basalt fiber, respectively. After 28 days, the UHPC beams reinforced with glass fiber yielded an average peak load of 793.18 lbf, which is 35% lower than the UHPC with micro-steel fibers but 2.95% and 14.60% higher than that of the UHPC with basalt and PVA fibers, respectively. The post-cracking behavior obtained from the load-deflection curves indicates that glass fibers provided a more effective reinforcing role than basalt and PVA fiber to improve the toughness of UHPC. This might be due to the effective bonding and pull-out behavior of glass fibers in the matrix of UHPC, which helped consume energy during the flexural test.

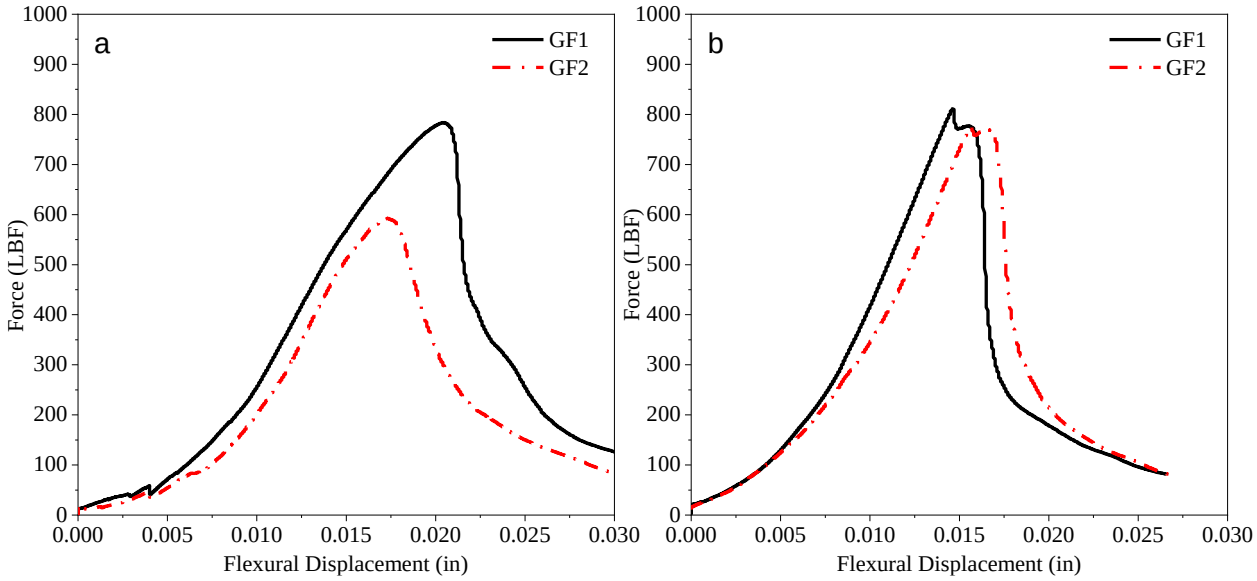


(a) 7-day and (b) 28-day flexural tests

**Figure 5.20: Load-deflection curves of UHPC with glass fibers**

The behavior of the non-steel fibers was drastically different than that of the mixes with the steel fibers. The UHPC with PVA, glass, and especially basalt fibers behaved much more brittle than the mixes with steel fibers and did not demonstrate any deflection hardening. The specimens behaved like conventional concrete, in that as soon as the specimen cracked the load dropped instantly and the deflection was extremely small when compared to the specimens with steel fibers. Following the drop in load the PVA and fiberglass specimens could still hold at least some load, whereas the basalt specimens did not hold any load after cracking and the test immediately came to an end. This means that the fibers could not take any significant flexural stresses. This is likely due to the low compatibility between the fiber and the cement matrix. This can be seen from the difference between the failure models UHPC reinforced with steel and non-steel fibers below. The steel fibers can be seen physically holding the two halves of the concrete together with a wide crack, while the

specimens with PVA and glass fibers exhibited extremely thin cracks. It was evident that only a few fibers extended across the gap and were not able to adequately withstand the tensile stresses. When the basalt specimen separated, no discernable fibers extended into the crack, which explains why the specimens failed so abruptly.

5.3.3.B Development of flexural strength

5.3.3.B.1 UHPC reinforced with micro-steel fibers

Based on the peak load obtained from the load-deflection curves, the average 7-day and 28-day flexural strength of each UHPC group after regular lime water curing and steam curing was determined. From Figure 5.21, it can be seen that a 7-day flexural strength of 2,710.05 psi under regular lime water curing was yielded by Mix 5, which is 17.87%, and 3.65% lower than that of Mix 1 and Mix 6, respectively. The 7-day flexural strength for Mix 1 is 57.21% higher than that of Mix 3. This is mainly due to the use of Type III cement, which accelerates the early strength gain. Mix 1 gained a flexural strength of 3,915 psi after 28 days, which is the highest amongst all four selected mixes and 3.47% higher than Mix 3. The 28-day flexural strength of Mix 1 is 15.35% and 26.13% higher than Mix 5 and Mix 6, respectively. The main difference between Mix 6 and Mix 5 lies in the use of metakaolin. It can be seen that the combination of metakaolin with Class C fly ash and silica fume can yield comparable early-age strength with the UHPC containing Class F fly ash and silica fume. From 7 days to 28 days, the flexural strength of Mix 5 increased by 25.24%. For Mix 3, the 28-day flexural strength is 80% higher than the 7-day strength gain. It can be stated that, although a lower 7-day strength was obtained from Mix 3, Class C fly ash along with silica fume can enhance the 28-day strength more significantly than Class F fly ash along with silica fume. A 10.5% strength increase was observed from Mix 6 from 7 days to 28 days.

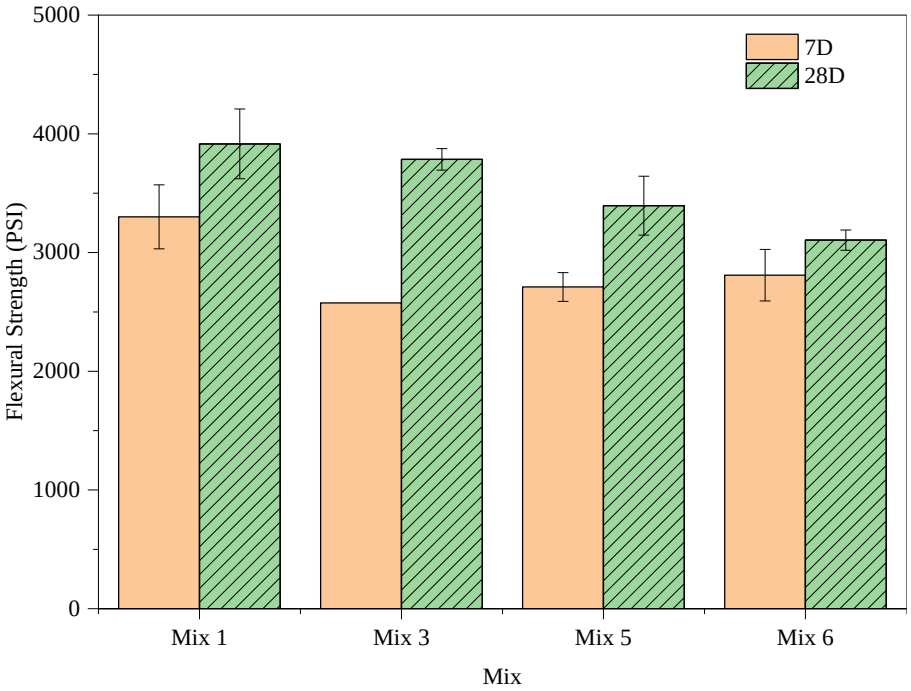


**Figure 5.21: Flexural strength of UHPC after regular curing**

Figure 5.22 shows the 7-day and 28-day flexural strength of the selected UHPC groups with 48 hours of steam curing. The 7-day flexural strength of Mix 1 reached 4,051.5 psi, which is 7.76%, 41.19%, and 15.90% higher than that of Mix 3, Mix 5, and Mix 6, respectively. After 28 days, the flexural strength of Mix 1, Mix 5, and Mix 6 showed a significant increase, which was also observed from the development of compressive strength of the steam-cured specimens. The 28-day flexural strength of the steam-cured Mix 1 is 4,515 psi, which is 14.47%, 14.40%, and 18.16% more than that of Mix 3, Mix 5, and Mix 6, respectively. Compared with Mix 3 and Mix 6, Mix 5 yielded 0.1% and 3.30% higher 28-day flexural strength, respectively, which is in line with the observations from the regularly cured specimens that Class C fly-ash can improve the flexural strength of UHPC more significantly than Class F fly-ash and the substitution of silica fume and fly ash with metakaolin is not helpful to increase the 28-day strength.

The comparison between the data shown in Figure 5.21 and Figure 5.22 indicates that steam curing is still an effective approach to enhance the strength gain of UHPC, which is in agreement with the compressive strength development. The steam-cured Mix 1 exhibited a 7-day flexural strength of 4,051 psi, which is 22.75% higher than that of the regular cured sample. Similarly, for Mix 3, Mix 5, and Mix 6, 79.07%, 5.13%, and 24.50% higher 7-day flexural strength was obtained from the steam-cured samples, respectively. A similar trend with less significant changes was also observed from the 28-day flexural strength results. The steam-cured Mix 1 yielded a 28-day flexural strength of 4,515 psi, which is 15.33% higher than that obtained from the regularly cured specimens. Likewise, after steam curing, the increase in the 28-day flexural strength of Mix 3, Mix 5, and Mix 6 is 4.22%, 16.30%, and 23.10%, respectively. These results indicate that, due to the extremely low water-to-cement (binder) ratio of UHPC, steam curing is an effective approach to enhance the hydration and pozzolanic reaction in the binder systems. It is worth noting that, although steam curing can help to increase both the early-age and later-age strength, its role is more significant for the gain of early-age strength.

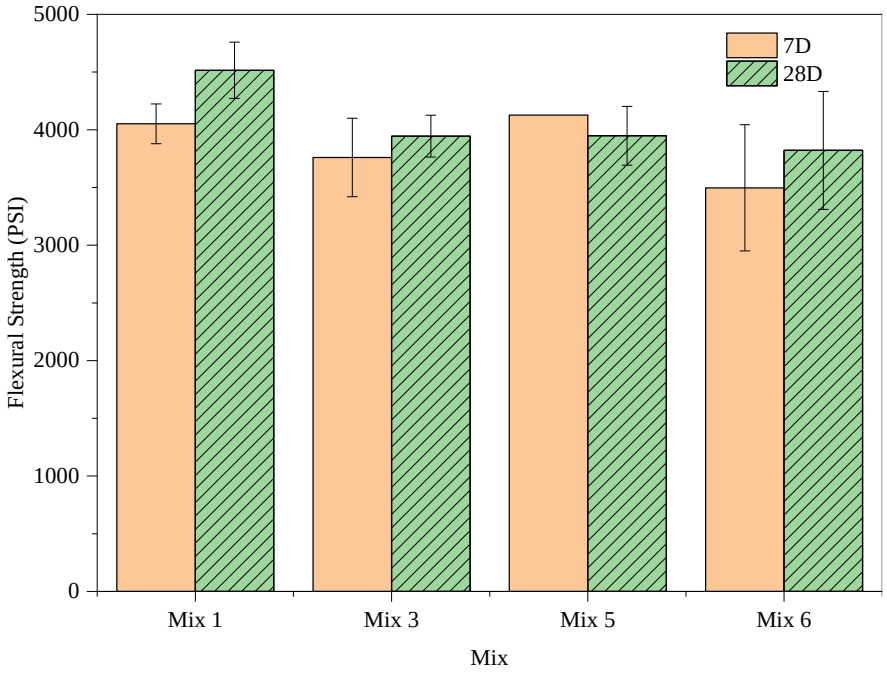


**Figure 5.22: Flexural strength of the steam-cured UHPC**

5.3.3.B.2 UHPC reinforced with basalt, PVA and glass fibers

Figure 5.23 shows the 7-day and 28-day flexural strength of UHPC with basalt, PVA, and glass fibers. From the result, it is observed that the average 7-day flexural strength of basalt, PVA, and glass fiber-reinforced UHPC is 1,546 psi, 1,641 psi, and 1,988 psi, while the average 28-day flexural strength of the UHPC beams with basalt fiber, PVA fiber, and glass fibers increased by 26%, 35%, and 15%, respectively. Compared with the UHPC with micro-steel fibers, the average 7-day flexural strength of UHPC reinforced with basalt fiber, PVA fiber, and glass fiber are 76%, 66%, and 37% lower, respectively. The same trend was also observed from the 28-day flexural strength, where the UHPC with micro-steel fibers is 40%, 22%, and 20% higher than that yielded by the UHPC with basalt fiber, PVA fiber, and glass fibers, respectively.

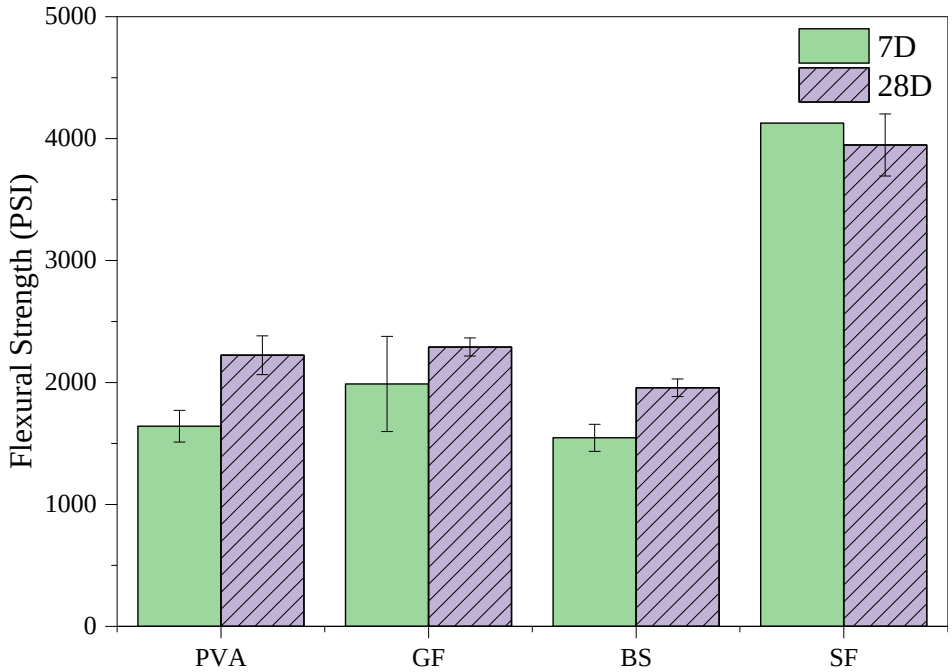


**Figure 5.23: Flexural strength of steam-cured UHPC**

5.3.3.C Failure mode analysis

5.3.3.C.1 UHPC reinforced with micro-steel fibers

Figures 5.24a and 5.24b show the crack zone of the micro-steel fiber-reinforced UHPC after the 3-point flexural strength test. From the figure, the micro-steel fibers bridging the major cracks can be clearly observed. The good bonding between the steel fiber and the UHPC matrix resulted in the elongation of the fibers in the cracking zone, which helps to transform the load and gives the beams a good load-carrying capacity and post-cracking behavior avoiding sudden failure. The well-distributed micro-steel fibers can be observed from the fiber avoiding the chances of agglomeration in the UHPC matrix.

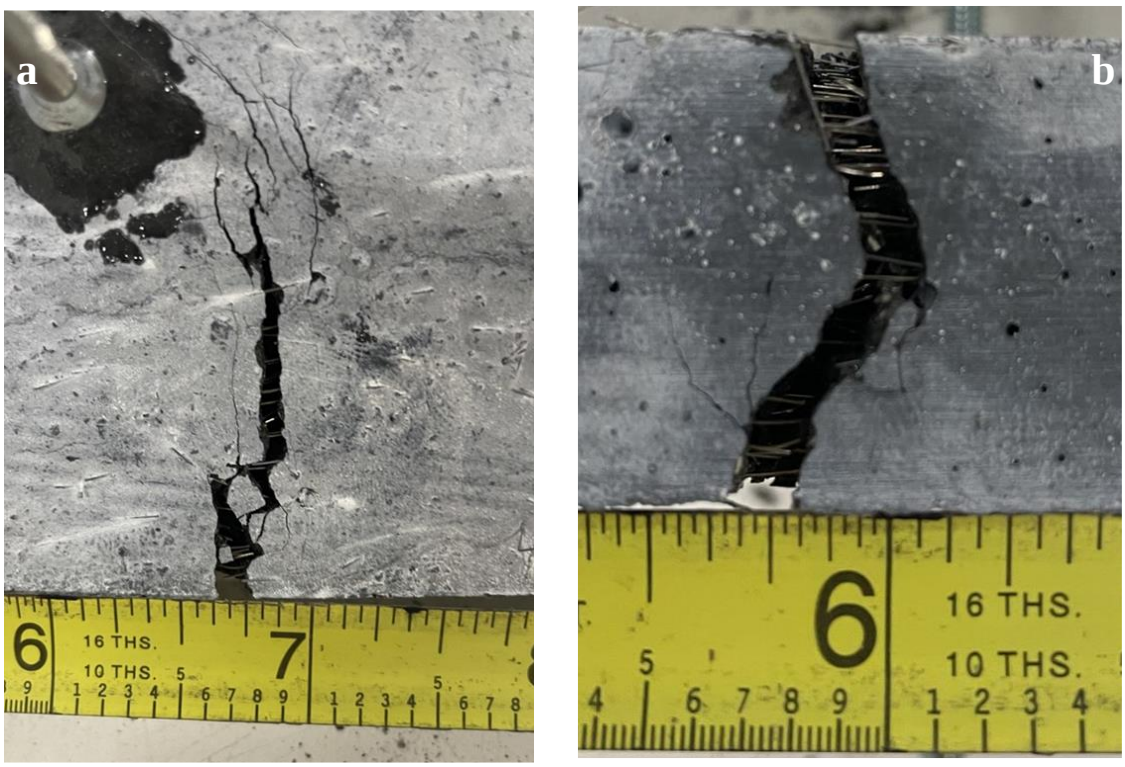


(a) side and (b) bottom views of the major cracks formed in micro-steel fiber-reinforced UHPC

**Figure 5.24: Cracks in UHPC after flexural test**

5.3.3.C.2 UHPC reinforced with basalt fibers

From Figures 5.25a, 5.25b, and 5.25c, it can be observed that the beam specimens reinforced with basalt fibers raptured after the 3-point flexural strength test with a clear fracture surface. Different from the UHPC with micro-steel fibers, the specimen with basalt fiber did not show the development of cracks with effective fiber bridging. Instead, the basalt fibers were broken or pulled out from the UHPC matrix. This might be due to the extremely small diameter and the smooth surface of the basalt fiber used in this study. And this is considered the primary reason for the sudden failure of the UHPC specimens once reaching their peak load. Since less energy was consumed from the easy pull out of the basalt fibers and there does not exist post-cracking behavior, the use of basalt fiber in the UHPC mix does not contribute to improving the flexural strength and toughness.

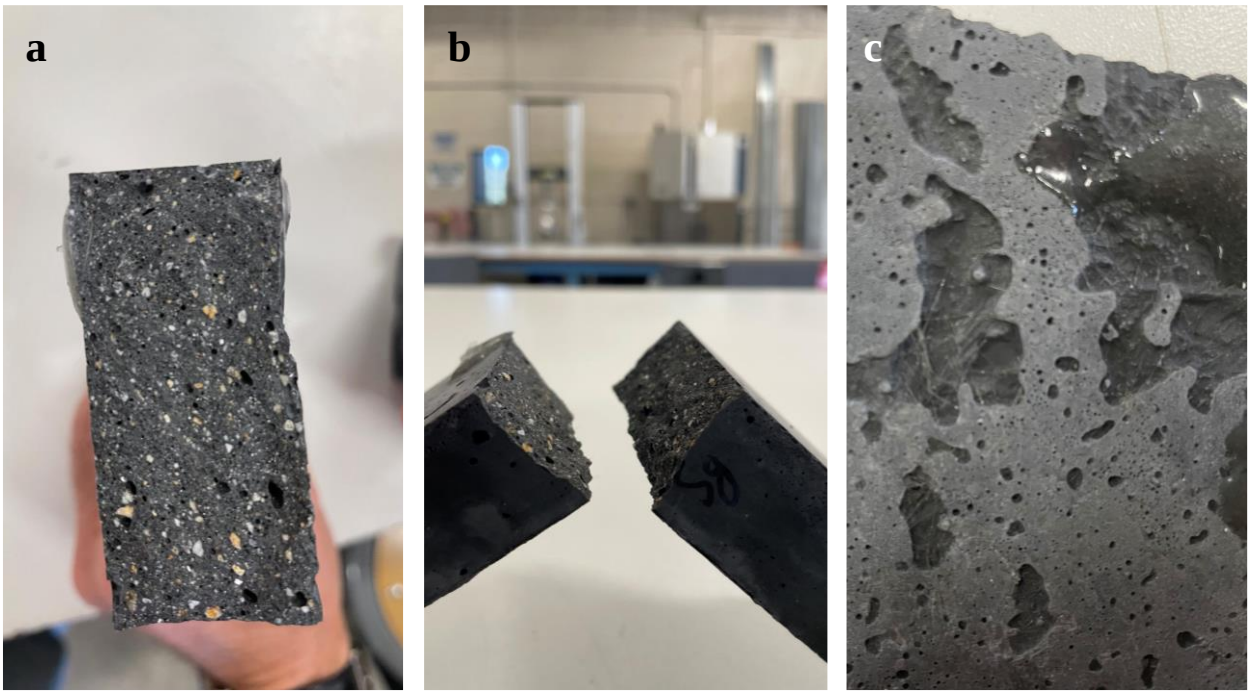


(a) and (b) fracture surface and (c) side surface of the UHPC beam specimen with basalt fibers after flexural test

**Figure 5.25: Surface of UHPC specimen**

5.3.3.C.3 UHPC reinforced with PVA fibers

Figures 5.26a, 5.26b, and 5.26c show the UHPC beam specimen with PVA fiber failed after the 3-point flexural strength test. Like the behavior of basalt fibers-reinforced UHPC, the use of PVA fibers in the UHPC mix did not result in gradual crack development. The PVA fibers were pulled out from the UHPC matrix and were not capable of bridging the cracks. Therefore, a sudden rapture occurred after reaching their peak loads. Due to the larger diameter, the pulled-out PVA fibers can be observed more easily than the basalt fibers from the fractured surface of UHPC beams. Even though the distribution of PVA fibers was seen to be better than basalt microfibers and PVA has a higher elongation rate than basalt fiber, the easy pull-out behavior makes it hard to improve the flexural strength and toughness of UHPC effectively.

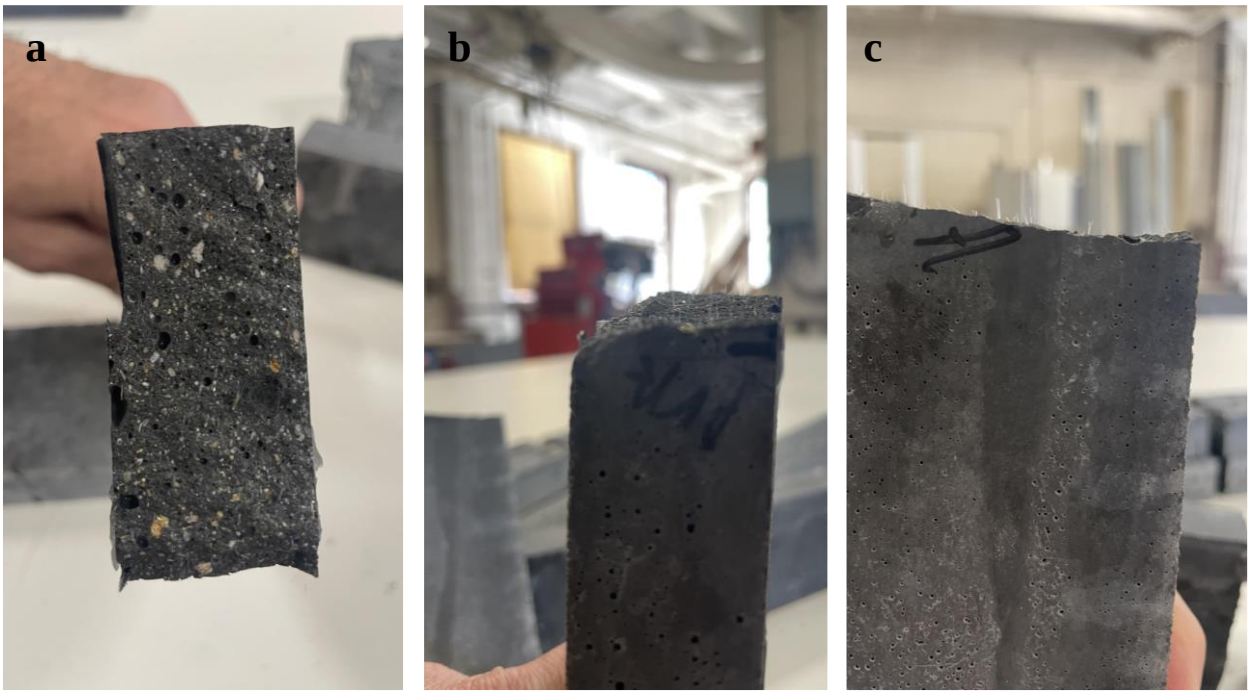


(a) Fracture surface of UHPC beam with PVA fibers, and (b) and (c) the pulled-out PVA fibers on the fracture surface of UHPC beams after flexural test

**Figure 5.26: Fracture surface of UHPC**

5.3.3.C.4 UHPC reinforced with glass fibers

From Figures 5.27a, 5.27b, and 5.27c, it can be observed that the beam specimen reinforced with glass fibers failed after the 3-point flexural strength test showed fracture surfaces with pulled-out fibers. Like the result of basalt and PVA fiber-reinforced UHPC, the use of glass fibers in the UHPC mix did not contribute to improving the flexural strength of UHPC. Due to the large number of fibers pulled out from the UHPC beam, more energy than that from basalt fiber and PVA fiber-reinforced UHPC was consumed due to the friction between the glass fibers and the matrix of UHPC. This explains the occurrence of post-racking behavior of the glass fiber-reinforced UHPC. Although the load kept decreasing after the peak load, the force didn't drop suddenly (see Figure 5.20). Given the failure modes, the morphology and the load-deflection curves obtained from the 3-point flexural tests, it is clear that the micro-steel fiber exhibited the most effective crack bridging and load transformation role in the UHPC when crack started forming and developed among the investigated fibers. Although the crack bridging role was not observed from glass fiber, its efficient pull-out behavior consumed more energy than basalt and PVA fibers. Therefore, the toughness of UHPC was slightly improved. Due to the poor bonding with the UHPC matrix, the reinforcing roles of basalt fiber and PVA fiber in UHPC are lower than that of glass fiber.

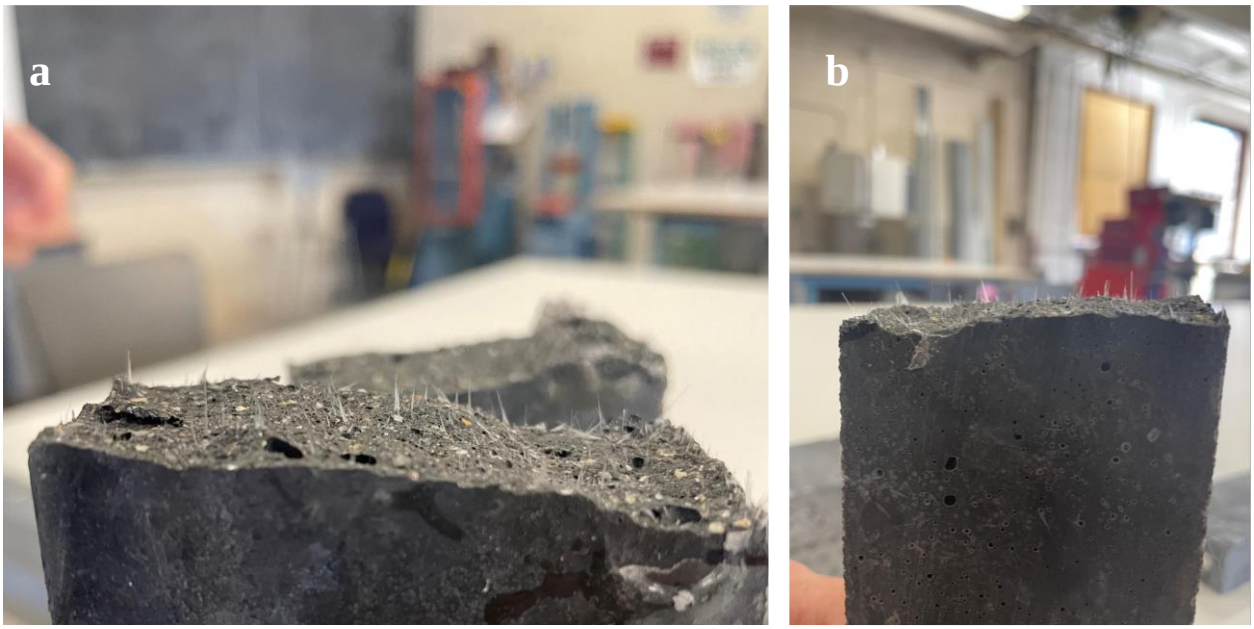


(a) and (b) Fracture surface of UHPC beam specimen with pulled-out glass fibers after flexural test

**Figure 5.27: Fracture surface of UHPC beam**

It is important to note how the crack propagated throughout the UHPC specimen. Initially, multiple cracks formed at the bottom of the specimen directly below the loading point (midspan). As shown in Figure 5.28, as the load increased, a single crack took the majority of the displacement, and the other cracks closed. At the end of the test, the crack ended up being anywhere from 0.125 in. wide to 0.25 in. wide. Steel fibers were observed to effectively enhance the post-cracking strength, deflection capacity, toughness, and cracking behavior of UHPC. The flexural behavior of UHPC is closely related to the crack propagation process, particularly in the post-cracking stage. After cracking, fibers inhibit the propagation of cracks by bridging fracture surfaces.

**Figure 5.28: Crack in UHPC beams under flexure loading**

Because of the randomness of the string potentiometer data, and since several times one or both sets of the data from the string potentiometers were not able to be used, some data manipulation had to be done. This consisted of averaging 10 data points so there was less noise in the data and shifting the data so that Young's Modulus lined up with zero. In the

cases where the string potentiometer data was not able to be used, the machine data was used. The two sets of data were verified as being interchangeable by comparing graphs where the potentiometer data was available. The shapes of the graphs were nearly identical, thus allowing the machine data to be used when necessary. Additional force-displacement graphs, testing data, and specimen images can be found at https://doi.org/10.7275/xgz6-se87.

### 5.3.4. Direct Tension Test

Due to the small deformations and the randomness of the string potentiometers, as well as the complexity of cementitious materials, there are certain differences among the two experimental curves for the specimens of each mix design and some manipulation of the data had to be done to shift the graphs to ensure that the elastic zone of each of the specimens started at zero strain and zero stress. Figure 5.29 features the idealized tensile response of UHPC. This behavior was only found in part of the specimens tested in this study, specifically the 28-day Mix 6-specimen 2 and 28-day Mix 1-specimen 2. Most of the other specimens followed a behavior shown in Figure 5.30, where the stress peaks and drops suddenly when the specimen cracks followed by a gradual strain softening. During this strain, softening fiber pullout occurs as the crack widens and fibers one by one pull out from the concrete. This can be seen in the curves in Figure 5.31, when a fiber pulls out, the stress drops suddenly then slowly increases again until another fiber pulls out leaving a jagged appearance to the curve.

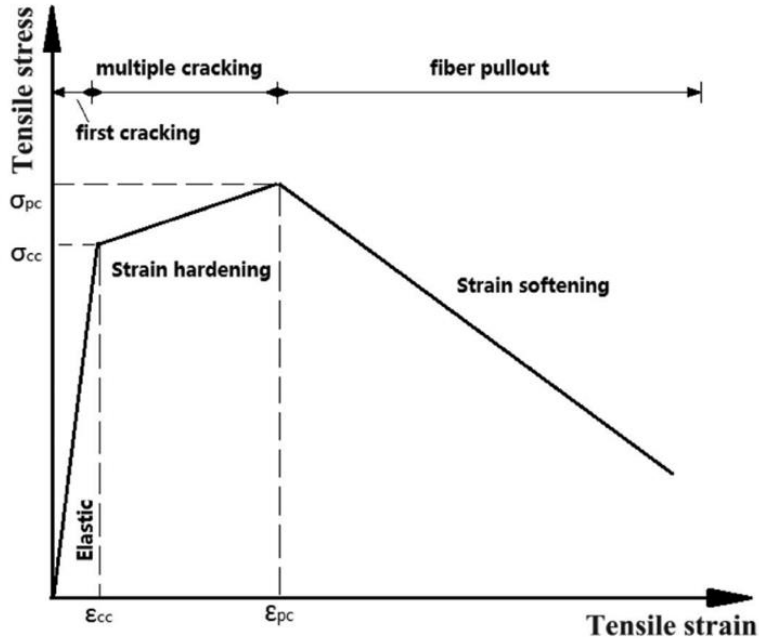


**Figure 5.29: Idealized simplified tensile response of UHPC from Zhou and Qiao (2020)**

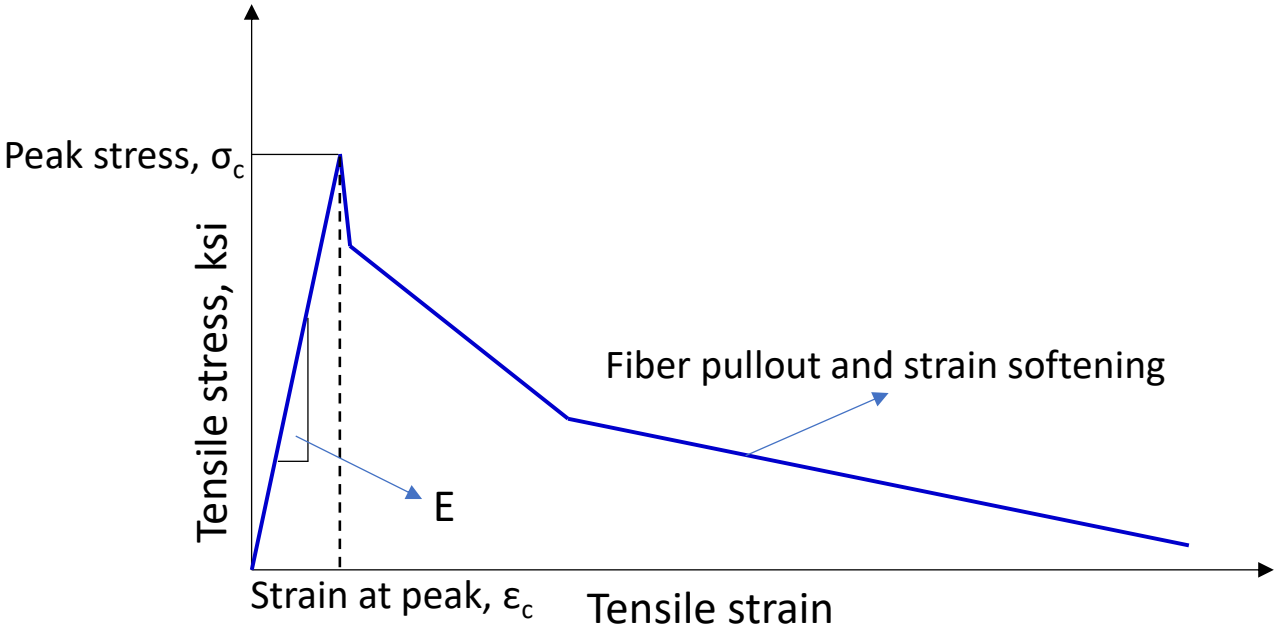


**Figure 5.30: Simplified observed tensile response of dog-bone specimens**

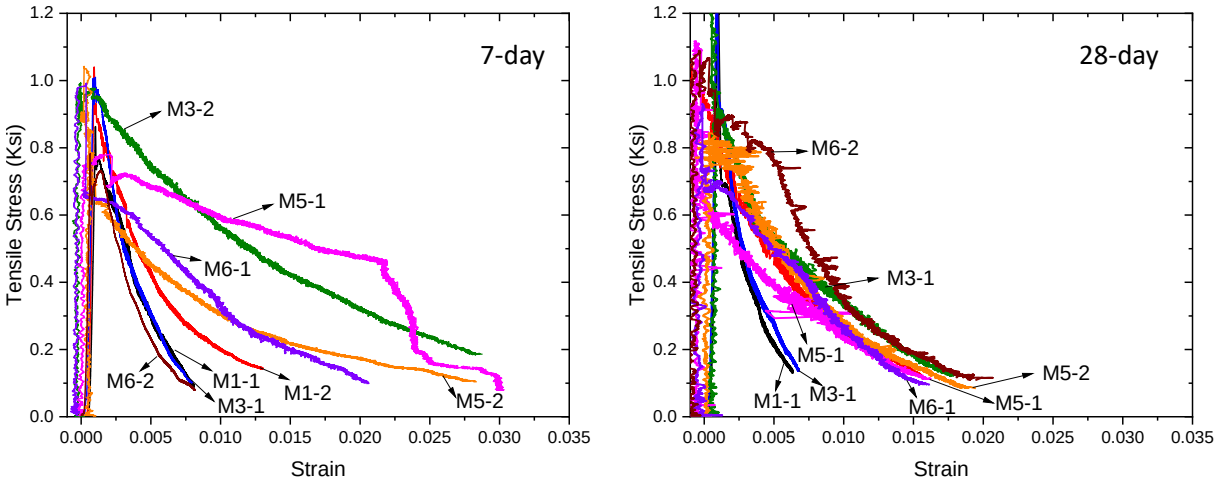


**Figure 5.31: Stress-Strain curves of UHPC under tension load**

Based on these curves, Three tensile material parameters, the peak tensile strength ($\sigma_c$), the tensile strain at peak strength ($\varepsilon_c$), and the tangent modulus of elasticity ($E_{cc}$), were extracted from each recorded stress–strain curves and these values for each specimen are summarized in Table 5.2.

**Table 5.2: Tensile material parameters from experiment**

| Mix, age, specimen | Max Force (kip) | $\sigma_c$ (ksi) | $\varepsilon_c$ (με) | E (ksi) |
|---|---|---|---|---|
| Mix 1, 7-day, specimen 1[1] | 1.997 | 0.968 | 42.0 | 2,308 |
| Mix 1, 7-day, specimen 2 [1] | 2.449 | 1.188 | 46.6 | 2,547 |
| Mix 1, 28-day, specimen 1[1] | 2.667 | 1.293 | 13.7 | 9,454 |
| Mix 1, 28-day, specimen 2 | 2.651 | 1.178 | 68.3 | 1,725 |
| Mix 3, 7-day, specimen 1[1] | 2.281 | 1.106 | 70.4 | 1,571 |
| Mix 3, 7-day, specimen 2 | 2.362 | 1.050 | 46.6 | 2,253 |
| Mix 3, 28-day, specimen 1 [1] | 2.775 | 1.346 | 90.5 | 1,487 |
| Mix 3, 28-day, specimen 2 | 2.696 | 1.198 | 54.7 | 2,190 |
| Mix 5, 7-day, specimen 1 | 1.766 | 0.785 | 221.1 | 355 |
| Mix 5, 7-day, specimen 2 | 2.408 | 1.070 | 21.5 | 4,988 |
| Mix 5, 28-day, specimen 1 | 2.514 | 1.117 | 10.9 | 10,264 |
| Mix 5, 28-day, specimen 2 | 1.899 | 0.844 | 39.4 | 2,139 |
| Mix 6, 7-day, specimen 1 | 2.294 | 1.019 | 67.4 | 1,513 |
| Mix 6, 7-day, specimen 2 [1] | 1.888 | 0.916 | 46.3 | 1,977 |
| Mix 6, 28-day, specimen 1 | 2.093 | 0.930 | 4.2 | 28,978 |
| Mix 6, 28-day, specimen 2 | 2.451 | 1.089 | 48.0 | 2,268 |

Note: [1] = failed outside of center region, thus machine data used for strain values

As seen in Table 5.2, the tensile strength at 7 days ranges from about 0.785 to 1.188 ksi while the values are in the range of 0.844 to 1.346 ksi at 28 days with an average increase of around 11% from the tensile strength at 7 days to 28 days. Mix 3 shows the greatest tensile strength values at both 7 and 28 days which might be due to the effect of Class C fly ash on strength development. Employing Class F fly ash typically leads to a decelerated initial strength gain, while the incorporation of Class C fly ash doesn't exhibit this delay and might bolster early strength development [203]. The key distinguishing factor between Class F and Class C fly ashes lies in their calcium (Ca) content, with Class F fly ash containing less than 18% Ca, whereas Class C fly ash boasts a higher Ca content, surpassing the 18% threshold [204]. This elevated calcium content in Class C fly ash contributes to additional hydration reactions, thereby enhancing the development of strength. The second high tensile strength values are observed in the specimens of Mix 1, where the incorporation of Type III cement and micro-fly ash might be the most significant reasons for this phenomenon. Type III cement results in a rapid strength gain at the age of less than 90 days and micro-fly ash with a smaller particle size than Class F and Class C fly ashes leads to a denser and stronger UHPC mixture. As seen in Table 5.2, the elastic modulus values at 28 days are about 234% higher than those at 7 days on average which is much higher than the difference between the tensile strength values of 7 and 28 days. This might be attributed to the specimens that are not broken in the middle region and the compliance issue with the data collected by the strain potentiometers.

In summary, direct tension tests of 16 dog-bone specimens were conducted to determine the tensile strength of UHPC mixes. The concrete used for the dog-bones specimens were Mix 1, Mix 3, Mix 5, and Mix 6. The primary objectives of the tests were to determine the tensile strength of these mixes at both 7 days and 28 days. The specimens were designed based on research by Zhou and Qiao [198] and tested under direct tension in an Instron machine at UMass Amherst. During the tests, cracks formed mainly within the desired region. However,

some failed outside this region. The specimens were tested by displacement-controlled loading until experiencing failure and stopped when the load reached 10% of the maximum loading allowing for complete stress–strain curves to be recorded. Based on the results of the tests, UHPC can be seen as having high tensile strength, with Mix 1 and Mix 3 performing the best reaching a 28-day tensile strength of over 1,200 psi. The results also indicate that the specimen design should be improved to account for the loss of area within the wider sections due to the location of the bolts at the end of the threaded rods.

### 5.3.5. Mechanical Properties of FRC

5.3.5.A Compressive strength

The compression test results show that the Enduro Prime and Novocon XR fibers performed the best, as seen in Figure 5.32. They both reached compressive strengths greater than 5,000 psi, much higher than the design strength of the mix which was 4,000 psi. Since both these fibers are crimped, it can be theorized that the shape of the fibers plays an important role in the compression strength of the concrete, and that crimped or corrugated fibers perform better than straight or hooked fibers.

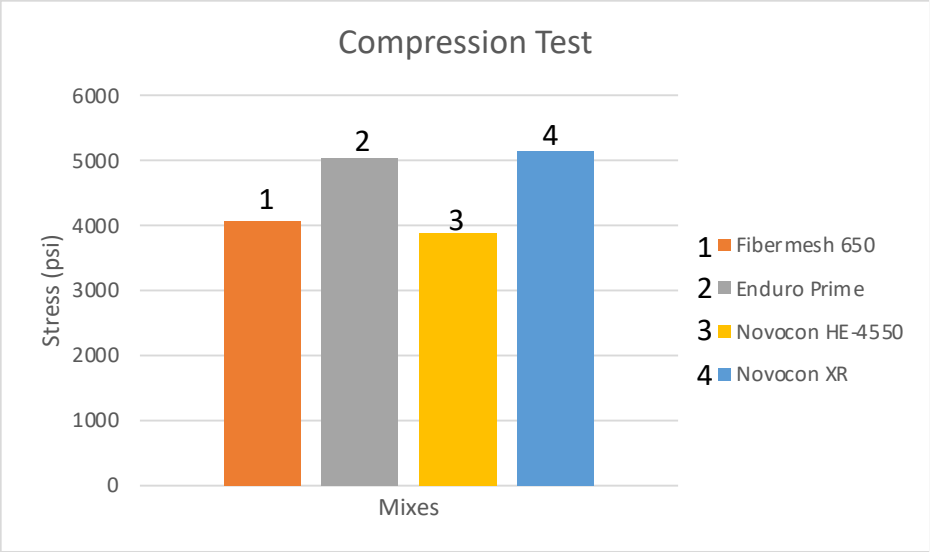


**Figure 5.32: 28-day compressive strength of FRC mixes**

5.3.5.B Splitting tensile strength

The splitting tensile results, seen in Figure 5.33, show that the steel fibers, mixes 3 and 4, perform better than the polypropylene fibers of Mix 1 and Mix 2. It can also be observed that the corrugated fibers, Mix 2 and Mix 4, resulted in slightly higher tensile strengths than the other fibers made of the same material, Mix 1 and Mix 3.

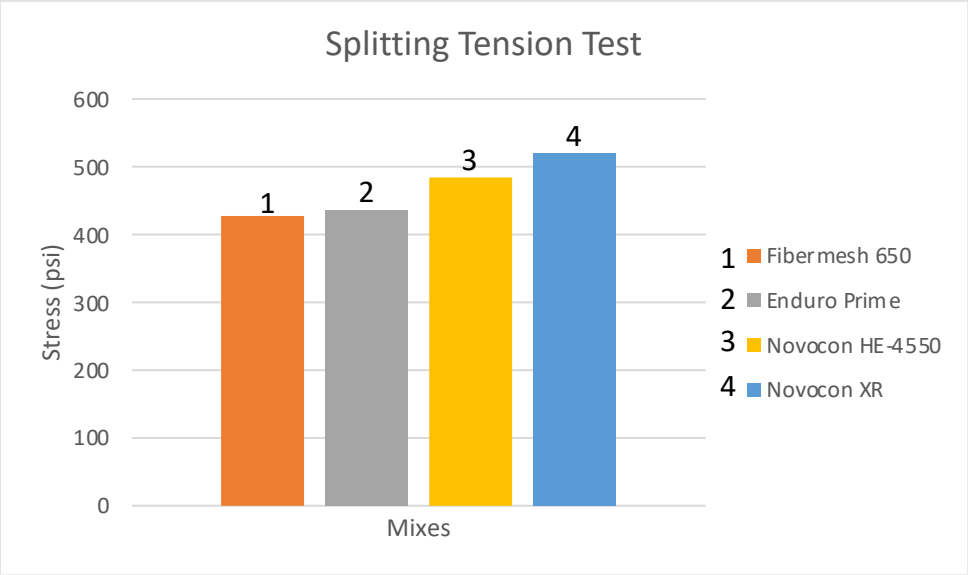


**Figure 5.33: 28-day splitting tensile strength of FRC mixes**

5.3.5.C Flexural strength

Similar to the splitting tensile test results, the flexure test results, found in Figure 5.34, show that again the steel fibers perform better than the polypropylene fibers. Additionally, the difference in the fiber shape is more pronounced in flexure test than the splitting tensile test. Both the corrugated fibers resulted in higher flexural strengths than the straight and hooked fibers for their respective material. The higher values of the flexural test are explained due to the fact that the FRC is unlikely to be homogenous. This causes there to be areas in the plane to be weaker and when subjected to only tensile forces under which all the fibers in the material are at the same stress and failure will initiate when that weaker point reaches its limiting tensile stress. Whereas in flexural tests only the extreme fiber is subjugated to the peak stresses and if that area does not have any weaknesses, the strength is determined by a stronger part.

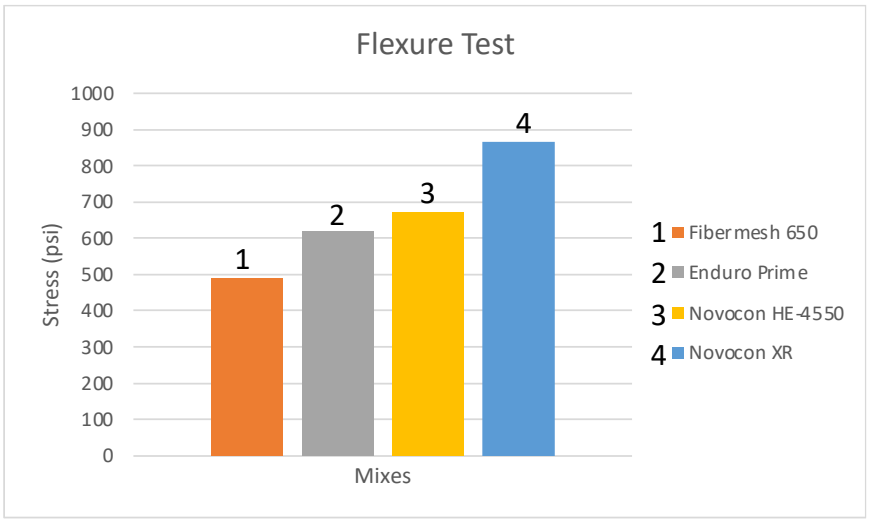


**Figure 5.34: 28-day flexural strength of FRC mixes**

### 5.3.6. Permeability

5.3.6.A Permeability of UHPC

The concrete durability can be impacted by the transport property, which can provide a path for external moisture and salts. The transport of ions, such as $Cl^-$, $SO_4^{2-}$, $OH^-$, and alkali ions through concrete pores or cracks can induce a variety of deteriorations, such as corrosion, sulfate attack, carbonation, and ASR. To evaluate the permeability of concrete, electrical bulk resistivity is commonly measured, where a high electrical bulk resistivity indicates low permeability. For the evaluation of electrical resistance, the concrete cylinder is connected with two electrodes on top and bottom to determine the transportation of free electrons in UHPC. Electrical resistivity can be affected by many parameters such as moisture content, ion motion, ion concentration, pore structure, and connectivity in concrete. To investigate the bulk resistivity of UHPC mixes, 3 by 6-in. cylinders of the UHPC mixes as mentioned in Chapter 3 were cast, cured, and compared with the bulk resistivity of regular concrete under the same curing condition [205]. To avoid the influence of steel fiber on the measurement of bulk resistivity, plain UHPC matrix without fibers were used in the permeability test. Figure 5.35 shows the bulk resistivity (kΩ-cm) of the seven UHPC groups along with the bulk resistivity of regular concrete. For each group, 2 cylinders are tested for bulk resistivity. From the results, it can be observed that the maximum average bulk resistivity of 120.1 kΩ-cm was yielded by Mix 1, which is in the "very low" chloride penetration range according to [206] (see Table 5.3). This high bulk resistivity indicates the low permeability of Mix 1, which eventually indicates high durability. The bulk resistivity of Mix 2 and Mix 3 is 34.64% and 82.43% lower than the bulk resistivity of Mix 1, respectively, which are still in the "very low" range. The difference between Mix 2 and Mix 3 is the use of UFFA along with silica fume and Class C fly ash. The bulk resistivity of Mix 5 is 60.86 kΩ-cm, which is 193% higher than Mix 4. The difference between Mix 4 and Mix 5 is the use of UFFA along with Class F fly ash and silica fume. From the comparisons between Mix 4 and Mix 5, as well as that between Mix 2 and Mix 3, the incorporation of UFFA can help to reduce the pore connectivity in UHPC in the presence of Class C fly ash, while its role is negligible in the presence of Class F fly ash. This might be due to the fact that UFFA is also a Class F fly ash. The bulk resistivity of Mix 6 and Mix 7 is 74.33% and 93.19%, respectively, lower than that of Mix 1. The bulk resistivity of Mix 6 is 30.83 kΩ-cm, which is 277% more than that of Mix 7. Although both Mix 6 and Mix 7 contain metakaolin, the difference between these two UHPC groups lies in the complete replacement of silica fume with metakaolin and the replacement of Class C fly ash with Class F fly ash in Mix 7. The difference in bulk resistivity indicates the beneficial role of silica fume in densifying the pore structure of UHPC.

It is worth noting that the UHPC mixes investigated in this study do not contain inert fillers, such as ground silica, quartz powders, limestone powders, or iron ore tailings. The use of filler materials in UHPC might result in loss of strength due to their restricted chemical when compared to Portland cement and SCMs. However, the use of inert fillers at a reasonable amount can further improve the particle packing density, reduce porosity, and hence decrease the permeability of UHPC. A comprehensive investigations on the role of inert fillers in UHPC performance will be conducted in our future works.

**Table 5.3: The range of chloride penetration based on bulk resistivity**

| Chloride penetration | 56-day rapid chloride permeability charge passed (Coulombs) | 28-day bulk electrical resistivity of saturated concrete (kΩ-cm) |
|---|---|---|
| High | >4,000 | <4 |
| Moderate | 2,000 to 4,000 | 4-8 |
| Low | 1,000 to 2,000 | 8-16 |
| Very Low | 100 to 1,000 | 16-190 |
| Negligible | <100 | >190 |

When compared with regular concrete, it is clear that the UHPC mixtures exhibited significantly higher bulk resistivity than that of the regular concrete. This result indicates that the UHPC mixes have denser microstructures and lower pore connectivity, and hence lower permeability, than the regular concrete. It can be anticipated that the UHPC mixtures, especially Mix 1, Mix 2, and Mix 5, possess higher resistance against deteriorations than regular concrete thereby with higher long-term performance and extended service life.

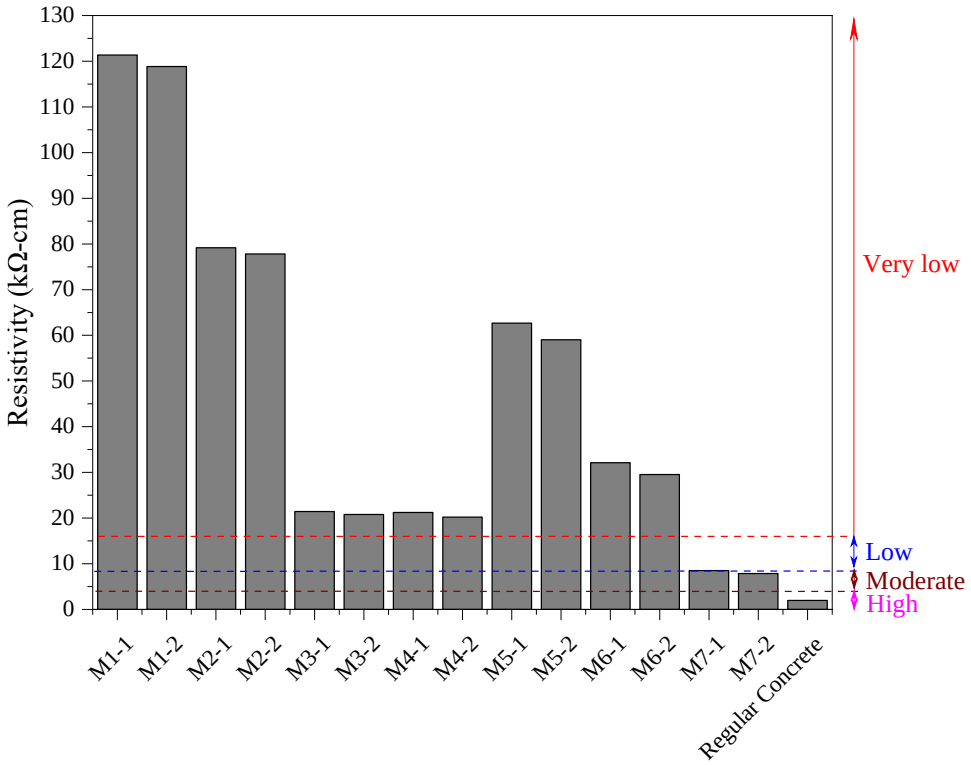


**Figure 5.35: Bulk resistivity of UHPC and a regular concrete.**

5.3.6.B Permeability of FRC

Permeability tests of FRC were carried out for Mix 1 and Mix 2, both mixes containing polypropylene fibers, at 7 days and 28 days. A summary of the tests can be found in Table 5.4 for 7 days and Table 5.5 for 28 days. For the 7-day test, the volume of the pour solution was 1.38 liters, and the diameter of the container was 4 in. For the 28-day test, the volume of the pour solution was 1.27 liters, and the diameter of the container was 4 in. For FRC Mix 1,

the average bulk resistivity was 3.90 kΩ-cm for 7 days and 10.92 kΩ-cm for 28 days. For FRC Mix 2, the average bulk resistivity was 4.59 kΩ-cm for 7 days and 12.83 kΩ-cm for 28 days.

From these results, it can be determined that Mix 2 has a higher bulk resistivity than Mix 1, and as such Mix 2 has a lower permeability than Mix 1. The differences in the bulk resistivity could be due to differences in concrete porosity as the fibers have different effects on the pore structure of the concrete. According to Roesler et al. [207], because macro-fibers can hold cracks together after the concrete has cracked, FRC has the potential to improve durability to deleterious materials compared to plain concrete through lower permeability and reduced crack widths. The corrugated fiber of Mix 2 could also have been better suited to limit cracks than the straight fibers of Mix 1, resulting in lower permeability.

**Table 5.4: 7-day permeability results**

| Sample | Diameter (d1) (in) | Diameter (d2) (in) | Mean Diameter (in) | CSA ($in^2$) | Length (in) | Bulk Resistivity (kΩ-cm) | Formation factor |
|---|---|---|---|---|---|---|---|
| Mix 1-1 | 3.991 | 4.049 | 4.02 | 12.69 | 8.00 | 3.89 | 226.82 |
| Mix 1-2 | 3.975 | 4.095 | 4.04 | 12.79 | 8.00 | 3.91 | 227.80 |
| Mix 2-1 | 3.980 | 4.049 | 4.01 | 12.66 | 8.00 | 4.62 | 269.56 |
| Mix 2-2 | 3.975 | 3.958 | 3.97 | 12.36 | 8.00 | 4.55 | 265.44 |

**Table 5.5: 28-day permeability results**

| Sample | Diameter (d1) (in) | Diameter (d2) (in) | Mean Diameter (in) | CSA ($in^2$) | Length (in) | Bulk Resistivity (kΩ-cm) | Formation factor |
|---|---|---|---|---|---|---|---|
| Mix 1-1 | 3.991 | 4.049 | 4.02 | 12.692 | 8.0 | 11.28 | 573.785 |
| Mix 1-2 | 3.975 | 4.095 | 4.035 | 12.787 | 8.0 | 10.56 | 536.784 |
| Mix 2-1 | 3.980 | 4.049 | 4.0145 | 12.657 | 8.0 | 13.30 | 676.441 |
| Mix 2-2 | 3.975 | 3.958 | 3.9665 | 12.356 | 8.0 | 12.38 | 628.441 |

### 5.3.7. Resistance Against Sulfate Attack

The length changes of mortar bars of the control group (regular mortar) and UHPC Mix 1, Mix 2, Mix 3, and Mix 5 in terms of exposure time to sodium sulfate solution are presented in Fig. 5.36. As can be seen, all UHPC groups show an initial rapid increase of length change in the first two weeks which continued almost in a similar range for the later weeks. However, the mortar bars of the control group behave differently so that a constantly increasing trend is observed in their length change. This indicates an appropriate resistance of

UHPC specimens to the sulfate attack which is due to the denser and more homogeneous microstructure with lower permeability of UHPC, making it less susceptible to the ingress of sulfate ions. The carefully selected materials and mix design of UHPC contribute to its resistance against sulfate attack. The control group, made of normal concrete, in contrast, is more vulnerable to sulfate attack. When exposed to sulfate ions, it can undergo a series of chemical reactions that lead to the formation of expansive compounds such as ettringite or gypsum. These reactions can result in the expansion of normal concrete, leading to cracking and deterioration over time.

As mentioned, sulfate ions from external sources can react with hydration products in two ways: one converts monosulfate into ettringite, and the other produces gypsum.

$$Ca_4Al_2(OH)_{12} \cdot SO_4 \cdot 6H_2O + 2Ca(OH)_2 + 2{SO_4}^{2-} + 2H_2O \leftrightharpoons Ca_6Al_2(OH)_{12} \cdot (SO_4)_3 \cdot 26H_2O + 4OH^- \quad (5.2)$$

$$Ca(OH)_2 + {SO_4}^{2-}(aq) + 2H_2O \leftrightharpoons CaSO_4 \cdot 2H_2O + 4OH^- \quad (5.3)$$

The alkalinity of the pore solution significantly impacts sulfate attack resistance. In line with the reactions, the formation of ettringite or gypsum raises $OH^-$ concentration in the pore solution and depletes portlandite. From a chemical equilibrium perspective, increasing the alkalinity in the pore solution can inhibit the formation of both ettringite and gypsum. Consequently, heightened alkalinity in the pore solution enhances the resistance of materials to sulfate attack.

Considering the variations of length change in the UHPC specimens, it can be observed that the regular mortar exhibited the highest expansion rate and magnitude among the investigated groups over the entire testing period. After 22 weeks, an expansion of 0.1082% was obtained from this control group. Due to the high volume of SCMs and denser microstructure, the four UHPC mixes exhibited lower sulfate-induced expansion than the regular mortar group. Mix 3 showed the lowest expansion values compared to the investigated UHPC mixes. It exhibited an expansion of ~0.0329% in 2 weeks, which was increased to ~0.0349% after 22 weeks. Mix 2 and Mix 1 showed the initial expansion of ~0.0438% and ~0.0468% after two weeks, respectively, and the expansion of ~0.0453% and ~0.0468% after 22 weeks of being exposed to sulfate solution, respectively. Although Mix 3 with an increment of ~0.002% between 2 and 22 weeks was higher compared to the expansion increases in Mix 2 and Mix 1 within the same period, it still possessed the minimum expansion values. This is related to the lower expansion recorded within the first two weeks for Mix 3, which might be due to the effect of Class C fly ash on strength development. Employing Class F fly ash typically leads to a decelerated initial strength gain, while the incorporation of Class C fly ash doesn't exhibit this delay and might bolster early strength development [203]. The key distinguishing factor between Class F and Class C fly ashes lies in their calcium (Ca) content, with Class F fly ash containing less than 18% Ca, whereas Class C fly ash boasts a higher Ca content, surpassing the 18% threshold [204]. This elevated calcium content in Class C fly ash contributes to additional hydration reactions,

thereby enhancing the development of strength. Accordingly, the result obtained for Mix 1 and Mix 2 that either include lower Class C fly ash or Class F micron fly ash can be reasonable. More importantly, the expansion induced by sulfate attack exhibited an inverse correlation with the permeability of the UHPC matrix. With a lower permeability, less sulfate ions and moisture can immigrate into UHPC, which explains the least expansion observed from Mix 3.

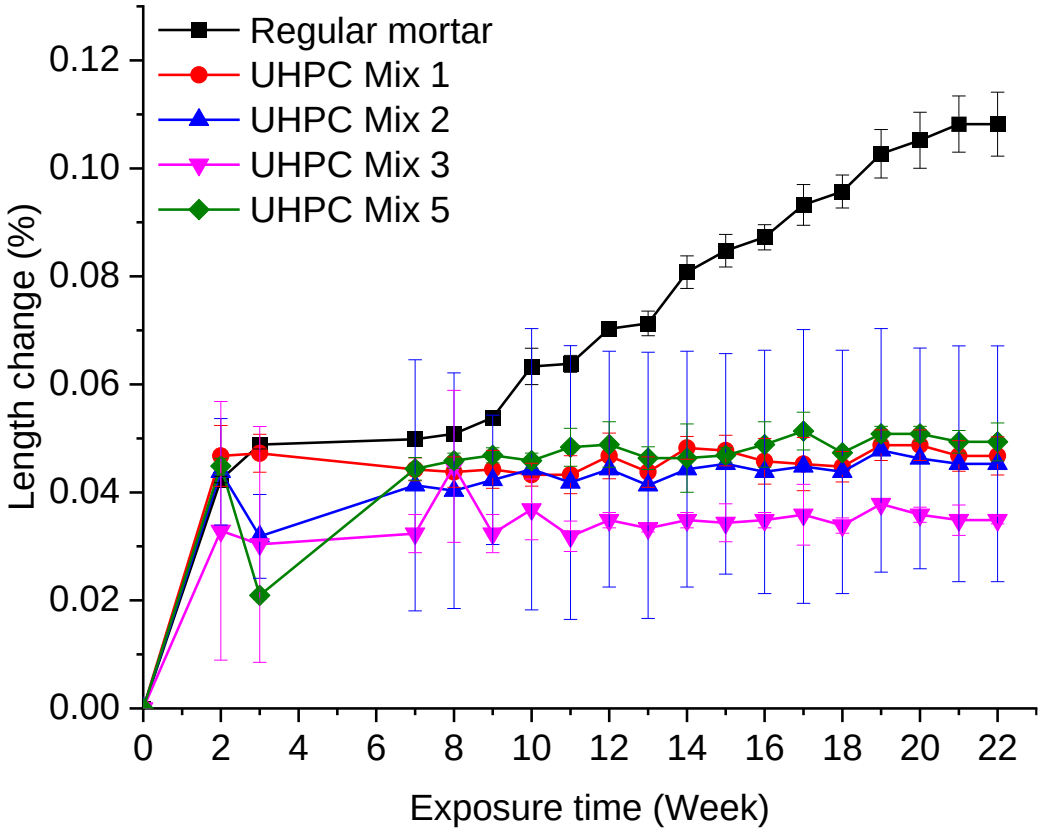


**Figure 5.36: Volume expansion of regular mortar and UHPC mixes in sulphate solution**

Detailed infomraton about the trial mixes and testing results of of FRC can be found from Appendix A and Appendix B at https://doi.org/10.7275/xgz6-se87

Detailed infomraton about the beam bending test results of UHPC containing steel, PVA, glass, and asalt fibers can be found from Appendix C, Appendix D and Appendix E at https://doi.org/10.7275/xgz6-se87

# 6.0 Mixtures for Large-Scale Batching and Field Applications

Based on the mixture design and the characterization of hydration of the cementitious binders in Task 3 and the property evaluation of the UHPC in Task 4, this task mainly focuses on the determination of FRC and UHPC mixtures suitable for large-scale batching. Toward this end, the mixtures of UHPC and FRC developed in this project are analyzed by considering mixture proportions, ease of mixing and batching, curing conditions, development of properties, and fiber selections.

## 6.1 Materials

For UHPC, as shown in Table 6.1, seven different mixture designs have been developed in this project, in which two types of Portland cement (Type I/II Portland cement and Type III Portland cement), three types of fly ash (Class C fly ash, Class F fly ash, micro-fly ash (a finer Class F fly ash)), silica fume, metakaolin, masonry sand, and four types of microfibers (steel fiber, PVA fiber, basalt fiber, and glass fiber) have been investigated. The proportions of the UHPC mixtures were developed by considering the optimal dosage range of each cementitious material and the maximum particle packing density of the system. A water-to-binder ratio of 0.19 and a fiber volume fraction of 2.0% were used.

**Table 6.1: Mixture proportions of UHPC**

| Groups/Materials | Mix 1 ($lb/yd^3$) | Mix 2 ($lb/yd^3$) | Mix 3 ($lb/yd^3$) | Mix 4 ($lb/yd^3$) | Mix 5 ($lb/yd^3$) | Mix 6 ($lb/yd^3$) | Mix 7 ($lb/yd^3$) |
|---|---|---|---|---|---|---|---|
| Type I/II cement | - | 1391.60 | 1391.60 | 1391.60 | 1391.60 | 1378.56 | 1413.58 |
| Type III cement | 1379.54 | - | - | - | - | - | - |
| Silica fume | 607.41 | 415.40 | 415.40 | 415.40 | 415.40 | 414.61 | - |
| Class F fly ash | - | - | - | 242.98 | 270.01 | - | 316.47 |
| Class C fly ash | - | 197.32 | 270.01 | - | - | 72.56 | - |
| Micron-fly ash | 72.07 | 72.70 | - | 27.03 | - | - | - |
| Metakaolin | - | - | - | - | - | 207.30 | 379.77 |
| Water | 391.21 | 394.63 | 394.63 | 394.63 | 394.63 | 393.88 | 400.87 |
| Masonry sand | 2516.57 | 2538.57 | 2538.57 | 2538.57 | 2538.57 | 2533.70 | 2578.67 |
| Superplasticizer | 58.58 | 66.21 | 66.21 | 66.21 | 66.21 | 70 | 70 |
| Micro-steel fiber | 262.95 | 262.95 | 262.95 | 262.95 | 262.95 | 262.95 | 262.95 |
| Micro-PVA fiber | - | - | - | - | 43.82 | - | - |
| Micro-basalt fiber | - | - | - | - | 88.66 | - | - |
| Micro-glass fiber | - | - | - | - | 91.02 | - | - |

By taking the complexity of constituents and ease of preparation into account, Mix 1, Mix 3, and Mix 5 use regular fly ashes only, which are more suitable for large-scale batching than Mix 2 and Mix 4. The difference between Mix 1 and Mix 3 lies in the type of cement. Type III cement has finer particles than Type I cement and hence it can generate slightly more hydration heat and higher early-age strength. Given its high pozzolanic activity, in Mix 6 and Mix 7, metakaolin was used to partially or completely replace silica fume. Regular fly ashes, silica fume, and metakaolin are widely available in the market. Type I/II cement is more commonly used than Type III cement in modern concrete structures.

For FRC, a concrete mixture design previously approved by MassDOT for the Concrete Sidewalk Project Phase II with a water-to-binder ratio of 0.44 and a fiber volume fraction of 1% was studied. To improve the workability of fresh FRC, the amount of water reducer was adjusted. As summarized in Table 6.2, four different fibers were used. Two polypropylene fibers, one crimped and one straight with a length of 2.4-inch and 1.75-inch, and two steel fibers, one hooked and one crimped with a length of 2-inch and 1.5-inch, respectively, were used. Both polypropylene fibers and steel fibers are widely used in FRC.

**Table 6.2: Mixture proportions of FRC**

| Materials | Mix 1 (lb/yd$^3$) | Mix 2 (lb/yd$^3$) | Mix 3 (lb/yd$^3$) | Mix 4 (lb/yd$^3$) | Mix 5 (lb/yd$^3$) |
|---|---|---|---|---|---|
| Coarse aggregate (3/4 inch) | 1750 | 1750 | 1750 | 1750 | 1750 |
| Sand | 1235 | 1235 | 1235 | 1235 | 1235 |
| Cement | 472 | 472 | 472 | 472 | 472 |
| Fly ash | 158 | 158 | 158 | 158 | 158 |
| Water | 275 | 275 | 275 | 275 | 275 |
| Fiber | Straight polypropylene fiber (Fibermesh®-650 from Sika) 15.34 | Straight polypropylene fiber (Fibermesh®-650 from Sika) 15.34 | Crimped polypropylene fiber (Enduro® Prime from Sika) 15.34 | Hooked steel fiber (Novocon® HE-4550 from Sika): 132.35 | Hooked steel fiber (Novocon® XR from Sika): 132.35 |
| Air entraining admixture | 2.5 oz/yd$^3$ | 2.5 oz/yd$^3$ | 2.5 oz/yd$^3$ | 2.5 oz/yd$^3$ | 2.5 oz/yd$^3$ |
| Water reducing admixture | 22.1 oz/yd$^3$ | 29.5 oz/yd$^3$ | 29.5 oz/yd$^3$ | 29.5 oz/yd$^3$ | 29.5 oz/yd$^3$ |
| Workability retaining admixture | 12.6 oz/yd$^3$ | 12.6 oz/yd$^3$ | 12.6 oz/yd$^3$ | 12.6 oz/yd$^3$ | 12.6 oz/yd$^3$ |

## 6.2 Mixing

It should be noted that, due to the ultra-low water-to-binder ratio, the UHPC mixtures are extremely dry before mixing. The high flowability cannot be achieved until the water and superplasticizer are uniformly dispersed and fully exposed to the cement and SCM grains. Therefore, the UHPC mixtures cannot be well mixed, at least in the initial mixing process, in regular drum concrete mixers, which utilize the materials' gravity to trigger mixing. A powerful shear mixing is required to disrupt the dry particles and their agglomeration and to trigger sufficient contact between the dry particles with water and superplasticizer. Shear mixers or pan mixers with blades are recommended to achieve uniform dispersion of water and dry particles (Figure 6.1). Compared with regular concrete, a longer mixing time (10 to 15 minutes) is needed to obtain homogeneously mixed UHPC mixtures. The ease of mixing also depends on the materials used in the mixtures. Due to its high water absorption capacity, the use of metakaolin resulted in significant decreases in the flowability of UHPC, and hence more superplasticizers and increased mixing time are needed for Mix 6 and Mix 7.


(a) regular drum concrete mixers, (b) and (c) pan mixers

**Figure 6.1: Concrete mixers**

For FRC, both the regular drum mixer and pan mixer can be used to obtain well-mixed mixtures by following ASTM C94. With a dosage of water reducer of 22.1 oz/yd$^3$, Mix 1 showed poor workability. Therefore, the dosage of the water reducer was increased to 29.5 oz/yd$^3$ to improve the ease of mixing and workability of FRC. It was found that, compared with the steel fibers, the polypropylene fibers, in particular the crimped polypropylene fiber, showed higher clumping, which made the mixing and casting process more difficult, and this might impact the quality of concrete in large-scale batching.

### 6.3 Curing Condition and Mechanical Properties

In this study, FRC was cured under the regular lime water curing condition. Table 6.3 shows the development of compressive strength, splitting tensile strength, and flexural strength of Mix 1, Mix 2, and Mix 3 after 7 days and 28 days. It can be found that, although the increase of water reducer dosage from 22.1 oz/yd$^3$ to 29.5 oz/yd$^3$ improved the workability of fresh FRC, decreases in compressive strength, splitting tensile strength, and flexural strength were observed. Compared with the straight polypropylene fiber, the crimped polypropylene fiber resulted in higher strength values.

**Table 6.3: Mechanical properties of FRC mixtures**

| Properties, specimen | Mix 1 Force (lb) | Mix 1 Stress (psi) | Mix 2 Force (lb) | Mix 2 Stress (psi) | Mix 3 Force (lb) | Mix 3 Stress (psi) |
|---|---|---|---|---|---|---|
| 7-day compressive strength, specimen 1 | 42,650 | 3,395 | 34,145 | 2,717 | - | - |
| 7-day compressive strength, specimen 2 | 48,905 | 3,890 | 37,655 | 2,996 | - | - |
| 7-day compressive strength, specimen 3 | 49,420 | 3,930 | 36,220 | 2,882 | - | - |
| **7-day compressive strength, average** | **46,992** | **3,738** | **36,007** | **2,865** | - | - |
| 28-day compressive strength, specimen 1 | 63,190 | 5,085 | 50,465 | 4,016 | 63,625 | 5,065 |
| 28-day compressive strength, specimen 2 | 58,700 | 4,670 | 51,495 | 4,095 | 65,495 | 5,210 |
| 28-day compressive strength, specimen 3 | - | - | 51,305 | 4,080 | 60,840 | 4,840 |
| **28-day compressive strength, average** | **60,945** | **4,878** | **51,088** | **4,064** | **63,320** | **5,038** |
| 28-day splitting tensile strength, specimen 1 | 23,255 | 463 | 22,825 | 454 | 51,180 | 453 |
| 28-day splitting tensile strength, specimen 2 | 22,115 | 440 | 20,285 | 404 | 47,535 | 420 |
| **28-day splitting tensile strength, average** | **22,685** | **451** | **21,555** | **429** | **49,357** | **436** |
| 28-day flexural strength, specimen 1 | 7,322 | 610 | 6,236 | 519 | 6,756 | 563 |
| 28-day flexural strength, specimen 2 | 7,120 | 593 | 5,540 | 461 | 8,068 | 672 |
| **28-day flexural strength, average** | **7,221** | **602** | **5,888** | **490** | **7,412** | **618** |

For UHPC, two curing conditions have been investigated in this project: (i) regular lime water curing, and (ii) steam curing. As shown in Figure 6.2, in the regular lime water curing, the specimen was immersed in a saturated Calcium Hydroxide solution at room temperature (23 ± 2°C) until the age of testing. In the steam curing, the UHPC specimens were first cast in the molds and sealed at room temperature for 24 hours, followed by steam curing at 90°C and relative humidity of 100% for 48 hours, which were then cooled down to room temperature and switched to regular lime water curing until tests. It was found that the

hydration of cement and pozzolanic reactions of the SCMs can be accelerated thereby resulting in significantly enhanced strength gain.

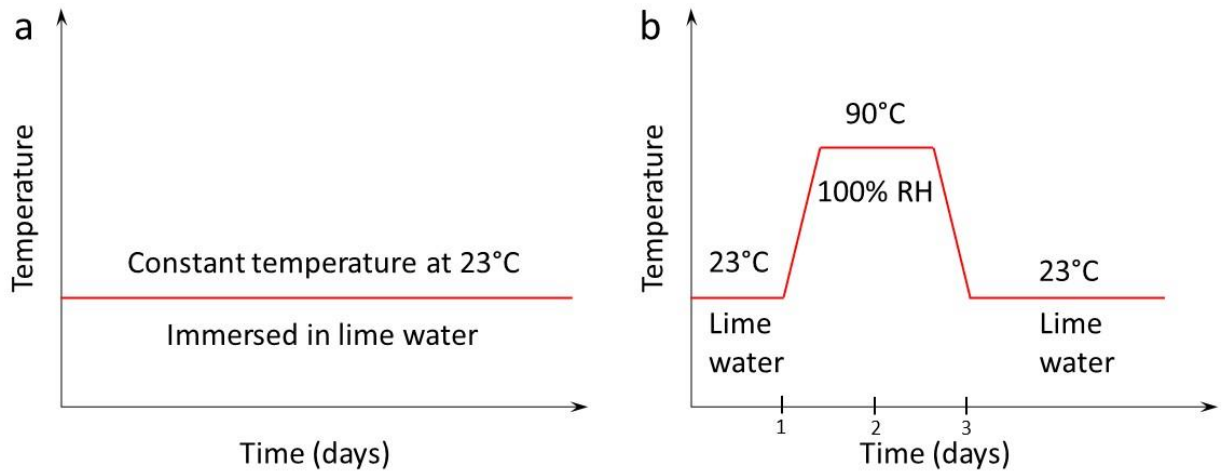


(a) regular lime water curing and (b) steam curing

**Figure 6.2: Curing conditions for UHPC.**

As shown in Figure 6.3, the strength development of UHPC can be enhanced by steam curing. The 3-day strength of steam-cured UHPC yielded strength values comparable to or exceeding the 28-day strength of the same mixtures cured in regular condition. This is found to be the most favorite role of steam curing. No significant increase in compressive strength was observed from the steam-cured UHPC after 3 days. Although the regularly cured UHPC specimens showed slower strength gain, their ultimate compressive strength after 60 days is comparable with the steam-cured specimens. Although the development of flexural strength exhibits lower dependence on the curing condition than compressive strength, the specimens under steam curing sill yielded higher strength (Figure 6.4). From the results of compressive and flexural strength development of UHPC under these two curing conditions, it was found that steam curing can trigger rapid strength gain in UHPC but the ultimate strength of mature UHPC specimens was not significantly changed. Therefore, depending on the need for early-age strength and the availability of steam curing facilities, steam curing can be employed to accelerate the strength development in the field. It should be noted that the steam curing should be initiated at least 1 day after casting. If steam curing starts before hardening or gaining a certain strength, the high temperature and moisture will result in swelling and cracking of the young UHPC specimens.

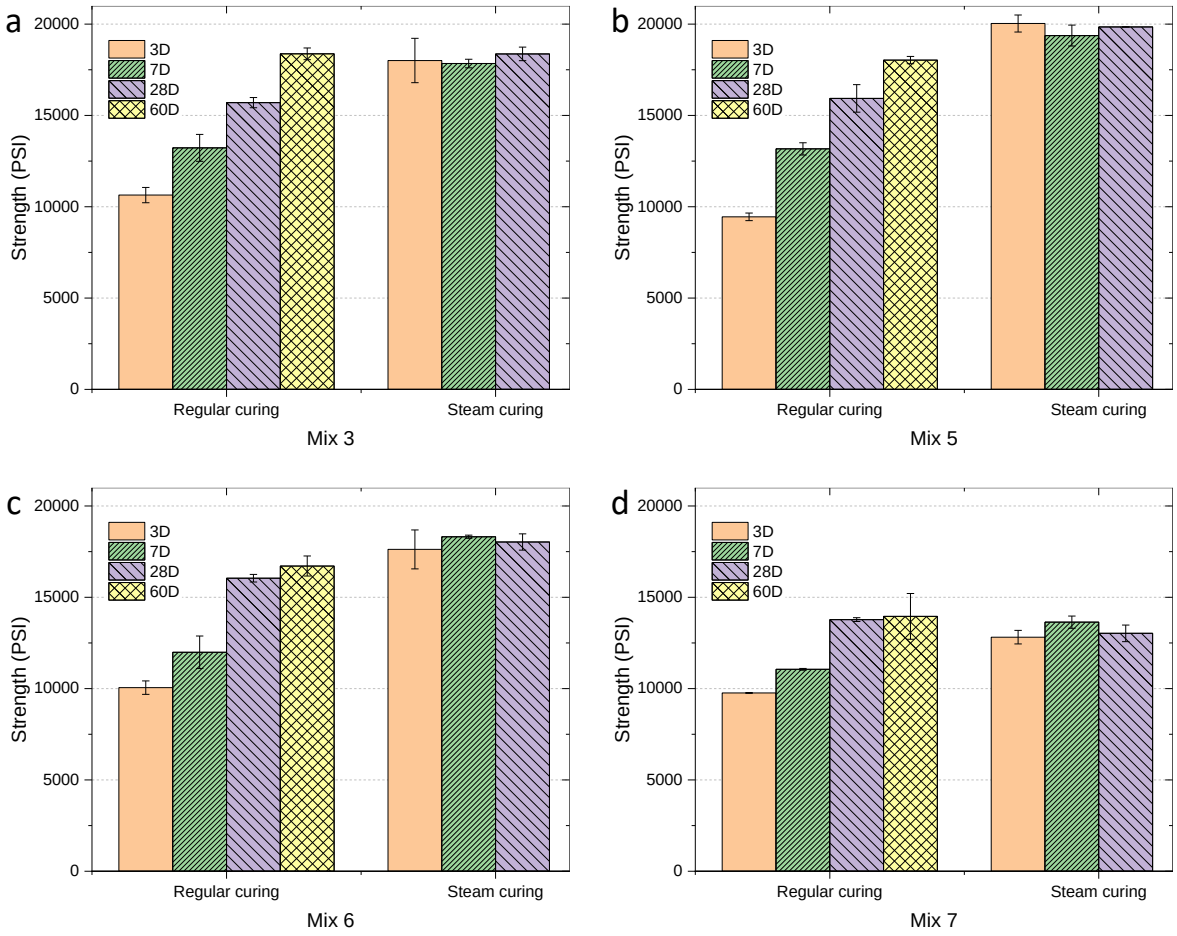


(a) Mix 3, (b) Mix 5, (c) Mix 6, and (d) Mix 7

**Figure 6.3: Compressive strength of UHPC**

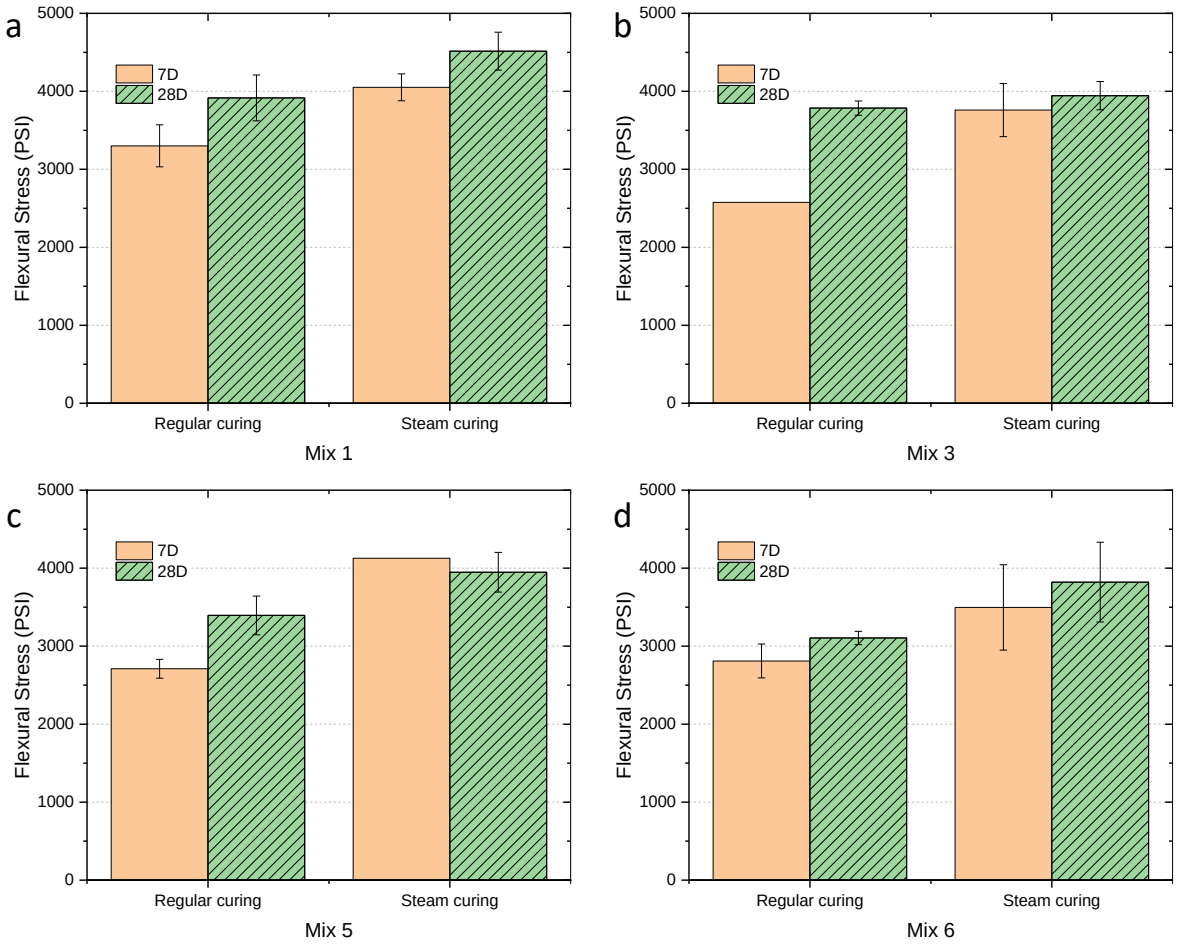


UHPC mixtures in regular lime water curing and steam curing: (a) Mix 1, (b) Mix 3, (c) Mix 5, and (d) Mix 6

**Figure 6.4: Flexural strength of UHPC**

## 6.4 Fibers for UHPC

Based on the availability of the materials, the ease of mixture design, as well as the mechanical properties, Mix 5, which uses Type I/II, silica fume, and Class F fly ash as cementitious materials, is considered one of the optimal mixture design for large-scale batching. A further study has been conducted to understand the type of fibers on the mechanical strength of this UHPC mixture design. Four different fibers with a length of 12-13 mm were invested at a constant volume fraction of 2%. As shown in Fig. 6.5, decreases in compressive strength were observed from the steam-cured UHPC with PVA and glass fiber, which might be due to the low compatibility between the fiber and the cement matrix or the deterioration in the alkaline, the hydrothermal environment of cement. The UHPC specimens reinforced with steel fiber exhibited higher compressive and flexural strength than the same mixture design with other fibers.

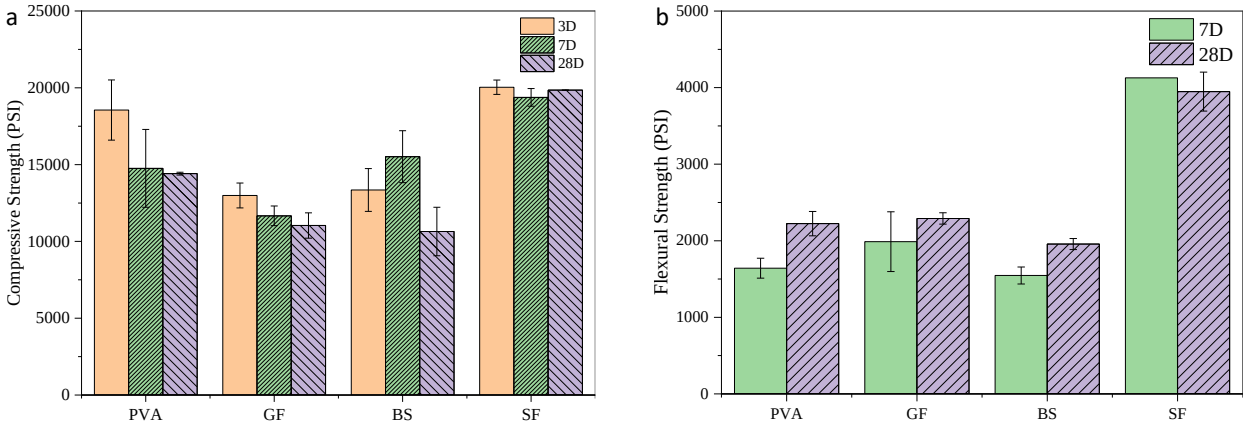


Development of (a) compressive strength and (b) flexural strength of the UHPC Mix 5 with different fibers under steam curing (GF: glass fibers, BS: basalt fibers, SF: steel fibers)

**Figure 6.5: Strength of UHPC Mix 5**

# 7.0 Closure Gap Test

## 7.1 Overview

Results from two large-scale laboratory tests conducted at UMass Amherst on concrete closure gap connections were used to determine if the UHPC mixture developed was viable to be used in this type of transportation infrastructure. This test was done because closure pour tests were already completed at UMass Amherst and detailed in the thesis by Ramos [208]. The tests were performed using the UHPC mixture 5 developed by UMass Lowell. The mixture was used to fabricate the longitudinal closure pour cast between two panels to simulate the connection between two bridge deck panels.

Specimen design, fabrication, design strength, testing procedure, and test results are presented in this section. These tests were not intended to characterize the long-term cyclic performance of the connection; the objectives were only to evaluate whether the connection develops the required strength. A second goal of these tests was to investigate whether narrow closure pours could be used in combination with the developed mixture without negative effects on transverse strength between the panels. A third goal was to determine if straight bars, rather than the typical hooped bars, were able to develop the required strength within the UHPC which would ease the manufacturing of molds and construction of the closure gaps.

## 7.2 Specimen Design

The test specimens were designed to represent the typical deck portion of two adjacent Decked Bulb Tee girders connected through a longitudinal joint. The design was done following PCI Northeast Deck Bulb Tee Guidelines (NEDBT) in coordination with AASHTO LRFD Bridge Design Specifications. Drawing details for straight bar connection from the guide provided guidance on the selection of closure pour width, dimensions for the deck panels, and steel reinforcement used in this experiment. The guide indicated that the closure pour width generally varies from 6.5 in. to 24 in. depending on the strength of the concrete used. The higher strength mixes of UHPC may be used which could result in a narrow closure pour connection. Following this recommendation, the specimen in this experiment uses joint widths of 8 in. and 6 in. with the UHPC to determine the behavior of the specimens with a smaller joint. To achieve the 6 in. gap requires that the tolerance is reduced from 1 in. to 0.5 in.

Two specimens with similar dimensions were fabricated for testing. Each specimen consisted of two conventional concrete precast panels connected using a narrow closure pour that contains a triangular shear key filled with the closure pour material. Elevation view, joint section view, plan view, and reinforcement details of the specimens can be seen in Figure 7.2, Figure 7.3, and Figure 7.4 below. Each panel was 44 in. long and 8 in. deep. Panels for specimen 1 were 34 in. wide and connected with the 8 in. wide longitudinal connection.

Panels for specimen 2 were 35 in. wide and connected with the 6 in. joint. The total length of the specimens after connecting the panels together was 76 in. long, 44 in. wide, and 8 in. deep. The spacing and size of the deck longitudinal bars were designed using AASHTO provisions. The resulting longitudinal reinforcement was as follows: No. 5 bars spaced at 9 in. top and bottom for specimen 1; No. 5 bars spaced at 9.5 in. top and bottom for specimen 2. Four longitudinal No. 5 bars run through under and above bars in the closure pour connection as shown in the drawings.

The transverse reinforcement details were established by replicating the detailing for straight bars connection from section NEDBT – 05 Beam Deck Details found in the guideline. Specification for the connection reinforcement (transverse bars) requires No. 4 bars to be placed along the entire width of the panels with 6 in. spacing. The transverse bars of two deck panels are staggered at 3 in. in the closure pour connection as seen in Figures 7.1 and 7.2 to avoid interference of bars between adjacent panels and to facilitate construction. These bars project 7 in. and 5.5 in. into the joint with an overlap length of 6 in. and 5 in. for specimen 1 and specimen 2, respectively, as depicted in Figure 7.3. The clear cover for the reinforcing bars was designed to be 2.5 in. on the top and 1.5 in. on the bottom for both specimens. All reinforcement used in the specimens satisfied ASTM 615 grade 60 reinforcement and contained epoxy coating.

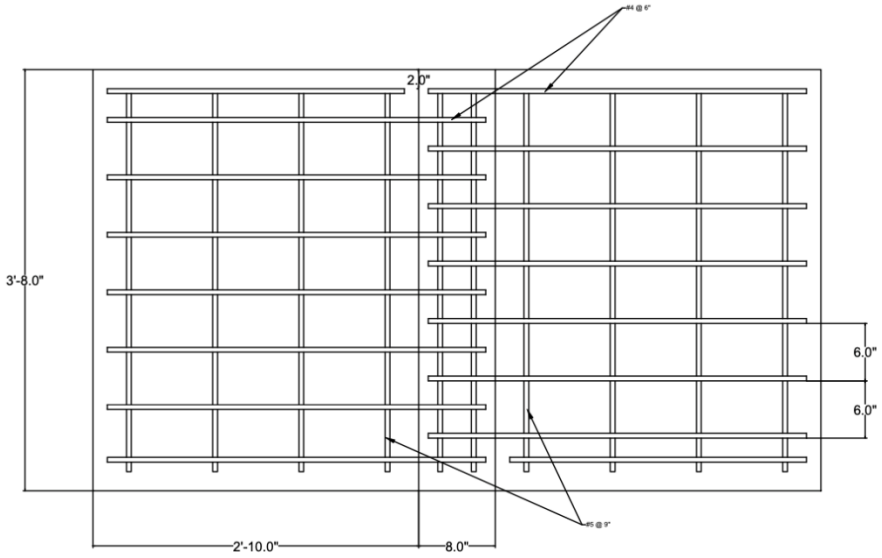


**Figure 7.1: Plan view of test specimen 1 (8 in. closure gap)**

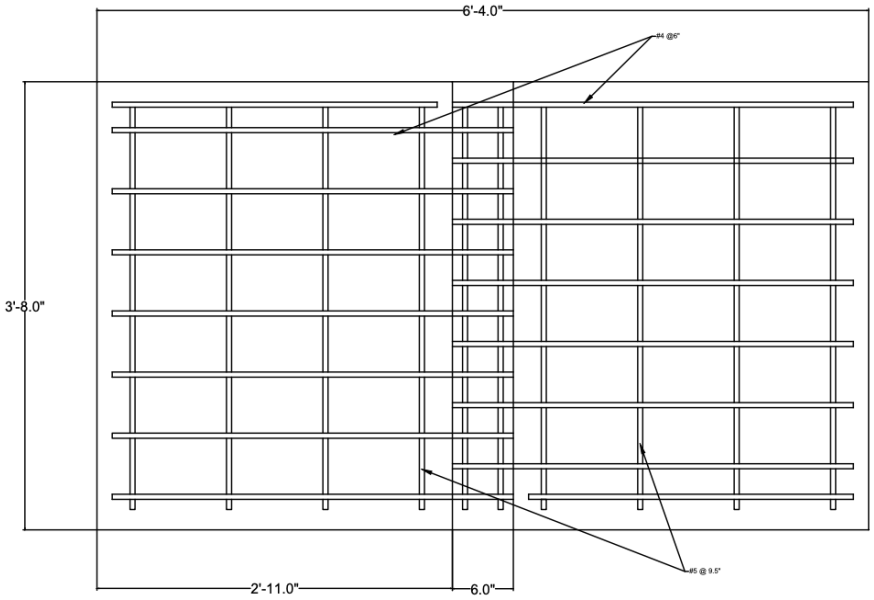


**Figure 7.2: Plan view of test specimen 2 (6 in. closure gap)**

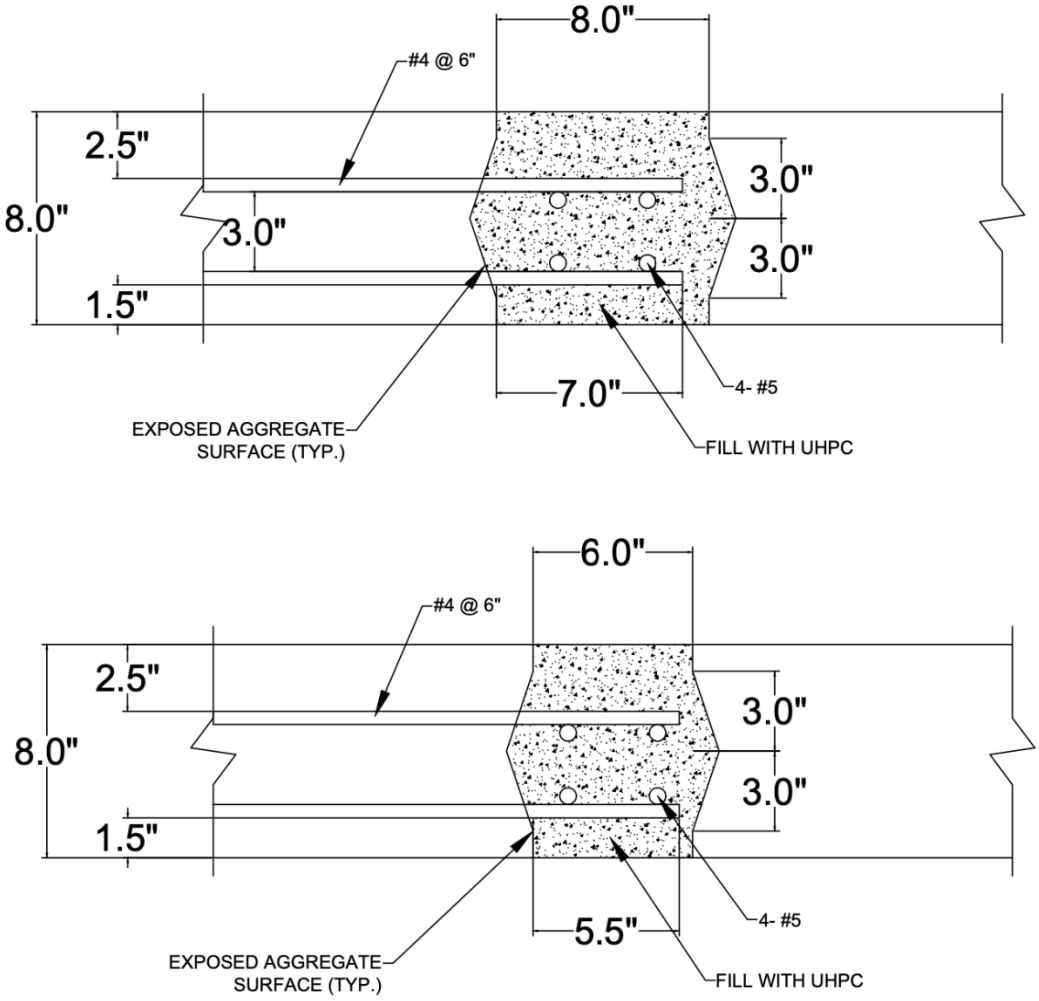


**Figure 7.3: Elevation profile of test specimen closure gap details**

## 7.3 Specimen Fabrication

The specimens were fabricated in two steps, with the first step involving building formwork and casting of the deck panels, followed by the second step which involved the casting of the closure pour connection. Test specimens were fabricated and tested in the Gunness Structural Engineering Laboratory at the University of Massachusetts Amherst.

In the first step, four panels were formed and poured with 4 ksi concrete from Construction Service in Wilbraham, MA. Following the casting of the panels the closure gap could then be formed and cast. Two panels of each specimen were positioned and properly oriented to satisfy the overlap lap length and spacing of the bars in the closure pour connection. Plywood sheets were used to form the two free edges of the closure pour region and the joint was prepared for casting a slightly modified version of the UHPC mixture.

Due to the fact we could not get the superplasticizer that was used in Mix 5 from UMass Lowell in a timely manner, another superplasticizer was used. In coordination with a team from GCP, it was determined that a combination of two superplasticizers could be used to replicate the mix. GCP Advacast 555 and GCP Advacast 593 were used. Calculations were completed to keep the water-to-cement ratio the same in both mixes, which resulted in a reduction of the water used in the modified mix. The modified mix is detailed in Table 7.1 below.

**Table 7.1: Mixture proportions of UHPC Mix 5 and modified Mix 5**

| Groups/Materials | Mix 5 (lb./yd$^3$) | Mix 5 modified (lb./yd$^3$) |
|---|---|---|
| Type I/II cement | 1391.60 | 1391.60 |
| Silica fume | 415.40 | 415.40 |
| Class F fly ash | 270.01 | 270.01 |
| Water | 394.63 | 350.67 |
| Masonry Sand | 2538.57 | 2538.57 |
| Optimum 380 superplasticizer | 66.21 | - |
| GCP Advacast 555 superplasticizer | - | 72.21 |
| GCP Advacast 593 superplasticizer | - | 43.81 |
| Micro-steel fibers | 262.95 | 262.95 |

The mix for the pour was done in the same manner as had been done by UMass Lowell previously in a pan mixer. During the mix, the materials were first all weighed out and the mixing bowl and paddle were wetted. The dry solid materials were added to the mixer and mixed for 2 minutes. Half of the water and half of the superplasticizer were added and mixed for another 2 minutes or more until there was an even distribution. The remaining water and superplasticizer were added and mixed until a homogenous mixture was achieved, which took 10 to 15 minutes. Half of the fibers were added and mixed for about 2 minutes and then the remaining fibers were added until there was a uniform dispersion of the fibers.

### 7.4 Test Setup and Procedure

Both specimens were tested under the loading and boundary conditions shown in the schematic of the specimen test set up in Figure 7.4. The specimens were tested in a rigid loading frame composed of steel beams and columns. A 110 kip hydraulic actuator fitted with a load cell was used to apply the load. The actuator load was transferred to the specimens via a transverse rigid steel spreader beam and two steel beams that distributed the load across the width of the panels. The load from the spreader beams was transferred to the concrete surface through elastomeric pads.

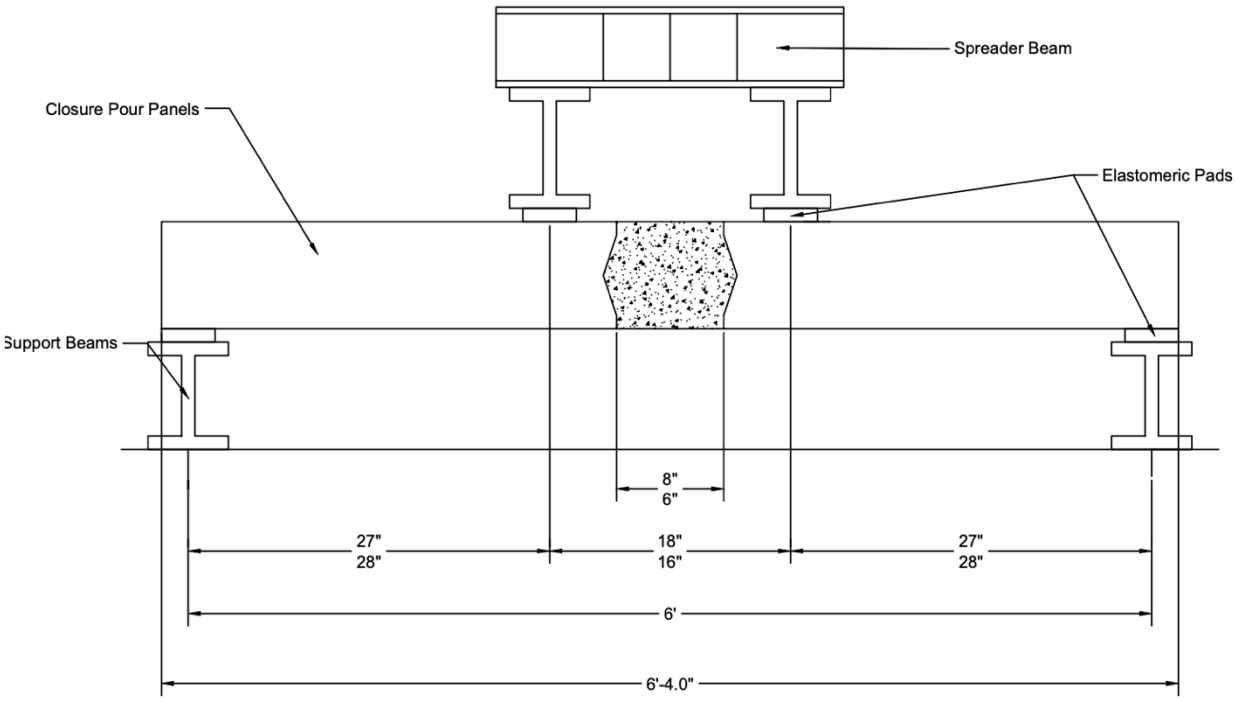


Note: top dimension for specimen 1, bottom dimensions for specimen 2

**Figure 7.4: Closure pour test setup**

The specimens were simply supported with a 6 ft. span. A 4-inch wide elastomeric bearing pad having a 1 inch. thickness was placed between the slabs and the support steel beams to ensure boundary condition was achieved. The shear span for specimen 1 and specimen 2 were 27 in. and 28 in. as shown in the schematic drawing where the top and bottom dimensions are those corresponding to specimens 1 and 2, respectively. These dimensions for the shear span consider the distance from the center to the center of the bearing pads. The joint zone was in the center of the span and experienced a maximum constant moment and zero shear. String potentiometers were used to find the center deflection of the specimens. One was positioned and centered on the top surface of the specimens to record deflection. Two were placed at the ends of each panel to determine the deflection of the pads on the bottom. An additional was placed from the actuator to the top of the loading frame to account for any displacement of the rig itself, although after testing this displacement was found to be negligible. A photograph of the final test setup including the loading frame, specimen, actuator, and potentiometer is shown in Figure 7.5.

**Figure 7.5: Finalized closure pour test setup**

Specimen 1, 8 in. closure gap, was tested on July 12, 2023, which was 68 days after casting of the UHPC in the closure pour connection. Specimen 2, 6 in. closure gap, was tested on July 14, 2023, 70 days after casting. During the test, the specimens were loaded in steps of 4 kips roughly every minute. After cracking the load was applied at steps of 2 kips. Displacement and load were recorded every 10 times per second throughout the test. Failure was identified as the formation of large wide cracks and crushing of concrete. Each specimen was visually observed multiple times throughout the test to document the behavior of the slabs. The specimens were inspected using visual crack techniques to monitor crack formation.

## 7.5 Design Strength

The capacity of each specimen was determined in two ways using nominal and measured material properties. The calculation for nominal material strength considers a compressive strength of 20 ksi and a yield strength of 60 ksi. In the calculation for measured material strength, the reinforcing steel was assumed to have an over strength of 20%, reaching a yield strength of 72 ksi; the average concrete compressive strength of the panels was 5,138 psi at 28 days; the average compressive strength of the UHPC in the closure gaps was 15.4 ksi on the day of the test. The strengths of the panel concrete obtained from the 4 in. by 8 in. cylinder tests are presented in Table 7.2. Three batches of UHPC were produced due to the limited size of the mixer. Batch 1 and 2 were part of the 6 in. closure gap and batches 2 and 3 were in the 8 in. closure gap. The 28-day strengths of the UHPC batch 1 and 3 are presented in Table 7.3, and the 70-day strengths of the UHPC are presented in Table 7.4.

**Table 7.2: Compressive strength of panel concrete**

| Specimen | Force (lbs.) | Stress (psi) |
|---|---|---|
| 1 | 65,395 | 5,205 |
| 2 | 65,745 | 5,230 |
| 3 | 62,565 | 4,980 |
| Average | 64,568 | 5,138 |

**Table 7.3: 28-day compressive strength of UHPC**

| Batch | Specimen | Force (lbs.) | Stress (psi) |
|---|---|---|---|
| 1 | 1 | 167,670 | 13,340 |
| 1 | 2 | 158,285 | 12,595 |
| 1 | 3 | 150,130 | 11,945 |
| 1 | Average | 158,695 | 12,627 |
| 3 | 1 | 192,260 | 15,300 |
| 3 | 2 | 200,375 | 15,945 |
| 3 | 3 | 191,325 | 15,225 |
| 3 | Average | 194,653 | 15,490 |
| Average | - | 176,674 | 14,058 |

**Table 7.4: 70-day compressive strength of UHPC**

| Specimen | Force (lbs.) | Stress (psi) |
|---|---|---|
| 1 | 193,880 | 15,430 |
| 2 | 192,085 | 15,285 |
| 3 | 195,106 | 15,525 |
| Average | 193,690 | 15,413 |

The load was taken as two equal point loads positioned at the distance shown in the drawing with respect to each joint width. The shear (V) is equal to the load divided by two (P/2). The maximum moment ($M_{max}$) is determined by multiplying the point load (P/2) by the shear span.

Calculation results for specimen capacity in the closure gap are shown in Table 7.5. and specimen capacity in the panels are shown in Table 7.6.

**Table 7.5: Specimen capacity in the closure gap**

| Specimen | Nominal $M_n$ (kip-ft) | Nominal P (kips) | Measured $M_n$ (kip-ft) | Measured P (kips) |
|---|---|---|---|---|
| 1 (8 in. gap) | 59.3 | 52.7 | 71.3 | 63.4 |
| 2 (6 in. gap) | 59.3 | 50.8 | 71.3 | 61.1 |

**Table 7.6: Specimen capacity in the panel**

| Specimen | Nominal $M_n$ (kip-ft) | Nominal P (kips) | Measured $M_n$ (kip-ft) | Measured P (kips) |
|---|---|---|---|---|
| 1 (8 in. gap) | 60.7 | 53.9 | 72.5 | 64.4 |
| 2 (6 in. gap) | 60.7 | 52.0 | 72.5 | 62.1 |

The calculated capacity using nominal and measured material strength in the closure gap for specimen 1 was 52.7 kips and 63.4 kips, respectively. The calculated capacity using nominal and measured material strength for specimen 2 was 50.8 kips and 61.1 kips, respectively. The calculated capacity using nominal and measured material strength of the panel for specimen 1 was 53.9 kips and 64.4 kips, respectively. The calculated capacity using nominal and measured material strength for specimen 2 was 52.0 kips and 62.1 kips, respectively. The strength calculated using nominal material strength resulted in a more conservative load while the strength using measured material properties gave a higher load which is consistent with the load obtained from the experimental tests presented in the test results section. The strengths found in the panels was found to be higher than material strengths of the closure gaps, thus failure was expected to occur within the closure gap.

## 7.6 Test Results and Discussion

Top, front, and bottom views of specimen 1 throughout the test are shown in Figures 7.6 through 4.30 below. In specimen 1, the first cracking was observed in the panel at 47.2 kips. The cracks formed at the bottom of panels to the left and right of the closure gap. Additionally, a crack formed at the interface between the panel and closure gap and extended up to the apex of the shear key and from there extended towards the load point detailed in Figure 7.7. Following these first cracks the load was then applied at 2 kip intervals. At 50 kips cracks and crushing of the concrete was noticed at the surface of the panels between the elastomeric pad and the closure gap which can be seen in Figure 7.9. Continued loading resulted in the expansion of cracks and the separation of the panel from the closure gap. A view of the final behavior of the specimen can be seen in Figure 7.10.

Top and front views of specimen 2 throughout the test are shown in Figures 7.11 through 7.15 below. Cracking in specimen 2 occurred at 35.5 kips in the panel to the right of the gap, additional cracking occurred at 54 kips in a similar behavior to specimen 1 which can be seen in Figure 7.11. This includes a crack forming at the interface of the panel and the gap which caused the joint separation depicted in Figure 7.13. Concrete crushing at the top surface also occurred in specimen 2 and can be seen in Figure 7.13. The final behavior of the specimen can be seen in Figure 7.14.

The failure mode of the two specimens is a typical flexural failure with concrete crushing at the top surface of the panels and cracks forming and widening from the bottom surface of the panels that are subjected to tension forces. Specimen 1 reached a maximum load of 76.25 kips at a deflection of 1.14 in. Specimen 2 registered a maximum load of approximately 74.75 kips corresponding to a deflection of about 1.35 in. Globally, specimen 1 and specimen 2 showed same general behavior as the deformation was concentrated in the panels rather than the closure gap.

**Figure 7.6: Initial cracking behavior of specimen 1**

Left: 48 kips, Right: maximum load

**Figure 7.7: Crack from shear key of specimen 1**

Left: 48 kips, Right: maximum load

**Figure 7.8: Concrete crushing of specimen 1**

**Figure 7.9: Cracks extending underneath specimen 1**

**Figure 7.10: Final behavior of specimen 1**

**Figure 7.11: Initial cracking behavior of specimen 2**


Left: 54 kips, Right: 62 kips

**Figure 7.12: Joint separation of specimen 2**


**Figure 7.13: Concrete crushing of specimen 2**

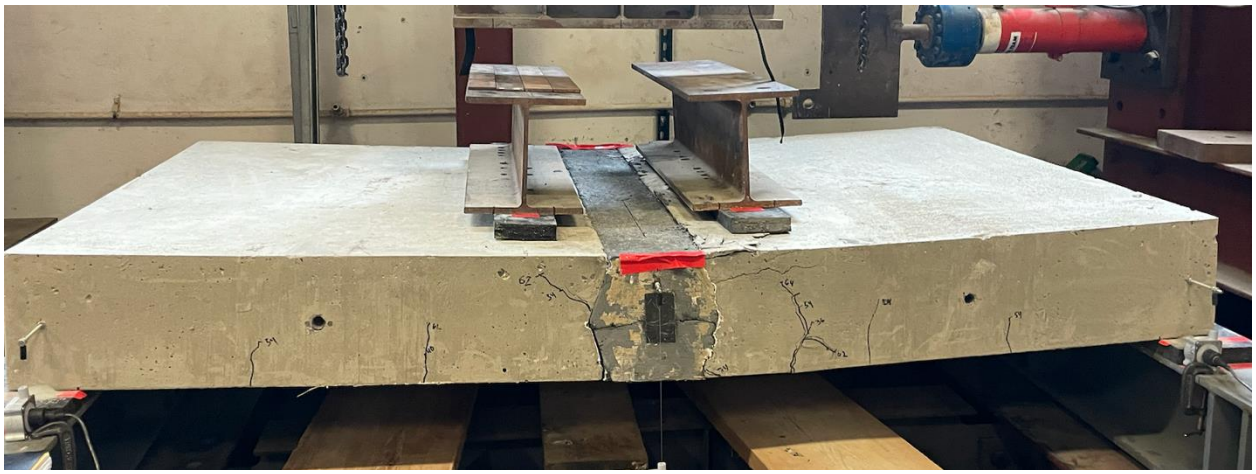

**Figure 7.14: Final behavior of specimen 2**

The load-deflection relationship for specimen 1 and specimen 2 is shown in Figures 7.15 and 7.16 respectively. In the plot for specimen 1 there is a linear load deflection relationship from initial loading to a load of approximately 40 kips at a deflection of about 0.21 in. After this point, a change in stiffness can be observed from the curve. The change in stiffness can be assumed to be the result of cracks that formed in the panels. For specimen 2 the linear load deflection relationship can be observed from initial loading again to a load of 40 kips also around a deflection of 0.21 in. Design loads using nominal and measured material strength are displayed with dashed lines in the plots to be compared with the peak load measured in the tests.

Calculated capacity using nominal and measured material properties of the panels along with the failure load obtained from the experiment are presented in Table 7.7. For purposes of comparison, the percentage difference between calculated capacities and experimental failure load is also presented in the table. The design capacity using nominal material properties results in a lower capacity when compared with experimental results, underestimating the failure load by more than 40%. The design load using measured material properties is close to the failure load from the experiment, with a percent difference of 18.5% for specimen 1 and 20.4% for specimen 2.

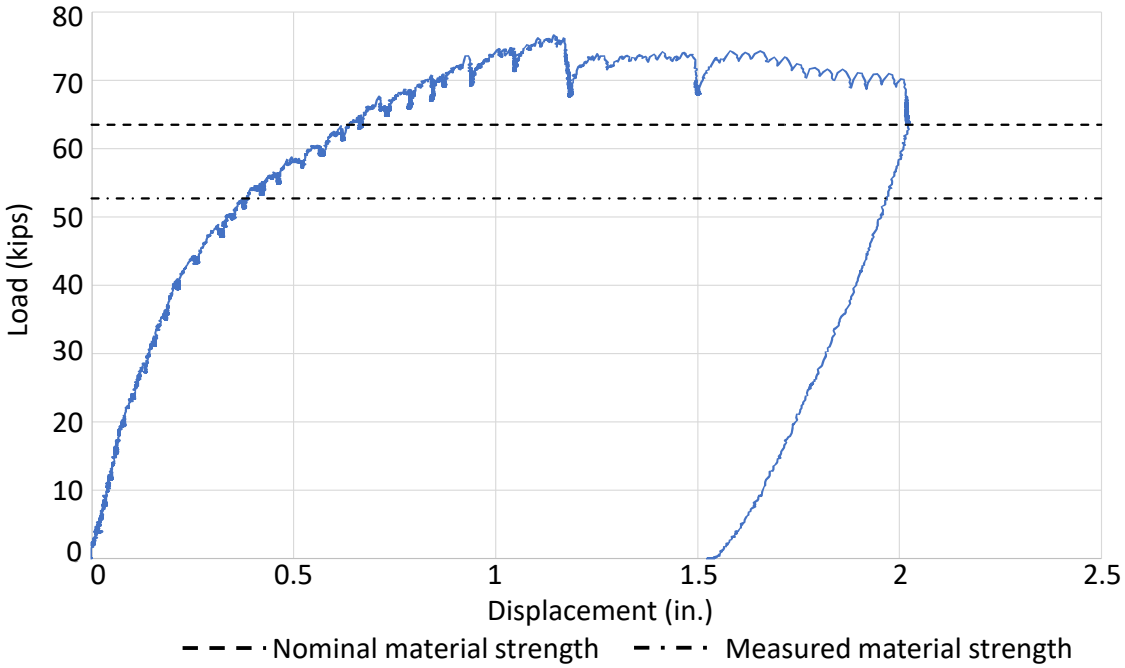


**Figure 7.15: Load-deflection curve of specimen 1**

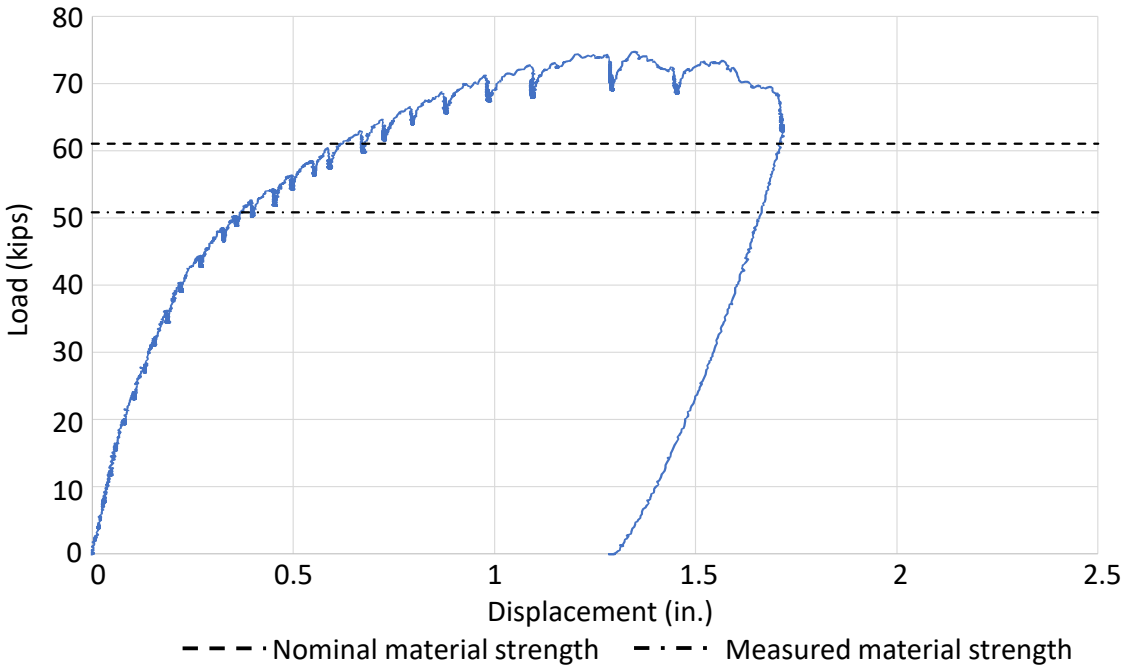


**Figure 7.16: Load-deflection curve of specimen 2**

**Table 7.7: Calculated capacity and experimental failure load comparison**

| Specimen | Nominal material strength | Measured material strength | Experiment failure load | Nominal and experimental % difference | Measured and experimental % difference |
|---|---|---|---|---|---|
| 1 | 53.9 kip | 64.4 kip | 76.25 kip | 41.5% | 18.4% |
| 2 | 52.0 kip | 62.1 kip | 74.75 kip | 43.8% | 20.4% |

## 7.7 Conclusion

Two large-scale tests were conducted to investigate the performance of longitudinal closure pour connections between two panels representing typical decks of Decked Bulb Tee girders. The concrete used for the closure pour was a modified version of the UHPC mix 5 developed by UMass Lowell. The primary objectives of the tests were to evaluate whether the connection performed adequately to develop the strength required to use UHPC in this type of transportation infrastructure. Another goal was to investigate whether narrow closure pours can be used in combination with the UHPC mix without negative effects on transverse strength between the panels. Finally, it was to determine if straight bars, rather than hooped bars which are typical with normal strength concrete can be used. The two specimens were designed, fabricated, and tested under four-point bending in the structural laboratory. During the tests, flexural cracks and crushing of concrete were observed on the panels made of normal-strength concrete, outside of the closure pour region which used the UHPC. The specimens were loaded continuously until experiencing flexural failure characterized by concrete crushing at the top surface and cracks forming and widening from the bottom surface.

Based on the results of the tests, the concrete closure pour connection comprised of straight bars detailing according to recommended practice obtained from PCI Northeast for decks of Decked Bulb Tee girders in combination with the developed mixture performed well in the experiment. The connections could reach the required strength and provide adequate transfer of forces between the structural components.

# 8.0 Conclusions

In this project, four FRC mixes and seven UHPC mixes based on two types of Portland cement (Type I/II and Type III), five supplementary cementitious materials (silica fume, ultra-fine fly ash, Class C fly ash, Class F fly ash, and metakaolin) were developed and evaluated. The hydration behavior of the cementitious binders was characterized and linked to the evolutions of the physical and mechanical properties of UHPC. To understand the influence of fibers and curing conditions on the development of mechanical properties of UHPC, four types of fiber (micro-steel fiber, polyvinyl alcohol fiber, basalt fiber, and glass fiber) and two curing conditions (regular lime water curing and steam curing) were investigated. Early-age shrinkage behavior, permeability, and the development of compressive strength, flexural strength, direct tensile strength, and resistance against sulfate attack of the UHPC groups were analyzed. Laboratory mock-up tests on concrete closure gap connections cast between two panels were conducted to simulate the connection between two bridge deck panels and to confirm the viable applications of the developed UHPC mixture in this type of transportation infrastructure. The following key findings can be drawn from this thesis study:

(1) Fiber characterization – micro-fibers for UHPC. Glass fibers excited an average tensile strength of 1,134.2 MPa and an elongation rate of 28.63 at failure from the direct tension test, while PVA fiber showed 98% higher tensile strength and 3.1 times higher strain capacity at failure. The basalt fiber yielded an average tensile strength of 2,935 MPa, which is even higher than the micro-steel fiber (2,850 Mpa). However, due to the high modulus of elasticity and the brittle behavior, an average elongation rate of 40.64, which is comparable to the glass fiber but lower than PVA fiber, was obtained from the basalt fiber. The micro-steel fiber, PVA fiber, basalt fiber, and glass fiber are of comparable length (12-13 mm) but with different diameters, which are 200 μm, 100 μm, 16 μm, and 10 μm, respectively. The different microstructure, tensile strength, elastic modulus, and elongation rate determine the roles of these micro-fibers in the matrix of UHPC.

(2) Fiber characterization – macro-fibers for FRC. The hooked steel fiber showed an average tensile strength of 1,896.8 MPa, which is 72.4% higher than the provided strength (1,100 MPa). However, the crimped steel fiber yielded an average tensile strength of 628.7 MPa, which is 34.9% lower than the manufacturer's reported strength (965 MPa). Compared with steel fibers, the crimped synthetic fiber showed a lower average tensile strength of 69.06 MPa. The hooked steel fiber yielded average elongation rates (strain) at the peak stress and failure of 0.0648 and 0.0922, while the crimped steel fiber exhibited higher elongation rates of 0.1251 and 0.1425 at the peak stress and failure, respectively. Similar to the observations from the load-displacement curves, the crimped synthetic fiber yielded average elongation rates (strain) at the peak stress and failure of 0.1124 and 0.1324, which are comparable with the values obtained from the crimped steel fiber.

(3) Mix design – FRC. The development of FRC mixes was done using mixes from MassDOT. Modified versions of the mixes and modified procedure resulted in demonstrating that the mixes could adequately incorporate the fibers. Two mix designs from MassDOT were identified to be possible candidates to use for FRC, one with fly ash and the other with slag. A mix design based on Portland Cement Association (PCA) method for 4,000 psi concrete was also calculated to compare to the MassDOT mix. The mix design that was calculated using the PCA method was close to the MassDOT mixes thus it was decided to proceed using the already approved MassDOT mix designs with both the fly ash and slag mixes being tested. Four trial mixes of FRC were investigated and all the studied mixes exceeded the design strength of 4,000 psi, except for trial Mix 3. It was determined that either MassDOT mix works well with the incorporation of polypropylene or steel fibers. However, it is important to note that the fibers should be added directly after mixing the aggregates and letting it mix for 5 minutes to avoid clumping of the fibers and have a good distribution of fibers within the concrete.

(4) Mix design – UHPC. If only relying on the Modified Andersen-Andersen model and the least square method for the maximization of particle packing density in mixture design, the proportions of UHPC are reasonable and practical. Based on the literature review, the optimum contents of the binder in UHPC, as well as the optimum contents of each cementitious material in the binder, were determined in this study. It was found that, to tailor high strength in UHPC, a binder content between 45% and 62% is preferred. Based on the 28-day strength of UHPC, the optimum contents of cement, silica fume, fly ash, and metakaolin in the binder (paste) are 60% to 67%, 15% to 30%, 3.5% to 15%, and 10% to 20%, respectively. To address the current challenges of UHPC design, a novel two-step particle packing optimization method was developed in this study for the mixture design of UHPC. Step (i): based on the Modified Andreasen-Andersen model, particle size distributions of the studied materials were used to create the target curve for the maximized particle packing density. By employing the optimum binder content (i.e., 45% to 62%) and the optimum contents of each supplementary cementitious material (e.g., 60% to 67% for cement, 15% to 30% for silica fume, and 3.5 to 15% for fly ash) in the binder, the contents of SCMs were calculated. The outcome of this step is the optimum content of the entire binder in UHPC based on the selected materials to reach the target model curve (i.e., the maximized particle packing density). Step (ii): based on the identified binder content in Step (i), the content ranges of cement and supplementary cementitious materials in the binder were further refined, which were used as the new constraints for the least square method fitting. The outputs of this step are the final proportions of the UHPC, which not only ensure the proper contents of each constituent but also ensure the optimization of particle packing density based on the selected materials. Based on this new two-step method, seven UHPC mixes were developed based

on two types of Portland cement (Type I/II and Type III), five supplementary cementitious materials (silica fume, ultra-fine fly ash, Class C fly ash, Class F fly ash, and metakaolin)

(5) Hydration behavior of cementitious binder of the developed UHPC mixes. The isothermal calorimetry data showed that, compared with the Type I/II cement blends, not only the amplitude of the peaks was further raised, but they also occurred earlier from Mix 1, in which Type III cement was used indicating the enhanced initial cement hydration. The same phenomenon was also observed from the cumulative heat release curves, wherein more early-age hydration heat was released from Mix 1, which contains Type III cement. Compared with Class C fly ash, although the occurrence of the exothermic peak was moved earlier, lower peaks with a larger slope of acceleration stage were observed in the presence of Class F fly ash (Mix 2 vs. Mix 4 and Mix 3 vs. Mix 5). The high aluminate content of the metakaolin particles redefined the Al/Si ratio of the cement system and resulted in enhanced hydration of aluminates in Mix 6 and Mix 7.

(6) Reaction products of the UHPC binders – chemical bond. From the FTIR results, it is observed that Mix 1 exhibited higher Si-O and Si-O-Si bond intensity than Mix 2 indicating the formation of more C-S-H in Mix 1 at an early age due to the fast hydration reactions of Type III cement. However, comparable ultimate amounts of hydration products can be formed in Type I/II and Type III cements at later ages. The comparisons between Mix 2 and Mix 3, as well as that between Mix 4 and Mix 5, indicate that the use of UFFA can enhance the formation of the Si-O bond in the presence of both Class C and Class F fly ashes. The complete replacement of silica fume with metakaolin resulted in the decreased intensity of the Si-O bond.

(7) Reaction products of the UHPC binders – calcium hydroxide and C-S-H. The development of CH and bonder water contents in the UHPC cementitious binders as a function of time was determined through TGA. In line with the calorimetry results, Mix 1 showed a higher amount of C-S-H and ettringite than other binders. As the hydration and the pozzolanic reaction proceeded, the difference in C-S-H contents of the binders decreased. Although Type III cement exhibited a higher degree of hydration, the content of calcium hydroxide was lower than other groups. This indicates that the pozzolanic reactions between Type III cement and the supplementary cementitious materials, such as silica fume and micro-fly ash, have a higher reaction degree than other groups.

It should be noted that the content of calcium hydroxide decreased over time in all the groups along with the increased content of C-S-H, which is believed to have a positive correlation with strength development. Mix 2 showed more C-S-H and less calcium hydroxide than Mix 3 during the first 3 and 7 days. However, after 28 days and 60 days of hydration, Mix 3 showed less calcium

hydroxide than Mix 2 along with the formation of more C-S-H. This indicates the high pozzolanic reactivity of Class C fly ash for long-term reactions. A less significant role of micro-fly ash in the Class F binders (Mix 4 and Mix 5) than that in Class C fly ash binders (Mix 2 and Mix 3) was observed. This might be due to the fact that ultra-fine micro-fly ash (UFFA) is a type of Class F fly ash but with finer particles, and it can enhance the cement hydration in Mix 2 at early ages, while the pozzolanic reactions that consume CH are more significant in Mix 3. Different from the other binders, the two groups with metakaolin (Mix 6 and Mix 7) exhibited increases in CH contents with time.

(8) Reaction products of the UHPC binders – bond water and degree of hydration. The development of bound water content formed in the hydrates is commonly used to evaluate the degree of cement hydration. In agreement with the observations obtained from the calorimetry test, the UHPC binder of Mix 1 exhibited higher bound water content than Mix 2 indicating a higher hydration degree of Type III cement than Type I/II cement at the investigated ages. The use of UFFA in the presence of silica fume and Class C fly ash can enhance the early-age cement hydration, while after 28 days, the mix without UFFA showed a higher hydration degree. The incorporation of metakaolin resulted in high bound water contents in Mix 6 and Mix 7 indicating enhanced cement hydration.

The XRD results showed similar observations that, due to the fast hydration of the Type III cement, the binder of Mix 1 showed higher intensity of ettringite and lower hydrated phases than other binders at early ages, while more significant decreases in the unhydrated phases were observed from the Type I/II cement-based binders (Mix 2 to Mix 5) along with the higher intensity of cement hydration products, such as calcium hydroxide. Due to the high CaO content in Class C fly ash and their fast hydration, the binders of Mix 2 and Mix 3 showed a higher intensity of calcium hydroxide than that of Mix 4 and Mix 5 at the early ages. The benefit of the micro-fly ash in enhancing phase evolutions was observed. In line with the TGA results, it is observed that more CH was formed in the UHPC matrix with metakaolin. It was observed that silica fume showed a more effective CH-consuming capacity than metakaolin.

Due to the layered clay structure, metakaolin can absorb more water than silica fume, which negatively impacts the hydration of cement and pozzolanic reactions in the UHPC binder with extremely low water-to-binder ratios. The hydration of cement might need more than 0.25 g water/ g binder. Therefore, the cement is far from 100% degree of hydration in the UHPC groups. This highlights the necessity to improve the degree of reaction in the UHPC system, in particular, that with metakaolin, through physical or chemical approaches, such as steam curing. Toward this end, steam curing was used in this study as a secondary curing condition to investigate the influence of the curing process on the strength development of UHPC.

(9) UHPC performance – autogenous shrinkage. Due to the optimization of the particle packing density and the dense structure, the investigated UHPC mixes showed lower early-age autogenous shrinkage than neat Type I/II cement, except for Mix 4. UFFA can help to decrease the shrinkage of UHPC in the presence of Class C fly ash, while it can increase the initial autogenous shrinkage along with Class F fly ash.

(10) UHPC performance – compressive strength and influence of curing. The regularly cured Mix 1 exhibited the highest average 3-day compressive strength of 11,013 psi. This high early-age strength is due to the use of Type III cement, which is finer than Type I/II cement with a larger surface area. After 28 days and 60 days, the regularly cured Mix 1 exhibited average compressive strength of 17,817 psi and 18,986 psi, respectively, which are still the highest values among the investigated UHPC groups. The use of UFFA did not result in a higher strength in Mix 2.

The average 28-day compressive strength of the regularly cured Mix 3 is 3.6% higher than that of Mix 2, while the two groups yielded comparable strength after 60 days. The same trend is seen in the comparison of Mix 4 and Mix 5. After 60 days, the difference in strength between Mix 4 and Mix 5 is negligible. Based on the comparison between Mix 2 and Mix 3, as well as the comparison between Mix 4 and Mix 5, the use of UFFA did not play a critical role in enhancing the compressive strength of UHPC. The higher reactivity of Class F fly ash resulted in higher strength early-age than the mixes with Class C fly ash, while the later-age strength is less sensitive to the fly ash type. In line with the cement hydration data, silica fume was found to play a critical role in enhancing the strength development of UHPC, and metakaolin cannot completely replace silica fume.

The steam-cured Mix 3 yielded a 3-day compressive strength of 18,009 psi, which is 70% higher than its strength obtained from regular lime water curing. Likewise, the 7-day and 28-day compressive strength of the steam-cured Mix 3 is 35% and 17% higher than the regularly cured ones, respectively. The same enhancement in strength gain was also observed in other groups. It was observed that steam curing can provide sufficient humidity to UHPC, which improves cement hydration. This is considered the primary reason for the enhanced strength gain in steam curing, which is faster than that under regular lime water curing.

Decreased strength was obtained after replacing micro-steel fiber with other fibers (i.e., PVA, glass, and basalt fibers). This might be due to the less effective crack bridging role as they show smaller diameters and also the poor dispersion as clusters were observed, which might increase the porosity of the UHPC matrix.

(11) UHPC performance – flexural strength and influence of curing. The UHPC groups with micro-steel fibers showed ductile behavior under flexural loads with post-cracking loading capacities. The benefit of steam curing was again observed from the flexural behavior. The steam-cured UHPC specimens exhibited higher overall loading capacities under steam curing, which is in agreement with the development of compressive strength. The elevated temperature and relative humidity in steam curing help accelerate the hydration and strength of UHPC, in which the cement cannot fully hydrate in the presence of the extremely low water-to-cement ratio.

In contrast to the ductile behavior obtained from the micro-steel fiber-reinforced UHPC, no post-cracking behavior was observed from the UHPC with basalt and PVA fibers. Therefore, sudden failures were obtained from these groups. The UHPC with glass fiber showed a slight loading capacity after cracking, but the performance is far from the UHPC with micro-steel fibers. In line with the compressive strength results, the overall loading capacity of the UHPC decreased after replacing the micro-steel fiber with the three types of fibers, even after steam curing.

A 7-day flexural strength of 2,710.05 psi under regular lime water curing was yielded by the regularly cured Mix 5, which is 17.87%, and 3.65% lower than that of Mix 1 and Mix 6, respectively. The 7-day flexural strength of the regularly cured Mix 1 is 57.21% higher than that of Mix 3. Mix 1 gained a flexural strength of 3,915 psi after 28 days, which is the highest amongst all four selected mixes and 3.47% higher than Mix 3. The 28-day flexural strength of Mix 1 is 15.35% and 26.13% higher than Mix 5 and Mix 6, respectively. The combination of metakaolin with Class C fly ash and silica fume can yield comparable early-age strength with the UHPC containing Class F fly ash and silica fume. Class C fly ash along with silica fume can enhance the 28-day strength more significantly than Class F fly ash along with silica fume.

The steam-cured Mix 1 exhibited a 7-day flexural strength of 4,051 psi, which is 22.75% higher than that of the regular cured sample. Similarly, for Mix 3, Mix 5, and Mix 6, 79.07%, 5.13%, and 24.50% higher 7-day flexural strength was obtained from the steam-cured samples, respectively. A similar trend with less significant changes was also observed from the 28-day flexural strength results. These results indicate that, due to the extremely low water-to-cement (binder) ratio of UHPC, steam curing is an effective approach to enhance the hydration and pozzolanic reaction in the binder systems. It is worth noting that, although steam curing can help to increase both the early-age and later-age strength, its role is more significant for the gain of early-age strength.

(12) UHPC performance – flexural strength and influence of fiber. Compared with the UHPC with micro-steel fibers, the average 7-day flexural strength of UHPC reinforced with basalt fiber, PVA fiber, and glass fiber is 76%, 66%, and 37% lower, respectively. The same trend was also observed from the 28-day flexural

strength, where the UHPC with micro-steel fibers is 40%, 22%, and 20% higher than that yielded by the UHPC with basalt fiber, PVA fiber, and glass fibers, respectively.

(13) UHPC performance – failure modes under flexural loading. The micro-steel fibers bridging the major cracks can be clearly observed. The good bonding between the steel fiber and the UHPC matrix resulted in the elongation of the fibers in the cracking zone, which helps to transform the load and gives the beams a good load-carrying capacity and post-cracking behavior avoiding sudden failure. The well-distributed micro-steel fibers can be observed from the fiber avoiding the chances of agglomeration in the UHPC matrix. Different from the UHPC with micro-steel fibers, the specimen with basalt fiber, PVA fiber, and glass fiber did not show the development of cracks with effective fiber bridging. Instead, the fibers were broken or pulled out from the UHPC matrix. This might be due to the extremely small diameter and the smooth surface of these fibers. Since less energy was consumed from the easy pull out of these fibers and there does not exist post-cracking behavior, the uses of basalt fiber and PVA fiber in the UHPC mix did not contribute to improving the flexural strength and toughness.

Due to a large number of fibers pulled out from the UHPC beam, more energy than that from basalt fiber and PVA fiber reinforced UHPC was consumed due to the friction between the glass fibers and the matrix of UHPC. This explains the occurrence of post-racking behavior of the glass fiber-reinforced UHPC. Although the load kept decreasing after the peak load, the force didn't drop suddenly.

Given the failure modes, the morphology, and the load-deflection curves obtained from the 3-point flexural tests, it is clear that the micro-steel fiber exhibited the most effective crack bridging and load transformation role in the UHPC when crack started forming and developed among the investigated fibers. Although the crack bridging role was not observed from glass fiber, its efficient pull-out behavior consumed more energy than basalt and PVA fibers. Therefore, the toughness of UHPC was slightly improved. Due to the poor bonding with the UHPC matrix, the reinforcing roles of basalt fiber and PVA fiber in UHPC are lower than that of glass fiber.

(14) UHPC performance – direct tensile strength. Direct tension tests were conducted on dog-gone specimens of selected UHPC groups (Mix 1, Mix 3, Mix 5, and Mix 6). Three tensile material parameters, the peak tensile strength, the tensile strain at peak strength, and the tangent modulus of elasticity, were extracted from each recorded the stress–strain curve. The tensile strength at 7 days ranges from about 0.92 to 1.0 ksi while the values are in the range of 1.0 to 1.27 ksi at 28 days with an average increase of around 11% from the tensile strength at 7 days to 28 days. Mix 3 shows the greatest tensile strength values at both 7 and 28 days which might be due to the effect of Class C fly ash on

strength development. The second high tensile strength values are observed in the specimens of Mix 1, where the incorporation of Type III cement and micro-fly ash might be the most significant reasons for this phenomenon. The tangent elastic modulus values at 7 days are in the range of about 1745 to 2672 ksi while those values at 28 days are in the range of 1838 to 15623 ksi. The elastic modulus values at 28 days are about 234% higher than those at 7 days on average which is much higher than the difference between the tensile strength values of 7 and 28 days. This might be attributed to the specimens that are not broken in the middle region and the compliance issue with the data collected by the strain potentiometers.

(15) UHPC performance – permeability. The maximum average bulk resistivity of 120.1 kΩ-cm was yielded by Mix 1, which is in the "very low" chloride penetration range. This high bulk resistivity indicates the low permeability of Mix 1, which eventually indicates high durability. The bulk resistivity of Mix 2 and Mix 3 is 34.64% and 82.43% lower than the bulk resistivity of Mix 1, respectively. The bulk resistivity of Mix 2 is 78.49 kΩ-cm, which is still in the "very low" chloride penetration range, while the bulk resistivity of Mix 3 and Mix 4 indicate that the chloride penetrations of these two groups are on the board between "low" and "very low" levels. The incorporation of UFFA can help to reduce the pore connectivity in UHPC in the presence of Class C fly ash, while its role is negligible in the presence of Class F fly ash. This might be due to the fact that UFFA is also a Class F fly ash. The beneficial role of silica fume in densifying the pore structure of UHPC outperforming metakaolin was observed. When compared with regular concrete, UHPC mixtures exhibited significantly higher bulk resistivity indicating the denser microstructures, lower pore connectivity, and hence lower permeability of UHPC. It can be anticipated that the UHPC mixtures, especially Mix 1, Mix 2, and Mix 5, possess higher resistance against deteriorations than regular concrete thereby with higher long-term performance and extended service life.

(16) UHPC performance – resistance against sulfate attack. The volume expansion of regular mortar and UHPC Mix 1, Mix 2, Mix 3, and Mix 5 in terms of length change of prismatic bar specimens in sodium sulfate solution were investigated. All UHPC groups show an initial rapid increase of length change in the first two weeks which continued almost in a similar range for the later weeks. The regular mortar exhibited the highest expansion rate and magnitude among the investigated groups over the entire testing period. After 22 weeks, an expansion of 0.1082% was obtained from this control group. Due to the high volume of SCMs and denser microstructure, the four UHPC mixes exhibited lower sulfate-induced expansion than the regular mortar group. Mix 3 showed the lowest expansion values compared to the investigated UHPC mixes. It exhibited an expansion of ~0.0329% in 2 weeks, which was increased to ~0.0349% after 22 weeks. Mix 2 and Mix 1 showed the initial expansion of ~0.0438% and ~0.0468% after two weeks, respectively, and the expansion of ~0.0453% and ~0.0468% after 22 weeks of being exposed to sulfate solution,

respectively. The expansion induced by the sulfate attack exhibited an inverse correlation with the permeability of the UHPC matrix. With a lower permeability, less sulfate ions and moisture can immigrate into UHPC, which explains the least expansion observed from Mix 3.

(17) FRC performance – mechanical properties. The compression test results show that the Enduro Prime and Novocon XR fibers performed the best. They both reached compressive strengths greater than 5,000 psi, which is higher than the design strength of the mix which was 4,000 psi. Since both these fibers are crimped, it can be theorized that the shape of the fibers plays an important role in the compression strength of the concrete, and that crimped or corrugated fibers perform better than straight or hooked fibers. The splitting tensile results showed that the steel fibers performed better than the polypropylene fibers. The corrugated fibers (Mix 2 and Mix 4) resulted in slightly higher tensile strengths than the other fibers made of the same material (Mix 1 and Mix 3). The flexure test results also indicate the better performance of steel fibers than the polypropylene fibers. The difference in the fiber shape is more pronounced in the flexure test than in the splitting tensile test. Both the corrugated fibers resulted in higher flexural strengths than the straight and hooked fibers for their respective material.

(18) FRC performance – permeability. Permeability tests of FRC were carried out for Mix 1 and Mix 2, both mixes containing polypropylene fibers, at 7 days and 28 days. A summary of the tests can be found in Table 5.3 for 7 days and Table 5.4 for 28 days. For the 7-day test, the volume of the pour solution was 1.38 liters, and the diameter of the container was 4 in. For the 28-day test, the volume of the pour solution was 1.27 liters, and the diameter of the container was 4 in. For FRC Mix 1, the average bulk resistivity was 3.90 kΩ-cm for 7 days and 10.92 kΩ-cm for 28 days. For FRC Mix 2, the average bulk resistivity was 4.59 kΩ-cm for 7 days and 12.83 kΩ-cm for 28 days. The differences in the bulk resistivity could be due to differences in concrete porosity as the fibers have different effects on the pore structure of the concrete.

(19) Recommendations of UHPC mix design for large-scale batching and field application. By taking the complexity of constituents and ease of preparation into account, Mix 1, Mix 3, and Mix 5 use regular fly ashes only, which are more suitable for large-scale batching than Mix 2 and Mix 4. The difference between Mix 1 and Mix 3 lies in the type of cement. Type III cement has finer particles than Type I cement and hence it can generate slightly more hydration heat and higher early-age strength. Given its high pozzolanic activity, in Mix 6 and Mix 7, metakaolin was used to partially or completely replace silica fume. Regular fly ashes, silica fume, and metakaolin are widely available in the market. Type I/II cement is more commonly used than Type III cement in modern concrete structures. Based on the availability of the materials, the ease

of mixture design, as well as the mechanical properties, Mix 5, which uses Type I/II, silica fume, and Class F fly ash as cementitious materials, is considered one of the optimal mixture design for large-scale batching.

(20) Recommendations of mixing process for UHPC. Due to the ultra-low water-to-binder ratio, the UHPC mixtures are extremely dry before mixing. The high flowability cannot be achieved until the water and superplasticizer are uniformly dispersed and fully exposed to the cement and SCM grains. Instead of the regular drum concrete mixers, a powerful shear mixing is required to disrupt the dry particles and their agglomeration and to trigger sufficient contact between the dry particles with water and the superplasticizer. Shear mixers or pan mixers with blades are recommended to achieve uniform dispersion of water and dry particles. Compared with regular concrete, a longer mixing time (10 to 15 minutes) is needed to obtain homogeneously mixed UHPC mixtures.

(21) Recommendations of curing process for UHPC. In this project, two curing conditions have been investigated of UHPC: (i) regular lime water curing at room temperature, and (ii) steam curing consisting of 24-hour curing in molds at room temperature followed by steam curing at 90°C and relative humidity of 100% for 48 hours, which were then cooled down to room temperature and switched to regular lime water curing until tests. The hydration of cement and pozzolanic reactions of the SCMs can be accelerated thereby resulting in significantly enhanced strength gain, especially in early ages. The 3-day strength of steam-cured UHPC yielded strength values comparable to or exceeding the 28-day strength of the same mixtures cured in regular condition. This is found to be the most favorite role of steam curing. No significant increase in compressive strength was observed from the steam-cured UHPC after 3 days. Although the regularly cured UHPC specimens showed slower strength gain, their ultimate compressive strength after 60 days is comparable with the steam-cured specimens. From the results of compressive and flexural strength development of UHPC under these two curing conditions, it was found that steam curing can trigger rapid strength gain in UHPC but the ultimate strength of mature UHPC specimens was not significantly changed. Therefore, when high early-age strength is needed and steam curing facilities are available, steam curing can be employed to accelerate the strength development in the field.

(22) Recommendations of fiber reinforcement for UHPC. To understand the influence of fibers on the development of mechanical strength of UHPC (Mix 5), four types of fiber (PVA fiber, AR glass fiber, basalt fiber, and steel fiber) with the same fiber length (12-13 mm) at a constant volume fraction of 2% were investigated. Decreases in compressive strength were observed from the steam-cured UHPC with PVA and glass fiber. The UHPC specimens reinforced with steel fiber exhibited higher compressive and flexural strength than the same mixture design with other fibers. The results indicate that, at least based

on the UHPC mix investigated in this project, steel fiber with a diameter of $7.87 \times 10^{-3}$ inch (200 μm) and length of 0.51-inch (13 mm) exhibited the best reinforcing role in UHPC among the investigated fibers.

(23) Structural performance of UHPC – closure gap test. Two large-scale tests were conducted in this project to investigate the performance of longitudinal closure pour connections between two panels representing typical decks of Decked Bulb Tee girders. The concrete used for the closure pour was a modified version of the UHPC Mix 5 developed in this project. The two specimens were designed, fabricated, and tested under four-point bending in the structural laboratory. During the tests, flexural cracks and crushing of concrete were observed on the panels made of normal-strength concrete, outside of the closure pour region which used the UHPC. The specimens were loaded continuously until experiencing flexural failure characterized by concrete crushing at the top surface and cracks forming and widening from the bottom surface. The testing results indicate that the concrete closure pour connection comprised of straight bars detailing according to recommended practice obtained from PCI Northeast for decks of Decked Bulb Tee girders in combination with the developed mixture performed well in the experiment. The connections could reach the required strength and provide adequate transfer of forces between the structural components.

This page left blank intentionally.

# 9.0 References


[1] 544.4R, A., Guide to design with Fiber reinforced concrete, 2018.
[2] ASTM-C1116, *Standard Specification for Fiber-Reinforced Concrete*, ASTM International, West Conshocken, PA, 2015.
[3] Qureshi, L., An investigation on Strength Properties of Glass Fiber Reinforced Concrete, *International Journal of Engineering and Technical Research*, 2013.
[4] Chandramouli, K., P.S.R. Rao, P. Narayanan, S. Sekhar tirumala, P. Sravana, Strength properties of glass fiber concrete, *ARPN J Eng Appl Sci*, 5, 2010, pp. 1-6.
[5] Soutsos, M.N., T.T. Le, A.P. Lampropoulos, Flexural performance of fibre reinforced concrete made with steel and synthetic fibres, *Construction and Building Materials*, 36, 2012, pp. 704-710.
[6] Branston, J., S. Das, S.Y. Kenno, C. Taylor, Mechanical behaviour of basalt fibre reinforced concrete, *Construction and Building Materials*, 124, 2016, pp. 878-886.
[7] Sivakumar, A., M. Santhanam, A quantitative study on the plastic shrinkage cracking in high strength hybrid fibre reinforced concrete, *Cement and Concrete Composites*, 29, 2007, pp. 575-581.
[8] Simões, T., H. Costa, D. Dias-da-Costa, E. Júlio, Influence of fibres on the mechanical behaviour of fibre reinforced concrete matrixes, *Construction and Building Materials*, 137, 2017, pp. 548-556.
[9] Nili, M., V. Afroughsabet, Property assessment of steel–fibre reinforced concrete made with silica fume, *Construction and Building Materials*, 28, 2012, pp. 664-669.
[10] Naraganti, S.R., R.M.R. Pannem, J. Putta, Impact resistance of hybrid fibre reinforced concrete containing sisal fibres, *Ain Shams Engineering Journal*, 10, 2019, pp. 297-305.
[11] Alberti, M.G., A. Enfedaque, J.C. Gálvez, Fracture mechanics of polyolefin fibre reinforced concrete: Study of the influence of the concrete properties, casting procedures, the fibre length and specimen size, *Engineering Fracture Mechanics*, 154, 2016, pp. 225-244.
[12] Alberti, M., A. Enfedaque, J. Galvez, Fibre reinforced concrete with a combination of polyolefin and steel-hooked fibres, *Composite Structures*, 171, 2017.
[13] Amin, A., S.J. Foster, R.I. Gilbert, W. Kaufmann, Material characterisation of macro synthetic fibre reinforced concrete, *Cement and Concrete Composites*, 84, 2017, pp. 124-133.
[14] Soulioti, D., N.-M. Barkoula, A. Paipetis, T. Matikas, Effects of Fibre Geometry and Volume Fraction on the Flexural Behaviour of Steel-Fibre Reinforced Concrete, *Strain*, 47, 2009, pp. e535-e541.
[15] Li, Z., X. Wang, L. Wang, Properties of hemp fibre reinforced concrete composites, *Composites Part A: Applied Science and Manufacturing*, 37, 2006, pp. 497-505.
[16] Boulekbache, B., M. Hamrat, M. Chemrouk, S. Amziane, Flowability of fibre-reinforced concrete and its effect on the mechanical properties of the material, *Construction and Building Materials*, 24, 2010, pp. 1664-1671.
[17] Qian, C.X., P. Stroeven, Development of hybrid polypropylene-steel fibre-reinforced concrete, *Cement and Concrete Research*, 30, 2000, pp. 63-69.
[18] Acikgenc Ulas, M., K.E. Alyamac, Z.C. Ulucan, Development of nomogram for the practical mix design of steel fiber reinforced concrete, *Construction and Building Materials*, 181, 2018, pp. 437-446.

[19] ASTM-C150, *Standard Specification for Portland Cement*, ASTM International, West Conshocken, PA, 2000.
[20] *ACI 544.9R-17 Report on Measuring Mechanical Properties of Hardened Fiber-Reinforced Concrete (Reported by ACI Committee 544)*, American Concrete Institute, Farmington Hills, MI, 2017.
[21] Andreasen, A., Über die Beziehung zwischen Kornabstufung und Zwischenraum in Produkten aus losen Körnern (mit einigen Experimenten), *Kolloid-Zeitschrift*, 50, 1930, pp. 217-228.
[22] Funk, J.E., D.R. Dinger, *Predictive process control of crowded particulate suspensions: applied to ceramic manufacturing*, Springer Science & Business Media2013.
[23] Brouwers, H., Particle-size distribution and packing fraction of geometric random packings, *Physical review E*, 74, 2006, pp. 031309.
[24] Brouwers, H., H. Radix, Self-compacting concrete: theoretical and experimental study, *Cement and concrete research*, 35, 2005, pp. 2116-2136.
[25] Hunger, M., *An integral design concept for ecological self-compacting concrete*, University of Technology2010.
[26] Kang, S.T., B.Y. Lee, J.-K. Kim, Y.Y. Kim, The effect of fibre distribution characteristics on the flexural strength of steel fibre-reinforced ultra high strength concrete, *Construction and Building Materials*, 25, 2011, pp. 2450-2457.
[27] Kim, D.J., S.H. Park, G.S. Ryu, K.T. Koh, Comparative flexural behavior of Hybrid Ultra High Performance Fiber Reinforced Concrete with different macro fibers, *Construction and Building Materials*, 25, 2011, pp. 4144-4155.
[28] Hassan, A.M.T., S.W. Jones, G.H. Mahmud, Experimental test methods to determine the uniaxial tensile and compressive behaviour of ultra high performance fibre reinforced concrete (UHPFRC), *Construction and Building Materials*, 37, 2012, pp. 874-882.
[29] Abbas, S., A.M. Soliman, M.L. Nehdi, Exploring mechanical and durability properties of ultra-high performance concrete incorporating various steel fiber lengths and dosages, *Construction and Building Materials*, 75, 2015, pp. 429-441.
[30] Yoo, D.-Y., J.-H. Lee, Y.-S. Yoon, Effect of fiber content on mechanical and fracture properties of ultra high performance fiber reinforced cementitious composites, *Composite Structures*, 106, 2013, pp. 742-753.
[31] Yu, R., P. Spiesz, H.J.H. Brouwers, Development of Ultra-High Performance Fibre Reinforced Concrete (UHPFRC): Towards an efficient utilization of binders and fibres, *Construction and Building Materials*, 79, 2015, pp. 273-282.
[32] Arel, H.Ş., Effects of curing type, silica fume fineness, and fiber length on the mechanical properties and impact resistance of UHPFRC, *Results in Physics*, 6, 2016, pp. 664-674.
[33] Gesoglu, M., E. Güneyisi, G.F. Muhyaddin, D.S. Asaad, Strain hardening ultra-high performance fiber reinforced cementitious composites: Effect of fiber type and concentration, *Composites Part B: Engineering*, 103, 2016, pp. 74-83.
[34] Liu, J., F. Han, G. Cui, Q. Zhang, J. Lv, L. Zhang, Z. Yang, Combined effect of coarse aggregate and fiber on tensile behavior of ultra-high performance concrete, *Construction and Building Materials*, 121, 2016, pp. 310-318.
[35] Kang, S.-T., J.-I. Choi, K.-T. Koh, K.S. Lee, B.Y. Lee, Hybrid effects of steel fiber and microfiber on the tensile behavior of ultra-high performance concrete, *Composite Structures*, 145, 2016, pp. 37-42.

[36] Wu, Z., C. Shi, W. He, L. Wu, Effects of steel fiber content and shape on mechanical properties of ultra high performance concrete, *Construction and Building Materials*, 103, 2016, pp. 8-14.
[37] Alsalman, A., C.N. Dang, W. Micah Hale, Development of ultra-high performance concrete with locally available materials, *Construction and Building Materials*, 133, 2017, pp. 135-145.
[38] Park, J.-J., D.-Y. Yoo, G.-J. Park, S.-W. Kim, Feasibility of Reducing the Fiber Content in Ultra-High-Performance Fiber-Reinforced Concrete under Flexure, *Materials*, 10, 2017, pp. 118.
[39] Su, Y., J. Li, C. Wu, P. Wu, M. Tao, X.-b. Li, Mesoscale study of steel fibre-reinforced ultra-high performance concrete under static and dynamic loads, *Materials & Design*, 116, 2017, pp. 340-351.
[40] Wu, Z., C. Shi, K.H. Khayat, Multi-scale investigation of microstructure, fiber pullout behavior, and mechanical properties of ultra-high performance concrete with nano-CaCO3 particles, *Cement and Concrete Composites*, 86, 2018, pp. 255-265.
[41] Chun, B., D.-Y. Yoo, Hybrid effect of macro and micro steel fibers on the pullout and tensile behaviors of ultra-high-performance concrete, *Composites Part B: Engineering*, 162, 2019, pp. 344-360.
[42] Wu, Z., K.H. Khayat, C. Shi, How do fiber shape and matrix composition affect fiber pullout behavior and flexural properties of UHPC?, *Cement and Concrete Composites*, 90, 2018, pp. 193-201.
[43] Arora, A., Y. Yao, B. Mobasher, N. Neithalath, Fundamental insights into the compressive and flexural response of binder- and aggregate-optimized ultra-high performance concrete (UHPC), *Cement and Concrete Composites*, 98, 2019, pp. 1-13.
[44] Chkheiwer, A.H., J.A. Kadim, Factors effecting on the compressive and tensile strength of reactive powder concrete made with local materials, *IOP Conference Series. Materials Science and Engineering*, 584, 2019.
[45] Fan, D.Q., R. Yu, Z.H. Shui, C.F. Wu, Q.L. Song, Z.J. Liu, Y. Sun, X. Gao, Y.J. He, A new design approach of steel fibre reinforced ultra-high performance concrete composites: Experiments and modeling, *Cement and Concrete Composites*, 110, 2020, pp. 103597.
[46] Ragalwar, K., W.F. Heard, B.A. Williams, D. Kumar, R. Ranade, On enhancing the mechanical behavior of ultra-high performance concrete through multi-scale fiber reinforcement, *Cement and Concrete Composites*, 105, 2020, pp. 103422.
[47] Yan, P., B. Chen, S. Afgan, M. Aminul Haque, M. Wu, J. Han, Experimental research on ductility enhancement of ultra-high performance concrete incorporation with basalt fibre, polypropylene fibre and glass fibre, *Construction and Building Materials*, 279, 2021, pp. 122489.
[48] Mustapha A. Ibrahim, M.F.M.A.I., H. Jessica Amanda, Effect of Material Constituents on Mechanical and Fracture Mechanics Properties of Ultra-High-Performance Concrete, *ACI Materials Journal*, 114.
[49] Endicott, W., A whole new cast - Innovative concrete used on Iowa bridge eliminates reinforcement and creates new concept for precast concrete bridges *ASPIRE*, 2007, pp. 26.
[50] Brian Keierleber, B.C., Dean Bierwagen, Terry Wipf, Ahmad Abu-Hawash, FHWA, Iowa optimize pi girder - Buchanan County constructs a bridge using ultra-high performance concrete girders, *ASPIRE*, 2010, pp. 24.

[51] Shutt, C.A., UHPC Joint Provides New Solution - New York State's first application of deck bulb-tee girders results from new joint design, *ASPIRE*, 2009, pp. 28.
[52] Brian P. Moore, W.C., Little Cedar Creek Bridge— Big Innovation, *ASPIRE*, 2012, pp. 27.
[53] Arash Esmaili Zaghi, K.W., Kevin Zmetra, Kevin McMullen, *Repair of steel beam/girder ends with ultra high strength concrete (phase I)*, 2015.
[54] McMullen, K.F., A.E. Zaghi, *Evaluation of UHPC as a Repair Material for Corroded Steel Bridge Girders*, International Interactive Symposium on Ultra-High Performance Concrete, Iowa State University Digital Press, 2019.
[55] Farzad, M., M. Shafieifar, A. Azizinamini, Retrofitting of Bridge Columns Using UHPC, *Journal of Bridge Engineering*, 24, 2019, pp. 04019121.
[56] Sritharan, S., G. Doiron, D. Bierwagen, B. Keierleber, A. Abu-Hawash, First Application of UHPC Bridge Deck Overlay in North America, *Transportation Research Record*, 2672, 2018, pp. 40-47.
[57] Berry, M., R. Scherr, K. Matteson, Feasibility of Non-Proprietary Ultra-High Performance Concrete (UHPC) for use in Highway Bridges in Montana: Phase II Field Application, 2021.
[58] ASTM-C230/C230M, *Standard Specification for Flow Table for Use in Tests of Hydraulic Cement*, ASTM International, West Conshohocken, PAWest Conshohocken, PA, 2021.
[59] ASTM-C1437, *Standard Test Method for Flow of Hydraulic Cement Mortar*, ASTM International, West Conshohocken, PAWest Conshohocken, PA, 2015.
[60] EN, D., Methods of Test for Mortar for Masonry–Part 3: Determination of Consistence of Fresh Mortar, 2007.
[61] Institution, B.S., *BS-EN-12350-9:2010-Testing fresh concrete Part 9: Self-compacting concrete — V- funnel test*, BSI, London, UKLondon, UK, 2010.
[62] Kim, H., T. Koh, S. Pyo, Enhancing flowability and sustainability of ultra high performance concrete incorporating high replacement levels of industrial slags, *Construction and Building Materials*, 123, 2016, pp. 153-160.
[63] Abdulkareem, O.M., A.B. Fraj, M. Bouasker, A. Khelidj, Effect of chemical and thermal activation on the microstructural and mechanical properties of more sustainable UHPC, *Construction and Building Materials*, 169, 2018, pp. 567-577.
[64] Liu, K., R. Yu, Z. Shui, X. Li, C. Guo, B. Yu, S. Wu, Optimization of autogenous shrinkage and microstructure for Ultra-High Performance Concrete (UHPC) based on appropriate application of porous pumice, *Construction and Building Materials*, 214, 2019, pp. 369-381.
[65] ASTM-C1202, Standard test method for electrical indication of concrete's ability to resist chloride ion penetration, *Annual book of ASTM standards*, 4, 1997, pp. 639-644.
[66] Yu, R., P. Spiesz, H. Brouwers, Development of an eco-friendly Ultra-High Performance Concrete (UHPC) with efficient cement and mineral admixtures uses, *Cement and Concrete Composites*, 55, 2015, pp. 383-394.
[67] ASTM-C642, *Standard Test Method for Density, Absorption, and Voids in Hardened Concrete*, ASTM International, West Conshohocken, PAWest Conshohocken, 2006.
[68] Ganesan, K., K. Rajagopal, K. Thangavel, Rice husk ash blended cement: Assessment of optimal level of replacement for strength and permeability properties of concrete, *Construction and building materials*, 22, 2008, pp. 1675-1683.

[69] Kollek, J., The determination of the permeability of concrete to oxygen by the Cembureau method—a recommendation, *Materials and structures*, 22, 1989, pp. 225-230.
[70] Loosveldt, H., Z. Lafhaj, F. Skoczylas, Experimental study of gas and liquid permeability of a mortar, *Cement and concrete research*, 32, 2002, pp. 1357-1363.
[71] Concrete, P.C., Evaluation of Rapid Determination of the Chloride Permeability of Portland Cement Concrete By AASHTO T277-83, 1987.
[72] Coutinho, J.S., The combined benefits of CPF and RHA in improving the durability of concrete structures, *Cement and Concrete Composites*, 25, 2003, pp. 51-59.
[73] Xie, T., C. Fang, M.M. Ali, P. Visintin, Characterizations of autogenous and drying shrinkage of ultra-high performance concrete (UHPC): An experimental study, *Cement and Concrete Composites*, 91, 2018, pp. 156-173.
[74] Standard, A., *AS/NZS 2350.13. Methods for Testing Portland, Blended and Masonry Cements – Determination of Drying Shrinkage of Cement Mortars*, Standards Australia, Sydney, AustraliaSydney, Australia, 2000.
[75] ASTM-C1698, *Standard Test Method for Autogenous Strain of Cement Paste and Mortar*, ASTM International, West Conshohocken, PAWest Conshohocken, PA, 2009.
[76] Liu, Y., Y. Wei, Effect of calcined bauxite powder or aggregate on the shrinkage properties of UHPC, *Cement and Concrete Composites*, 118, 2021, pp. 103967.
[77] Yalçınkaya, Ç., H. Yazıcı, Effects of ambient temperature and relative humidity on early-age shrinkage of UHPC with high-volume mineral admixtures, *Construction and Building Materials*, 144, 2017, pp. 252-259.
[78] Valipour, M., K.H. Khayat, Coupled effect of shrinkage-mitigating admixtures and saturated lightweight sand on shrinkage of UHPC for overlay applications, *Construction and Building Materials*, 184, 2018, pp. 320-329.
[79] ASTM-C1856/C1856M, *Standard Practice for Fabricating and Testing Specimens of Ultra-High Performance Concrete1*, ASTM International, West Conshohocken, PAWest Conshohocken, 2017.
[80] Xu, Y., J. Liu, J. Liu, P. Zhang, Q. Zhang, L. Jiang, Experimental studies and modeling of creep of UHPC, *Construction and Building Materials*, 175, 2018, pp. 643-652.
[81] Garas, V., K. Kurtis, L. Kahn, Creep of UHPC in tension and compression: effect of thermal treatment, *Cement and Concrete Composites*, 34, 2012, pp. 493-502.
[82] Zhu, L., J.-J. Wang, X. Li, G.-Y. Zhao, X.-J. Huo, Experimental and numerical study on creep and shrinkage effects of ultra high-performance concrete beam, *Composites Part B: Engineering*, 184, 2020, pp. 107713.
[83] Kusumawardaningsih, Y., E. Fehling, M. Ismail, UHPC compressive strength test specimens: Cylinder or cube?, *Procedia Engineering*, 125, 2015, pp. 1076-1080.
[84] 17671-, G.T., *Method of testing cements-Determination of strength*, Chinese Standard Institution Press Beijing, China, 1999.
[85] Su, Y., J. Li, C. Wu, P. Wu, Z.-X. Li, Effects of steel fibres on dynamic strength of UHPC, *Construction and Building Materials*, 114, 2016, pp. 708-718.
[86] Shafieifar, M., M. Farzad, A. Azizinamini, Experimental and numerical study on mechanical properties of Ultra High Performance Concrete (UHPC), *Construction and Building Materials*, 156, 2017, pp. 402-411.
[87] Concrete, A.I.C.C.o., C. Aggregates, *Standard test method for compressive strength of cylindrical concrete specimens*, ASTM international2014.

[88] ASTM, *Standard test method for compressive strength of hydraulic cement mortars (using 2-in. or [50-mm] cube specimens)*, ASTM International2013.
[89] Abellán-García, J., Four-layer perceptron approach for strength prediction of UHPC, *Construction and Building Materials*, 256, 2020, pp. 119465.
[90] ASTM, Annual Book of ASTM Standards: nonferrous metal products, electrical conductors, 1989.
[91] Abellán-García, J., K-fold validation neural network approach for predicting the one-day compressive strength of UHPC, *Advances in Civil Engineering Materials*, 10, 2021, pp. 223-243.
[92] Wu, Z., C. Shi, K.H. Khayat, L. Xie, Effect of SCM and nano-particles on static and dynamic mechanical properties of UHPC, *Construction and Building Materials*, 182, 2018, pp. 118-125.
[93] Zhang, Y., C. Zhang, Y. Zhu, J. Cao, X. Shao, An experimental study: various influence factors affecting interfacial shear performance of UHPC-NSC, *Construction and Building Materials*, 236, 2020, pp. 117480.
[94] Alkhrdaji, T., E.R. Fyfe, V.M. Karbhari, M. Schupack, C.E. Bakis, A. Ganjehlou, J.G. Korff, D.W. Scott, P. Balaguru, D.J. Gee, Guide Test Methods for Fiber-Reinforced Polymers (FRPs) for Reinforcing or Strengthening Concrete Structures, 2004.
[95] Zeng, J.-J., Y.-Y. Ye, W.-M. Quach, G. Lin, Y. Zhuge, J.-K. Zhou, Compressive and transverse shear behaviour of novel FRP-UHPC hybrid bars, *Composite Structures*, 281, 2022, pp. 115001.
[96] Jang, H.-O., H.-S. Lee, K. Cho, J. Kim, Experimental study on shear performance of plain construction joints integrated with ultra-high performance concrete (UHPC), *Construction and Building Materials*, 152, 2017, pp. 16-23.
[97] Chen, Q., R. Ma, H. Li, Z. Jiang, H. Zhu, Z. Yan, Effect of chloride attack on the bonded concrete system repaired by UHPC, *Construction and Building Materials*, 272, 2021, pp. 121971.
[98] Ghafari, E., M. Arezoumandi, H. Costa, E. Julio, Influence of nano-silica addition on durability of UHPC, *Construction and Building Materials*, 94, 2015, pp. 181-188.
[99] Poursaee, A., Potentiostatic transient technique, a simple approach to estimate the corrosion current density and Stern–Geary constant of reinforcing steel in concrete, *Cement and Concrete Research*, 40, 2010, pp. 1451-1458.
[100] ASTM-C1260, *StandardTest Method for Potential Alkali Reactivity of Aggregates (Mortar-Bar Method)*, ASTM International, West Conshohocken, PAWest Conshohocken, PA, 2014.
[101] Piérard, J., B. Dooms, N. Cauberg, *Durability evaluation of different types of UHPC*, Proceedings of the RILEM-fib-AFGC International Symposium on Ultra-High Performance Fiber-Reinforced Concrete, 2013, pp. 275-284.
[102] C1260, A., *Standard test method for potential alkali reactivity of aggregates (mortar–bar method)*, ASTM International West Conshohocken, PA, USA, 2007.
[103] Graybeal, B.A., *Material property characterization of ultra-high performance concrete*, United States. Federal Highway Administration. Office of Infrastructure …, 2006.
[104] Abbas, S., M. Nehdi, M. Saleem, Ultra-high performance concrete: Mechanical performance, durability, sustainability and implementation challenges, *International Journal of Concrete Structures and Materials*, 10, 2016, pp. 271-295.

[105] Aguayo, F.M., T. Drimalas, K.J. Folliard, An Accelerated Test Method to Evaluate Cementitious Mixtures Subjected to Chemical Sulfate Attack, *Advances in Civil Engineering Materials*, 8, 2019, pp. 190-206.
[106] Faried, A.S., S.A. Mostafa, B.A. Tayeh, T.A. Tawfik, Mechanical and durability properties of ultra-high performance concrete incorporated with various nano waste materials under different curing conditions, *Journal of Building Engineering*, 43, 2021, pp. 102569.
[107] Lessly, S.H., S.L. Kumar, R.R. Jawahar, L. Prabhu, Durability properties of modified ultra-high performance concrete with varying cement content and curing regime, *Materials Today: Proceedings*, 45, 2021, pp. 6426-6432.
[108] Matalkah, F., P. Soroushian, Freeze thaw and deicer salt scaling resistance of concrete prepared with alkali aluminosilicate cement, *Construction and Building Materials*, 163, 2018, pp. 200-213.
[109] ASTM-C672, *Standard Test Method for Scaling Resistance of Concrete Surfaces Exposed to Deicing Chemicals*, ASTM International, West Conshohocken, PA West Conshohocken, PA, 2003.
[110] ASTM-C666/C666M, *Standard Test Method for Resistance of Concrete to Rapid Freezing and Thawing1*, ASTM International, West Conshohocken, PAWest Conshohocken, 2016.
[111] Paul, S.C., G.P.A.G. van Zijl, B. Šavija, Effect of Fibers on Durability of Concrete: A Practical Review, *Materials*, 13, 2020, pp. 4562.
[112] Guerini, V., A. Conforti, G. Plizzari, S. Kawashima, Influence of Steel and Macro-Synthetic Fibers on Concrete Properties, *Fibers*, 6, 2018, pp. 47.
[113] Yadav, M., M.A. Sharma, Comparative Analysis between Use of Polypropylene Fibers and Steel Fibers in Fiber Reinforced Concrete–A Review, 2020.
[114] Wilson, E., N. Philip, The Influence of Fibres in Concrete: A Review, *International Journal of Civil Engineering (IJCE)*, 4, 2015, pp. 1-10.
[115] Singh, A.P., D. Singhal, Permeability of Steel Fibre Reinforced Concrete Influence of Fibre Parameters, *Procedia Engineering*, 14, 2011, pp. 2823-2829.
[116] Eren, Ö., K. Marar, Effect of steel fibers on plastic shrinkage cracking of normal and high strength concretes, *Materials Research*, 13, 2010, pp. 135-141.
[117] Zhang, L., J. Zhao, C. Fan, Z. Wang, Effect of Surface Shape and Content of Steel Fiber on Mechanical Properties of Concrete, *Advances in Civil Engineering*, 2020, pp. 8834507.
[118] Choi, W.-C., S.-J. Jang, H.-D. Yun, Interface Bond Characterization between Fiber and Cementitious Matrix, *International Journal of Polymer Science*, 2015.
[119] Sadiqul Islam, G.M., S.D. Gupta, Evaluating plastic shrinkage and permeability of polypropylene fiber reinforced concrete, *International Journal of Sustainable Built Environment*, 5, 2016, pp. 345-354.
[120] E701, A.C.I.C., *E-2(00) Reinforcement for Concrete*, 2003.
[121] Lee, S.-J., D.-Y. Yoo, D.-Y. Moon, Effects of Hooked-End Steel Fiber Geometry and Volume Fraction on the Flexural Behavior of Concrete Pedestrian Decks, *Applied Sciences*, 9, 2019, pp. 1241.
[122] Barman, M., B. Hansen, T. Burnham, M. Masten, Structural fiber choice for thin concrete pavements can have a significant impact on quality, *Roads & Bridges*, January, 2020.

[123] Khazanovich, L., D. Tompkins, Thin Concrete Overlays : [techbrief], 2017.
[124] Akhnoukh, A.K., H. Xie, Welded wire reinforcement versus random steel fibers in precast/prestressed ultra-high performance concrete I-girders, *Construction and Building Materials*, 24, 2010, pp. 2200-2207.
[125] Arora, A., A. Almujaddidi, F. Kianmofrad, B. Mobasher, N. Neithalath, Material design of economical ultra-high performance concrete (UHPC) and evaluation of their properties, *Cement and Concrete Composites*, 104, 2019, pp. 103346.
[126] Arora, A., Y. Yao, B. Mobasher, N. Neithalath, Fundamental insights into the compressive and flexural response of binder-and aggregate-optimized ultra-high performance concrete (UHPC), *Cement and Concrete Composites*, 98, 2019, pp. 1-13.
[127] Bonneau, O., M. Lachemi, E. Dallaire, J. Dugat, P.-C. Aitcin, Mechanical properties and durability of two industrial reactive powder concretes, *Materials Journal*, 94, 1997, pp. 286-290.
[128] Cao, Y., Q. Yu, H. Brouwers, W. Chen, Predicting the rate effects on hooked-end fiber pullout performance from Ultra-High Performance Concrete (UHPC), *Cement and Concrete Research*, 120, 2019, pp. 164-175.
[129] Chang, W., W. Zheng, Effects of key parameters on fluidity and compressive strength of ultra-high performance concrete, *Structural Concrete*, 21, 2020, pp. 747-760.
[130] Chen, T., X. Gao, M. Ren, Effects of autoclave curing and fly ash on mechanical properties of ultra-high performance concrete, *Construction and Building Materials*, 158, 2018, pp. 864-872.
[131] Fan, D., R. Yu, Z. Shui, K. Liu, Y. Feng, S. Wang, K. Li, J. Tan, Y. He, A new development of eco-friendly Ultra-High performance concrete (UHPC): Towards efficient steel slag application and multi-objective optimization, *Construction and Building Materials*, 306, 2021, pp. 124913.
[132] Fang, Z., H. Fang, P. Li, H. Jiang, G. Chen, Interfacial shear and flexural performances of steel–precast UHPC composite beams: Full-depth slabs with studs vs. demountable slabs with bolts, *Engineering Structures*, 260, 2022, pp. 114230.
[133] Graybeal, B.A., J.L. Hartmann, *Strength and durability of ultra-high performance concrete*, Concrete Bridge Conference, 2003, pp. 20.
[134] Gu, C., G. Ye, W. Sun, Ultrahigh performance concrete-properties, applications and perspectives, *Science China Technological Sciences*, 58, 2015, pp. 587-599.
[135] Hisseine, O.A., N.A. Soliman, B. Tolnai, A. Tagnit-Hamou, Nano-engineered ultra-high performance concrete for controlled autogenous shrinkage using nanocellulose, *Cement and Concrete Research*, 137, 2020, pp. 106217.
[136] Homel, M.A., J. Iyer, S.J. Semnani, E.B. Herbold, Mesoscale model and X-ray computed micro-tomographic imaging of damage progression in ultra-high-performance concrete, *Cement and Concrete Research*, 157, 2022, pp. 106799.
[137] Huang, H., X. Gao, K.H. Khayat, Contribution of fiber orientation to enhancing dynamic properties of UHPC under impact loading, *Cement and Concrete Composites*, 121, 2021, pp. 104108.
[138] Huang, H., X. Gao, K.H. Khayat, Contribution of fiber alignment on flexural properties of UHPC and prediction using the Composite Theory, *Cement and Concrete Composites*, 118, 2021, pp. 103971.

[139] Huang, H., L. Teng, X. Gao, K.H. Khayat, F. Wang, Z. Liu, Effect of carbon nanotube and graphite nanoplatelet on composition, structure, and nano-mechanical properties of CSH in UHPC, *Cement and Concrete Research*, 154, 2022, pp. 106713.
[140] Huang, H., L. Teng, X. Gao, K.H. Khayat, F. Wang, Z. Liu, Use of saturated lightweight sand to improve the mechanical and microstructural properties of UHPC with fiber alignment, *Cement and Concrete Composites*, 129, 2022, pp. 104513.
[141] Huang, H., L. Teng, K.H. Khayat, X. Gao, F. Wang, Z. Liu, For the improvement of mechanical and microstructural properties of UHPC with fiber alignment using carbon nanotube and graphite nanoplatelet, *Cement and Concrete Composites*, 129, 2022, pp. 104462.
[142] Jung, M., Y.-s. Lee, S.-G. Hong, J. Moon, Carbon nanotubes (CNTs) in ultra-high performance concrete (UHPC): Dispersion, mechanical properties, and electromagnetic interference (EMI) shielding effectiveness (SE), *Cement and Concrete Research*, 131, 2020, pp. 106017.
[143] Le Hoang, A., E. Fehling, D.-K. Thai, C. Van Nguyen, Evaluation of axial strength in circular STCC columns using UHPC and UHPFRC, *Journal of Constructional Steel Research*, 153, 2019, pp. 533-549.
[144] Lee, N., K. Koh, S. Park, G. Ryu, Microstructural investigation of calcium aluminate cement-based ultra-high performance concrete (UHPC) exposed to high temperatures, *Cement and Concrete Research*, 102, 2017, pp. 109-118.
[145] Lee, N.K., K. Koh, M.O. Kim, G. Ryu, Uncovering the role of micro silica in hydration of ultra-high performance concrete (UHPC), *Cement and Concrete Research*, 104, 2018, pp. 68-79.
[146] Li, P., Q. Yu, H. Brouwers, W. Chen, Conceptual design and performance evaluation of two-stage ultra-low binder ultra-high performance concrete, *Cement and Concrete Research*, 125, 2019, pp. 105858.
[147] Li, Y., P. Pimienta, N. Pinoteau, K.H. Tan, Effect of aggregate size and inclusion of polypropylene and steel fibers on explosive spalling and pore pressure in ultra-high-performance concrete (UHPC) at elevated temperature, *Cement and Concrete Composites*, 99, 2019, pp. 62-71.
[148] Liu, K., C. Wu, X. Li, M. Tao, J. Li, J. Liu, S. Xu, Fire damaged ultra-high performance concrete (UHPC) under coupled axial static and impact loading, *Cement and Concrete Composites*, 126, 2022, pp. 104340.
[149] Máca, P., R. Sovják, P. Konvalinka, Mix design of UHPFRC and its response to projectile impact, *International Journal of Impact Engineering*, 63, 2014, pp. 158-163.
[150] Meng, W., K.H. Khayat, Effect of hybrid fibers on fresh properties, mechanical properties, and autogenous shrinkage of cost-effective UHPC, *J. Mater. Civ. Eng*, 30, 2018, pp. 04018030.
[151] Miller, R.A., T. Ahlborn, L. Johal, S. Ahmad, P. Jost, J. Billerbeck, C. Leidholdt, W. Boles, C. Magnesio, M. Bury, High Performance Concrete Showcase Bridges, 2001.
[152] Mobasher, B., A. Li, Y. Yao, A. Arora, N. Neithalath, Characterization of toughening mechanisms in UHPC through image correlation and inverse analysis of flexural results, *Cement and Concrete Composites*, 122, 2021, pp. 104157.
[153] Nguyen, T.-T., H.-T. Thai, T. Ngo, Optimised mix design and elastic modulus prediction of ultra-high strength concrete, *Construction and Building Materials*, 302, 2021, pp. 124150.

[154] Norhasri, M.M., M. Hamidah, A.M. Fadzil, Inclusion of nano metaclayed as additive in ultra high performance concrete (UHPC), *Construction and Building Materials*, 201, 2019, pp. 590-598.
[155] Ouyang, X., C. Shi, Z. Wu, K. Li, B. Shan, J. Shi, Experimental investigation and prediction of elastic modulus of ultra-high performance concrete (UHPC) based on its composition, *Cement and Concrete Research*, 138, 2020, pp. 106241.
[156] Pezeshkian, M., A. Delnavaz, M. Delnavaz, Development of UHPC mixtures using natural zeolite and glass sand as replacements of silica fume and quartz sand, *European Journal of Environmental and Civil Engineering*, 25, 2021, pp. 2023-2038.
[157] Reda, M., N. Shrive, J. Gillott, Microstructural investigation of innovative UHPC, *Cement and Concrete Research*, 29, 1999, pp. 323-329.
[158] Riedel, P., T. Leutbecher, S. Piotrowski, C. Heese, Ratios of compressive strengths of ultra-high-performance concrete specimens of different shapes and sizes, *ACI Materials Journal*, 116, 2019, pp. 139-149.
[159] Rui, Y., L. Kangning, Y. Tianyi, T. Liwen, D. Mengxi, S. Zhonghe, Comparative study on the effect of steel and polyoxymethylene fibers on the characteristics of Ultra-High Performance Concrete (UHPC), *Cement and Concrete Composites*, 2022, pp. 104418.
[160] Shah, H.A., Q. Yuan, N. Photwichai, Use of materials to lower the cost of ultra-high-performance concrete–A review, *Construction and Building Materials*, 327, 2022, pp. 127045.
[161] Shi, Y., G. Long, X. Zen, Y. Xie, T. Shang, Design of binder system of eco-efficient UHPC based on physical packing and chemical effect optimization, *Construction and Building Materials*, 274, 2021, pp. 121382.
[162] Sobuz, H., P. Visintin, M.M. Ali, M. Singh, M. Griffith, A. Sheikh, Manufacturing ultra-high performance concrete utilising conventional materials and production methods, *Construction and Building materials*, 111, 2016, pp. 251-261.
[163] Sohail, M.G., B. Wang, A. Jain, R. Kahraman, N.G. Ozerkan, B. Gencturk, M. Dawood, A. Belarbi, Advancements in concrete mix designs: High-performance and ultrahigh-performance concretes from 1970 to 2016, *Journal of Materials in Civil Engineering*, 30, 2018, pp. 04017310.
[164] Soliman, N., A. Tagnit-Hamou, Partial substitution of silica fume with fine glass powder in UHPC: Filling the micro gap, *Construction and Building Materials*, 139, 2017, pp. 374-383.
[165] Tafraoui, A., G. Escadeillas, S. Lebaili, T. Vidal, Metakaolin in the formulation of UHPC, *Construction and Building Materials*, 23, 2009, pp. 669-674.
[166] Teng, L., H. Huang, J. Du, K.H. Khayat, Prediction of fiber orientation and flexural performance of UHPC based on suspending mortar rheology and casting method, *Cement and Concrete Composites*, 122, 2021, pp. 104142.
[167] Teng, L., H. Huang, K.H. Khayat, X. Gao, Simplified analytical model to assess key factors influenced by fiber alignment and their effect on tensile performance of UHPC, *Cement and Concrete Composites*, 127, 2022, pp. 104395.
[168] Teng, L., W. Meng, K.H. Khayat, Rheology control of ultra-high-performance concrete made with different fiber contents, *Cement and Concrete Research*, 138, 2020, pp. 106222.
[169] Wang, J., Q. Sun, Experimental study on improving the compressive strength of UHPC turntable, *Advances in Materials Science and Engineering*, 2020, 2020.

[170] Wang, J., R. Yu, D. Ji, L. Tang, S. Yang, D. Fan, Z. Shui, Y. Leng, K. Liu, Effect of distribution modulus (q) on the properties and microstructure development of a sustainable Ultra-High Performance Concrete (UHPC), *Cement and Concrete Composites*, 125, 2022, pp. 104335.
[171] Wang, X., D. Wu, J. Zhang, R. Yu, D. Hou, Z. Shui, Design of sustainable ultra-high performance concrete: A review, *Construction and Building Materials*, 307, 2021, pp. 124643.
[172] Wang, X., R. Yu, Q. Song, Z. Shui, Z. Liu, S. Wu, D. Hou, Optimized design of ultra-high performance concrete (UHPC) with a high wet packing density, *Cement and Concrete Research*, 126, 2019, pp. 105921.
[173] Wille, K., A.E. Naaman, S. El-Tawil, G.J. Parra-Montesinos, Ultra-high performance concrete and fiber reinforced concrete: achieving strength and ductility without heat curing, *Materials and structures*, 45, 2012, pp. 309-324.
[174] Willey, J.A., *Use of ultra-high performance concrete to mitigate impact and explosive threats*, Missouri University of Science and Technology2013.
[175] Wu, Z., K.H. Khayat, C. Shi, Changes in rheology and mechanical properties of ultra-high performance concrete with silica fume content, *Cement and Concrete Research*, 123, 2019, pp. 105786.
[176] Wu, Z., K.H. Khayat, C. Shi, B.F. Tutikian, Q. Chen, Mechanisms underlying the strength enhancement of UHPC modified with nano-SiO2 and nano-CaCO3, *Cement and Concrete Composites*, 119, 2021, pp. 103992.
[177] Wu, Z., C. Shi, W. He, D. Wang, Static and dynamic compressive properties of ultra-high performance concrete (UHPC) with hybrid steel fiber reinforcements, *Cement and Concrete Composites*, 79, 2017, pp. 148-157.
[178] Yang, J., J. Xia, Z. Zhang, Y. Zou, Z. Wang, J. Zhou, *Experimental and numerical investigations on the mechanical behavior of reinforced concrete arches strengthened with UHPC subjected to asymmetric load*, Structures, Elsevier, 2022, pp. 1158-1175.
[179] Yang, R., R. Yu, Z. Shui, C. Guo, S. Wu, X. Gao, S. Peng, The physical and chemical impact of manufactured sand as a partial replacement material in Ultra-High Performance Concrete (UHPC), *Cement and Concrete Composites*, 99, 2019, pp. 203-213.
[180] Yoo, D.-Y., S. Kim, Comparative pullout behavior of half-hooked and commercial steel fibers embedded in UHPC under static and impact loads, *Cement and Concrete Composites*, 97, 2019, pp. 89-106.
[181] Yu, R., P. Spiesz, H. Brouwers, Mix design and properties assessment of ultra-high performance fibre reinforced concrete (UHPFRC), *Cement and concrete research*, 56, 2014, pp. 29-39.
[182] Zhu, Y., H. Hussein, A. Kumar, G. Chen, A review: Material and structural properties of UHPC at elevated temperatures or fire conditions, *Cement and Concrete Composites*, 123, 2021, pp. 104212.
[183] Zhu, Y., Y. Zhang, H.H. Hussein, J. Liu, G. Chen, Experimental study and theoretical prediction on shrinkage-induced restrained stresses in UHPC-RC composites under normal curing and steam curing, *Cement and Concrete Composites*, 110, 2020, pp. 103602.
[184] Kim, T., J. Olek, Effects of sample preparation and interpretation of thermogravimetric curves on calcium hydroxide in hydrated pastes and mortars, *Transp. Res. Rec.*, 2290, 2012, pp. 10-18.

[185] Costoya Fernández, M.M., *Effect of particle size on the hydration kinetics and microstructural development of tricalcium silicate*, EPFL, 2008.
[186] Lothenbach, B., K. Scrivener, R. Hooton, Supplementary cementitious materials, *Cem. Concr. Res.*, 41, 2011, pp. 1244-1256.
[187] Lin, R.-S., X.-Y. Wang, H.-S. Lee, H.-K. Cho, Hydration and microstructure of cement pastes with calcined Hwangtoh clay, *Materials*, 12, 2019, pp. 458.
[188] Luo, D., J. Wei, Hydration kinetics and phase evolution of Portland cement composites containing sodium-montmorillonite functionalized with a Non-Ionic surfactant, *Construction and Building Materials*, 333, 2022, pp. 127386.
[189] Ellerbrock, R., M. Stein, J. Schaller, Comparing amorphous silica, short-range-ordered silicates and silicic acid species by FTIR, 2022.
[190] Gu, C., J. Yao, Y. Yang, J. Huang, L. Ma, T. Ni, J. Liu, The Relationship of Compressive Strength and Chemically Bound Water Content of High-Volume Fly Ash-Cement Mortar, *Materials*, 14, 2021, pp. 6273.
[191] Young, J.F., W. Hansen, Volume relationships for CSH formation based on hydration stoichiometries, *MRS Online Proceedings Library Archive*, 85, 1986.
[192] Wang, X., H. Lee, Modeling the hydration of concrete incorporating fly ash or slag, *Cem. Concr. Res.*, 40, 2010, pp. 984-996.
[193] ASTM, *Standard Practice for Making and Curing Concrete Test Specimens in the Field*, 2019.
[194] ASTM, *C1698-19 Standard Test Method for Autogenous Strain of Cement Paste and Mortar*, West Conshohocken, PA, 2019.
[195] ASTM, *Standard Test Method for Bulk Electrical Conductivity of Hardened Concrete*, 2012.
[196] ASTM, C109/C109M-16a," Standard Test Method for Compressive Strength of Hydraulic Cement Mortars (using 2-in. Or [50-mm] Cube Specimens)," *Committee C-1 on Cement, ed. West Conshohocken, PA, USA: ASTM International*, 2013.
[197] ASTM, *Standard Test Method for Flexural Performance of Fiber-Reinforced Concrete (Using Beam With Third-Point Loading)*, 2012.
[198] Qiao, P., Z. Zhou, Direct Tension Test for Characterization of Tensile Behavior of Ultra-High Performance Concrete, *Journal of Testing and Evaluation*, 2018.
[199] ASTM, D., Standard test method for length change of hydraulic-cement mortars exposed to a sulfate solution, 2012.
[200] Xu, X., Z. Jin, Y. Yu, N. Li, Impact properties of Ultra High Performance Concrete (UHPC) cured by steam curing and standard curing, *Case Studies in Construction Materials*, 17, 2022, pp. e01321.
[201] Wu, Z., C. Shi, W. He, Comparative study on flexural properties of ultra-high performance concrete with supplementary cementitious materials under different curing regimes, *Construction and Building Materials*, 136, 2017, pp. 307-313.
[202] Roberti, F., V.F. Cesari, P.R. de Matos, F. Pelisser, R. Pilar, High-and ultra-high-performance concrete produced with sulfate-resisting cement and steel microfiber: Autogenous shrinkage, fresh-state, mechanical properties and microstructure characterization, *Construction and Building Materials*, 268, 2021, pp. 121092.
[203] Wardhono, A., *Comparison study of class F and class C fly ashes as cement replacement material on strength development of non-cement mortar*, IOP Conference Series: Materials Science and Engineering, IOP Publishing, 2018, pp. 012019.

[204] Concrete, A.C.C.-o., C. Aggregates, *Standard specification for coal fly ash and raw or calcined natural pozzolan for use in concrete*, ASTM international2023.
[205] Sinha, A., D.Z.H. Lim, J. Wei, A lignin-based capsule system with tunable properties tailored for robust self-healing concrete, *Cement and Concrete Composites*, 132, 2022, pp. 104643.
[206] Association, C.S., Concrete Materials and Methods of Concrete Construction/Test Methods and Standard Practices for Concrete (CSA A23. 1-19), *CSA, Toronto, ON, Canada*, 2019.
[207] Roesler, J., A. Bordelon, A.S. Brand, A. Amirkhanian, *Fiber-Reinforced Concrete for Pavement Overlays: Technical Overview*, Iowa Department of Transportation, 2019.
[208] Ramos, G., Behavior of Prestressed Concrete Bridges with Closure Pour Connections and Diaphragms, 2019.

This page left blank intentionally.

# 10.0 Appendices

This report and the full version of Appendices A to E can be found at https://doi.org/10.7275/xgz6-se87